## Energy concentration by converging shock waves in gases

by

Malte Kjellander

2012 Technical Reports from Royal Institute of Technology KTH Mechanics SE-100 44 Stockholm, Sweden

Akademisk avhandling som med tillstånd av Kungliga Tekniska Högskolan i Stockholm framlägges till offentlig granskning för avläggande av teknologie doktors-examen den 25:e maj 2012, kl. 10:00 i sal D2, Lindstedtsvägen 5, Kungliga Tekniska Högskolan, Stockholm.

© Malte Kjellander 2012
Universitetsservice US-AB, Stockholm 2012

#### Energy concentration by converging shock waves in gases

Malte Kjellander Department of Mechanics, Royal Institute of Technology (KTH) SE–100 44 Stockholm, Sweden

Abstract Converging shock waves have been studied experimentally in a shock tube, and numerically using inviscid calculations and the theory of geometrical shock dynamics. The converging shock waves were created in a shock tube with two modular test sections designed to create cylindrical respectively spherical waves. In the spherical case the shock waves take the shape of spherical cap before propagating into a cone, while the cylindrical shocks converge in a fully circular cylindrical chamber.

The dynamics and symmetry of circular and polygonal cylindrical shock waves with initial Mach numbers ranging from 2 to 4 were studied. The shocked gas at the centre of convergence attains temperatures high enough to emit radiation which is visible to the human eye. The strength and duration of the light pulse due to shock implosion depends on the medium. In this study, shock waves converging in air, argon, nitrogen and propane have been studied. Circular shock waves are very sensitive to disturbances which deform the shock front, decreasing repeatability. Shocks consisting of plane sides making up a symmetrical polygon have a more stable behaviour during focusing, which provides less run-to-run variance in light strength. The radiation from the gas at the implosion centre has been studied photometrically and spectrometrically. The full visible spectrum of the light pulse created by a shock wave in argon has been recorded, showing the gas behaving as a blackbody radiator with apparent temperatures up to 6,000 K. This value is interpreted as a modest estimation of the temperatures actually achieved at the centre as the light has been collected from an area larger than the bright gas core. Circular shock waves attained higher temperatures but the run-to-run variation was significant. The propagation of circular and polygonal shocks was also studied using schlieren photography and compared to the self-similar theory and geometrical shock dynamics, showing good agreement.

Real gas effects must be taken into consideration for calculations at the implosion focal point. Ideal gas numerical and analytical solutions show temperatures and pressures approaching infinity, which is clearly not physical. Real gas effects due to ionisation of the argon atoms have been considered in the numerical work and its effect on the temperature has been calculated.

A second convergent test section was manufactured, designed to smoothly transform a plane shock wave into the shape of a spherical cap. After the convergent transformation the spherical shock propagates through a conical section, where it is aimed to retain the spherical shape and converge in the tip of the truncated cone, which has an end radius of  $0.3 \, \mathrm{mm}$ . Spherical implosion is

more efficient than cylindrical and the target volume is much smaller than that in the cylindrical chamber. The new set-up does not suffer from large losses through reflections. Spectrometric and photometrical measurements of the implosion show significantly stronger radiation of longer duration. Preliminary results show measured apparent blackbody temperatures up to 27,000 K during implosion of shock waves of initial Mach number  $M_S=3.9$ .

**Descriptors:** Shock waves, converging shocks, ionisation, shock dynamics, shock tubes, black body radiation.

#### **Preface**

This doctoral thesis in Engineering Mechanics deals with converging shock waves. The work is mainly experimental and complemented with numerical and theoretical work. The advisors for the project have been Dr. Nicholas Apazidis and Dr. Nils Tillmark. An overview is presented in Part I and Part II consists of the papers listed below. The papers published in journals have been adjusted to the thesis format but except minor corrected typographic errors, their content is otherwise unchanged. The respondent's contributions to each paper are summarised in Part I, Chapter 8.

#### Paper 1

M. Kjellander, N. Tillmark & N. Apazidis, 2010

Thermal radiation from a converging shock implosion. Phys. Fluids 22, 046102.

#### Paper 2

M. Kjellander, N. Tillmark & N. Apazidis, 2010

Shock dynamics of imploding spherical and cylindrical shock waves with real gas effects. *Phys. Fluids* **22**, 116102.

#### Paper 3

V. Eliasson, M. Kjellander & N. Apazidis, 2007

Regular versus Mach reflection for converging polygonal shocks. Shock Waves  ${f 17},$  43–50.

#### Paper 4

M. KJELLANDER, N. TILLMARK & N. APAZIDIS, 2011

Polygonal shock waves: comparison between experiments and geometrical shock dynamics. In proceedings: 28th International Symposium on Shock Waves, 2011, University of Manchester, Manchester, United Kingdom

#### Paper 5

M. Kjellander, N. Tillmark & N. Apazidis, 2011

Experimental determination of self-similarity constant for converging cylindrical shocks. *Phys. Fluids* **23**, 116103.

#### Paper 6

M. Kjellander & N. Apazidis, 2012

Numerical assessment of shock tube with inner body designed to create cylindrical shock waves.  $Technical\ report$ 

#### Paper 7

M. Kjellander, N. Tillmark & N. Apazidis, 2012

Generation of spherical converging shocks in a shock tube by wall shaping. *Manuscript*.

May 2012, Stockholm

Malte Kjellander

#### Contents

Abstract	iii
Preface	v
Part I: Overview and summary	
Chapter 1. Introduction	1
Chapter 2. Basic equations	3
2.1. Equations of motion	3
2.2. Equation of state and equilibrium conditions	4
2.3. Shock waves	6
2.4. Pseudo-steady shock reflections	12
Chapter 3. Shock tubes	14
3.1. The simple shock tube	14
Chapter 4. Converging shock waves	20
4.1. Theoretical background	20
4.2. Experiments in shock tubes	21
4.3. Shocks waves initiated by detonations or explosic	ons 23
4.4. Dynamic instability	26
4.5. Previous work at KTH	27
Chapter 5. Experimental equipment	32
5.1. Shock tube	32
5.2. Cylindrical test section	35
5.3. Flow visualisation: Schlieren optics	41
5.4. Converging test section	48
5.5. Spectroscopic instrumentation and its calibration	50 a
Chapter 6. Numerical calculations	53
Chapter 7. Conclusions and contributions	59
7.1. Cylindrical shock waves	59
7.2. Spherical shock waves	60
Chapter 8. Papers and authors contributions	61

Acknowledgements	65
Appendix A. Specific heat and speed of sound from $\alpha$	66
Appendix B. Coulomb effects on thermodynamic variables	68
References	73
Part II: Papers	
Paper 1: Thermal radiation from a converging shock implosion	85
Paper 2: Shock dynamics of imploding spherical and cylindrical shock waves with real gas effects	115
Paper 3: Regular versus Mach reflection for converging polygonal shocks	135
Paper 4: Polygonal shock waves: comparison between experiments and geometrical shock dynamics	151
Paper 5: Experimental determination of self-similarity constant for converging cylindrical shocks	161
Paper 6: Numerical assessment of shock tube with inner body designed to create cylindrical shock waves	185
Paper 7: Generation of spherical converging shocks in a shock tube by wall shaping.	217

# Part I Overview and summary

#### CHAPTER 1

#### Introduction

Shock waves are essentially waves propagating at velocities higher than the speed of sound. They are very thin and sharply raise the temperature and pressure in the medium they travel through - the stronger the shock, the higher the increase in pressure and temperature. Shock waves can be said to be one of nature's way of spreading local concentrations of energy and are created by sudden releases of energy, such as lightning strikes or explosions. A shock wave created in a point propagates outwards in all directions, weakening in strength, slowing down, as its front swells. Some energy is dissipated through non-reversible processes within the shock front, which further takes energy away and weakens the shock wave. The shock wave heats the gas it propagates through and in this manner the released energy is spread over a large space. Now reverse the process. By some means, create a shock wave spherical in shape which propagates inwards. Although the dissipative losses within the shock front are still present, the shock wave now accelerates as the available space becomes smaller and gets increasingly stronger. Given perfect symmetry, the shock wave will all but coalesce unto a point, creating a very high concentration of energy.

Converging shocks occur naturally in collapsing spheres, ranging in size from microbubbles to supernovae. Except being of interest from a physicist's point of view, present and potential applications are found in e.g. medicine and material science. A regular method to deal with troubling kidney or gallstones is by extracorporeal shock wave lithotripsy. Shock waves generated outside of the body are focused on the stones inside the body, which shatters them. The possibility to use similar methods on other types of unwanted intruders, e.g. some types of cancer cells, is being studied. The shock waves generated to break kidney stones are extremely weak, barely stronger than sound waves. Strong converging shock waves are of interest in material synthesis, where the phase, hardness or other characteristics of a material can be changed through shock wave compression: one example is the synthesis of diamonds from carbon. Attempts to initiate fusion reactions which generally required extremely high temperatures have also been made; e.g. gamma-rays have been detected escaping from shock waves converging in deuterium. All these applications have at least one thing in common: it is of importance to be able to create symmetric shock waves converging to a well-defined focus. To create extreme conditions intuition says symmetry is necessary to focus the energy to an as small volume as possible, whereas in the case of lithotripsy, the shock waves must focus on the target stones so that surrounding body tissue is not damaged.

The first work on converging shocks was an analytical study by Guderley (1942), which was followed by experimentally produced shocks about a decade later (Perry

#### 2 1. INTRODUCTION

& Kantrowitz 1951). Already during the first experiments it was found that the amplification of the converging shocks of initially moderate strength heated the gas at focus to such a degree that it became radiating.

The present work is one of basic research. The aim is to study the dynamics of converging shock waves and the light emissions they create in order to determine what level of energy concentrations are achievable. Converging shock waves were produced in a shock tube with two modular test sections: one designed to create cylindrical shock waves and a second designed to shape the plane circular shocks into the shape of a spherical cap. The propagation of the shocks is studied with schlieren photography and the light pulse from the shock implosions investigated by photometry and spectrometry. Figure 1.1 shows a photograph of the light during a run with the cylindrical test section.

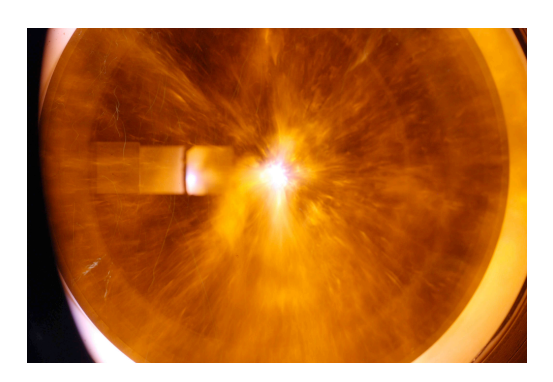


Figure 1.1: Photograph of radiating argon heated by converging shock wave.

#### $1.0.1. \ Thesis \ structure$

The main parts of the thesis are the papers presented in Part II. In the introductory Part I the Chapters 2,3 and 4 are essentially a literature study intended to give an introduction to the topics at hand whereas Chapter 5, 6 and 7 summarise the experimental facility and the results of the present work. The contributions of the individual authors to each paper are stated in Chapter 8. Part II contains seven papers, arranged in the following order: the first three papers appeared in the author's licenciate thesis whereas the remaining four are added to them in chronological order. Papers 1 and 7 are spectrometric studies on the light emissions created by cylindrical respectively spherical shock waves in argon. Paper 2 is a study concerning the influence of real gas effects on converging shocks using the approximate theory of geometric shock dynamics. Papers 3, 4 and 5 deal with the propagation and dynamics of converging cylindrical shock waves of polygonal and circular forms.

#### CHAPTER 2

#### Basic equations

This chapter provides a physical and mathematical description of the gases involved, shock wave jump relations and an introduction to pseudo-steady shock reflections. The gas models used in the thesis are either the standard perfect gas model or the equilibrium model for monatomic gases described in this section.

#### 2.1. Equations of motion

The governing equations of an compressible inviscid fluid are the Euler equations. For an inviscid gas with volumetric mass density  $\rho$ , temperature T, pressure p, internal energy per unit mass e and velocity  $\mathbf{u} = (u, v, w)$  they are written in the conservation form as follows, neglecting body forces and heat addition (see e.g. Anderson 2003).

The conservation of mass:

$$\frac{\partial \rho}{\partial t} + \nabla \cdot (\rho \mathbf{u}) = 0 \tag{2.1}$$

The conservation of momentum:

$$\frac{\partial(\rho \mathbf{u})}{\partial t} + \mathbf{u}\nabla \cdot (\rho \mathbf{u}) = -\nabla p \tag{2.2}$$

The conservation of energy:

$$\frac{\partial}{\partial t} \left[ \rho \left( e + \frac{u^2}{2} \right) \right] + \nabla \cdot \left[ \rho \left( e + \frac{u^2}{2} \right) \mathbf{u} \right] = -\nabla \cdot (p\mathbf{u}) \tag{2.3}$$

The equations need to be closed with an equation of state. At low pressures and temperatures, most real gases behave as thermodynamically perfect gases and fulfil

$$p = \rho RT = nkT \tag{2.4}$$

where R is the specific gas constant, n the number of atoms per unit volume and k the Boltzmann constant. Departures from the perfect state typically occur when the gas attains very high pressures or temperatures but the simplest definition of a real gas is a gas that does not fulfil the perfect gas law. As a

#### 4 2. BASIC EQUATIONS

general equation of state does not exist different models for different regimes must be used. For the present study the most important and influential departures are caused by ionisation in argon, which is covered in the following chapter.

### **2.2.** Ionised monatomic gases: equation of state and equilibrium conditions

This section described how the monatomic gases accounting for ionisation are modelled. The model is taken from established theory, see Vincenti & Kruger (1966), Zel'dovich & Raizer (2002) or Cambel & Jennings (1967). Consider a volume of monatomic gas that is heated to high temperatures. As the translational energy of the gas increases, collisions between particles become more frequent and violent. Through the collisions translational energy is transferred to excite electrons to higher levels or transfer them into a free state, ionising the gas. The gas now consists of several components: neutral atoms, electron and ions of different charge. New variables are needed: generally, the subscript i will used for values connected to the ions and e to the electrons. The electron number density is denoted as  $n_e$  (dimension m<sup>-3</sup>) and the number densities of the heavy particles  $n_i$ ,  $i = 0, 1, ..., \ell$  where i is the charge state of the ion and  $\ell$ the atomic number. For the neutral atoms, i = 0. The total number density of all heavy particles is denoted  $n_H$  and is the sum of all  $n_i$ . The number fraction or degree of ionisation is defined as  $\alpha_e = n_e/n_H$ . The variable  $\alpha_e$  may also be seen as the average number of electrons released by the atoms. The number fractions of heavy particles in ionisation stage i is defined as  $\alpha_i = n_i/n_H$ . From from these definitions follows that

$$\sum_{i=0}^{N} \alpha_i = 1 \tag{2.5}$$

Charge is conserved and an ion in stage i has released i free electrons, which translates into

$$n_e = \sum_{i=1}^{\ell} i n_i = n_H \sum_{i=1}^{\ell} i \alpha_i = n_H \alpha_e \quad \text{and}$$
 (2.6)

$$\alpha_e = \sum_{i=1}^{\ell} i\alpha_i \tag{2.7}$$

The gas consists of a mixture of electron and ionised gases. Assuming that each component individually can be treated as a perfect gas, each has a partial pressure

$$p_e = n_e k T_e \tag{2.8}$$

$$p_i = n_i k T_i, \quad i = 0, 1...\ell$$
 (2.9)

for the electrons and ionic components respectively. If the gases are in local thermodynamic equilibrium they may all be described by a single translational temperature,  $T_e = T_i = T$ . Using the particle fractions as defined above, the total pressure can then be written according to Dalton's law as follows, yielding an equation of state for a partially ionised gas,

$$p = \sum_{i=0}^{\ell} p_i + p_e = kT(\sum_{i=0}^{\ell} n_i + n_e) = n_H kT(1 + \alpha_e)$$
 (2.10)

This can be reformulated using  $k = R_i m_i$ , where  $R_i$  and  $m_i$  is the specific gas constant and molecular mass for the component i. The weight differences between ions of different stages are negligible and the weights and specific gas constants of all ionic components can be approximated with those of neutral argon,  $m_i \approx m_A$  and  $R_i \approx R_A$ . Dropping the index from the gas constant, this leads to  $\rho \approx m_A n_H$  and

$$p = \rho RT(1 + \alpha_e) \tag{2.11}$$

The internal energy content at equilibrium of the gas is divided into translational energy, potential energy of the ions and energy bound in excited electronic states. Each atom, ion or electron has three degrees of freedom and each therefore contributes 3/2kT. When a heavy particle is ionised, the energy required to remove the electron becomes bound as potential energy. The energy required to ionise an atom or ion from state i-1 to state i is  $I_i$ . The total energy required to remove N electrons from an atom is therefore  $I_{tot} = I_1 + I_2 + ... + I_N$ . There also exist electrons excited to higher levels within the ions, whose excitation energy is designated  $W_i$ . Summarising, the internal energy per unit mass of the ionised gas may be expressed as (remembering that  $k/m_i = R_i \approx R$ )

$$e = \frac{3}{2}(1 + \alpha_e)RT + R\sum_{i=1}^{\ell} \alpha_i \sum_{j=1}^{i} \frac{I_j}{k} + R\sum_{i=0}^{\ell} \alpha_i \frac{W_i}{k}$$
 (2.12)

The energy of the excited states may be found from statistical mechanics,

$$W_i = kT^2 \frac{\partial ln Q_i^{el}}{\partial T} \tag{2.13}$$

where  $Q_i^{el}$  is the electronic partition function of component i. The equilibrium values of the ionisation fractions can be determined from the Saha equation, which rewritten using the particle fractions becomes

$$\frac{\alpha_{i+1}}{\alpha_i} = \frac{1 + \alpha_e}{\alpha_e} \left(\frac{2\pi m_e}{h^2}\right)^{3/2} \frac{(kT)^{5/2}}{p} \frac{2Q_{i+1}^{el}}{Q_i^{el}} \exp\left(-\frac{I_{i+1}}{kT}\right)$$
(2.14)

where  $m_e$  is the electron mass and h the Planck constant. For a given p and T equation 2.14 can be solved, e.g. by the iterative method of Trayner & Glowacki (1995). Appendix B contains derivations of the energy and Saha equations and for further reading on the topic ionisational equilibrium, see e.g. Drellishak et al. (1963) or Ebeling (1976).

#### 2.3. Shock waves

A shock wave can be briefly described as a wave with finite amplitude, travelling in a medium at velocities higher than the speed of sound in that medium. Over the shock wave the pressure, velocity, temperature and density change abruptly. This change is not reversible: inside the shock wave dissipation of energy occurs, the entropy increases. Shock waves occur in nature when excessive amounts of energy is released rapidly, such as the crack of lightning or during volcano eruptions<sup>1</sup>. They also occur when an object is travelling at supersonic speed in a medium – or vice versa, if the medium itself is travelling at supersonic speed compared to its surroundings. The physical shock wave is very thin - of the order of a few mean free paths. The entire width of a shock wave therefore only contains a small number of particles in the longitudinal direction and thus the shock appears as nearly a singularity in the continuum model - vet the existence of shock waves was predicted by considering certain waves travelling in a fluid governed by the Euler equations. Before they were studied in any laboratory, what is now called shock waves were discussed as a mathematical peculiarity by prominent 19th century scientists. It was for a long time an open question whether they existed at all in the physical world. A short summary is provided here – for a more in-depth description on the historical development, see e.g. Salas (2007).

Poisson (1808) was the first to solve the propagation of a wave in a fluid described by the Euler equations. A problem, or "a difficulty" as Stokes (1848) called it in his paper treating the subject, appears when considering that different parts of a sinusoidal wave travel at different velocities. Given enough time, the front of the wave will steepen until it becomes vertical: suddenly the solution breaks down. Although he later changed his mind, Stokes suggested that once such a breakdown appears a possible physical result is that the front of the wave continues its motion as a sharp discontinuity.

Riemann (1860) solved the propagation of various initial discontinuities, although he assumed the jumps to be isentropic. He introduced the invariants now bearing his name and the method of characteristics to trace the paths of

<sup>&</sup>lt;sup>1</sup>If these examples interest the reader he is diverted to e.g. Jones *et al.* (1968); Saito *et al.* (2001).

the jumps. Working from a thermodynamic rather than mathematical point of view, Rankine (1870) and Hugoniot (1889) presented the well-known jump conditions over a discontinuity by considering the conservation of mass, momentum and energy. Without the entropy condition, solutions exist for both compression and rarefaction shocks (i.e. where pressure increases and decreases, respectively). The laws of thermodynamics had not yet been firmly established and even though Hugoniot stated that the entropy increases over the compression shocks, it was not until the early 20th century that Lord Rayleigh and Taylor determined that only compression shocks exists in nature, due to the second law of thermodynamics.

The first to actually observe and visualise shock waves was Töpler in 1864. For the purpose he used the schlieren technique that he had recently invented and observed shocks created by electric discharges. Using a precise timing circuit he flashed the schlieren light source after a certain duration from each discharge. By continuously discharging the source and by flashing at the same moment a seemingly stationary schlieren image could be seen in the viewing telescope, which he documented by drawing them by hand. Some of his images and a biography has been published by Krehl & Engemann (1995). Töpler intended to visualise sound and it was not clear what actually had been observed - he designated them as sound waves, travelling at the speed of sound. It would be Mach who, in a set of experiments during 1875-1888 – partly using Töpler's techniques - would not only visualise shock waves but also conclude that these were not sound but the discontinuities described by Riemann. Among other things, Mach also experimentally showed the steepening of a pressure-pulse into a shock wave, the irregular reflections that bear his name and a host of other contributions to many fields of research. The study of shock waves may have had little practical use in the 19th and early 20th century, but with the advent of supersonic flight and high-speed internal flows the purely mathematical and slightly academic discontinuities of Stokes and Riemann have become a major research field.

#### 2.3.1. Generalised Rankine-Hugoniot relations

Figure 2.1(a) illustrates a standing normal shock wave and particle paths. The frame of reference is chosen so that the shock is stationary. The gas upstream is in a known state (1) and flows into the standing shock with a supersonic Mach number  $M_1 = u_1/a_1$ . After passing through the shock, which is treated as a sharp discontinuity, the gas continues at a lower and subsonic Mach number  $M_2 = u_2/a_2$  being in a new state (2). The unknown state (2) is sought. Assuming that the change of quantities is immediate, consider the states immediately up- and downstream of the shock.

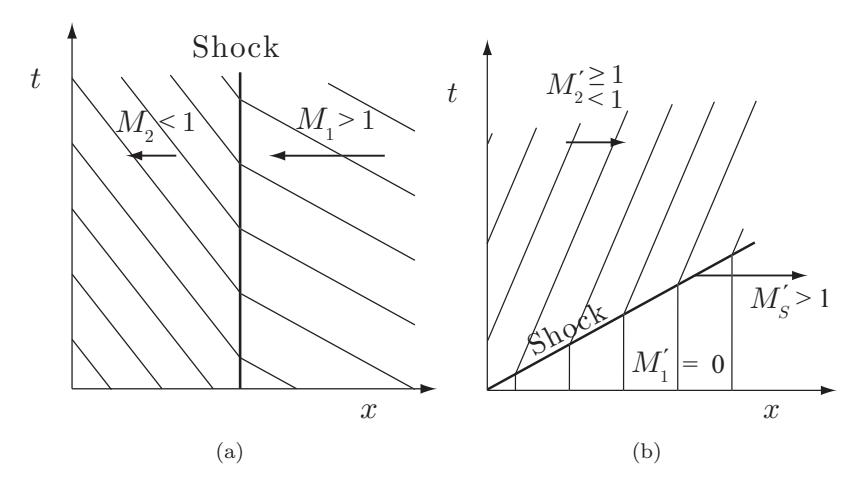


Figure 2.1: Normal shock wave and particle paths in x - t space in a frame moving with the shock (a) and in a laboratory frame (b). After Oertel (1966).

By the laws of conservation,

$$\rho_1 u_1 = \rho_2 u_2 \tag{2.15}$$

$$\rho_1 u_1^2 + p_1 = \rho_2 u_2^2 + p_2 \tag{2.16}$$

$$h_1 + \frac{u_1^2}{2} = h_2 + \frac{u_2^2}{2} \tag{2.17}$$

where h=e+pV is the enthalpy. The entropy condition demands that dissipation causes the entropy of the gas to increase when it passes the shock, or  $s_2 \geq s_1$ . For calorically perfect gases, where  $p=\rho RT$  and  $h=c_pT$  with a constant  $c_p$ , the above set of equations can be solved to give the well-known normal shock relations presented by Rankine and Hugoniot. For many problems a more intuitive approach is from a frame of reference that is at rest with the flow ahead of the shock. The system can be transformed to such a laboratory frame where the shock wave is moving with a velocity  $u'_s = M'_s/a_1$  into an undisturbed state (1) by setting  $u'_s = -u_1$  and  $u'_2 = u_2 - u_1$ . This is illustrated in Fig. 2.1(b): note that the Mach number of the flow behind the shock  $M'_2$  might now be either sub- or supersonic in that frame. The jump relations solved by Eqs. 2.15-2.17 are identical for both frames.

Consider now a shock so strong that the gas in the post-shock condition (2) may no longer be considered perfect. Depending on the gas, it might experience vibrational and rotational excitation, chemical reactions, dissociation or ionisation. It is no longer possible to close the system with a simple equation of state, and iterative methods are needed to find a solution, see for example

$$\begin{array}{c|ccccc} M_{_{\!\!2}}<1 & & M_{_{\!\!1}}>1 \\ & & & \\ \hline p_{_{\!\!2}},\,T_{_{\!\!2}},\,\rho_{_{\!\!2}}, & & & \\ u_{_{\!\!2}},\,h_{_{\!\!2}},\,\alpha_{_{\!\!i,2}} & & p_{_{\!\!1}},\,T_{_{\!\!1}},\,\rho_{_{\!\!1}},\,u_{_{\!\!1}}, \\ h_{_{\!\!1}},\,\,\alpha_{_{\!\!i,1}}\!=0 & & & \end{array}$$

Figure 2.2: Normal shock wave. The state (1) ahead of the shock is known and the equilibrium state (2) is sought.

Resler et al. (1952), Kozlov & Stupitskii (1968), Nieuwenhuijzen et al. (1992) or Michaut et al. (2004). In this overview a short description of the solution procedure for shocks in monatomic gases is added: a strong shock wave is moving into a gas with known conditions  $p_1, T_1, \rho_1, u_1, h_1$  and ionisation  $\alpha_{i,1}$ . The gas in region (1) is in such a state that  $\alpha_{i,1} = [\alpha_1, \alpha_2, ..., \alpha_\ell]_1$  can be considered equal to zero. In a frame attached to the shock wave the system is such as illustrated in Fig. 2.2. To find the state (2) the set of Eqs. 2.15-2.17 needs to be solved. The enthalpy for a monatomic gas in the upstream condition is  $h_1 = 3/2RT + pV = 5/2RT$ . In the post-shock state the gas is ionised; with the energy equation Eq. 2.12 and equation of state Eq. 2.11 the enthalpy in state (2) becomes

$$h_2 = \frac{5}{2}(1 + \alpha_{e,2})RT_2 + R\sum_{i=1}^{\ell} \alpha_{i,2} \sum_{j=1}^{i} \frac{I_j}{k} + RT_2^2 \sum_{i=0}^{\ell} \alpha_{i,2} \frac{\partial \ln Q_i^{el}(T_2)}{\partial T}$$
 (2.18)

The last term, the electronic excitation energy, is often much smaller than the first two and may then be neglected. To calculate  $\alpha$ , local thermodynamic equilibrium is assumed to be established instantaneously and the species distribution is found from the Saha equation, Eq. 2.14. The set of equation is closed, but an iterative method is necessary to find the post-shock conditions:

- 1. An initial value of  $\rho_1/\rho_2$  is estimated, based on e.g. the standard Rankine-Hugoniot equations.
- 2. New values of  $p_2$ ,  $u_2$  and  $h_2$  are calculated using Eqs. 2.15-2.17.
- 3. With the new values, a temperature that simultaneously fulfils the enthalpy according to Eq. 2.18 and the equilibrium conditions according to Eq. 2.14 is found using a numerical method.
- 4. A new  $\rho_1/\rho_2$  can now be found from the equation of state, Eq. 2.11, which is used as a new guess in step 1. The process is repeated until the

error between the guessed and resulting values is as small as acceptable or machine allows.

Figure 2.3 shows the equilibrium conditions behind a normal shock wave in argon with initial temperature T=293 K and three different initial pressures  $p_1=0.1,\ 0.01$  and 0.001 atm. The dashed lines are the Rankine-Hugoniot relations for a perfect gas without ionisation depending only on Mach number. The ionisation has a strongly limiting effect on the temperature as energy is transferred from translational to potential energy. Whereas the compression approaches an asymptotic value  $(\rho_2/\rho_1=4$  for  $\gamma=5/3)$  for the constant-composition gas this is not the case for the ionising shock. The peak corresponds to the maximum of the first ionisation stage, whereafter the translational energy increases relative to the potential energy, resulting in a decrease of density.

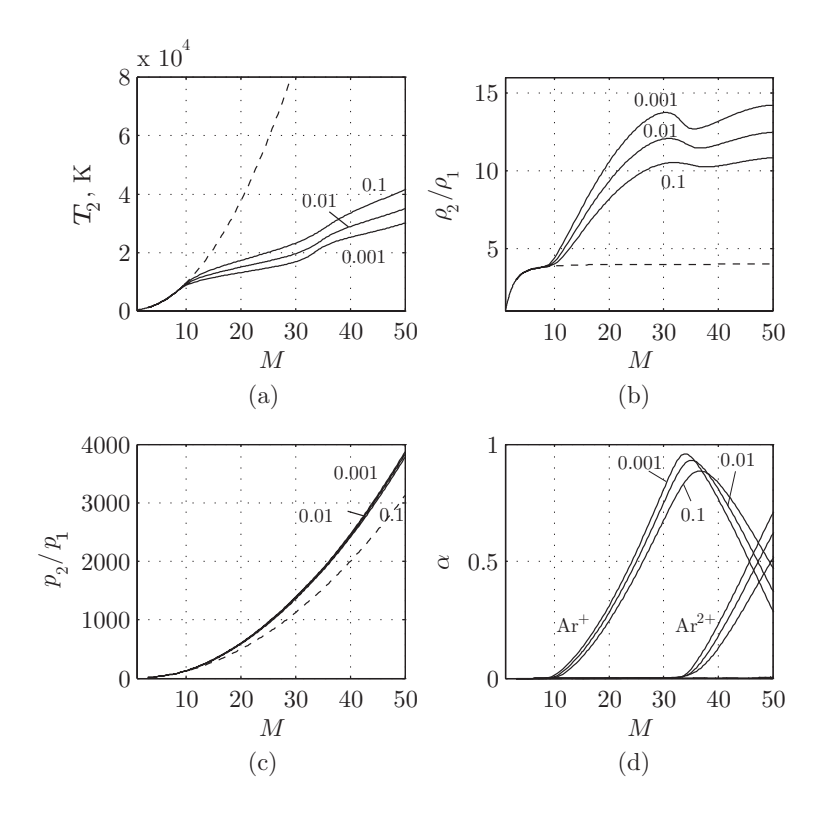


Figure 2.3: Effect of ionisation on shock jump conditions (a-c) at three different initial pressures  $p_1 = 0.1$ , 0.01 and 0.001 atm. Dashed lines represent the non-reacting Rankine-Hugoniot solution. The ionisation is presented in (d).

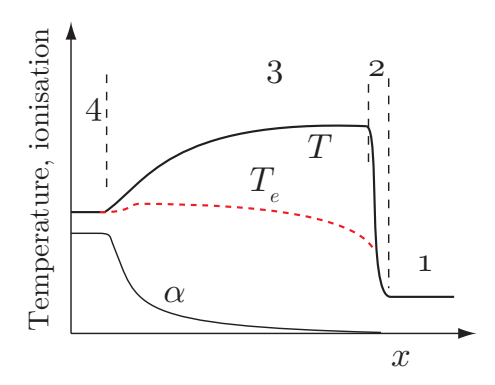


Figure 2.4: Structure of an ionising shock in a monatomic gas, moving towards the right in the positive x-direction: sketch of the temperature and ionisation distribution. Region 1: undisturbed gas, 2: shock front, 3: relaxation zone, 4: equilibrium post-shock state.

#### 2.3.2. Shock structure

In the previous sections it was stated that the shock front was only a few mean free paths thick, and that the gas assumes equilibrium conditions after shock passage. However, the picture becomes more complicated when the temperature jump is so large that reaction processes start behind the shock. The structure of strong shocks in argon has been studied extensively and a working model for the processes has been developed for shock Mach numbers  $M\approx 15-30$ : see e.g. the theoretical studies (Bond 1954; Gross 1965; Wong & Bershader 1966; Hoffert & Lien 1967; Biberman et al. 1971; Matsuzaki 1974; Kaniel et al. 1986) and experimental (Petschek & Byron 1957; Fomin et al. 2003; Yakovlev 2006). Without going into detail, the basic features are presented here.

Figure 2.4 shows a qualitative sketch of the shock structure in a monatomic gas with the variation of temperatures and ionisation fraction. Region (1) contains the undisturbed gas, while region (4) is the post-shock state in thermodynamic equilibrium. Region (2) is the very front of the shock, where translational equilibrium is reached after only a few collisions. The thickness of this region is thereby a few mean free paths. Immediately behind the front is the so called frozen condition as determined with the standard Rankine-Hugoniot equations. Region (3) is the relaxation zone, in which the gas attains its equilibrium values. In this non-equilibrium area the electron and ion gases have different translational temperatures,  $T_e$  and T. A commonly used model is the two-step ionisation process: in the first step atoms are excited to the first electronically excited state and in the second step the excited atoms are subsequently

#### 12 2. BASIC EQUATIONS

ionised. Catalysts for both reactions are either heavy particles or electrons. Once a certain number of energetic electrons have been generated the process increases rapidly – giving rise to a so-called electron avalanche – which can be seen in the sudden increase in ionisation in the figure. The relaxation zone can be substantial: e.g. for a shock of strength  $M \approx 10$  in initial  $p_1 \approx 1$  kPa and  $T_1 = 300$  K it is several centimetres. Increasing the shock strength to  $M_S \approx 20$  decreases the relaxation zone to less than 0.1 mm (Zel'dovich & Raizer 2002).

#### 2.4. Pseudo-steady shock reflections

The interactions between several shock waves or between shocks and solid boundaries are important in this work, so a brief introduction will be given here. The categorisation and transition of reflections are subject to ongoing research and this section is based on the review of the current state of research by Ben-Dor & Takayama (1992) and Ben-Dor (2006). The reflection pattern appearing when a shock wave collides with an inclined solid surface is dependent on the wall inclination  $\theta_w$  and Mach number M of the incoming shock wave (and also on the state of the gas; this introduction only deals with ideal conditions).

The different patterns are categorised in two main groups, regular and irregular reflections. Figure 2.5 illustrates some of the possible shock reflections. A plane shock wave i is moving perpendicularly along a surface from left to right, with velocity  $u_S$  and Mach number  $M_S$ . The shock propagates into a gas at rest. At a certain point it strikes a wall inclination with angle  $\theta_w$ . If  $\theta_w$  is large enough, regular reflection occurs, Fig. 2.5 (a), where the reflected shock r is connected to the incident shock at the surface (point P). Although the shock waves are not stationary in the laboratory frame, the flow is steady in a reference frame attached to point P and such systems are referred to as pseudo-steady.

Irregular reflections occur when the angle  $\theta_w$  is so small that a physical flow can not be established by the regular reflection pattern (a). Irregular reflection includes von Neumann reflection and different forms of Mach reflections. Two different Mach reflections are shown in (b) and (c). A shock wave m normal to the surface appears – called a Mach stem after its first observer – inducing a parallel flow close to the surface. The incident and reflected shock waves instead coalesce with the stem at a point away from the wall, called the triple point (T). A slip line divides the gas that has passed the incident and reflected shock from the gas affected by the stem. If the flow immediately behind the triple point between r and s is supersonic relative to T, the near part of the reflected shock wave becomes straight. This pattern is designated as a transitional Mach reflection (c). A von Neumann reflection is a weaker form of irregular reflection, where the reflected shock r is a compression wave. Experimental visualisation of many types of reflections can be found in e.g. Takayama & Ben-Dor (1993). The different reflection domains are sketched in Fig. 2.6 for shock waves in

perfect air and argon up to  $M_S = 5$ . It should be noted, that for high Mach numbers non-ideal gas effects have large influences on the regimes (see e.g. Ben-Dor & Glass 1979, 1980).

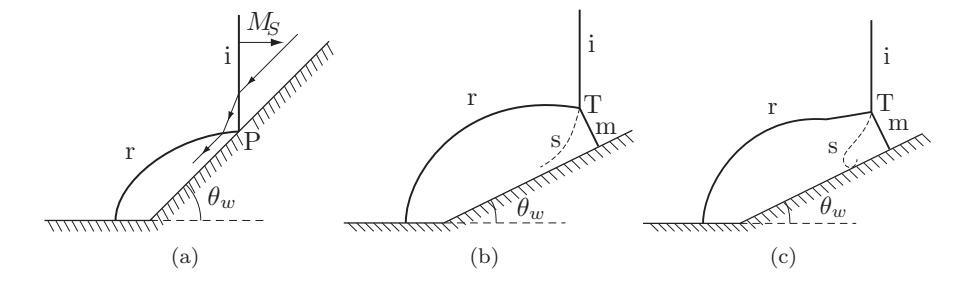


Figure 2.5: A few shock reflection types: (a) regular reflection; (b) single Mach reflection; (c) transitional Mach reflection. The streamlines in figure (a) are presented as seen from a frame of reference attached to the intersection point P.

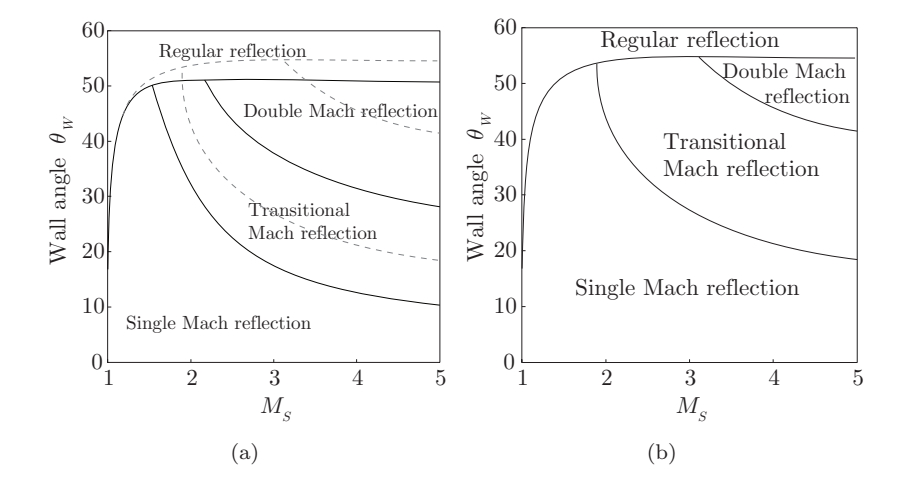


Figure 2.6: Approximate reflection regimes for shock waves in perfect air (a,  $\gamma$ =1.40) and argon (b,  $\gamma$ =1.66), after Ben-Dor (2006) and Lee & Glass (1984) respectively. The transition lines from (b) are inserted as dashed lines in (a) for comparison.

#### CHAPTER 3

#### Shock tubes

Shock tubes are devices used primarily to study high temperature gas kinetics, shock wave interactions and high speed flow. The first shock tube was built slightly more than a century ago: the originator was the French chemist and inventor Paul Vieille (1854-1934) who, working for the French armouries, also invented the smokeless gunpowder. During experiments with detonations he had detected waves in non-reacting gas. For the purpose of investigating if these were the discontinuous waves then recently described by Hugoniot, he constructed the first of the devices which are now called shock tubes: a four meter long tube divided in two sections by a thin diaphragm. One end was filled with air at atmospheric pressure, the other at a high pressure. In a series of experiments, using purely mechanical detectors he registered shock waves travelling at about 600 m/s (Vieille 1899-1900) as well as the expansion wave travelling the opposite direction. A few shock tubes experiments were conducted during the Interwar period (Schardin 1932) but it was not until after the Second World War that a large number of shock tubes appeared in research facilities in many countries, beginning with Payman & Shepherd (1946) in the UK, Bleakney et al. (1949) in the US and Soloukhin (1957) in the USSR. This chapter provides a short introduction to the workings of the simple shock tube. Much of the collected information is based on Oertel (1966) and references therein.

#### 3.1. The simple shock tube

A simple shock tube is a long tube, usually with a rectangular or circular cross section, consisting of two sections separated by a thin membrane. The first is called the driver section and is filled with a gas at high pressure. The other, low pressure section is called the driven section. A shock tube at initial conditions is sketched in Figure 3.1. When the membrane is broken, a shock wave is formed, travelling down the tube. After reflecting on the end wall, the shock wave travels through the previously shock-heated gas compressing and heating it further. The gas is ideally at rest in this hot reflected zone and is used for studying thermodynamics and reactions in hot gases.

3.1.0a. *Flowfield*. In the ideal situation, a one-dimensional flow without viscosity where a shock wave and expansion is instantly formed at membrane burst,

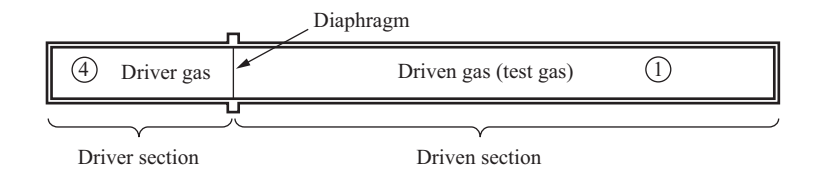


Figure 3.1: Shock tube before membrane burst. Initially the high and low pressure gases are in states (4) and (1) respectively.

the flow field and wave propagation can be solved explicitly from the known initial conditions in states (1) and (4). Fig. 3.2 shows the ideal solution of a shock tube run with air in both sections ("air-air") with  $p_4=14$  atm and  $p_1=1$  atm. At t=0 the membrane bursts and two waves are formed: one shock wave travelling downstream with constant velocity  $u_S$  and Mach number  $M_S = u_S/a_1$  and one expansion wave propagating with u - a or in words, propagating upstream relative to the gas with the local speed of sound. When the gas in the driven section is passed by the shock wave it is compressed to a state (2) and a momentarily accelerated to a velocity  $u_2$ . The high pressure gas is expanded in the expansion wave to a state (3) with the same pressure as the shock-compressed gas and is moving into the driven section with the same velocity as the shock-induced flow,  $p_3 = p_2$  and  $u_3 = u_2$ . The front of the expansion travels upstream with velocity  $-a_4$  (as  $u_4=0$ ) and the tail with velocity  $u_3 - a_3$ : the tail may move either towards the left or right depending on whether  $u_3$  is sub- or supersonic. The whole flow can thus be divided into a number of states: (1) the pre-shock initial low pressure state, (2) the shock-compressed state, (3) the expanded cold state, (4) the initial high pressure state. Between states (3) and (4) is the expansion wave wherein the gas conditions change continuously.

The shock Mach number  $M_S$  is dependent on the pressure, the speed of sound and heat capacity ratio in the initial high and low pressure gases. An expression relating the pressure ratio to the Mach number is given in below (for an explicit derivation, see e.g. Resler *et al.* 1952):

$$\frac{p_4}{p_1} = \left[\frac{2\gamma_1 M_S^2 - (\gamma_1 - 1)}{\gamma_1 + 1}\right] \left[1 - \frac{\gamma_4 - 1}{\gamma_1 + 1} \frac{a_1}{a_4} (M_S - \frac{1}{M_S})\right]^{-\frac{2\gamma_4}{\gamma_4 - 1}}$$
(3.1)

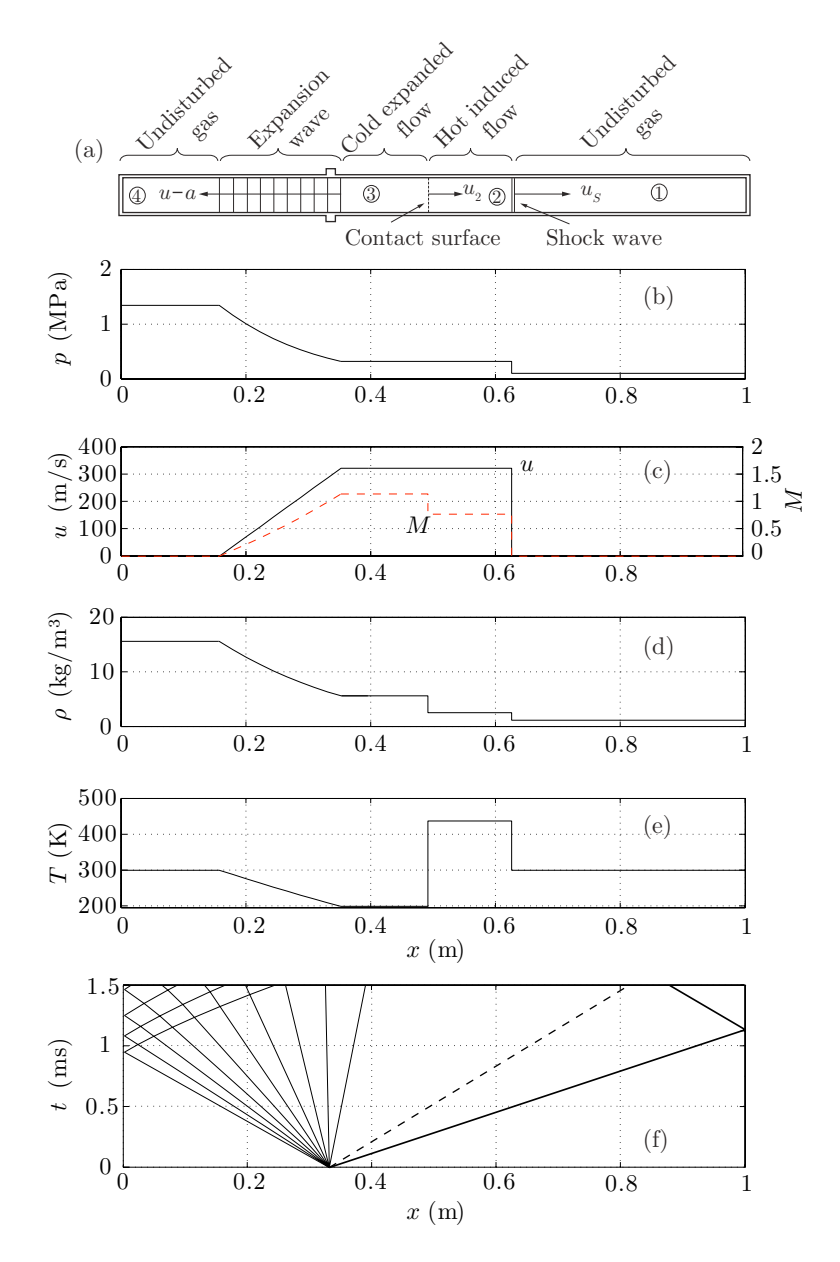


Figure 3.2: An example run in air-air:  $p_4=14$  atm and  $p_1=1$  atm,  $T_4=T_1=300$  K,  $M_S=1.7$ . Flow field (a) and gas conditions at time t=0.5 ms (b) through (e). A wave diagram is shown in (f). The diaphragm is situated at x=0.33 m.

With a known  $M_S$ , state (2) is determined from the normal shock relations. State (3) can then be determined as the velocity and pressure are the same as in state (2) and as it has been isentropically expanded from state (4), the isentropic relations give the density and temperature. When the expansion front reaches the left wall it will reflect and travel back into the expansion, creating a complex region. The values in the expansion, including the complex region, can be calculated using the method of characteristics. The velocity and Mach number  $M_R$  of the reflected shock wave at the right wall are determined by considering that the gas behind it must be at rest. With a known  $M_R$  state (5) behind the reflected shock can be acquired from the shock jump conditions.

Returning to Eq. 3.1: the Mach number of the shock wave  $M_S$  apparently depends on the initial ratios of the pressures  $p_1$  and  $p_4$  and the speeds of sound  $a_1$  and  $a_4$ . Considering the limit  $p_4/p_1 \to \infty$  yields and interesting result,

$$M_{max} = \frac{\gamma_1 + 1}{\gamma_4 - 1} \frac{a_4}{2a_1} + \sqrt{1 + \left(\frac{\gamma_1 + 1}{\gamma_4 - 1} \frac{a_4}{2a_1}\right)^2}$$
(3.2)

or, for strong Mach numbers,

$$M_{max} \approx \frac{\gamma_1 + 1}{\gamma_4 - 1} \frac{a_4}{a_1} \tag{3.3}$$

An upper limit for the achievable Mach number is set by the ratio of speeds of sound no matter how much the pressure is increased. Lighter driver gases thereby generate stronger shock waves and common drivers are, besides cheap air,  $H_2$  and  $H_2$ . Figure 3.3 shows ideal shock Mach numbers  $M_S$  for different gas combinations and pressure ratios.

3.1.0b. Measurement times. During studies of e.g. reaction rates in the hot gas in the zone behind the reflected shock, designated here as state (5), it is essential that the measurement time is long enough. The available time for measurements can be determined and optimised by studying the wave propagation. As such wave diagrams as the one presented in Fig. 3.2 are helpful tools. The measurement time is the time from the instant the shock arrives at the end wall until the first disturbance - a reflected shock or expansion reaches the end wall and changes the gas conditions. By changing the lengths of the low and high pressure sections the wave pattern can be altered in such a way that the measurement time is prolonged. In general the optimal time is when the reflected shock wave, the reflected expansion from the left wall and the contact surface all confluence at the same time.

The measurement time can be increased if the gases and  $M_S$  are chosen such that the reflected shock passes the contact surface without reflection. This can only happen if the driver gas after passing of the reflected shock comes to rest and the pressures in the reflected states 1' and 2' (the states of 1 and 2 that has been passed by the reflected shock) are equal. The contact

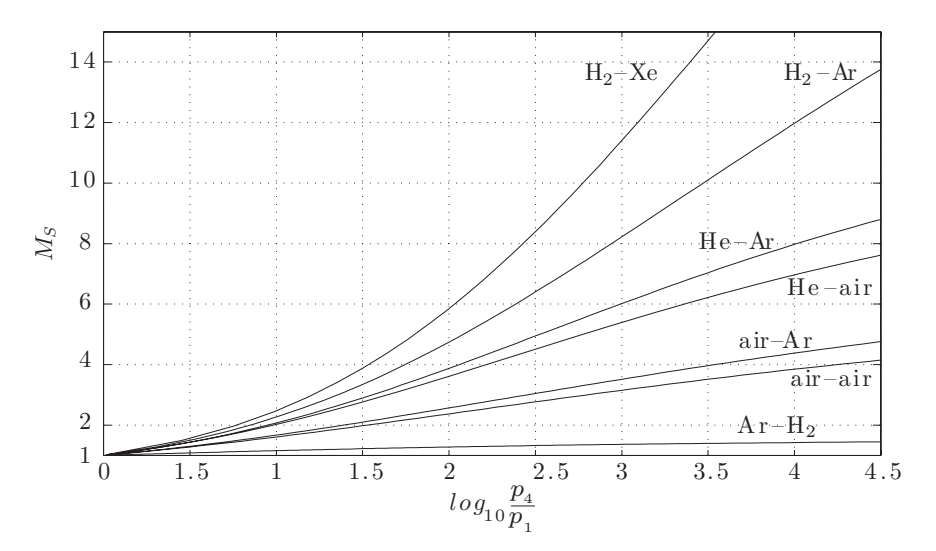


Figure 3.3: Shock Mach number as a function of pressure ratio for different driver-driven gas combinations according to the ideal solution Eq. 3.1. Driven and driver gases are assumed to have the same initial temperature.

surface in this case remains stationary after colliding with the shock. It is not trivial to achieve such a tailored contact especially as it sometimes involves preheating gases to tune the speed of sound, but, for a given Mach number, it can increase the measurement times by roughly a factor 4. Palmer & Knox (1961) have presented tailoring conditions for He-Ar. Hong et al. (2009) presented tailoring conditions for a number of common gases for tubes with difference cross-sections.

As the calculations on measurement times are somewhat lengthy the reader is referred to Oertel (1966).

3.1.0c. Non-ideal effects. Various processes create large or small deviations from the ideal calculations. For the prediction of the shock Mach number, experiments have shown good agreement with the ideal solution for low pressure ratios, but for higher ratios,  $p_4/p_1 \gtrsim 10^4$ , the ideal solution predicts lower Mach numbers than experiments have shown. Causes for this discrepancy may be heating of the high pressure vessel during filling of the pressurised gas, multi-dimensional effects and finite formation of the shock. The membrane opening is finite and a shock is not instantly formed. When the membrane bursts pressure waves start propagating into the low pressure gas. The speed of sound behind the successive waves increases, resulting in a compression of the waves into a shock wave – a compression shock. White (1958) developed a

one-dimensional theory for a finite opening, which was closer to experimental results but still under-predicted the Mach number. Axisymmetric calculations on multi-dimensional effects were carried out by Petrie-Repar & Jacobs (1998) showing that this too had effect.

Behind the shock front a viscous a boundary layer is formed along the walls. For combinations of geometry and shock strength the boundary layers of opposite walls may even unite and the flow is completely turbulent. After reflection, the shock wave will propagate into the boundary layer it had induced and a bifurcation zone is formed as the reflected shock interacts with the boundary layer. Boundary layer effects are large and interactions of boundaries and the contact surface can have great impact on the flow, even decelerating the shock front (Emrich & Wheeler 1958).

#### CHAPTER 4

#### Converging shock waves

This chapter recounts past studies of converging shock wave in a brief review. A large number of papers have been published on the topic, and far from all are mentioned here. Instead a selection has been made that connects more closely to the present study.

#### 4.1. Theoretical background

The first study of converging shock waves was made by Guderley (1942). For the implosion of strong cylindrical and spherical shock waves in an inviscid, perfect gas he derived a local self-similar solution to the gas-dynamic equations of the form

$$\frac{r}{r_0} = \left(1 - \frac{t}{t_0}\right)^{\alpha} \tag{4.1}$$

where  $r_0$  is the initial radius at the time t=0 and  $t_0$  is the instant of focusing, when r=0. The self-similarity exponent  $\alpha$  governs the acceleration of the front, where  $\alpha = 1$  implies a constant velocity. The solution to the problem is not trivial and values of the exponent, which is dependent on the gas in which the shock is propagating, are determined numerically<sup>1</sup>. Solutions to the local and global – taking into consideration the initiation of the shock – problems and determinations of self-similar exponents with an increasing number of significant digits have been made in a great number of studies, e.g. Butler (1954), Stanyukovich (1960), Fujimoto & Mishkin (1978), Lazarus & Richtmyer (1977), Lazarus (1981), Van Dyke & Guttman (1982) and Ponchaut et al. (2006). Table 4.1 shows the history of the exponent for cylindrical and spherical shock waves for  $\gamma = 7/5$  and  $\gamma = 5/3$  and corresponding shock trajectories and velocity increase are plotted in Fig. 4.1. Fujimoto & Mishkin (1978) used a different approach and claimed that the problem might be solved in closed form, which yielded quite different values compared to the rest. Other authors challenged the validity of their method (Lazarus 1980; Van Dyke & Guttman 1982; Wang 1982). Nakamura (1983) used the method of characteristics to solve the problem and acquired exponents agreeing well with the self-similar

 $<sup>^1\</sup>mathrm{An}$  overview of the solution process, and of self-similar problems in general, is presented by Zel'dovich & Raizer (2002), pp. 794–806

solution. Chisnell (1998) made an approximate analytical determination of the exponent agreeing very well with those acquired from the exact form. His solution also gave a description of the flow field at all points behind the converging shock front.

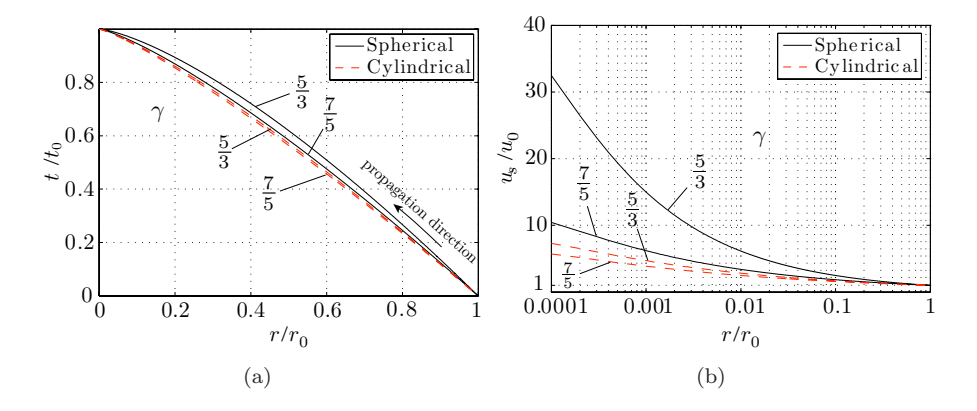


Figure 4.1: Spherical and cylindrical solutions to the self-similar solution Eq. 4.1 for two different  $\gamma$  (values for  $\alpha$  taken from Tab. 4.1). Shock trajectories (a) and velocity amplification for shocks with the same initial velocity at  $u(r = r_0) = u_0$  (b).

Approximate methods neglecting the influence of the flow behind the shock wave were developed independently by Chester (1954), Chisnell (1955, 1957) and Whitham (1958). It is a geometrical approach based on tracking the shock fronts along rays perpendicular to the fronts, analogous to acoustic wave theory. The approach, called the CCW-method after the listed authors above, or geometrical shock dynamics (GSD), works well also with converging shocks and results in good approximations of the similarity solutions. The theory has been expanded by Whitham to allow uniform flow in front of the shock and by Apazidis et al. (2002) to also account for shocks propagating into non-uniform flows. A comparison of the solutions of self-similar theory, geometric shock dynamics as well that of a numerical Euler solver was presented by Hornung et al. (2008), showing good agreement.

#### 4.2. Experiments in shock tubes

To create a radially diverging shock wave is relatively uncomplicated. An explosion or electric spark generates an even shock, propagation radially from the point of the charge. To create a converging shock wave is, naturally, more

 $<sup>^2{\</sup>mbox{Value}}$  depending on intital Mach number.

	Cylindrical	Cylindrical	Spherical	Spherical
	$\gamma = 7/5$	$\gamma = 5/3$	$\gamma = 7/5$	$\gamma = 5/3$
Guderley (1942)	0.834	_	0.717	-
Butler (1954)	0.835	-	0.717	0.688
Stanyukovich (1960)	0.834	-	0.717	-
Welsh (1967)	0.835	0.816	0.717	0.688
Lazarus & Richtmyer (1977)	0.835	0.816	0.717	0.688
Fujimoto & Mishkin (1978)	-	-	0.707	0.687
Mishkin & Fujimoto (1978)	0.828	0.814	-	-
de Neef & Hechtman (1978)	0.835	-	-	-
Van Dyke & Guttman (1982)	0.835	-	0.717	0.688
Nakamura (1983)	0.834	-	0.717	-
Hafner (1988)	0.835	0.816	0.717	0.688
Chisnell (1998)	0.835	0.816	0.717	0.688
Ponchaut et al. (2006)	0.835	0.816	0.717	0.688
Experiments:				
Baronets (1984)		$0.816 \text{ to } 1.0^2$		
Kleine (1985)	0.832 (+0.028, -0.043)			
Takayama et al.(1987)	$0.831 \pm 0.002$			

Table 4.1: Guderley's self-similarity exponent. Significant digits of numerical values reduced to three.  $M_S$  is the initial shock strength during the experiments.

problematic. The methods used by researchers have in principle been variations of two different methods. One, to do the opposite of the point explosion and diverging shock: to generate a shock by placing explosives or an array of spark plugs on a spherical (or cylindrical) periphery, and two: to generate a plane or diverging shock wave and shape it into a converging spherical (or cylindrical) shape by shock reflection and diffraction. In this section is a short review and references to past experiments. Fig. 4.2 shows a collection of different means of creating shock waves.

The first experiments on converging shock waves were carried out by Perry & Kantrowitz (1951). They used a standard shock tube with a tear drop-shaped and centrally aligned inner body, sketched in Fig. 4.2 (a). It's a device that belongs to the second category described above: initially plane shock waves are reflected and diffracted around the tear-drop to form cylindrical shock waves on the downstream side – the shock front at two instants is illustrated in the figure. They found that the shock waves managed to concentrate enough energy to make the gas at the centre of implosion emit light – even more so when argon was used as a test medium. The production of light was believed to be caused by ionised gas and taken as an indicator of high pressures and

temperatures. Two different initial Mach numbers were studied, 1.4 and 1.8. The convergence process was studied with schlieren optics. They observed that symmetrical shapes were more difficult to achieve when the shock waves were initially stronger. For stronger shock waves, reflections appeared on the front breaking up the symmetry.

The design of Perry & Kantrowitz inspired several other works. Kleine (1985) and Takayama et al. (1987) investigated the dynamics and stability of converging circular cylindrical shock waves in air in two different shock tubes with similar construction. The stability and propagation was investigated and they found experimental values for the self-similarity exponent, which agreed well with theory (see Table 4.1). Watanabe & Takayama (1991) continued the stability experiments.

To avoid the need for supports of the inner body that generate the disturbances, a vertical shock tube with an an annular membrane was built at the Tohoku University (Watanabe et al. 1995; Hosseini et al. 2000). The resulting converging shocks kept the circular form better than in shock tubes with supports for the inner body. Deformation of the shock shape still occurred however, and reason for this was believed to be small changes in area between the inner and outer body of the coaxial channel. Also in this experiment cylindrical rods were placed in the test section to introduce corresponding disturbances in a controlled way. One conclusion was that when several modes were combined, the lowest dominated the others.

Hosseini & Takayama (2005b) also constructed a hemispherical chamber for focusing of shock waves created by explosives. The final Mach number of the converging shock was between 2.5 and 8. They created a transparent chamber with aspheric outer surface in order to use holographic interferometry. They produced high-speed video recordings of the shock wave propagation and discussed the influence of different methods of shock generation had on shock stability.

#### 4.3. Shocks waves initiated by detonations or explosions

Lee, Lee and Knystautas at the McGill University in Montreal performed experiments with converging detonation and shock waves in different cylindrical chambers filled with acetylene-oxygen mixtures. Lee & Lee (1965) used a cylindrical drum - a "bomb" - divided in two halves by a disc, with an annular opening between the disc and drum wall that allowed the shock to pass from one section to the other. The explosive gas was ignited in the centre of one of the sections, creating a diverging detonation wave entering the second section where it imploded. They found that the detonation strengthened and imploded as a strong shock.

A second implosion chamber (Knystautas & Lee 1967; Knystautas *et al.* 1969) was created which essentially was a cylindrical disc with a large number of spark plugs positioned in the ends of channels entering the chamber wall.

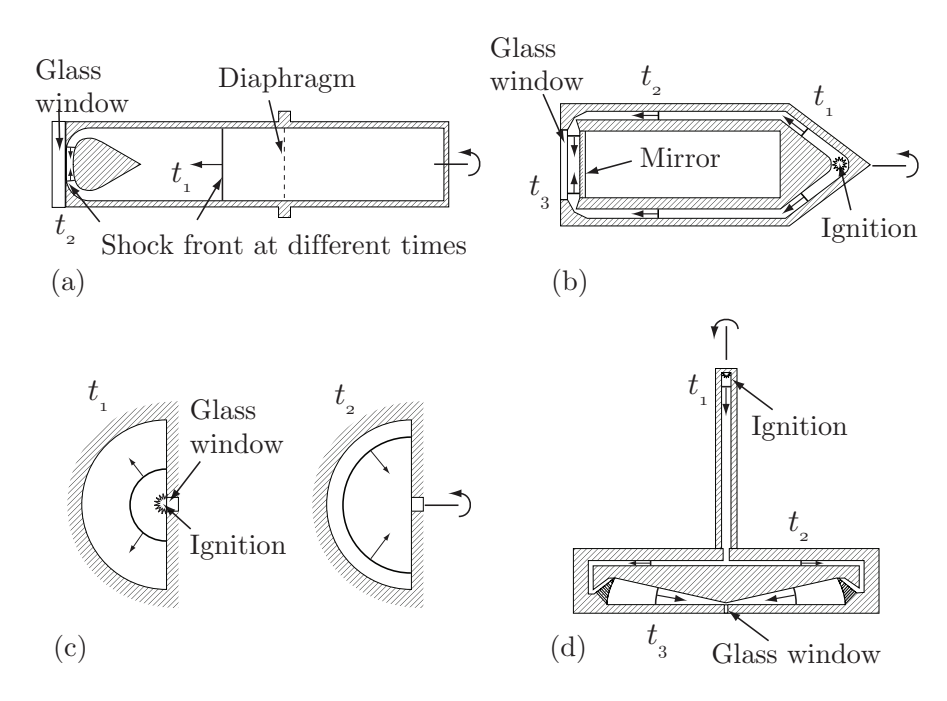


Figure 4.2: Principle of operation of a few experimental devices designed to create converging shock waves. Devices (a) and (b) create cylindrical shocks, (c) and (d) spherical. Part (a), the first experiments: the shock tube of Perry & Kantrowitz (1951). The plane shock is transformed into a cylindrical shape by the tear drop. A glass window provides optical access. Part (b), the cylindrical implosion device of Knystautas & Lee (1971). The gas is ignited in one end and the detonation wave propagates through the annular section  $(t_1 - t_2)$ . Before entering the implosion chamber  $(t_3)$  it passes through a converging duct to compensate for the attenuation in the bend. Part (c), a hemispherical implosion chamber such as the one employed by Glass (1967). The chamber is filled with an explosive gas which is ignited at the centre. A detonation wave is created (time  $t_1$ ), which reflects on the wall and converges as a strong shock ( $t_2$ ). Part (d), the spherical implosion chamber of Terao (1984). Detonation is initiated by a spark plug at the top of the inlet tube  $(t_1)$ . The wave enters a cylindrical space  $(t_2)$  before it is diverted via a large number of ducts into the implosion chamber into the shape of a spherical segment  $(t_3)$ .

Arranged in an even array, they were simultaneously discharged to ignite the gas around the periphery. The detonation waves exit the channel and enter the cylindrical chamber. Knystautas et~al.~(1969) measured the intensity of the light from the implosion focus at two wavelengths and compared to a blackbody radiator, estimating a maximum temperature of  $18.9 \times 10^4$  K. The stability of cylindrical shocks was investigated with a third chamber which was a much improved version of the drum (Knystautas & Lee 1971); it is shown in Fig. 4.2(b). They reported that transverse waves distributed local perturbations thereby attenuating disturbances. Another conclusion was that the energy densities attainable at implosion focus are practically limited by the degree of symmetry.

A considerable amount of work has been made at the University of Toronto by I. I. Glass and co-workers (Flagg & Glass 1968; Roberts & Glass 1971; Glass et al. 1974; Glass & Sharma 1976; Roig & Glass 1977; Glass & Sagie 1982; Saito & Glass 1982). Their research was focused on a hemispherical implosion chamber – a simple sketch of its workings is shown in Fig. 4.2(c) – working on the following principles: in the geometrical centre of the chamber, detonation or shock waves are initiated by explosives or exploding wires. The waves reflect off the periphery and converge as strong shock waves. As a shock wave implodes and reflects from the geometrical centre, a high pressure and temperature region is produced. Roberts & Glass (1971) measured the emission from the light produced during and after implosion. The chamber was filled with a oxygenhydrogen gas at high pressures (6.8–27.2 atm). They found the radiation to be continuous with an apparent blackbody temperature of  $\sim 5000$  K. Saito & Glass (1982) made further spectrometric studies in  $H_2 - O_2$ . A smaller area was investigated and higher temperatures could be measured as averaging effects with colder regions could be avoided: around  $10-13 \times 10^3$  K for regular runs and up to  $17 \times 10^3$  K when the imploding shock was boosted by explosives lined on the periphery. Except for studies on the gas conditions at implosion, the device was also used as a shock tube driver (Glass et al. 1974), to launch projectiles (Flagg & Glass 1968), to synthesise diamonds (Glass & Sharma 1976) and, filled with deuterium-oxygen, in fusion initiation experiments (Glass & Sagie 1982).

Matsuo et al. at the Kumamoto University have conducted a series of investigations using a cylindrical implosion chamber, in which converging shocks are generated by explosives lined on the circular periphery. The light emission at the focus, produced by shocks in air, was measured and compared to the blackbody function. Time-resolved intensity was measured with photomultiplier tubes at a number of separate wavelengths between 400 and 500 nm and temperatures in the range of 13,000-34,000 K were found (Matsuo & Nakamura

 $<sup>^3</sup>$ It was later pointed out by Ref. Roberts & Glass (1971) that the temperature analysis was flawed due to erroneous use of Wien's law.

1980, 1981; Matsuo *et al.* 1983, 1985). Numerical work was made in connection to the experiments (Matsuo 1983; Matsuo & Fujiwara 1990).

Terao (1983) constructed a cylindrical and a hemispherical chamber to study converging cylindrical and spherical shock waves, carrying out pressure and propagation measurements. In a number of papers measurements on spherical converging detonation waves in a propane-oxygen gas were presented (Terao 1984; Terao & Wagner 1991; Terao et al. 1995). The propagation and pressure evolution of the shocks were studied and compared with theory. Spectrometric measurements on the light emissions were made and high gas and electron temperatures at the implosion focus (Terao et al. 1995) were reported. One of his constructions is sketched in Fig. 4.2 (d).

#### 4.4. Dynamic instability

The question whether converging shocks are dynamically stable is of great importance. Perry and Kantrowitz observed how "shock-shocks", appeared on a circular shock front breaking up the symmetry. The disturbances had been introduced by the supporting struts of the inner body. Butler (1954) conducted perturbation calculations showing that strong cylindrical shocks are unstable and Whitham (1973) used his ray-shock formulation to come to the same conclusion. Neemeh & Ahmad (1986) studied the stability of cylindrical shock waves, experimentally and theoretically. Perturbations were introduced externally, by placing cylindrical rods in the path of the shocks. They made a number of conclusions: the region of collapse was shifted due to the disturbance and depending on whether the shock was strong or weak, the shift was either on the disturbed side of the centre or beyond. Perturbations were found to grow exponentially, in good agreement with Butler's theoretical work, indicating that cylindrical shocks are unstable.

Stability was investigated by Takayama et al. (1987) in two tubes (in Sendai, Japan and Aachen, Germany) of similar design: one tube had three supporting struts for the inner body and the other four. In the tube with three struts the deformations became triangular, while square deformations appeared in the second tube. The deformations were designated as three- and four-mode instabilities. The stability of cylindrical shock waves was further studied in the Sendai tube by Watanabe & Takayama (1991). Using holographic interferometry the shock waves and density variations in the whole flow field behind them were studied. They showed how initial disturbances in the density and pressure fields behind a shock that initially looked completely circular grew as the shock converged. The shock shape slowly deformed until the gradients behind the front became so large Mach reflections occurred.

The tube at KTH, which works on similar principles, also exhibits the four-mode instability due to the struts. The multiple-exposure schlieren image in Fig. 4.3(a) shows how the initially circular shock is progressively deformed and eventually collapses as Mach reflections occur. Fig. 4.3(b) shows a reflected

shock wave and how the circular shape is retained. Close-ups of initially circular shock waves are presented in Fig 4.4, at radii equal and less than that of the last central exposure in Fig. 4.3(a). Fig 4.4(d) shows a reflected shock that regains the circular shape almost instantly.

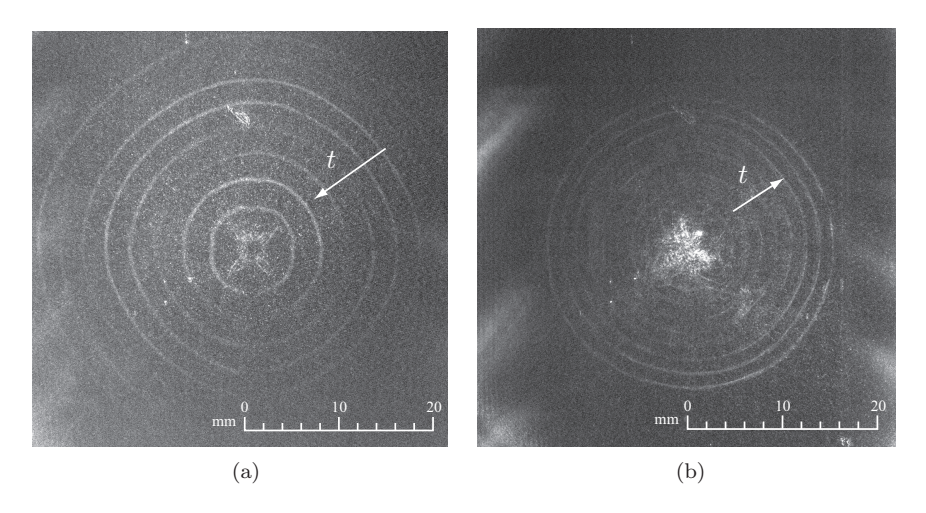


Figure 4.3: Multiply exposed schlieren images of circular cylindrical shock wave: (a) converging shock; (b) diverging shock after focus. The gradual collapse of the circular shape that culminates in the appearance of reflections may be seen in (a). Each exposure is  $0.3~\mu s$  and the delays between them are  $2.2~\mu s$ .

## 4.5. Previous work at KTH

Experiments on converging shock wave were initiated at KTH Fluids Physics Laboratory in 1996. Apazidis & Lesser (1996) conducted a theoretical study using Whitham's geometrical shock dynamics to design a chamber aimed to produce converging polygonal shock waves. The background to this was the numerical work by Henshaw et al. (1986) and Schwendeman & Whitham (1987) who found that a symmetric polygonal shock is dynamically stable in the sense that the shock front will undergo a periodic transformation between n and 2n sided polygonal form while retaining the symmetry of the shock structure. (Johansson et al. 1999; Apazidis et al. 2002) proceeded to build a confined cylindrical chamber with smooth exchangeable boundaries. A shock wave was generated in the centre of the chamber by electric discharges or exploding wires. The shock wave diverged, reflected on the smooth polygonal boundary and converged. Schlieren photography was used for visualisation. The experimental results agreed well with the modified geometrical shock dynamics for shocks

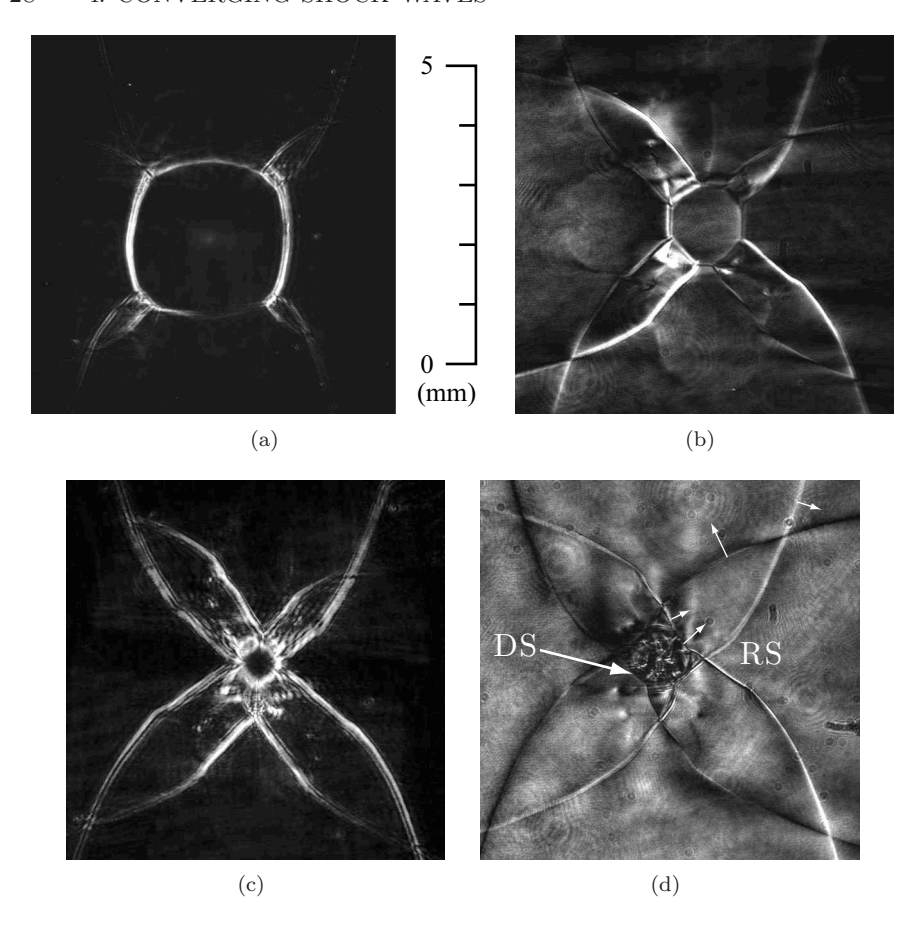


Figure 4.4: Schlieren photographs of the collapse of cylindrical shock waves. The scale applies for all images. The photographs are from separate runs. Image (d) shows a reflected diverging shock wave (DS). The shock wave is clearly seen framing the turbulent region. The eight reflected shocks (RS) are those created from the Mach reflections seen in Figs. (a)–(c). Small arrows indicate wave direction.

moving into a non-uniform flow. More information can be found in the licentiate thesis by Johansson (2000).

However, the method of initiating the shock in the chamber created a disturbance zone in the centre. To avoid these disturbances a horizontal shock tube was constructed. The tube works on similar principles as that of Perry & Kantrowitz (1951) and Takayama  $et\ al.\ (1987)$  and is described in Chapter 5.

The shock tube has exchangeable reflector boundaries akin to those used in the confined chamber. Polygonal shocks with different number of sides were generated in the tube and studied with schlieren optics (Eliasson  $et\ al.\ 2006$ ). The four-mode instability reported by Takayama  $et\ al.\ (1987)$  was also observed in the KTH tube. Another way of reshaping the shocks was used, previously employed by Wu  $et\ al.\ (1977)$ , Neemeh & Ahmad (1986): small cylinders were inserted in the tube to deform the shocks into polygonal shapes (Eliasson  $et\ al.\ 2007\ a$ ). The light production was also studied with a photomultiplier tube (Eliasson  $et\ al.\ 2007\ b$ ). The total intensity of the light pulse was measured for polygonal and circular shock shapes. It was shown that the light intensity between different shock tube runs was more consistent when the shocks had polygonal shapes, albeit not as strong. More information can be found in the doctoral thesis by Eliasson (2007).

## Summary converging shock waves

Table 4.2 lists a number of experimental studies, covering the past six decades. The Method column specifies how the shock waves are initiated and their geometry: C for cylindrical and S for spherical (including hemispherical etc.). In the detonation-driven experiments the test gas itself is ignited, while in those categorised as "explosive" shock waves in non-combustible gas are created with explosive charges. The Measurement column briefly lists which methods of diagnostics were used and/or what was the focus of the study: the temperature measurements were made by spectroscopy while visualisation was made with various methods and therefore written out explicitly. Although the author makes no pretence that the list is complete,<sup>4</sup> it gives an overview of the past and present experiments and groups. The possibility or promise to generate extremely high temperatures and pressures continues to drive interest in the field. New methods of shock shaping are investigated to overcome the problems with asymmetric or unstable shock waves (e.g. Dimotakis & Samtaney 2006; Zhai et al. 2010; Vandenboomgaerde & Aymard. 2011) and new experiments continues to appear.

 $<sup>^4\</sup>mathrm{Especially}$  a large number of Russian works are left out (see e.g. Sokolov 1990, and references therein).

Measurements

temperature

stability

temperature

smoke film

temperature

temperature

Author(s) (year) Test gas Method (geometry) Perry & Kantrowitz (1951) air, Ar shock tube (C) schlieren, photometry (C) Belokon et al. (1965)  $C_2H_2$ - $O_2$ Lee & Lee (1965) detonation (C) streak photography, pressure Knystautas & Lee (1967)  $C_2H_2-O_2$ detonation (C) schlieren photography Flagg & Glass (1968)  $H_2$ - $O_2$ detonation (S) applied: hyper-velocity launcher Knystautas et al. (1969)  $C_2H_2-O_2$ detonation (C) streak photography, temperature Lee & Knystautas (1971)  $C_2H_2-O_2$ detonation (C) Knystautas & Lee (1971)  $C_2H_2-O_2$ detonation (C) schlieren photography Roberts & Glass (1971)  $H_2$ - $O_2$ -Hedetonation (S) Fujiwara et al. (1971)  $H_2$ - $O_2$ detonation (C) Glass (1972) comprehensive report on project Setchell et al. (1972) Arshock tube (conical) velocity (piezo-electric probe), schlieren photography Fujiwara & Taki (1974)  $C_2H_2-O_2$ detonation (C) Glass & Sharma (1976)  $H_2$ - $O_2$ detonation (S) applied: diamond synthesis Wu et al. (1977) shock tube (C) air Matsuo & Nakamura (1980) explosives (C) photography, streak photography air Wu et al. (1980) air shock tube (C) schlieren photography, pressure Baronets (1981) Ar induction-discharge (C) photography, schlieren Glass & Sagie (1982)  $D_2$ - $O_2$ detonation (S) scintillator, applied: fusion initiation Saito & Glass (1982)  $H_2$ - $O_2$ detonation (S) Baronets (1984) Ar induction-discharge (C) photography, schlieren, temperature Matsuo (1983) air explosives (C) spectrometry, photometry  $C_3H_8-O_2$ Terao (1984) detonation (S) gas and electron temperature

Table 4.2: waves in gases. Continues on the next page. Sixty years of experiments with converging shock and detonation

Author(s) (year)	Test gas	Method (geometry)	Measurements	
Berezhetskaya et al. (1984)	air	spark discharge (C)	shadowgraphy, pressure	
Kleine (1985)	air	shock tube (C)	schlieren	
Takayama et al. (1987)	air	shock tubes (C)	stability, holographic interferometry, pressure	
Matsuo et al. (1985)	air	explosives (C)	spectrometry, photometry, shadowgraphy	
Barkhudarov et al. (1988)		spark discharge (C)	shadowgraphy	
de Rosa <i>et al.</i> (1991)	air	electric discharge (S)	interferometry, shadowgraphy	
Terao & Wagner (1991)	$C_3H_8$ - $O_2$	detonation (S)	pressure, temperature	
Baronets (1994)	Ar	induction-discharge (C)	wave propagation (shadowgraphy)	
Fujiwara et al. (1992)	air	detonation, flyer disc (C)	propagation (photography)	
Watanabe & Takayama (1991)	air	shock tube(C)	stability, interferometry, pressure	
Terao et al. (1995)	$C_3H_8$ - $O_2$	detonation (S)	temperature	
Watanabe $et~al.~(1995)$	air	vertical shock tube (C)	proof of concept	
Johansson et al. (1999)	air	electric discharge (C)	schlieren	
Hosseini et al. (2000)	air	vertical shock tube (C)	interferometry	
Hosseini & Takayama (2005 $a$ )	various	vertical shock tube (C)	Richtmyer-Meshkov instability, interferometry, $\boldsymbol{p}$	
Hosseini & Takayama (2005 $b$ )	air	explosives (S)	propagation, stability, shadowgraphy	
Eliasson et al. (2006, 2007a)	air	shock tube (C)	schlieren	
Eliasson et al. $(2007b)$	air, Ar	shock tube (C)	photometry, schlieren	
Bond <i>et al.</i> (2009)	$CO_2$ , $N_2$	shock tube (wedge)	schlieren, pressure	
Hosseini & Takayama (2009)	air	vertical shock tube (C)	interferometry, pressure	
Zhai et al. (2010)	air	shock tube (C)	schlieren	
Kjellander et al. (2010, 2011)	various	shock tube (C)	schlieren, photometry (this work)	

#### CHAPTER 5

# Experimental equipment

The experiments were performed at the shock tube facility of the *Fluid Physics Laboratory* at *KTH Mechanics*. The facility consists of a shock tube with circular cross section and equipment for detection and measurement of shock propagation and light emissions. Two end sections ("test sections") on the tube have been used; one designed to create cylindrical converging shock waves and a second to obtain spherical shocks. This chapter describes the experimental setup and serves as an introduction to future users of the facility.

# 5.1. Shock tube

This section describes the shock tube and equipment common to both test sections whereas the test sections are described in separate sections. The common section of the shock tube is circular with an inner diameter of 80 mm and a length of 1830 mm including the driver section. An outline of the facility is given in Figure 5.1, where the capital letters designate different parts of the tube: (A) is the driver section, (B) and (C) the driven section. The diaphragm is located at the intersection of parts (A) and (B). The driven section consists of an inlet tube (B), its purpose is to allow the shock wave to attain a plane form before entering the test section (C). The low pressure section is evacuated by a two-stage rotary vacuum pump connected to the tube at (6.). Test gas is introduced into the tube through the valve at (5.). When a test gas other than air is used, the section is repeatedly evacuated and filled with the gas twice to ensure pure test gas in the test section. After the final evacuation the gas is allowed to retain room temperature, a process that takes about two minutes. The argon gas used in the present experiments had a purity rate of 99.99%.



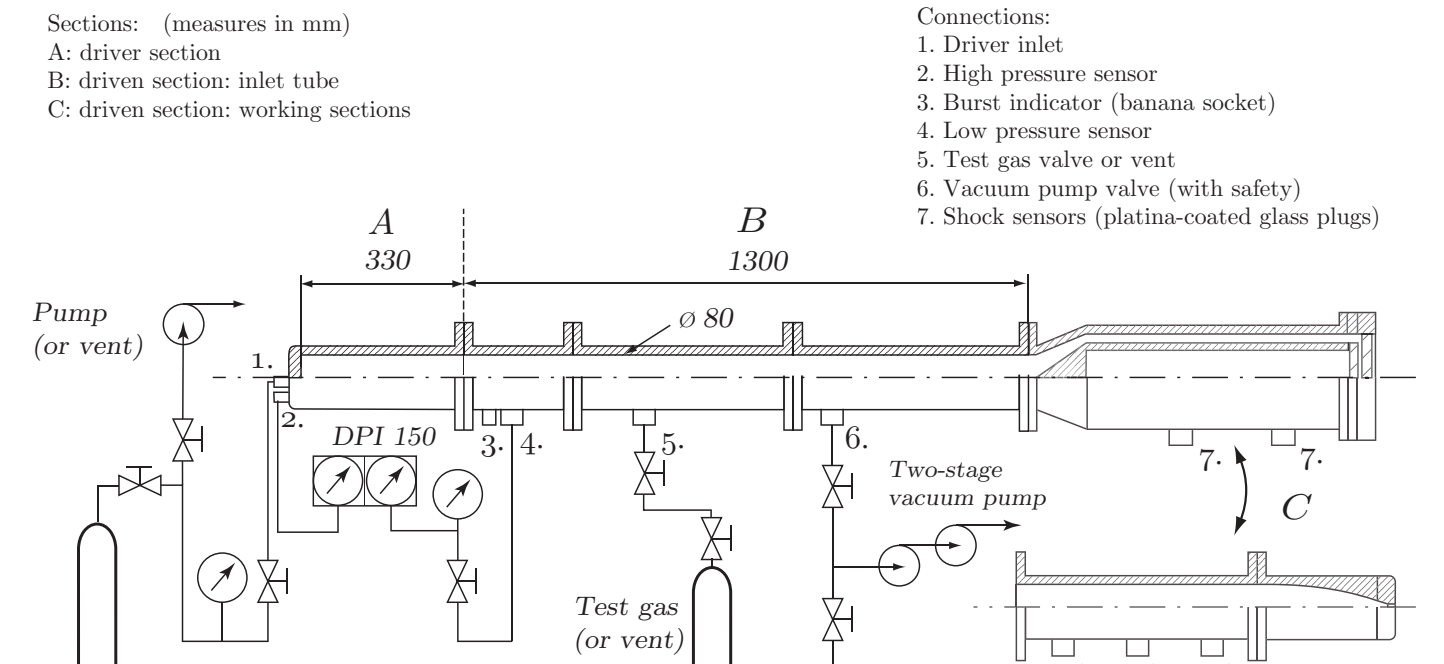


Figure 5.1: Schematic of the shock tube facility. The two working sections (C) are described in separate parts. DPI 150: the Druck pressure indicator recording  $p_4$  and  $p_1$ , the high and low pressures before membrane rupture.

Driver gas

Membrane	Breaking pressure	Typical $M_s$
Al 0.3 mm	0.8 MPa	1.7 - 2.5
Al $0.5 \text{ mm}$	1.6 MPa	2 - 6
Al $0.7 \text{ mm}$	2.3 MPa	4 - 8
Mylar 0.05 mm	0.3  MPa	1.3 - 2

Table 5.1: Breaking pressures  $(p_4 - p_1)$  for membranes of different material and thickness and typical Mach number ranges for which the membranes were used. Depending on driver filling time and knife sharpness the measured pressures could be varied with about 200 kPa for the thicker Al membranes and 100 kPa for the thinner. The plastic mylar membranes were used only occasionally and no such variation has been tested. Run-to-run variations for all diaphragms were around 10-20 kPa.

Regular air or commercial helium were used as driver gas and introduced at connection (1.). To get full control over the driver gas composition when only helium was used the driver section was evacuated to about 2.5 kPa prior to filling. Filling the driver section must be done slowly. It is essential that the high pressure gas is in thermal equilibrium with its surrounding to obtain a correct gas temperature. Moreover the pressure transducer is located some distance from the membrane and connected through a small tube, which in the case of a rapid gas filling would give a false pressure reading.

The membranes are inserted in a flange between sections (A) and (B). The driver section is mounted on slides attached to the driven section. A cross-shaped knife that ensures consistency in the mechanical opening process and membrane ruptures at a set pressure difference is located behind the diaphragm at the low-pressure side. The pressure difference required forcing the diaphragm to- wards the knife is determined by the thickness and strength of the membrane. During present experiments mostly aluminium diaphragms were used but plastic mylar-film was also used to obtain weaker shocks. Table 5.1 shows the bursting pressures and Fig. 5.2 shows a photograph of ruptured membranes. The 0.3 mm aluminium diaphragms had a tendency to be ripped apart and clutter the tube with debris, and were for that reason used sparingly. The burst pressure and its variation between runs are dependent on the handling of the filling of the gas and may thus differ from the tabulated values. The sharpness of the knife-edge also influences the bursting pressure. If care is taken to fill the tube in the same manner each run, experience shows that the variation between shots is as low as 10 kPa.

The pressures in the sections are measured with a pressure transducer and indicator (GE Druck DPI 150), connected to the driver section at (2.) and to the driven section at (4.). An external module (GE Druck IDOS) connected to

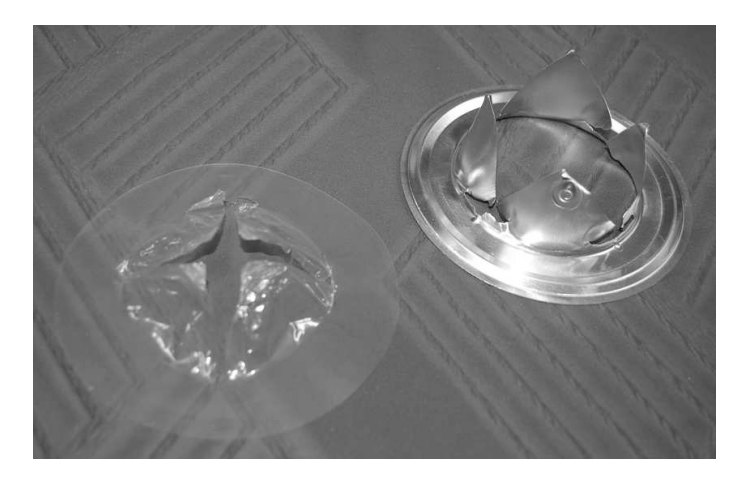


Figure 5.2: Two used membranes; one 0.05 mm plastic film and one 0.5 mm aluminium membrane. The Al membrane shows the imprint of the burst indicator on the tip of one leaf.

the indicator is used to measure the high pressure. The pressure at the instant of membrane rupture is registered and assumed to be the high pressure  $p_4$ . The shock speed is measured by means of temperature sensors sensing the shock passing the sensor, The sensor element is a strip of platinum film painted on the flat surface at the end of a 10 mm diameter glass cylinder inserted through the shock tube wall and aligned flush with the inner surface of the tube. They are mounted on the test sections but are de-scribed here as they are common to both sections. The platinum strip is connected to a high frequency amplifier through a high pass filter and the resistance change in the strip is instant when the shock passes its surface. The circuit diagram is shown in Fig. 5.3. Fig. 5.4 shows a graph over measured Mach numbers compared with the ideal solution Eq. 3.1. The measured Mach numbers are smaller than the ideal values except for the smallest pressure ratios. The plotted Mach numbers have been measured in either of the two test sections; they have not been distinguished in the graph as no different trend could be seen.

# 5.2. Cylindrical test section

One working section is designed to create cylindrical converging shock waves. It is similar in principle to the shock tubes of Perry & Kantrowitz (1951) and Takayama et al. (1987). A coaxially aligned conical inner body transforms the plane tube cross-section to an annular channel, which opens into an open compartment where the shock wave converges cylindrically. The total cross-section is kept constant through the plane tube, transformation section and

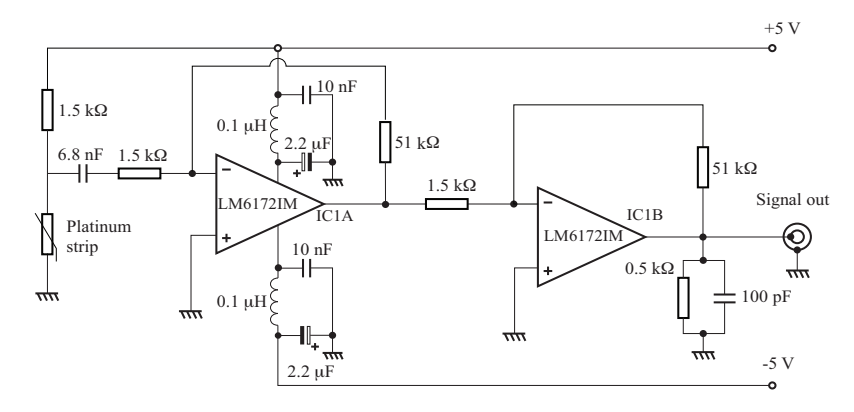


Figure 5.3: Circuit diagram of shock sensor amplifier.

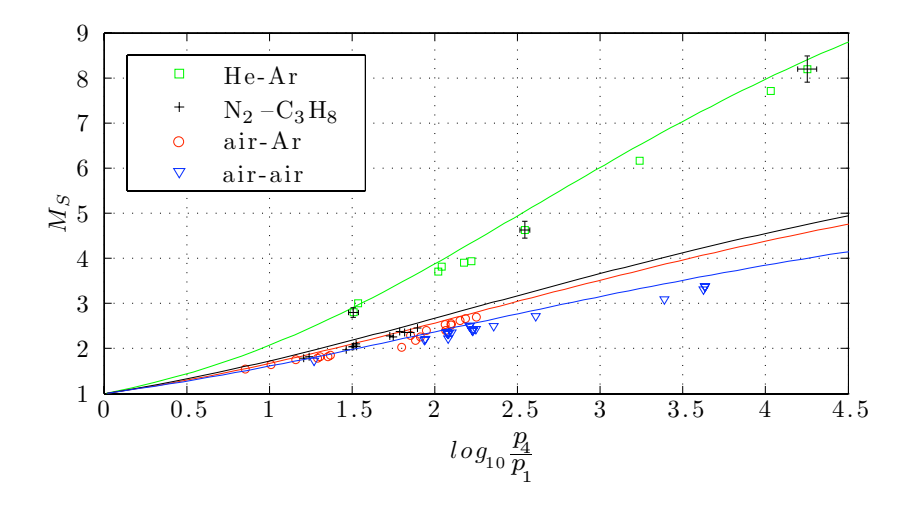


Figure 5.4: Measured Mach numbers  $M_S$  for different pressure ratios compared with the ideal solution Eq. 3.1. Typical measurement errors for a few Mach numbers and pressure ratios have been added; they are similar for all gas combinations.

annular channel. The height of the channel is 10 mm and ends into the open chamber with a  $90^{\circ}$  bend. The test section is made up of this open chamber and is 5 mm wide and has a radius of 70 mm. The shock wave reflects off the end wall of the annular channel and diffracts down into the test section. A high pressure and temperature region created by the reflection off the end wall

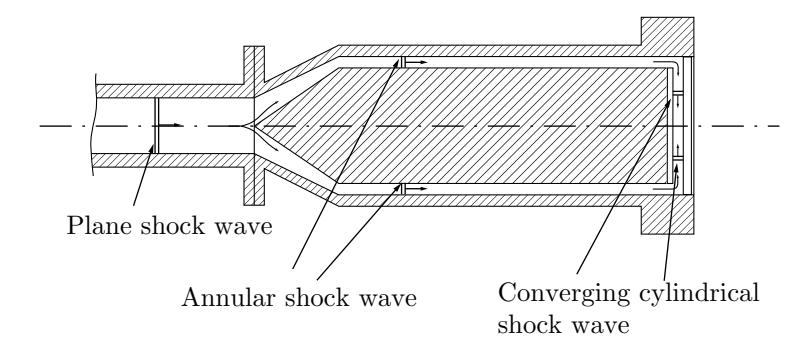


Figure 5.5: Sketch of the shock wave propagation through the tube. The plane shock enters the transformation section from the inlet tube, becomes annular before going through the bend into the cylindrical test section. The part of the shock wave that reflects on the test section wall and returns up the annular channel is omitted for clarity.

drives the flow towards the centre of the cylindrical test section. A drawing of the construction is shown in Figure 5.6; note that the second set of supports is rotated by 45° around the central axis from the first set. The shock propagation is illustrated in Figure 5.5. The test section is framed on both sides by glass windows for easy visualisation: the inner body is hollow to allow equipment for illumination of the test section. The observation window is a 15 mm thick thermal-resistant borosilicate glass (Borofloat 33) disc with optical transmission down to the UV wavelengths.

The shock sensors are inserted flush with the outer wall of the annular channel and separated by 25.0 cm.

## 5.2.1. Triggering and Synchronisation

Capturing images or spectra of a very rapid phenomenon requires an accurate triggering system to turn on cameras or other equipment. Several triggering methods have been used: using the shock sensors, a shock-deflected laser system and photo-multiplier tubes.

5.2.1a. Shock sensor triggering. The temperature sensors positioned on the outer surface of the annular tube may be used for triggering. It is a robust system and apt for all triggering purposes except when rapid events very close to the focal region are studied, when a more precise system is necessary. The shock wave propagation time from passing the downstream shock sensor to implosion in the test section is several hundred  $\mu$ s and the time variation between runs

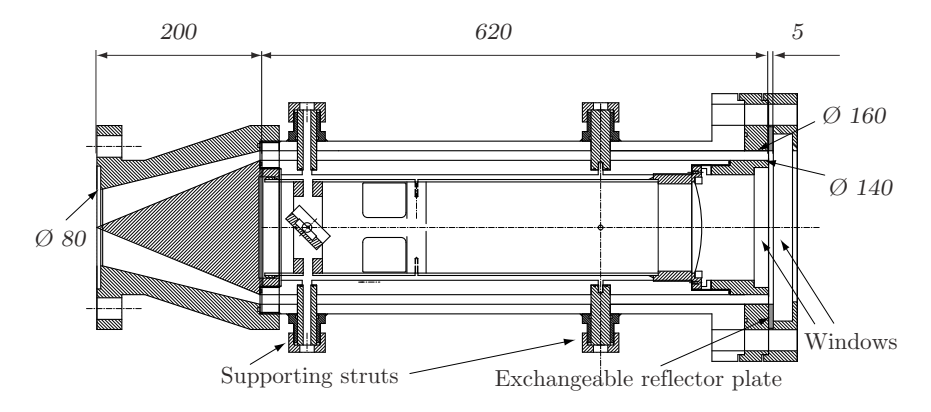
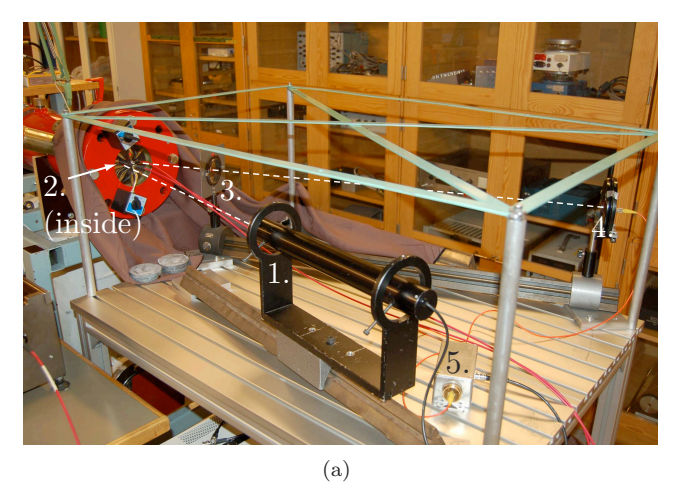


Figure 5.6: Drawing of the annular-cylindrical unit. The second set of supporting struts is rotated by 45° from the first around the axis. The first set is hollow to allow a laser beam to illuminate the test section. Measures in mm.

amounts to several microseconds. Typically, the signal output is connected to a time delay unit (DG525, Stanford Research Systems), which in turn triggers a laser, camera, oscilloscope or spectrometer.

5.2.1b. Laser triggering. A system for detecting the shock waves close to the implosion point was designed for the cylindrical convergence section as the precision using the shock sensors is too low. A non-intrusive method was therefore developed to detect the shock closer to the focus. A continuous laser beam is directed through the test section, about 15 mm from the centre. Deflections of the laser beam caused by the passing shock wave are detected by a photodiode.

Figure 5.7 shows a photograph and a principal sketch of the set-up. A HeNe laser beam is directed through the test section at a small angle, passes through both glass windows and is reflected back by a mirror inside the inner body. The beam path is in the horizontal plane of the tube centreline. The beam exits the test section on the opposite side of the centre. A lens (f=+80 cm) focuses the beam on an optical fibre that leads the light to a fast photodiode (Hamamatsu S5973). The circuit that amplifies the photodiode current is given in Fig. 5.8. It consists of a primary current amplifier with very fast response and a secondary amplifier to increase the output voltage to the triggering levels of the time delay unit. Characteristics were determined with a pulse laser: the rise time of the primary amplifier is about 20 ns and the rise time of the combined circuit including the secondary amplifier is 100 ns.



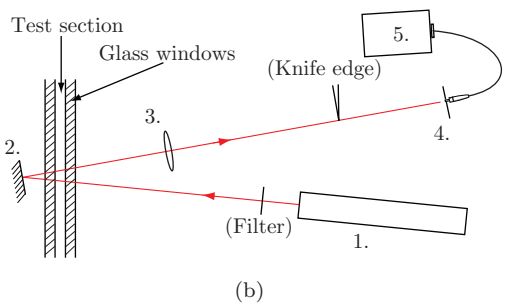


Figure 5.7: Photograph and sketch of the laser triggering set-up. Description for both: (1.) HeNe laser; (2.) mirror (inside tube); (3.) 80 mm lens, focusing the laser beam on (4.) optical fibre mounted in a traverse, which is connected to a (5.) photodiode and amplifier. The path of the laser beam is sketched in the photo. Two fibres collecting light from the implosion to the photo-multiplier tube and spectrometer (lower left corner) can also be seen in the photo. A damping filter and a knife edge may be used additionally.

The response to a passing shock wave consists of four peaks: the first two correspond to the converging shock wave passing the laser beam going into and out from the test section respectively, while the second pair corresponds to the outgoing reflected shock wave. The peaks have a certain slope depending on the angle between the laser beam and test section. The angle of the laser varied between experiments, depending on the other measurement equipment placed in front of the test section. For triggering, the photodiode signal is set to the trigger input of the delay unit. The system is very sensitive to the position

## 40 5. EXPERIMENTAL EQUIPMENT

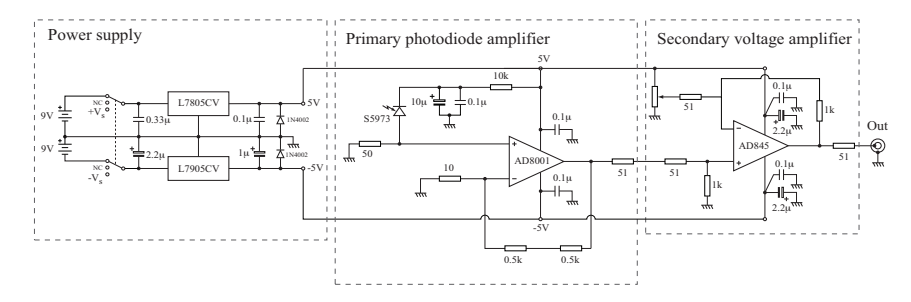


Figure 5.8: Circuit diagram of the photodiode amplifier.  $V_s$  may be set to  $5-15~\rm{V}.$ 

of the receiving optical fibre. The fibre is fastened on a traversing system and before each run it is moved to its most sensitive position where it generates the maximum signal. The triggering level on the DG535 is set to just below the value of the maximum: when the shock passes the generated signal drops.

5.2.1c. Photo-multiplier signal. A simple way to trigger the spectrometer is to use the photomultiplier tube detecting the light created by the shock wave itself. It is particularly useful for measuring the light spectrum after shock focusing, during the relaxation phase of the gas in the centre, but the small rise in emission just prior to the collapse enables this method to be used to detect the beginning of the implosion pulse as well. The problem that arises in the latter case is that this initial light increase is relatively slow and shows large variations in terms of amplitude, which reduces the likelihood of triggering at the same instant relative to implosion each run.

5.2.1d. Burst indicator. Immediately downstream of the membrane in the driven section, an electric conductor runs through the tube wall at connection (2.) in Figure 5.1. The conductor is electrically insulated from the metal tube and the conductor terminal is aligned flush with the inner side of the tube. When the membrane bursts it hits the conductor tip, connecting it with the tube. The change in potential may be used as an indicator for the membrane burst event or as a trigger.

5.2.1e. Pressure triggering. To take schlieren or normal photographs with the Nikon camera the system is in enclosed in a blacked-out enclosure, the camera shutter opened before membrane rupture and left open for 30 seconds exposing during the whole experiment (see Section 5.3.1 below). To do this an automatic system was built that monitors the pressure in the driver section and triggers an infrared remote control (a modified Nikon ML-L3) to turn on the camera once the pressure reaches a predetermined value, slightly below what is required to

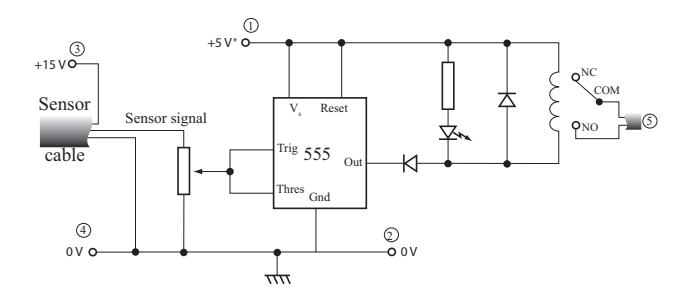


Figure 5.9: Circuit diagram of pressure comparator. Connectors (1.) and (2.): power supply for comparator, (3.) and (4.): power supply for pressure transducer. Output cable to IR remote (5.).

break the membrane. A pressure transducer (Keller Series 21R) was connected on a T-joint inserted on the tube between the Druck pressure indicator and the driver section (not shown in the drawing). The sensor signal is connected to a comparator circuit, drawn in Fig. 5.9, which toggles a relay when the pressure signal exceeds 2/3 of the comparator supply voltage. A potentiometer is used to tweak the triggering voltage/pressure and a LED indicates when the relay is activated. The circuit connects the two conductors in the output cable to the infrared remote that triggers the camera.

## 5.3. Flow visualisation: Schlieren optics

Flow visualisation is provided with schlieren optics. A schlieren system makes use of the density-dependence of the refractive index of light. Here follows a short introduction and description of the present set-up. Three main components are necessary: a collimated light source, a light blocker - called a schlieren stop - and a camera. The principle is simple: the parallel light rays illuminate the test section of interest and are afterwards focused on the stop, which partially or completely blocks the light. Density gradients in the test section make the parallel rays deflect. Light that would otherwise have been blocked by the stop will now pass it (or vice versa - light that would have passed may instead be blocked). The density changes will thereby appear as darker or brighter areas on the image plane after the schlieren stop.

Two principal optical set-ups were used. One that had all optical elements arranged on the centre line of the shock tube and one that made use of the Schlieren Optical Unit (SOU) seen in Figure 5.10 and 5.11 where the optical axis was twice folded. A schematic drawing of the latter system is presented in figure 5.10. Light was provided with laser. The laser head is mounted outside of the shock tube, perpendicular to it. The beam enters the inner body of the annular section through one of the support struts and expands, thereby

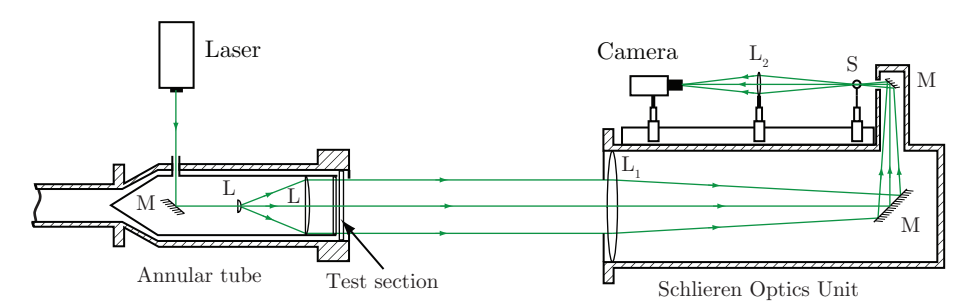


Figure 5.10: Schematic drawing of schlieren set-up. The laser beam enters the tube through a hollow support and is directed through the test section via a mirror and two lenses. M: mirrors, L: lenses, S: schlieren stop.

illuminating the test section through the glass window. On the receiving side the collimated light was focused with lens  $L_1$  (f=1350 mm) on a schlieren stop. To be able to detect density gradients in all radial directions a circular stop was used. Either a small micro-sphere blocking most of the beam - typically a 0.67 mm ball bearing - or a pinhole were used, the former shown in Fig. 5.12. The pinhole blocks light from areas of large gradients, generating bright images with dark shock waves, and the other way around for the sphere.

A second lens  $L_2$  creates an image for the camera. Magnification is decided through choices of lenses  $L_1$  and  $L_2$  and the distances between them and the object plane (the test section). When the SOU is used, the lens  $L_1$  is an inbuilt 1350 mm lens. The system that does not use the SOU is in principle no different, except in that the optical axis is not mirrored.

#### 5.3.1. Cameras

Two CCD cameras are used: a PCO SensiCam and a Nikon D80 system camera. The SensiCam (12 bits, 1280x1024 pixels, pixel size: 6.7x6.7  $\mu$ m) is equipped with a 80 mm Canon lens and can take either singly or multiply exposed images. It is controlled by a computer that receives an external TTL-level trigger signal via a PCI-board. For single exposures, an Nd:YAG laser (New Wave Orion) is used with both cameras. The pulse length of the laser is about 4-5 ns. The timing of the pictures is determined with the laser: the camera was left open for a longer interval (5  $\mu$ s for the SensiCam and 30 s for the Nikon) and the laser fired at the desired instant for photographing.

The Nikon D80 is a regular digital system camera equipped with a Micro Nikkor 60 mm macro lens. The shutter of the Nikon D80 could not be satisfactory triggered without internal modification of the camera, so the shutter was simply left open for 30 seconds. It was triggered using the pressure comparator

described above. At a pressure just below membrane burst pressure, the output triggered a commercial infra-red remote (Nikon ML-L3) which opened the camera shutter. The remote was modified to be triggered by the relay circuit. The delay between the given IR signal and the shutter opening was very long - longer than the propagation time of the shock wave from membrane rupture and focusing, which made it necessary to trigger the camera before the actual membrane opening. Although the optical set-up is shielded from stray light, an exposure problem occurs with the Nikon camera with the shutter left open for long periods. This causes the camera to not only capture the schlieren image enlightened by the laser beam, but also to be exposed to the implosion light pulse. The implosion pulse may be very bright and over-expose the photograph. The unwanted exposure due to the implosion light flash is damped by placing neutral filters in front of the camera and compensating with increased laser power.

## 5.3.2. Lasers

And Orion Nd:YAG pulse laser was used as light source for the schlieren photography. The laser Q-switch can be triggered internally or externally. In each mode, it first receives a TTL signal to start the flash lamp ("Fire lamp"). In internal QS mode, the laser pulse follows the "Fire lamp" signal after 328  $\mu$ s. In the external mode, the laser is fired after receiving a second triggering signal ("Fire QS"), typically around 200  $\mu$ s after the "Fire lamp" signal. The external handling of the Q-switch generates much stronger light than in internal mode. The output laser beam strength is controlled manually. Two energy modes, called High and Low, are available and is supplemented with an energy scale ranging from 0-99. Typical used values were Low 4 with the external Q-switch mode, and Low 15 with internal Q-switch mode. The effective exposure time for the schlieren photographs when using the Orion is determined by the laser pulse length, which is 4-5 ns.

The Orion laser could not be used for multi-exposed images since its maximum pulse frequency is 1 Hz. Instead a continuous laser was used as light source: an argon-ion (Spectra-Physics BeamLok 2060) and a HeNe laser were used interchangeably.

#### 5.3.3. Arrangement procedure

To arrange the system the following procedure is followed.

The first step is to find the optical axis. The axis follows the centre line of the shock tube and is relatively easy to find if the optics are to be aligned in a straight line. However, when the SOU is used the optical axis is twice folded by 90° and SOU must first be aligned. Starting in the camera end might be the simplest course of action. A HeNe laser can be used as an alignment assistant. First, the laser is placed at the position of the camera and the beam

## 44 5. EXPERIMENTAL EQUIPMENT



Figure 5.11: Set-up for schlieren photography: (a) laser light source; (b) 1350 mm lens (inside tube); (c) schlieren stop; (d) focusing lens; (e) camera.



Figure 5.12: The etched 0.67 mm micro-sphere used as a schlieren stop.

is aligned straight with the the optical rail on top of the SOU and directed through the centre of the light hole on the tower. A mirror should be used to control that the beam is aligned along the optical axis of the system. With the laser beam coming out of the SOU along its optical axis, the whole unit can be positioned by moving it until the HeNe beam enters the centre of the shock tube perpendicularly. When properly aligned, the laser beam should go through the whole system and hit the schlieren laser orifice.

The illumination laser should be aligned through the hollow support perpendicular to the tube. The alignment of the mirror M inside the tube can be made from outside. A remote-controlled electric motor controls the motion of the mirror around the vertical axis. The motion around the horizontal axis is handled with a manual screw going through the hollow strut on the opposite side of the light-entering strut.

With the SOU and schlieren laser aligned, the optical instruments - lenses, stop and camera - can be placed. A clear camera image is obtained by putting a semitransparent paper grid in the centre of the test section and focusing the camera on the grid. When all optical elements are aligned, the schlieren stop is positioned at the focus point of the laser light.

#### 5.3.4. Shock wave shaping

Two different methods have been employed to shape the shock waves from cylindrical into primarily polygonal forms: by cylindrical obstacles creating a reflection and diffraction pattern or by wings dividing the test section into radial channels where plane sides are created. The annular-cylindrical tube was designed to create shock waves shaped as polygons by using replaceable reflector plates around the periphery of the test section. This method has not been used in the work but is mentioned for completeness (for details see Eliasson et al. 2006).

5.3.4a. Cylindrical obstacles. By placing small cylindrical objects in the test section, the diffraction of the converging cylindrical shock wave around the obstacles changes the overall form. If the size and position of the obstacles are arranged in certain way, symmetrical polygonal forms may be achieved. The diameters of the cylindrical objects ranges from 7.5 to 15 mm. They are positioned between the glass windows using guides. During mounting they are temporarily kept in position with a small amount of glue: equipped with orings they are afterwards kept in place mechanically by the pressure from the glass windows.

5.3.4b. Biconvex wing profiles. Another method is to place biconvex wings in the test section with their chords aligned radially. The incoming shock wave reflects on the wings and if arranged properly, the shock wave attains polygonal structure with almost plane sides when leaving the channels. Since the wings have sharp leading and trailing edges, less pressure is lost compared to the case when circular objects are used, in which case reflected waves travel upstream. Figure 5.13(a) shows the test section with the wing dividers. The leading edges are aligned flush with the inner surface of the annular channel and the trailing edges end 20 mm from the centre of the test section. Calculations were made to find the appropriate lengths and widths to ensure plane shock wave exiting the channels into the open centre of the chamber. One purpose of the wings is

## 46 5. EXPERIMENTAL EQUIPMENT

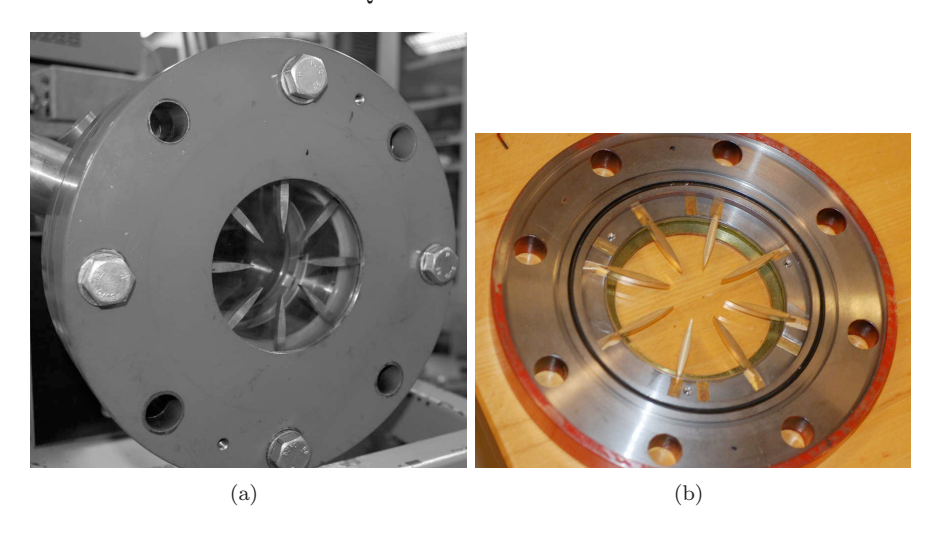


Figure 5.13: Wing matrix mounted in the test section (a) and before assembly (b).

to improve the control of shock shaping and to allow the same blockage ratio no matter the number of wings - and consequently the number of sides of the polygonal shock wave - by altering the thickness and length of the wings from case to case. The measurements in the present study however, only feature a configuration with eight such dividers, creating a cylindrical octagonal shock wave.

## 5.3.5. Inner body alignment

The eccentricity of the inner body inside the shock tube has major impact on the symmetry of the shock waves. Referring to Figure 5.1, the inner body is supported by two sets of struts. The downstream set is located close to the test section and may be aligned with the help of a mechanical guide. The upstream set is situated too far upstream for this method to be useful. It was found that the wings provided a good tool for tuning the position of the body. The wing matrix divided the test section in eight radial channels and the velocity of each segment of the otherwise connected circular shock wave could be seen in detail.

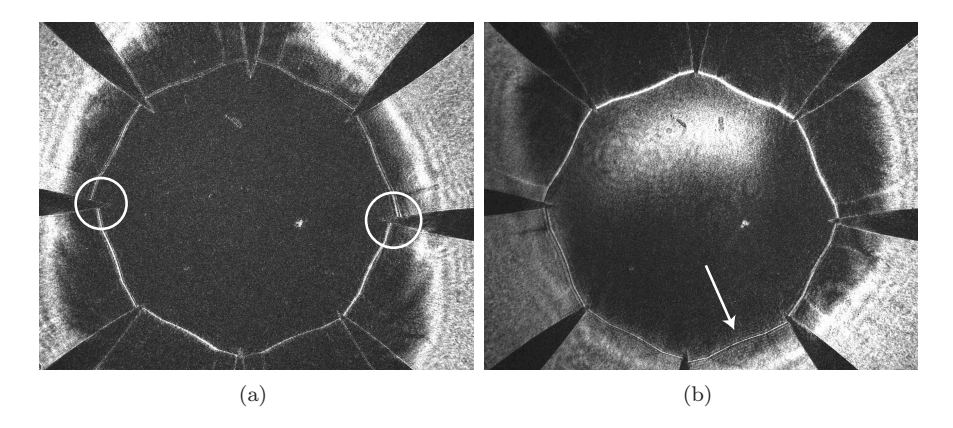


Figure 5.14: Schlieren images of shocks arriving at the open center of the test section to illustrate the effect of non-aligned inner body: (a) before and (b) after alignment.

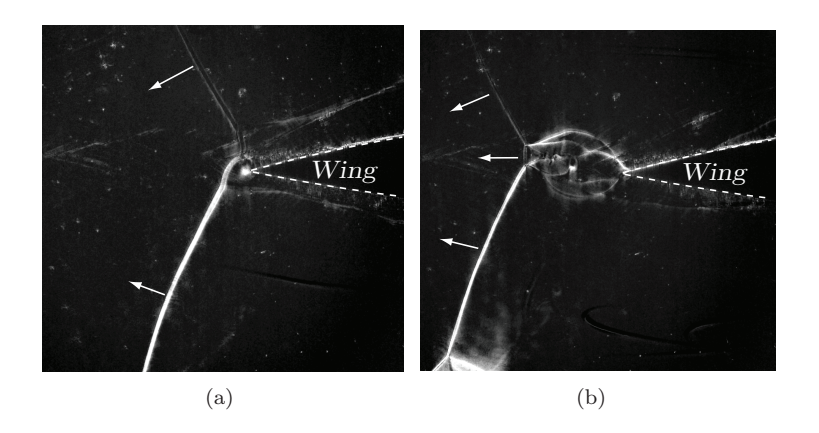


Figure 5.15: Interaction of two shock waves close to the trailing edge of a wing (outlined with dashed lines) at slightly different times. In (a) the lower shock wave has already arrived and diffracted around the tip and reflected with the upper shock wave. A vortex can be seen forming due the shear flow. A Mach stem is formed as the shocks reflect. It is shifted upwards due to the asymmetric reflection (b). At the bottom of the image the Mach reflection coming from the lower wing tip can be seen. Arrows indicate wave direction. Each image is from a separate run.

Figure 5.14 shows schlieren photographs of shock waves exiting the channels. The shocks have clearly different velocities as they arrive at different instants. This suggests that the inner body is eccentric with the annular channel being slightly narrower at the part of the channel corresponding to the position of the faster shocks and vice versa. To ensure that asymmetric construction of the matrix did not give rise to the irregularities, the matrix was gradually rotated between several runs. The shock pattern was unchanged with rotation and it was concluded that the matrix construction was good. The struts were adjusted accordingly to the schlieren photographs. By trial and error the arrival of the shock fronts at the end of the matrix could be improved. Figure 5.14 (a) shows the shock pattern before alignment: the whole lower half of the shock is faster than the upper. Figure 5.14(b) shows the pattern after alignment: the general shape is much improved. Photomultiplier records measuring the light of the implosion pulse showed a large increase in strength after the alignment indicating a more symmetric implosion. Figure 5.15 shows reflections around the right encircled wing-tip in Fig. 5.14(a).

# 5.4. Converging test section

A second test section was designed to create shocks with spherical symmetry. The section is joined to the main shock tube and consists of a converging pipe with a smoothly changing cross section. The idea is to form the wall in such a way that the shock wave foot remains normal to the wall without reflection (or with minimal reflection) and that the shock front has a spherical shape as it leaves the section. If the pressure is evenly distributed behind the shock and all parts of the shock front propagates at the same speed, the front will be close to spherical. The existence of such a solution was discussed and proved by Dumitrescu (1983, 1992); Saillard *et al.* (1985). Fig. 5.16 shows a sketch of the principle: a plane shock wave enters the tube and where the cross section changes disturbances move along the curved shock progressively increasing the curvature and gradually accelerating it. In order for the shock front not only to have a circular symmetry in the propagation axis plane but also to have the same speed at all parts, to ensure a continued spherical shock front, a series of calculations were made to find the wall shape. The final design is shown in Fig. 5.17. It consists of an extended inlet tube (with shock-sensors) followed by a smooth contraction and a small conical end. Eq. 5.1 provides the shape of the contracting surface in parameter form. The cone half angle is 21°.

$$x = Asin\theta y = B - R(1 - cos\theta)$$
 for  $0 \le \theta \le 0.35\pi$  (5.1)

where A=300.7 mm, B=40 mm and R=57.3 mm. The transformation part was constructed by casting a plastic material around a steel mold. The cast part is housed in a steel tube with a flange and fastened to the shock tube. It is

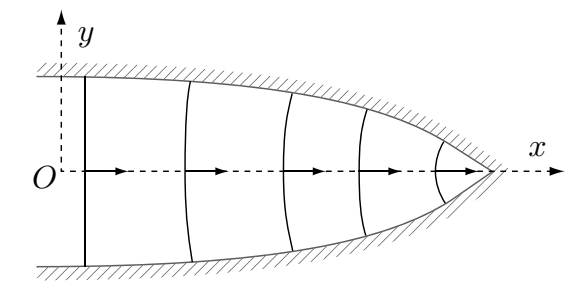


Figure 5.16: Sketch of the conversion of a planar shock to a spherical. Axial symmetry applies.

291 mm in total length and terminates in a straight cone of 21 mm. The cone is made of steel truncated 0.4 mm from its tip leaving a circular opening with a radius of 0.3 mm. The opening is covered with a 1.5 mm thick quartz window fixed to its position by a threaded brass sleeve. The conical part is shown in section in Fig. 5.18. The sleeve contains optical fibre mounts. One fibre is mounted coaxially, viewing straight into the tube. A second fibre views the opening at an oblique angle covering a volume stretching no more than 0.5 mm into the tube. The surface inside the contraction and cone is smooth in order to avoid disturbances introduced into the very sensitive converging process.

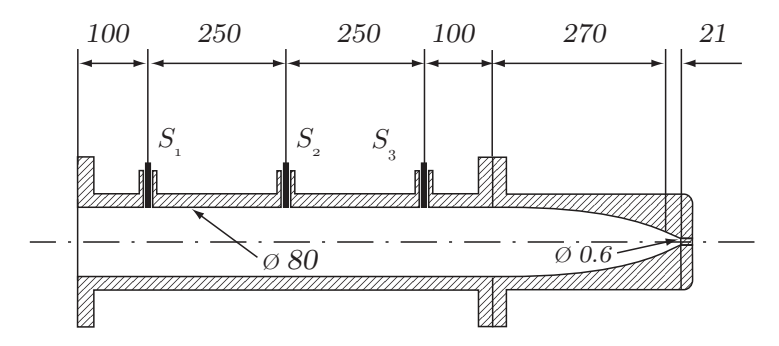


Figure 5.17: Convergence section for three-dimensional implosion. Inlet tube with shock sensors  $S_1$ ,  $S_2$  and  $S_3$ , a smoothly changing contraction and 21 mm conical end cone. The end diameter of the conical section is 0.6 mm. A quartz window closes the tube. Measures in millimetres.

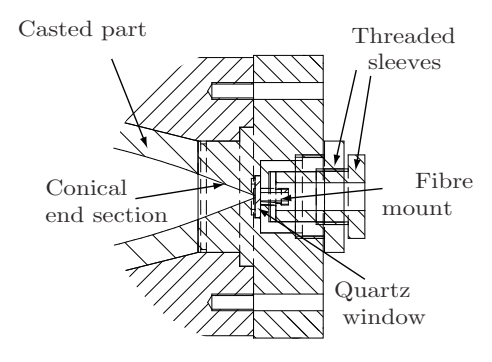


Figure 5.18: Drawing of the conical end and fittings. Courtesy of Nils Tillmark.

## 5.5. Spectroscopic instrumentation and its calibration

Two spectrometers have been used in the experiments, both on loan from the KTH Physics Department. They are both of echelle type and the diffracted light is recorded on an intensified charge-coupled device (ICCD). The final spectrum is analysed though computer software. The first spectrometer, which was used for the measurements on the cylindrical implosions (Paper 1) was a Mechelle 7500 (Multichannel Systems, Sweden) equipped with in Andor Istar ICCD. Details about the specific and echelle spectrometers in general can be found in Lindblom (1998). The spectrometer was able to record spectra in the wavelength interval 180 - 880 nm. The sensitivity of the CCD is dependent on wavelength, which needs to be accounted for when analysing the data. Figure 5.19(a) shows the ICCD sensitivity. The test section glass window also limits the light transmission, to between roughly 350 and 880 nm. The transmittance of the 15 mm thick borosilicate glass is presented in Figure 5.19(b). During the measurements the spectrometer exposure was started by the laser triggering system with a precision of 10 ns relative the emission peak, which for synchronisation purposes was measured separately with a photomultiplier

The second spectrometer (Aryelle 200, Lasertechnik Berlin) used an improved version of the Andor Istar ICCD. A wavelength calibration was made with a mercury lamp with the aid of the supplied software. In order to reconstruct the spectrum a radiometric calibration against a calibrated deuterium lamp and, for the longer wavelengths, against a tungsten lamp with known filament temperature (3000  $\pm$  50 K) was carried out. The temperature of the tungsten filament was measured using two pyrometers and calculated by measuring the resistance  $R_{ref}$  at room temperature of the lamp and using tabulated values of  $R/R_{ref}$  vs T. The value of T is very sensitive to  $R_{ref}$ , and great care was taken to measure it. The lamp tension was measured at thes

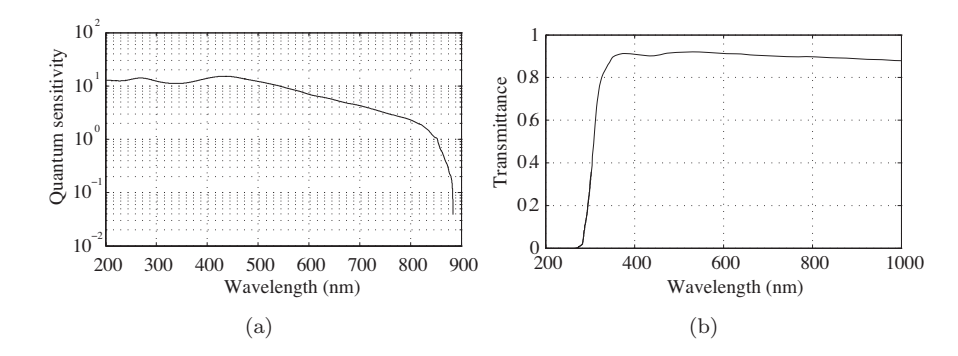


Figure 5.19: (a) Relative CCD wavelength sensitivity of the Mechelle 7500 system and (b) transmittance of the test section borosilicate window.

the bulb socket and the zero resistance was determined to  $R_0=0.28~\mathrm{k}\Omega$  by extrapolation of R=U/I to U=0, see Fig. 5.20.

The measured spectrum of the deuterium lamp is shown in Fig. 5.21 together with the given calibrated emission. The quickly decreasing sensitivity in the deep UV is due to the optical fibre as the manufacturer gives the ICCD sensitivity in the ultraviolet region as fairly constant. The red calibration using the tungsten lamp was patched with the ultraviolet calibration to create a single calibration file. The good agreement between the overlapping regions of the separate calibrations shown in Fig. 5.21 is taken as an indication of a successful calibration.

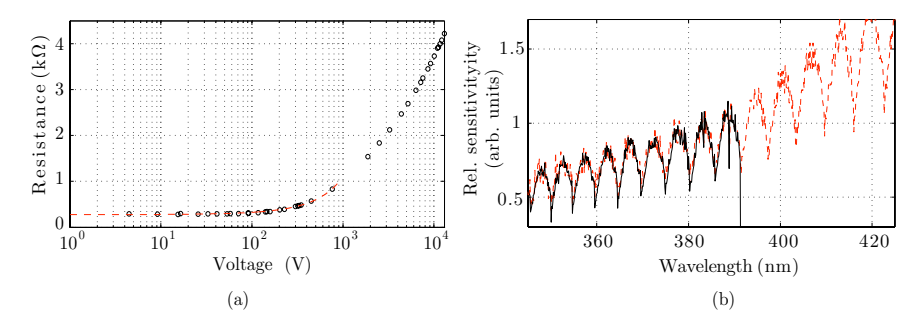


Figure 5.20: Radiometric calibration: (a) Determination of zero resistance  $R_{ref}$  and filament temperature.  $R_{ref}$  is determined through extrapolation to U=0 (red dashed line). The temperature can subsequently be estimated from  $R/R_{ref}$ . (b) Patching region of ratio between measured and known spectra for tungsten filament (dashed, red) and deuterium lamp (full line).

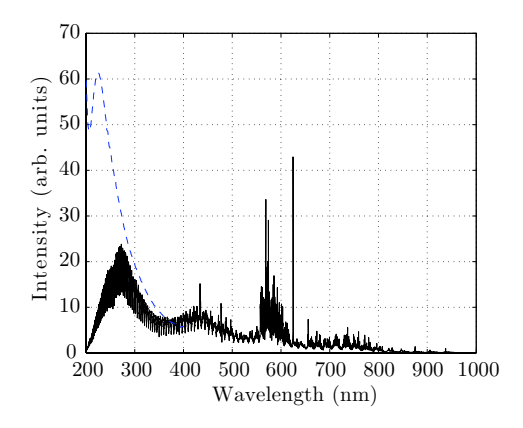


Figure 5.21: Raw spectrum of deuterium lamp compared to the given calibrated emission (blue dashed line).

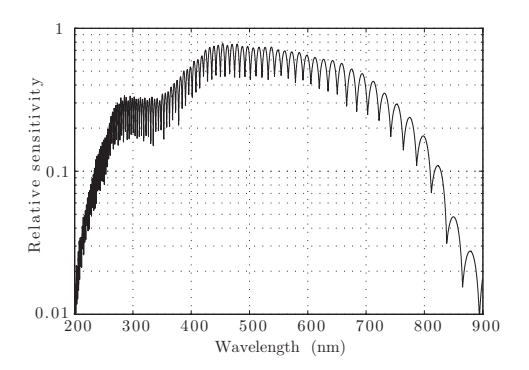


Figure 5.22: Relative sensitivity for the Aryelle system, including optical fibre (FC400 solarisation-resistant fibre) and observation window (quartz). The decrease per order is visible: the orders are denser at lower wavelengths.

The resulting sensitivity function is shown in Fig. 5.22. The periodicity is due to the varying sensitivity of each diffraction order. The sensitivity drastically drops below 250 nm and above 950 nm, reducing the accuracy in those parts of the spectrum.

#### CHAPTER 6

# Numerical calculations

Numerical calculations were made with Euler solvers unstructured triangular grids with or without adaptive mesh refinement. Three different solvers were used: a single-component and a multi-component solver and a single-component solver taking into account equilibrium ionisation. First- and second order finite volume discretisation schemes were used. The convective flux was in all cases calculated using the artificially upstream flux vector splitting (AUFS) scheme introduced by Sun & Takayama (2003), whose fundamental idea is to overcome the disadvantages of up-winding schemes by introducing artificial wave speeds into the flow which simplifies the discretisation. The single-component solvers are briefly described here while the multi-component solver is described in paper 6 including more details on the discretisation and mesh adaption also relevant for the single-component case. The 2D Euler equations for compressible inviscid flow:

$$\mathbf{U}_t + \mathbf{F}_x + \mathbf{G}_y = 0 \tag{6.1}$$

where the vector  ${\bf U}$  contains the conserved variables while  ${\bf F}$  and  ${\bf G}$  are the fluxes in x- and y-directions:

$$U = \begin{pmatrix} \rho \\ \rho u \\ \rho v \\ \rho E \end{pmatrix}, \qquad F = \begin{pmatrix} \rho u \\ \rho u^2 + p \\ \rho v u \\ \rho E u + p u \end{pmatrix}, \qquad G = \begin{pmatrix} \rho v \\ \rho u v \\ \rho v^2 + p \\ \rho E v + p v \end{pmatrix}$$
(6.2)

where  $\rho$  is the mass density,  $\rho u$  and  $\rho v$  and  $\rho E$  the energy per unit volume. The energy per unit mass is the sum of the specific internal energy and the kinetic energy  $E=e+|\mathbf{u}|^2/2$ . The equations were discretised on an unstructured triangular mesh. Referring to the grid cell illustrated in Figure 6.1, Eq. 6.2 may be formulated and calculated over the normal interfaces between the cells. Variables denoted L refer to the states inside the cell and R to those in the neighbouring cells. We have:

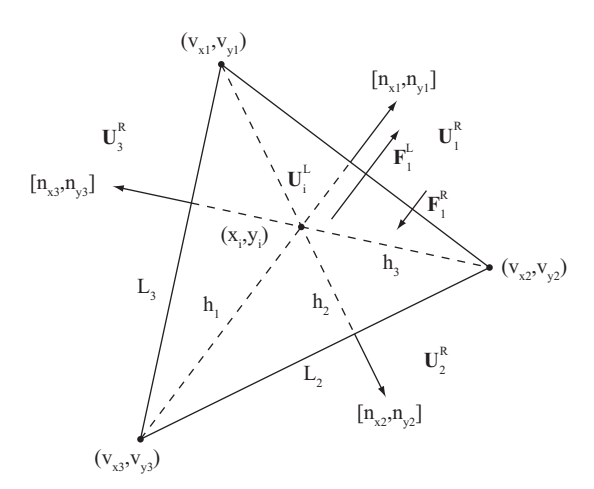


Figure 6.1: A grid cell i.  $\mathbf{U}_i^L$  is the state in the cell while  $\mathbf{U}_j^R, j=1,2,3$ , are the states in neighbouring cells.

$$\mathbf{U}_t + \mathbf{F}_n = 0 \leftrightarrow \mathbf{U}_t + \mathbf{A}\mathbf{U}_n = 0 \tag{6.3}$$

where **A** is the Jacobian matrix  $A_{ij} = \partial F_i/\partial U_j$  and n refers to the normal direction. The matrix **A** has four real eigenvalues corresponding to the four wave speeds of the system,  $(u_n - a, u_n, u_n, u_n + a)$ , where  $u_n = un_x + vn_y$  is the normal velocity across the interface. Provided that  $u_n < c$  somewhere, the system therefore contains waves going both upstream and downstream which makes up-winding difficult. However, observed from some frame of reference all waves propagate in the same directions. By introducing the artificial wave speeds  $s_1$  and  $s_2$  corresponding to such a moving frame of reference the flux can be rewritten to simplify the discretisation. After some manipulation the flux becomes:

$$\mathbf{F} = (1 - S)\mathbf{F}_1 + S\mathbf{F}_2 = (1 - S)\left[\frac{1}{2}(\mathbf{P}^L + \mathbf{P}^R) + \delta\mathbf{U}\right] + S\left[\mathbf{U}^d(u_n^d - s_2) + \mathbf{P}^d\right]$$
(6.4)

where  $S=s_1/(s_1-s_2)$ ,  $\delta \mathbf{U}$  artificial viscosity,  $\mathbf{P}=(0,pn_x,pn_y,pu_n)$  and d is either L (if  $s_1>0$ ) or R (if  $s_1\leq 0$ ), depending on whether the corresponding wave goes into or out of the cell. The pressure is acquired from the internal energy:  $e=p/(\gamma-1)=E-u^2/2$  while the temperature is attained from the perfect gas law.

The artificial viscosity term is:

$$\delta \mathbf{U} = \frac{1}{2\bar{a}} \begin{pmatrix} p^L - p^R \\ (pu)^L - (pu)^R \\ (pv)^L - (pv)^R \\ \frac{\bar{a}^2}{\gamma - 1} (p^L - p^R) + \frac{1}{2} ((pU^2)^L - (pU^2)^R) \end{pmatrix}$$
(6.5)

where  $U^2 = u^2 + v^2$  and  $\bar{a} = (a^L + a^R)/2$  is the average speed of sound of domains L and R. The artificial wave speeds were chosen as

$$s_1 = \frac{u_n^R + u_n^L}{2} \tag{6.6}$$

$$s_2 = \begin{cases} min(0, u_n^L - a^L, u_n^* - c^*) & s_1 > 0 \\ max(0, u_n^* + c^*, u^R + v^R) & s_1 \le 0 \end{cases}$$
 (6.7)

$$u^* = \frac{1}{2}(u_n^L + u_n^R) + \frac{a^L - a^R}{\gamma - 1}$$
(6.8)

$$c^* = \frac{1}{2}(a^L + a^R) + \frac{1}{4}(\gamma - 1)(u_n^L - u_n^R)$$
(6.9)

For details of the derivation the reader is to directed to Sun & Takayama (2003). The solution update for the grid i between time-steps n and n+1 is then calculated by a first-order method:

$$\mathbf{U}_i^{n+1} = \mathbf{U}_i^n - \sum_{k=1}^3 \frac{\Delta t}{h_k} \mathbf{F}_k \tag{6.10}$$

6.0.0a. Ionising shocks. Ionisation effects are introduced by modifying the energy and state equations accordingly. In the calculations only one level of ionisation was included since it was apparent that the number of ions with charge state i=2 or more were negligible for cylindrical shock waves with the initial parameters of the experiments. However, we present here the general equations for any number of stages of ionisation. Local thermodynamic equilibrium is assumed to be established everywhere in the flow and the additional variables are the ionisation fractions  $\alpha_i$ .

The primitive variables are the same, as is the up-winding scheme with modifications to the speed of sound which is presented further below. In the non-ionising case, the pressure is acquired directly from the energy and the temperature from the equation of state. A similar approach is taken in this case. The equation of state and internal energy, neglecting Coulomb forces and excitation energy, are now

$$p = (1 + \alpha_e)\rho RT \tag{6.11}$$

and

$$e = \frac{3}{2}(1 + \alpha_e)RT + R\sum_{i=1}^{\ell} \left(\alpha_i \sum_{j=1}^{i} \frac{I_j}{k}\right)$$
 (6.12)

where  $\alpha_e$  is the average ionisation fraction and  $I_j$  are the ionisation potentials as defined in chapter 2. With the additional variables  $\alpha_i$  the system is closed with the Saha equations which can be expressed as functions of T and  $\rho$  and solved in the same manner as presented by Trayner & Glowacki (1995):

$$\frac{\alpha_{i+1}}{\alpha_i} = \frac{1}{\alpha_e} \left(\frac{2\pi m_e}{h^2}\right)^{3/2} \frac{m_H (kT)^{3/2}}{\rho} \frac{2Q_{i+1}^{el}}{Q_i^{el}} \exp\left(-\frac{I_{i+1}}{kT}\right)$$
(6.13)

where  $m_H$  is the mass of the neutral atom. Solving the equation in terms of a given primitive variable  $\rho$  instead of p is preferred, since the latter is a derived variable. The temperature and ionisation fractions for each grid are carefully balanced and calculated from the given primitive variables during each timestep. An iterative method is used to find the ionisation and temperature that fulfils the energy requirement 6.12 as well as the set of Saha equations 6.13. This implies finding the root of the transcendental equation  $T - f(\alpha_e(T, \rho)) = 0$ , where the numerically evaluated function f is determined from the known energy 6.12. Explicitly written out this becomes

$$T - \left[ e - R \sum_{i=1}^{\ell} \left( \alpha_i(T, \rho) \sum_{j=1}^{i} \frac{I_j}{k} \right) \right] \left[ \frac{3}{2} (1 + \alpha_e(T, \rho)) R \right]^{-1} = 0$$
 (6.14)

Equation 6.14 may be solved by a bi-section method with initial lower bound  $T = T_0$  and upper bound set to the ideal non-ionising temperature. Once the temperature and ionisation fractions are found, the pressure is extracted from the equation of state 6.11.

The artificial wave speeds  $s_1$  and  $s_2$  are chosen in the same manner as previously, but the speed of sound now becomes the equilibrium speed of sound,  $a_e = (\partial p/\partial \rho)_s$ , which can be calculated from derivatives of  $\alpha$  (see Appendix A).

6.0.0b. Single ionisation. When only one stage of ionisation is likely to be present, Eqs. 6.13-6.14 can be simplified to significantly reduce calculation time. Such a scheme has been presented in Aslan & Mond (2005). Only one Saha equation remains, for i=1 where  $\alpha_0=1-\alpha_1$ , which does not need iteration. In this temperature range, the partition function ratio can be adequately approximated by a constant  $(2Q_1/Q_0 \approx g_0 \approx 11)$  and Eq 6.13 reduces to

$$\frac{\alpha_1^2}{1 - \alpha_1} = g_0 \left(\frac{2\pi m_e}{h^2}\right)^{\frac{3}{2}} \frac{m_H (kT)^{3/2}}{\rho} \exp\left(-\frac{I_1}{kT}\right) = g_0 C \frac{T^{3/2}}{\rho} \exp\left(-\frac{I_1}{kT}\right)$$
(6.15)

where the constant  $C \approx 1.603 \times 10^{-4} \text{ kg} \cdot \text{m}^{-3} \cdot \text{K}^{-3/2}$  for argon.

The approximation of the partition function ratio as a constant carries a certain error, which is exemplified in Fig. 6.2. The post-shock conditions resulting from the approximation are compared to those where the partition functions included a summation over the first few terms. As evident, the error is reasonably small until  $M \approx 30$ . Above that Mach number second stage ionisation becomes significant (compare with Fig. 2.3) and the model validity is in any case becoming questionable. The calculations are made with initial pressure 0.1 atm and T = 300 K.

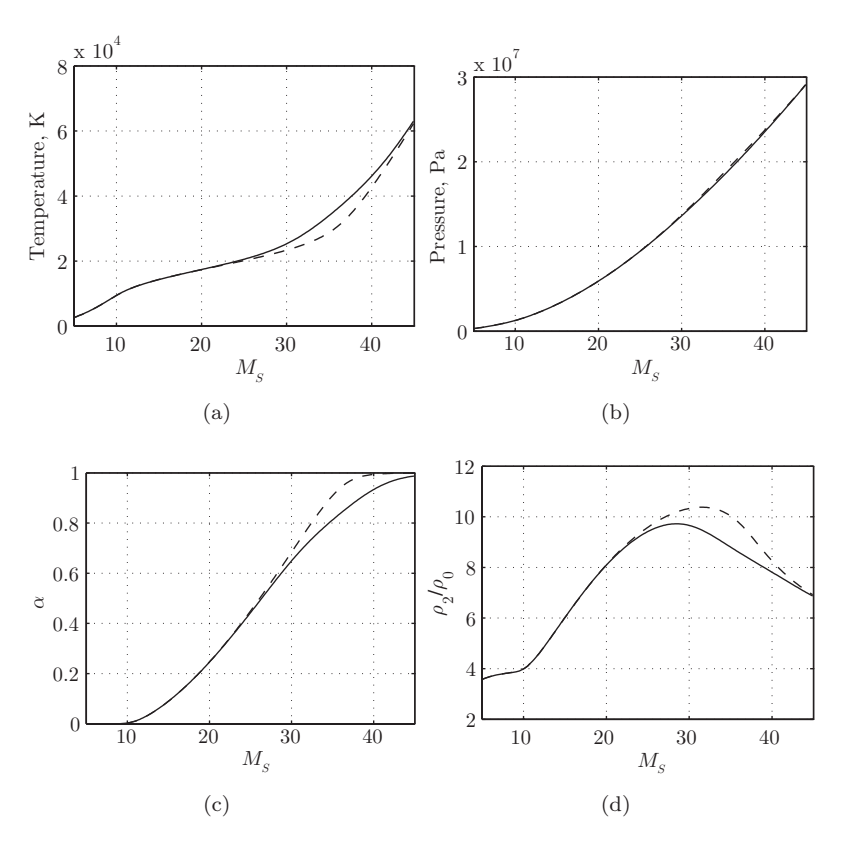


Figure 6.2: Error caused on shock relations by the assumption  $Q_1/Q_0=11$  (dashed line) compared to  $Q_1/Q_0=f(T)$ : (a) post-shock temperature; (b) pressure; (c) degree of ionisation and (d) shock compression.

#### CHAPTER 7

# Conclusions and contributions

This is a short summary of the results presented in the papers in Part II.

## 7.1. Cylindrical shock waves

- A new system of shaping the circular shock wave was introduced: the
  convergence chamber was divided into channels using wing profiles which
  split the incoming shock wave. For some wing lengths and widths, the
  shock waves exit the channels as straight sections and a polygonal shape
  is created.
- Spectrometric studies on shock convergence were made using polygonal shock waves. The shape had shown to produce more repeatable results in terms of the light emitted by the implosion than circular. Blackbody radiation was measured during the beginning of the implosion light pulse, showing a peak value of 6,000 K, which is lower than expected. Light was collected from an unnecessarily large area, which is significantly colder than the hot central core.
- The dynamics of symmetric polygonal shapes were studied in order to compare with theoretical studies on the peculiar behaviour of polygonal shock waves. The repeating and alternating formation of the initial polygon due to Mach reflections in the corners was seen and found to match the theory.
- Calculations using geometrical shock dynamics for converging cylindrical and spherical shock waves were performed taking in account real gas effects during the convergent process. Ionisation, electronic excitation and coulombic forces were taken into account.
- The design of the apparatus creating cylindrical shock waves was studied numerically by axi-symmetric Euler calculations: it was found that the 90° bend and contraction works to create strengthened converging cylindrical shock waves. The initially diffracted shock at the bend is weak and attenuated, but the shock reflected at the end wall turns into the flow field created by the diffraction, overtakes and merges with the diffracted shock. This strong shock converges efficiently, the flow driven by the high pressure created by the reflected shock in the annular channel. Three-dimensional effects due to the bend are initially large, but quickly diminish although they are not completely damped.

• The convergence of circular cylindrical shock waves was studied to determine the self-similarity exponent for shocks in three different gases, argon, nitrogen and propane. According to established theory, the exponent depends on the ratio of specific heats,  $\gamma$ . The experiments confirmed the variation and the acquired values agreed well with theory. The Mach numbers in these experiments were kept low so  $\gamma$  of the gas would not change due to real-gas effects (before implosion).

# 7.2. Spherical shock waves

- A new experimental section was designed and constructed for the shock tube. It consists of a transformation section with smoothly convergent cross-section ending with a straight cone. The wall curve was designed to slowly change the shape of the plane shock wave into the shape of a spherical disc (imagine a part of a spherical shell cut out by a cone with its apex in the sphere centre) when exiting the transformation section. Numerical calculations were made to test the shape and found to work well for a range of Mach numbers. In the first version of the experiment no sensors were inserted to avoid disturbing the flow.
- The radiation from the imploding shock in the conical section was measured for shock waves in air. Significantly stronger radiation was recorded than in the cylindrical case for the same initial Mach number. In the first part of the implosion light pulse a strong continuum was seen, while bound-bound line radiation of argon appeared in the cooling phase. Compared to the cylindrical case, more radiation from unwanted sources appeared: e.g. iron and aluminium from the shock tube and diaphragm. Preliminary results show a highest blackbody temperature of about  $2.7 \times 10^4$  K.
- The work on the spherical test section opens possibilities and raises several questions. Further experiments should be made to more accurately clarify what level of shock strengthening is achieved, which could be done by e.g. measuring the propagation. The end of the cone could be reconstructed to enable clearer measurements. Instead of an abrupt wall at the end of the cone, a small cavity or tube could be attached, into which the strengthened shock could propagate. The light emission could then be studied by placing the collecting fibres perpendicular to the axis instead of along it. On the numerical side, the addition of viscosity and/or a collisional-radiative model to the Euler calculations could provide better understanding of the fast processes around focus. With more accurate calculations the shape of the convergent section could be optimised.

## CHAPTER 8

# Papers and authors contributions

# Paper 1

Thermal radiation from a converging shock implosion. M. Kjellander (MK), N. Tillmark (NT) & N. Apazidis (NA). Phys. Fluids **22**, 046102 (2010).

This paper is a spectrometric and photometric study of the light emission produced by converging shock waves in argon. For repeatability purposes, polygonal shape shocks were created. The experiment was set up by MK and NT with assistance from Olli Launila and Lars-Erik Berg, KTH Applied Physics and performed by MK. Numerical calculations complemented the study, performed by NA and MK. The paper was written by MK and NA, with feedback from NT. Parts of this work has been presented at:

27<sup>th</sup> International Symposium on Shock Waves, 19 – 24 July 2009, S:t Petersburg, Russia

# Paper 2

Shock dynamics of imploding spherical and cylindrical shock waves with real gas effects.

M. Kjellander, N. Tillmark & N. Apazidis.

Phys. Fluids 22, 116102 (2010).

This paper is a study on the high temperature gas processes close to the centre of convergence of cylindrical and spherical shock waves in monatomic gases. The method of characteristics was used, with a gas model accounting for ionization and Coulomb effects. The initial idea was proposed by NA and the calculations were performed mostly by MK. Theoretical derivations were made by MK and NT. The paper was written by MK with feedback from the coauthors.

# Paper 3

Regular versus Mach reflection for converging polygonal shocks. V. Eliasson (VE), M. Kjellander & N. Apazidis. Shock Waves 17, 43–50 (2007).

Different reflection patters in polygonal shock waves were investigated. Square and triangular shocks were created by cylindrical rods placed in the path of the shocks. The experimental setup and work was mainly done by VE, but also by MK: MK set up and performed the experiments with the cylinders placed at 61.5 mm from the centre with higher optical magnification. The paper was written by VE with feedback from NA. Parts of this work was presented at:

# $60^{\rm th}$ Annual Meeting of the American Physical Society - Division of Fluid Dynamics,

18 – 20 November 2007, Salt Lake City, Utah, United States

# Paper 4

Polygonal shock waves: comparison between experiments and geometrical shock dynamics.

M. Kjellander, N. Tillmark & N. Apazidis.

In proceedings: 28th International Symposium on Shock Waves, 2011, University of Manchester, Manchester, United Kingdom

Schlieren photography is used to compare the dynamics of polygonal shocks with theory. Symmetric shock waves with 6, 8 and 12 sides were studied. The experimental set-up was made by MK and NT, the experiments were performed by MK. The writing was made by MK, with feedback from NA. This work has been presented at:

# 28<sup>th</sup> International Symposium on Shock Waves, 17 – 22 July 2011, Manchester, United Kingdom

# Paper 5

Experimental determination of the self-similarity constant for converging cylindrical shocks.

M. Kjellander, N. Tillmark & N. Apazidis.

Phys. Fluids 23, 116103 (2011).

This is a continuation of previous experiments concentrating on the dynamics of converging cylindrical shock waves. The self-similarity exponent for the motion of cylindrical imploding shock waves was measured for different gases.

The setup and experiments were made made by MK with support from NT. MK wrote the paper with feedback from NT and NA.

# Paper 6

Numerical assessment of shock tube with inner body designed to create cylindrical shock waves.

M. Kjellander & N. Apazidis

Technical report

This is a numerical study on the performance of the cylindrical convergence chamber. The numerical code was written by MK and NA; MK performed the calculations and wrote the report.

## Paper 7

Generation of spherical converging shocks in a shock tube by wall shaping. M. Kjellander, N. Tillmark & N. Apazidis. Manuscript.

A study on the convergence of shock waves in a smoothly convergent shock tube designed to create a spherical shape of the shock during the last stage of implosion. The design of the setup was made by the authors jointly. MK performed the experiments and wrote the paper, with feedback from NT and NA. Olli Launila and Lars-Erik Berg, KTH Applied Physics, provided invaluable contributions to the spectrometric setup and interpretation of the results.

# Acknowledgements

This project has been financially supported by the Swedish Research Council (Vetenskapsrådet) and the Göran Gustafson Foundation. Stiftelsen Erik Petersohns minne and the P F Lindström Foundation are acknowledged for funding participation at international conferences.

I would like to my thank my advisors Docent Nicholas Apazidis and Dr. Nils Tillmark for their enthusiasm and encouragement throughout the project, and for always trying to help me out whenever I got stuck. I would also like to thank Professor Henrik Alfredsson who was the one who gave me the opportunity to work with this project.

Great credit goes to Göran Rådberg and Kim Karlström the toolmakers, for ideas and manufacturing of the experimental equipment. I am also much obliged to Lars-Erik Berg and Olli Launila at KTH Applied Physics for the loan of spectrometers and input and insights on the physics involved.

I would also like to mention all the colleagues at the Mechanics lab, who have created a wonderful working environment! When you enjoy going to work it is a sure sign of having good people as co-workers. Special mention goes to Bengt, whom I particularly have pestered with all kinds of non-technical work and computer issues.

Lastly, I would like to thank my wife Irena, not least for having patience with me during the last hectic year.

May 2nd, 2012 Stockholm

Malte

### APPENDIX A

# Specific heat and speed of sound from $\alpha$

In the case of no Coulomb interactions the specific heats and equilibrium speed of sound can be rewritten in terms of derivatives of  $\alpha_i$ , which simplifies the numerical work in some cases where these are practically already calculated. The equilibrium speed of sound  $a_e$ ,

$$a_e^2 = \left(\frac{\partial p}{\partial \rho}\right)_s = \gamma \left(\frac{\partial p}{\partial \rho}\right)_T$$
 (A.1)

where  $\gamma = c_p/c_v$ . We aim to express  $a_e$  in terms of known quantities and derivatives. The heat capacities are found from the enthalpy and energy. Neglecting electronic excitation, these are

$$h = \frac{5}{2}(1 + \alpha_e)RT + R\sum_{i=1}^{\ell} \alpha_i \sum_{j=1}^{i} \frac{I_j}{k}$$
 (A.2)

$$e = \frac{3}{2}(1 + \alpha_e)RT + R\sum_{i=1}^{\ell} \alpha_i \sum_{j=1}^{i} \frac{I_j}{k}$$
(A.3)

so that

$$c_p = \left(\frac{\partial h}{\partial T}\right)_p = \frac{5}{2}(1 + \alpha_e)R + \frac{5}{2}TR\left(\frac{\partial \alpha_e}{\partial T}\right)_p + R\sum_{i=1}^{\ell} \left(\frac{\partial \alpha_i}{\partial T}\right)_p \sum_{j=1}^{i} \frac{I_j}{k} \quad (A.4)$$

and

$$c_v = \left(\frac{\partial e}{\partial T}\right)_v = \frac{3}{2}(1 + \alpha_e)R + \frac{3}{2}TR\left(\frac{\partial \alpha_e}{\partial T}\right)_v + R\sum_{i=1}^{\ell} \left(\frac{\partial \alpha_i}{\partial T}\right)_v \sum_{j=1}^{i} \frac{I_j}{k} \quad (A.5)$$

where

$$\left(\frac{\partial \alpha_e}{\partial T}\right)_F = \sum_{i=1}^{\ell} \left(\frac{\partial \alpha_i}{\partial T}\right)_F \tag{A.6}$$

With the equation of state Eq. 2.11 the speed of sound can then be written

$$a_e^2 = \gamma \left(\frac{\partial p}{\partial \rho}\right)_T = \frac{c_p}{c_v} \left(\frac{\partial p}{\partial \rho}\right)_T = \frac{c_p}{c_v} \frac{\partial}{\partial \rho} \left(\rho(1 + \alpha_e)RT\right)_T =$$

$$= \frac{c_p}{c_v} \left[ (1 + \alpha_e)RT + \rho RT \left(\frac{\partial \alpha_e}{\partial \rho}\right)_T \right]$$
(A.7)

The above expression together with A.4 and A.5 is used to calculate  $a_e$ . All thermodynamic variables are known but the derivatives of  $\alpha_i$  has to be evaluated numerically around the current state of the gas  $p, \rho, T, \alpha_i$ . A simple evaluation can be made as

$$\left(\frac{\partial \alpha_i}{\partial F}\right)_G = \frac{\alpha_i(F + dF_1, G) - \alpha_i(F - dF_2, G)}{dF_1 + dF_2} \tag{A.8}$$

#### APPENDIX B

# Coulomb effects on thermodynamic variables

In a partly ionised gas Coulomb forces between the charged particles lead to departures from the ideal state. When the effect is weak, consideration to the Coulomb interactions may be taken in form of correction terms to the thermodynamic variables. Different models exist for different gas conditions: here is a derivation using the Debye-Hückel model for the ion charges for weak Coulomb interactions. To derive the corrections due to the Coulomb forces on the thermodynamic state and the species distribution, the electrostatic energy contribution to the free energy is found, which in turn gives the desired corrections. The electrostatic potential around a point charge is found by considering the other particles not as individual charges but as a uniform charge cloud and solving the Poisson equation. The derivation of the potential may be found in e.g. Griem (1962), Ebeling (1976) or Salzmann (1998). The electrostatic energy of a gas in a volume V resulting from this first approximation is given as

$$E_c = -\frac{kTV}{8\pi r_D^3} \tag{B.1}$$

The parameter  $r_D$  is the Debye radius which is a characteristic of the surrounding charge cloud and determines the sphere of influence of the ion charge, which for a single-temperature plasma may be written

$$r_D = \left[ \frac{q^2}{\epsilon_0 kT} (n_e + \sum_{i}^{\ell} n_i z_i^2) \right]^{-1/2} = \left[ \frac{q^2}{\epsilon_0 kTV} (N_e + \sum_{i}^{\ell} N_i z_i^2) \right]^{-1/2}$$
(B.2)

where q is the elementary charge,  $\epsilon_0$  is the vacuum permittivity,  $z_i = i$  is the charge state of the ion i. Note that several of the cited authors have used other unit systems, while SI units are used here. The number of particles of ionic end electronic components  $N_i$  and  $N_e$  in the volume V and number densities  $n_i = N_i V$  and  $n_e = N_e V$  are defined as usual. Outside the Debye sphere, which is the sphere around the ion with a radius  $r_D$ , the ion is effectively screened by the cloud. A typical validity requirement for the statistical Debye-Hückel model is that several ions must be present within a Debye sphere.

The influence of the Coulomb forces on the free energy is expressed as a correction term to the ideal gas energy,  $F = F_{ig} + F_C$ , which derives from the electrostatic energy. Using  $E = -T^2 \partial/\partial T(F/T)$ , the correction to the free energy becomes

$$F_C = -\frac{kTV}{12\pi r_D^3} \tag{B.3}$$

### B.0.1. Equation of state

The pressure follows from the free energy as  $p = (\partial F/\partial V)_{N_i,T}$ . The ideal translational contribution to the pressure is given in Eq. 2.11. The correction term is then found from Eq. B.3,

$$\delta p_C = -\left(\frac{\partial F_C}{\partial V}\right)_{N_i,T} = \frac{kT}{12\pi r_D^3} - \frac{kTV}{12\pi r_D^3} \frac{3}{2V} = -\frac{kT}{24\pi r_D^3}$$
 (B.4)

For completeness the total pressure including the Coulomb correction is then written

$$p = p_{iq} + p_C = \rho(1 + \alpha_e)RT + \delta p_C \tag{B.5}$$

# B.0.2. Saha equation

The Saha equation may be derived from minimising the free energy considering the ionisation reaction where the (i+1)th electron is removed from the atomic species A,

$$A_i \rightleftharpoons A_{i+1} + e^-, \quad i = 0, 1, 2, \dots \ell - 1$$
 (B.6)

where  $\ell$  denotes the atomic number of A. The free energy of the ideal gas  $F_{ig}$  is given by statistical mechanics. With the Coulombic correction the free energy of a partially ionised gas in local thermodynamic equilibrium becomes

$$F = F_{ig} + F_C = -\sum_{i=1}^{\ell} N_i k T \ln \frac{Z_i e}{N_i} - N_e k T \ln \frac{Z_e e}{N_e} + F_C$$
 (B.7)

where  $Z_i$  and  $Z_e$  are the partition functions of the ions and free electrons. Differentiating and setting  $(\delta F)_{V,T} = 0$  gives

$$\delta F = \sum_{j} \frac{\partial (F_{ig} + F_c)}{\partial N_j} \delta N_j = \sum_{j} \left( \frac{\partial F_{ig}}{\partial N_j} + \mu_{j,C} \right) \delta N_j = 0$$
 (B.8)

where  $\mu_{C,j} = \partial F_C/\partial N_j$  and the summation j is made for j = i, j = i+1 and j = e.

According to the reaction in Eq. B.6  $\delta N_i = -\delta N_{i+1} = -\delta N_e$  and Eq. B.8 becomes

$$\left(\frac{\partial F_{ig}}{\partial N_i} - \frac{\partial F_{ig}}{\partial N_{i+1}} - \frac{\partial F_{ig}}{\partial N_e} + \mu_{C,i} - \mu_{C,i+i} - \mu_{C,e}\right) \delta N_i = 0 \rightarrow$$

$$-kT \ln \frac{Z_i e}{N_i} + N_i kT \frac{1}{N_i} + \mu_{C,i} +$$

$$-(-kT \ln \frac{Z_{i+1} e}{N_{i+1}} + N_{i+1} kT \frac{1}{N_{i+1}} + \mu_{C,i+i}) +$$

$$-(-kT \ln \frac{Z_e e}{N_e} + N_e kT \frac{1}{N_e} + \mu_{C,e}) = 0 \rightarrow$$

$$\ln \left(\frac{Z_{i+1} Z_e e N_i}{N_e}\right) - 1 = -\frac{\mu_{C,i} - \mu_{C,i+i} - \mu_{C,e}}{N_e} \qquad (E)$$

$$\ln\left(\frac{Z_{i+1}Z_{e}eN_{i}}{N_{i+1}N_{e}Z_{i}}\right) - 1 = -\frac{\mu_{C,i} - \mu_{C,i+i} - \mu_{C,e}}{kT}$$
(B.9)

Defining the reduction in ionisation potential due to the Coulomb interactions as

$$\Delta I_{i+1} \equiv \mu_{C,i} - \mu_{C,i+i} - \mu_{C,e}$$
 (B.10)

Eq. B.9 becomes

$$\frac{N_{i+1}N_e}{N_i} = \frac{Z_{i+1}Z_e}{Z_i} \exp\left(\frac{\Delta I_{i+1}}{kT}\right)$$
 (B.11)

This can be written in terms of the particles densities  $n_i$  by dividing with the volume V and using that  $N_j = n_j V$ :

$$\frac{n_{i+1}n_e}{n_i} = \frac{1}{V} \frac{Z_{i+1}Z_e}{Z_i} \exp\left(\frac{\Delta I_{i+1}}{kT}\right)$$
 (B.12)

The partition functions for a monatomic ion consist of one translational and one internal part,  $Z_i = Z_i^{tr} Z_i^{el}$ , the latter accounting for the excited electrons within the ion. The translational contributions is

$$Z_i^{tr} = V \left(\frac{2\pi m_i kT}{h^2}\right)^{3/2} \tag{B.13}$$

where  $m_i$  is the molecular weight of the i:th ion, k the Boltzmann constant and h the Planck constant. Since the weight difference of the successive ions are negligible the translational part of the partition functions cancel in Eq. B.11 and B.11. The electronic contribution can be written (Zel'dovich & Raizer 2002) as

$$Z_i^{el} = \sum_l e^{-\varepsilon_{l,i}/kT} = e^{-\varepsilon_{0,i}/kT} \sum_l e^{-(\varepsilon_{l,i} - \varepsilon_{0,i})/kT} = e^{-\varepsilon_{0,i}/kT} Q_i^{el}$$
(B.14)

where  $\varepsilon_0$  is the ground state of ion i and the summation is taken over all energy states. In other words the transformed partition function  $Q^{el}$  relates the energy of each electronic level to the ground state of the individual ions instead of to the ground state of the atom. The energy differences of the succesive ionic ground states are equal to the ionisation potentials,  $\varepsilon_{0,i+1} - \varepsilon_{0,i} = I_{i+1}$ .

The partition function of the free electrons has one temperature-dependent contribution from the translational energy and one constant contribution related to the spin,  $Z^{spin} = 2$ . The total electron partition function is then

$$Z_e = 2V \left(\frac{2\pi m_e kT}{h^2}\right)^{3/2} \tag{B.15}$$

where  $m_e$  is the electron weight. Inserting Eqs. B.13, B.14 and B.15 into Eq. B.12 yields the Saha equation:

$$\frac{n_{i+1}n_e}{n_i} = 2\left(\frac{2\pi m_e kT}{h^2}\right)^{3/2} \frac{Q_{i+1}^{el}}{Q_i^{el}} \exp\left(-\frac{I_{i+1} - \Delta I_{i+1}}{kT}\right)$$
(B.16)

Using the particle fractions  $\alpha_i = n_i/n_H$  and  $\alpha_e = n_e/n_H$  this is rewritten as

$$\frac{\alpha_{i+1}\alpha_e}{\alpha_i} = \frac{2}{n_H} \left(\frac{2\pi m_e kT}{h^2}\right)^{3/2} \frac{Q_{i+1}^{el}}{Q_i^{el}} \exp\left(-\frac{I_{i+1} - \Delta I_{i+1}}{kT}\right)$$
(B.17)

Noting that  $\rho \approx n_H m_H$ , Eq. B.17 has the same form as Eq. 6.13. The equation of state B.5 can be used to rewrite the equation as a function of temperature and pressure,

$$\frac{\alpha_{i+1}}{\alpha_i} = \frac{1 + \alpha_e}{\alpha_e} \left(\frac{2\pi m_e}{h^2}\right)^{3/2} \frac{(kT)^{5/2}}{p - \delta p_C} \frac{2Q_{i+1}^{el}}{Q_i^{el}} \exp\left(-\frac{I_{i+1} - \Delta I_{i+1}}{kT}\right)$$
(B.18)

The potential reduction according to the Debye-Hückel method is received by taking the derivative of Eq. B.3:

$$\Delta I_{i+1} = \frac{\partial F_C}{\partial N_i} - \frac{\partial F_C}{\partial N_{i+1}} - \frac{\partial F_C}{\partial N_e} = \frac{(i+1)q^2}{4\pi\epsilon_0 r_D}$$
 (B.19)

B.0.3. Energy and enthalpy

The expression for the energy may be calculated from  $E=-T^2\partial/\partial T(F/T)$  using the partition functions. Again  $F=F_{ig}+F_C$ , with  $F_{ig}$  for a partially ionised monatomic gas in local thermodynamic equilibrium given in Eq. B.7. The Coulombic correction from the electrostatic potential is given in Eq. B.1. Dividing the partition functions in their translational and electronic parts,  $Z=Z^{tr}Z^{el}$  yields

$$\left(\frac{\partial}{\partial T} \frac{F_{ig}}{T}\right)_{V,N} = -k \sum_{i=0}^{\ell} \left[ N_i \left(\frac{\partial \ln Z_i^{tr}}{\partial T}\right)_{V,N} + N_i \left(\frac{\partial \ln Z_i^{el}}{\partial T}\right)_{V,N} \right] - k N_e \left(\frac{\partial \ln Z_e^{tr}}{\partial T}\right)_{V,N} \\
= -k \sum_{i=0}^{\ell} \left[ N_i \frac{3}{2} \frac{1}{T} + N_i \left(\frac{\partial \ln Z_i^{el}}{\partial T}\right)_{V,N} \right] - k N_e \frac{3}{2} \frac{1}{T} \tag{B.20}$$

Inserting the total number of heavy particles  $N_H = \sum_{i=0}^{\ell} N_i$  the above yields

$$E_{ig} = -T^{2} \left( \frac{\partial}{\partial T} \frac{F_{ig}}{T} \right)_{V,N} = \frac{3}{2} (N_{H} + N_{e}) kT + kT^{2} \sum_{i=0}^{\ell} N_{i} \left( \frac{\partial \ln Z_{i}^{el}}{\partial T} \right)_{V,N} =$$

$$= \frac{3}{2} (1 + \alpha_{e}) N_{H} kT + kT^{2} N_{H} \sum_{i=0}^{\ell} \alpha_{i} \left( \frac{\partial \ln Z_{i}^{el}}{\partial T} \right)_{V,N}$$
(B.21)

The last term is rewitten using Eq. B.14,

$$\sum_{i=0}^{\ell} \alpha_i \left( \frac{\partial \ln Z_i^{el}}{\partial T} \right)_{V,N} = \sum_{i=0}^{\ell} \alpha_i \left( \frac{\partial \ln Q_i^{el}}{\partial T} \right)_{V,N} + \sum_{i=0}^{\ell} \alpha_i \left( \frac{\partial \ln e^{-\varepsilon_{0,i}/kT}}{\partial T} \right)_{V,N} =$$

$$= \sum_{i=0}^{\ell} \alpha_i \left( \frac{\partial \ln Q_i^{el}}{\partial T} \right)_{V,N} + \sum_{i=1}^{\ell} \alpha_i \sum_{j=1}^{i} \frac{I_j}{kT^2} \tag{B.22}$$

Using that the masses of the ionic species are approximately equal to the atomic mass  $M_i \approx M_A \rightarrow N_H k \approx m R_A$  and the energy is rewritten

$$E_{ig} = \frac{3}{2}(1 + \alpha_e)mR_A T + mR_A \sum_{i=1}^{\ell} \alpha_i \sum_{i=1}^{i} \frac{I_j}{k} + mR_A T^2 \sum_{i=0}^{\ell} \alpha_i \left(\frac{\partial \ln Q_i^{el}}{\partial T}\right)_{V,N}$$
(B.23)

The enthalpy per unit mass  $h=e+p/\rho$  is similarly divided into an ideal and Coulombic part:  $h=e_{ig}+e_C+(p_{ig}+p_C)/\rho$ . The ideal contribution to the enthalpy is acquired directly from Eq. B.5 and Eq. B.23:

$$h_{ig} = \frac{5}{2}(1 + \alpha_e)R_A T + R_A \sum_{i=1}^{\ell} \alpha_i \sum_{j=1}^{i} \frac{I_j}{k} + R_A \sum_{i=0}^{\ell} \alpha_i \frac{W_i}{k}$$
 (B.24)

where the energy of the electronic excitation is

$$W_{i} = kT^{2} \left( \frac{\partial \ln Q_{i}^{el}}{\partial T} \right)_{VN} \tag{B.25}$$

The two Coulomb corrections have been derived above and we have

$$h_C = e_C + p_C/\rho = \frac{1}{\rho V} E_C + p_C/\rho = -\frac{kT}{8\pi \rho r_D^3} - \frac{kT}{24\pi \rho r_D^3} = -\frac{kT}{6\pi \rho r_D^3}$$
 (B.26)

# References

- Anderson, J. D. 2003 Modern Compressible Flow, 3rd edn. McGraw-Hill, New York.
- APAZIDIS, N. & LESSER, M. B. 1996 On generation and convergence of polygonal-shaped shock waves. *J. Fluid Mech.* **309**, 301–319.
- Apazidis, N., Lesser, M. V., Tillmark, N. & Johansson, B. 2002 An experimental and theoretical study of converging polygonal shock waves. *Shock waves* 12, 39–58.
- ASLAN, N. & MOND, M. 2005 A numerical scheme for ionizing shock waves. J. Comput. Phys. **210**, 410–420.
- Barkhudarov, E. M., Kossyi, I. A., Mdivnishvili, M. O., Sokolov, I. V. & Taktakishvili, M. I. 1988 Non-one-dimensional convergent shock waves. *Fluid Dynamics* 23, 296–302.
- BARONETS, P. N. 1981 Formation and propagation of shock waves in a pulsed induction discharge. *Izv. Akad. Nauk SSSR*, *Mekh. Zhidk. Gaza* 1, 129–133.
- BARONETS, P. N. 1984 Imploding shock waves in a pulsed induction discharge. *Fluid Dynamics* **19**, 503–508.
- BARONETS, P. N. 1994 Cylindrical shock waves generated by a spark discharge and their interaction with the shock waves from a pulsed induction discharge. *Izv. Ross. Akad. Nauk, Mekh. Zhidk. Gaza* 1, 166–170.
- Belokon, V. A., Petrukhin, A. I. & Proskuryakov, V. A. 1965 Entrance of a strong shock wave into a wedge-like cavity. *Soviet Physics JETP* **21**, 33.
- Ben-Dor, G. 2006 A state-of-the-knowledge review on pseudo-steady shock-wave reflections and their transition criteria. *Shock Waves* 15, 277–294.
- Ben-Dor, G. & Glass, I. I. 1979 Domains and boundaries of non-stationary oblique shock-wave reflexions. 1. Diatomic gas. *J. Fluid Mech.* **92**, 459–496.
- Ben-Dor, G. & Glass, I. I. 1980 Domains and boundaries of non-stationary oblique shock-wave reflexions. 2. Monatomic gas. J. Fluid Mech. 96, 735–756.
- Ben-Dor, G. & Takayama, K. 1992 The phenomena of shock wave reflection a review of unsolved problems and future research needs. Shock Waves 2, 211–223.
- Berezhetskaya, N. K., Bol'shakov, E. F., Golubev, S. K., Dorofeyuk, A. A., Kossyi, I. A., Semenov, V. E. & Terekhin, V. E. 1984 Gasdynamic effects of a ring surface discharge. *Sov. Phys. JETP* **60**, 1108–1111.

- BIBERMAN, L. M., MNATSAKANYAN, A. K. & YAKUBOV, I. T. 1971 Ionization relaxation behind strong shock waves in gases. Sov. Phys. Usp. 13, 728–744.
- BLEAKNEY, W., WEIMER, D. & FLETCHER, C. H. 1949 The shock tube a facility for investigations in fluid dynamics. *Rev. Sci. Inst.* **20**, 807–815.
- Bond, C., Hill, D. J., Meiron, D. I. & Dimotakis, P. E. 2009 Shock focusing in a planar convergent geometry: experiment and simulation. *J. Fluid Mech.* **641**, 297–333.
- BOND, J. 1954 The structure of a shock front in argon. Los Alamos Sci. Lab Rept. LA-1693
- Butler, D. S. 1954 Converging spherical and cylindrical shocks, Report No. 54/54. Burgess Hill, New York.
- Cambel, A. B. & Jennings, B. H. 1967 Gas Dynamics. Burgess Hill, New York.
- CHESTER, W. 1954 The quasi-cylindrical shock tube. Phil. Mag. 45, 1293–1301.
- Chisnell, R. F. 1955 The normal motion of a shock wave through a nonuniform one-dimensional medium. *Proc. R. Soc. London* 232, 350–370.
- Chisnell, R. F. 1957 The motion of a shock wave in a channel, with applications to cylindrical and spherical shocks. *J. Fluid Mech.* **2**, 286–298.
- Chisnell, R. F. 1998 An analytic description of converging shock waves. *J. Fluid Mech.* **354**, 357–375.
- DIMOTAKIS, P. E. & SAMTANEY, R. 2006 Planar shock cylindrical focusing by a perfect-gas lens. *Phys. Fluids* **18**, 031705.
- Drellishak, K. S., Knopp, C. F. & Cambel, A. B. 1963 Partition functions and thermodynamic properties of argon plasma. *Phys. Fluids* 6, 1280–1288.
- DUMITRESCU, L. Z. 1983 Studies on shock amplifications, focusing and stability. In *Shock waves and shock tubes; Proc. 14th Intern. Symp.* (ed. R. Archer & B. Milton). Sydney, Australia: Univ. of New South Wales Press.
- Dumitrescu, L. Z. 1992 On efficient shock-focusing configurations. In 11th Australasian Fluid Mechanics Conference, pp. 723–725. Hobart, Tasmania: University of Tasmania.
- EBELING, W. 1976 Theory of bound states and ionization equilibrium in plasmas and solids. Akademie-Verlag, Berlin.
- ELIASSON, V. 2007 On focusing of shock waves. PhD thesis, KTH, Stockholm, TRITA-MEK Tech. Rep. 2007:06.
- ELIASSON, V., APAZIDIS, N. & TILLMARK, N. 2007a Controlling the form of strong converging shocks by means of disturbances. Shock Waves 17, 29–42.
- ELIASSON, V., APAZIDIS, N., TILLMARK, N. & LESSER, M. B. 2006 Focusing of strong shocks in an annular shock tube. *Shock Waves* **15**, 205–217.
- ELIASSON, V., TILLMARK, N., SZERI, A. & APAZIDIS, N. 2007b Light emission during shock wave focusing in air and argon. *Phys. Fluids* **19**, 106106.
- EMRICH, R. J. & WHEELER, D. B. 1958 Wall effects in shock tube flow. *Phys. Fluids* 1, 14–23.
- FLAGG, R. F. & GLASS, I. I. 1968 Explose-driven, spherical shock waves. *Phys. Fluids* 11, 2282.
- Fomin, V. M., Postnikov, B. V. & Yakovlev, V. I. 2003 Effect of the high rate of

- avalanche ionization behind a shock wave in a monatomic gas. *Doklady Physics* **48**, 418–421.
- Fujimoto, Y. & Mishkin, E. A. 1978 Analysis of spherically imploding shocks. *Phys. Fluids* **21**, 1933–1938.
- Fujiwara, K., Hiroe, T. & Matsuo, H. 1992 New method of generating cylindrical imploding shocks using a flyer disk. *Appl. Phys. Lett.* **61**, 3110–3112.
- Fujiwara, T., Mizoguchi, K. & Sugimura, T. 1971 Smoked film record for oxyhydrogen converging detonations. J. Phys. Soc. Jpn. 31, 621–622.
- Fujiwara, T. & Taki, S. 1974 A rotational temperature of oxyacetylene converging detonation. *Acta Astronaut.* 1, 863–872.
- Glass, I. I. 1967 Can. Aero. Space J. 13, 347–401.
- GLASS, I. I. 1972 Appraisal of UTIAS implosion-driven hypervelocity launchers and shock tubes. Institute for Aerospace studies, University of Toronto.
- GLASS, I. I., BRODE, H. L. & CHAN, S. K. 1974 Strong planar shock waves generated by explosively-driven spherical implosions. AIAA J. 12, 367–374.
- GLASS, I. I. & SAGIE, D. 1982 Application of explosive-driven implosions to fusion. *Phys. Fluids.* **25**, 269.
- GLASS, I. I. & SHARMA, S. P. 1976 Production of diamonds from graphite using explosive-driven implosions. AIAA J. 14, 402–404.
- Griem, H. R. 1962 High density corrections in plasma spectroscopy. *Phys. Rev.* 128, 997–1003
- GROSS, R. 1965 Strong ionizing shock waves. Rev. Mod. Phys. 37, 724–743.
- Guderley, G. 1942 Starke kugelige und zylindrische Verdichtungsstöße in der Nähe des Kugelmittelpunktes bzw. der Zylinderachse. Luftfahrtforschung 19, 302–313.
- Hafner, P. 1988 Strong convergent shock waves near the center of convergence: A power series solution. J. Appl. Math.. 48, 1244–1261.
- Henshaw, W. D., Smyth, N. F. & Schwendeman, D. W. 1986 Numerical shock propagation using geometrical shock dynamics. *J. Fluid Mech.* 171, 519–545.
- HOFFERT, M. I. & LIEN, H. 1967 Quasi-one-dimensional, nonequilibrium gas dynamics of partially ionized two-temperature argon. *Phys. Fluids* **10**, 1769.
- HONG, Z., DAVIDSON, D. & HANSON, R. K. 2009 Contact surface tailoring condition for shock tubes with different driver and driven section diameters. Shock Waves 19, 331–336.
- HORNUNG, H. G., PULLIN, D. I. & PONCHAUT, N. 2008 On the question of universality of imploding shock waves. *Acta Mech.* **201**, 31–35.
- HOSSEINI, S. H. R., ONODERA, O. & TAKAYAMA, K. 2000 Characteristics of an annular vertical diaphragmless shock tube. *Shock Waves* **10**, 151–158.
- HOSSEINI, S. H. R. & TAKAYAMA, K. 2005a Experimental study of richtmyer-meshkov instability induced by cylindrical shock waves. *Phys. Fluids* 17, 084101.
- HOSSEINI, S. H. R. & TAKAYAMA, K. 2005b Implosion from a spherical shock wave reflected from a spherical wall. *J. Fluid Mech.* **530**, 223–239.
- HOSSEINI, S. H. R. & TAKAYAMA, K. 2009 Experimental study of toroidal shock wave focusing in a compact vertical annular diaphragmless shock tube. *Shock Waves* **20**, 1–7.
- HUGONIOT, P.-H. 1889 Mémoire sur la propagation du mouvement dans les corps et

- plus spécialement dans les gaz parfaits, 2e partie. Journal de École Polytechnique.  $58. \ 1-125.$
- Johansson, B. 2000 Experimental study of shock wave focusing in a confined reflector. Lic. Thesis: Royal Institute of Technology, Stockholm, Sweden.
- Johansson, B., Apazidis, N. & Lesser, M. B. 1999 On shock waves in a confined reflector. Wear 233-235, 79–85.
- Jones, D. L., Goyer, G. G. & Plooster, M. N. 1968 Shock wave from a lightning discharge. J. Geophys. Res. 73, 3121–3127.
- Kaniel, A., Igra, O., Ben-Dor, G. & Mond, M. 1986 Ionization behind strong normal shock waves in argon. *Phys. Fluids* **29**, 3618–3625.
- KJELLANDER, M., TILLMARK, N. & APAZIDIS, N. 2010 Thermal radiation from a converging shock implosion. *Phys. Fluids* **22**, 046102.
- KJELLANDER, M., TILLMARK, N. & APAZIDIS, N. 2011 Experimental determination of the self-similarity constant for converging cylin- drical shocks. *Phys. Fluids* **23**, 116103.
- KLEINE, H. 1985 Time resolved shadow graphs of focusing cylindrical shock waves. *Tech. Rep.*. RWTH, Aachen, Germany.
- KNYSTAUTAS, R., LEE, B. H. K. & LEE, J. H. S. 1969 Diagnostic Experiments on Converging Detonations. *Phys. Fluids Suppl. I* pp. 165–168.
- KNYSTAUTAS, R. & LEE, J. H. 1967 Spark initiation of converging detonation waves. AIAA J. 5, 1209.
- KNYSTAUTAS, R. & LEE, J. H. S. 1971 Experiments on the stability of converging cylindrical detonations. *Combustion and Flame* **16**, 61–73.
- KOZLOV, G. I. & STUPITSKII, E. L. 1968 State of argon behind a shock wave at Mach numbers from 20 to 50, with allowance for excitation, multiple ionization, and Coulomb interactions. *Zh. Prikl. Mekh. Tekh. Fiz.* **9**, 94–97.
- Krehl, P. & Engemann, S. 1995 August Toepler the first who visualized shock waves. *Shock Waves* 5, 1–18.
- LAZARUS, R. B. 1980 Comments on "Analysis of spherical imploding shocks". *Phys. Fluids* 23, 844.
- LAZARUS, R. B. 1981 Self-similar solutions for converging shocks and collapsing cavities. SIAM J. Numer. Anal. 18, 316–371.
- LAZARUS, R. B. & RICHTMYER, R. D. 1977 Similarity Solutions for Converging Shocks. Los Alamos Scientific Laboratory of the University of California, Los Alamos, NM.
- Lee, J.-H. & Glass, I. I. 1984 Pseudo-stationary oblique-shock-wave reflections in frozen and equilibrium air. *Prog. Aerospace Sci.* 21, 33–80.
- Lee, J. H. S. & Knystautas, R. 1971 Experiments on the Stability of Converging Cylindrical Detonation. *Combust. Flame* **16**, 61.
- LEE, J. H. S. & LEE, B. H. K. 1965 Cylindrical imploding shock waves. *Phys. Fluids* 8, 2148.
- LINDBLOM, P. 1998 New compact Echelle spectrographs with multichannel time-resolved capabilities. *Anal. Chim. Acta* 380, 353–361.
- MATSUO, H. 1983 Cylindrically converging shock and detonation waves. *Phys. Fluids* **26**, 1755.

- Matsuo, H., Ebihara, K. & Nagayama, K. 1983 Optical study of cylindrically converging blast waves. J. Appl. Phys. 55, 271–272.
- Matsuo, H., Ebihara, K., Ohya, Y. & Sanematsu, H. 1985 Spectroscopic study of cylindrically converging shock waves. *J. Appl. Phys.* 58, 2487–2491.
- MATSUO, H. & FUJIWARA, K. 1990 Explosive-driven cylindrical imploding shocks. Phys. Fluids A  $\bf 2$ , 266–273.
- Matsuo, H. & Nakamura, Y. 1980 Experiments on cylindrically converging blast waves in atmospheric air. J. Appl. Phys. **51**, 3126–3129.
- MATSUO, H. & NAKAMURA, Y. 1981 Cylindrically converging blast waves in air. J. Appl. Phys. **52**, 4503–4507.
- Matsuzaki, R. 1974 Quasi-one-dimensional nonequilibrium flow of partially ionized argon with different species temperatures. J. Phys. Soc. Jpn. 38, 1488–1493.
- MICHAUT, C., STEHLÉ, C., LEYGNAC, S., LANZ, T. & BOIREAU, L. 2004 Jump conditions in hypersonic shocks. *Eur. Phys. J. D* 28, 381–392.
- MISHKIN, E. & FUJIMOTO, Y. 1978 Analysis of a cylindrical imploding shock wave. J. Fluid Mech. 89, 61–78.
- Nakamura, Y. 1983 Analysis of self-similar problems of imploding shock waves by the method of characteristics. *Phys. Fluids* **26**, 1234–1239.
- DE NEEF, T. & HECHTMAN, C. 1978 Numerical study of the low due to cylindrical implosion. Computers and Fluids 6, 185–202.
- NEEMEH, R. A. & AHMAD, Z. 1986 Stability and collapsing mechanism of strong and weak converging cylindrical shock waves subjected to external perturbation. In *Proc. 15th Intern. Symp. on Shock Waves and Shock Tubes* (ed. D. Bershader & R. Hanson), pp. 107–114. Stanford, CA: Stanford University Press.
- NIEUWENHUIJZEN, H., DE JAGER, C., CUNTZ, M., LOBEL, A. & ACHMAD, L. 1992 A generalized version of the rankine-hugoniot relations including ionization, dissociation, radiation and related phenomena. *Astron. Astrophys*, **28**, 195–200.
- OERTEL, H. 1966 Stossrohre. Springer-Verlag, Wien.
- Palmer, H. B. & Knox, B. E. 1961 Contact surface tailoring in a chemical shock tube. AIAA J. 1, 2161–2163.
- Payman, W. & Shepherd, W. C. F. 1946 Explosion Waves and Shock Waves. VI. The Disturbance Produced by Bursting Diaphragms with Compressed Air. *Proceedings of the Royal Society of London. Series A, Mathematical and Physical Sciences* **186** (1006), pp. 293–321.
- Perry, R. W. & Kantrowitz, A. 1951 The production and stability of converging shock waves. J. Appl. Phys 22, 878–886.
- Petrie-Repar, P. J. & Jacobs, P. A. 1998 A computational study of shock speeds in high-performance shock tubes. *Shock Waves* 8, 79–91.
- Petschek, H. & Byron, S. 1957 Approach to equilibrium ionization behind strong shock waves in argon. *Ann. Phys.* 1, 270–315.
- Poisson, S. D. 1808 Mémoire sur la theorie du son. *Journal de École Polytechnique*. **7**, 319–392.
- PONCHAUT, N. F., HORNUNG, H. G. & MOUTON, D. I. 2006 On imploding cylindrical and spherical shock waves in a perfect gas. J. Fluid. Mech. 560, 103–122.

- Rankine, W. J. M. 1870 On the thermodynamic theory of waves of finite longitudinal disturbances. *Phil. Trans. Roy. Soc. London* **160**, 277–286.
- RESLER, E. L., LIN, S. C. & KANTROWITZ, A. 1952 The production of high temperatures in shock tubes. *J. App. Phys.* 23, 1390–1399.
- RIEMANN, L. 1860 Über die Fortpflanzung ebener Luftwellen von endlicher Schwingungsweite. Abhandlungen der Königlichen Gesellschaft der Wissenschaften zu Göttingen. 8, 43–65.
- ROBERTS, D. E. & GLASS, I. I. 1971 Spectroscopic investigation of combustion-driven spherical implosion waves. *Phys. Fluids* **14**, 1662–1670.
- Roig, R. A. & Glass, I. I. 1977 Spectroscopic study of combustion-driven implosions. *Phys. Fluids* **20**, 1651–1656.
- DE ROSA, M., FAMÀ, F., HARITH, M. A., PALLESCHI, V., SALVETTI, A., SINGH, D. P., VASELLI, M., BARKUDAROV, E. M., MDIVNISHVILI, M. O., SOKOLOV, I. V. & TAKTASHVILI, M. I. 1991 Mach reflection phenomenon in the interaction of spherical shock waves in air. *Phys. Letters A* **156**, 89–95.
- Saillard, Y., Barbry, H. & Mournier, C. 1985 Transformation of a plane uniform or spherical shock by wall shaping. In *Shock waves and shock tubes; Proc. 15th Intern. Symp.*, pp. 147–154. Stanford, CA: Stanford University Press.
- Saito, T., Eguichi, T., Takayama, K. & Taniguchi, H. 2001 Hazard predictions for volcanic explosions. J. Volcanol. Geotherm. Res. 106, 39–51.
- Saito, T. & Glass, I. I. 1982 Temperature Measurements at an Implosion Focus. *Proc. R. Soc. Lon. A* **384**, 217–231.
- Salas, M. 2007 The curious events leading to the theory of shock waves. *Shock Waves* **16**, 477–487, 10.1007/s00193-007-0084-z.
- Salzmann, D. 1998 Atomic Physics in Hot Plasmas. Oxford University Press, New York.
- Schardin, H. 1932 Bemerkungen zum Druckausgleichsvorgang in einer Rohrleitung. *Phys. Zeit.* **33**, 60–64.
- SCHWENDEMAN, D. W. & WHITHAM, G. B. 1987 On Converging Shock Waves. Proc. R. Soc. Lon. A **413**, 297–311.
- SETCHELL, R. E., STORM, E. & STURTEVANT, B. 1972 An investigation of shock strengthening in a conical convergent channel. *Phys. Fluids* **56**, 505–522.
- Sokolov, I. V. 1990 Hydrodynamic cumulative processes in plasma physics. Sov. Phys. Uspekhi  ${\bf 33},\,960-973.$
- Soloukhin, R. 1957 Measurement of the pressure of finite-amplitude waves in water by piezoelectric sensors. In *Proc. 4th Scientific Conf. of the Young Scientists of the G. M. Krzhizhanovskii Institute of Power Engineering*. USSR Academy of Sciences.
- STANYUKOVICH, K. P. 1960 Unsteady motion of continous media. Pergamon, Oxford.
- STOKES, G. G. 1848 On a difficulty in the theory of sound. *Philosophical Magazine* 33, 349–356.
- Sun, M. & Takayama, K. 2003 An artificially upstream flux vector splitting scheme for the Euler equations. *J. Comput. Phys.* **189**, 305–329.
- Takayama, K. & Ben-Dor, G. 1993 State-of-the-art in research on mach reflection of shock waves.  $S\bar{a}dhan\bar{a}$  18, 695–710.

- TAKAYAMA, K., KLEINE, H. & GRÖNIG, H. 1987 An experimental investigation of the stability of converging cylindrical shock waves in air. Exps. Fluids 5, 315–322.
- Terao, K. 1983 Experimental study on cylindrical and spherical implosions. *Jpn. J. Appl. Phys* 22, 446–453.
- Terao, K. 1984 Experimental study on cylindrical and spherical implosions. *Jpn. J. Appl. Phys* 23, 27–33.
- TERAO, K., AKABA, H. & SHIRAISHI, H. 1995 Temperatures in imploding detonation waves. *Shock Waves* 4, 187–193.
- Terao, K. & Wagner, H. G. 1991 Experimental study on spherically imploding detonation waves. Shock Waves 1, 27–34.
- Trayner, C. & Glowacki, M. H. 1995 A new technique for the solution of the saha equation. *J. Sci. Comput.* **10**, 139–149.
- Van Dyke, M. & Guttman, A. J. 1982 The converging shock wave from a spherical or cylindrical piston. J. Fluid Mech. 120, 451–462.
- Vandenboomgaerde, M. & Aymard., C. 2011 Analytical theory for planar shock focusing through perfect gas lens and shock tube experiment designs. *Phys. Fluids* 23, 016101.
- VIEILLE, P. 1899–1900 Étude sur le rôle des discontinuités dans les phénomènes de propagation. *Mémorial des Poudres et Salpêtres* 10, 177–260.
- VINCENTI, W. & KRUGER, C. 1966 Introduction to Physical Gas Dynamics. John Wiley and Sons, New York.
- WANG, J. C. T. 1982 On the theory of imploding shocks. J. Appl. Math. Phys. 33, 53–62.
- WATANABE, M., ONODERA, O. & TAKAYAMA, K. 1995 Shock wave focusing in a vertical annular shock tube. In *Proc. 19th Intern. Symp. on Shock Waves* (ed. R. Brun & L. Z. Dumitrescu), pp. 61–79. Springer-Verlag, Berlin.
- WATANABE, M. & TAKAYAMA, K. 1991 Stability of converging cylindrical shock waves. Shock Waves 1, 149–160.
- Welsh, R. L. 1967 Imploding shocks and detonations. J. Fluid Mech, .
- White, D. R. 1958 Influence of diaphragm opening times on shock-tube flows. J. Fluid Mech. 4, 585–599.
- WHITHAM, G. B. 1958 On the propagation of shock waves through regions of non-uniform area or flow. *J. Fluid Mech.* 4, 337–360.
- WHITHAM, G. B. 1973 Linear and nonlinear waves. John Wiley and Sons, New York.
- WONG, H. & BERSHADER, D. 1966 Thermal equilibrium behind an ionizing shock. J. Fluid Mech. 26, 459–479.
- Wu, J. H. T., Elabdin, M. N., Neemeh, R. A. & Ostrowski, P. P. 1977 Production of converging cylindrical shock waves by finite element conical contractions. In Shock tube and shock wave research: Proc. Eleventh Intern. Symp. on Shock Tubes and Waves, pp. 107–114. Seattle, Wash., USA: University of Washington Press.
- Wu, J. H. T., Neemeh, R. A. & Ostrowski, P. P. 1980 Experimental studies of the production of converging cylindrical shock waves. AIAA J. 18, 47–48.
- Yakovlev, V. I. 2006 Radiative relaxation of argon plasma in shock waves. *Technical Physics Letters* **31**, 505–507.

## 80 REFERENCES

Zel'dovich, Y. B. & Raizer, Y. P. 2002 Physics of Shock Waves and High-Temperature Hydrodynamic Phenoma. Dover Publications, Mineola, New York. Zhai, Z., Liu, C., Qin, F., Yang, J. & Luo, X. 2010 Generation of cylindrical converging shock waves based on shock dynamics theory. Phys. Fluids 22, 041701. Part II

Papers

# Paper 1

# Thermal radiation from a converging shock implosion

By Malte Kjellander, Nils Tillmark and Nicholas Apazidis

KTH Mechanics, SE-100 44 Stockholm, Sweden

Published in Physics of Fluids 22, 046102 (2010)

High energy concentration in gas is produced experimentally by focusing cylindrical shock waves in a specially constructed shock tube. The energy concentration is manifested by the formation of a hot gas core emitting light at the center of a test chamber at the instant of shock focus. Experimental and numerical investigations show that the shape of the shock wave close to the center of convergence has a large influence on the energy concentration level. Circular shocks are unstable and the resulting light emission varies greatly from run to run. Symmetry and stability of the converging shock are achieved by wing-shaped flow dividers mounted radially in the test chamber, forming the shock into a more stable polygonal shape. Photometric an spectroscopic analysis of the implosion light flash from a polygonal shock wave in argon is performed. A series of 60 ns time-resolved spectra spread over the 8  $\mu$ s light flash show the emission variation over the flash duration. Blackbody fits of the spectroscopic data give a maximum measured gas temperature of 5,800 K in the beginning of the light flash. Line emissions originating in transitions in neutral argon atoms from energy levels of up to 14.7 eV were also detected.

### 1. Introduction

Converging shock waves have the ability to generate high energy concentrations at the implosion focus, and have been studied since the first analytical treatment by Guderley (1942). Experimentally, converging cylindrical shock waves were first produced by Perry & Kantrowitz (1951) in an annular shock tube with a tear-formed inner body. Further experiments in tubes following the basic principles of their design have been made by Wu et al. (1977), Takayama et al. (1987), Watanabe & Takayama (1991), Eliasson et al. (2006) and others. Shock waves of initially moderate strengths are, when converged, able to heat the gas at the focus to temperatures where the gas becomes radiating. The light emission allows temperature determination from spectrometric measurements. Spectrometric measurements on converging shock waves have been made by several authors, primarily using detonations to instigate the shocks.

Knystautas *et al.* (1969) made experiments with converging detonation waves in a cylindrical chamber filled with an acetylene-oxygen gas at an initial pressure of 120 Torr. They measured the intensity of the luminescent center at two wavelengths and compared to a blackbody radiator, estimating a maximum temperature of 189,000 K.

Roberts & Glass (1971) measured the emission from converging shock waves in a hemispherical chamber filled with a oxygen-hydrogen gas at high pressures (6.8-27.2 atm). The shock waves were generated with an exploding wire in the center of the chamber. The radiation was continuous with a blackbody temperature of  $\sim 5,000$  K. They also noticed that the temperature reported by Knystautas *et al* was estimated too high due to erroneous use of Wien's law. The work was continued by Roig & Glass (1977), who presented time resolved blackbody temperatures from measurements on six wavelength regions, with similar peak temperatures (4,500-6,000 K).

Saito & Glass (1982) made further spectrometric measurements with a hemispherical implosion chamber filled with a hydrogen-oxygen mixture. To initiate the shock, they used an exploding wire at the center or explosives attached directly at the walls. Time-resolved recordings on the radiation intensity were made at eight wavelengths in the visible region. The emission was found to be continuous and comparisons with the blackbody function yielded temperatures in the range 10,000-13,000 K for the exploding wire runs and 15,000-17,000 K for the explosive runs.

Matsuo et al. (1985) conducted spectrometric measurements on converging shock waves in air. Strong shock waves were created by detonation in the center of a circular test chamber, which reflected at the walls and focused. The light emission at the focus was measured and compared to the blackbody function. Time-resolved intensity was measured with photomultiplier tubes at a number of separate wavelengths between 400 and 500 nm and revealed blackbody temperatures in the range of 13,000-34,000 K.

The present work aims to study the nature of the light emission from converging cylindrical shock waves in argon and to estimate the temperatures achieved at the focus. As opposed to the previously listed, the shock waves are not generated by explosives or wires, but in a shock tube designed along the same principles as those of Perry & Kantrowitz (1951) and Takayama *et al.* (1987). The light pulse at the center of the test chamber is investigated photometrically and spectroscopically. A new echelle-type spectrometer is used in order to measure the complete spectrum between 300 and 900 nm.

Fig. 1 shows the hot luminescent region of compressed argon produced by a strong polygonal imploding shock of final Mach number  $M \sim 10$  created from an initial shock at Mach number M=3.8 in the shock tube facility at KTH Mechanics. The illumination of the test section is provided by the gas

radiation. The wing shaped profiles serve as shock stabilizers, as described below.



Figure 1: Hot luminescent gas core at the middle of the convergence chamber.

The converging cylindrical shock will produce a high energy concentration under the condition that its symmetry is preserved during the convergence process. It is interesting to note that the most natural circular shape of the converging shock is unstable. Perry and Kantrowitz showed experimentally that a converging cylindrical shock becomes unstable once its strength exceeds Mach 2.4. A small deviation from a circular shape tends to increase and eventually produce a plane portion on the shock front. This leads to a loss of symmetry and a substantial decrease in the focusing effect since various parts of the shock front arrive at different instants and locations in the focal region.

Strong converging shocks have an inherent property to form plane sides and sharp corners. It has been shown theoretically, numerically and experimentally, among others by the present researchers, that curved strong converging shocks tend to planarity. A strong shock that is initially curved tends to form a polygonal front with plane sides and corners at the focal regions where the shock strength increases drastically. Sturtevant & Kulkarny (1976) showed experimentally the formation of plane sides of an initially smooth shockfront at the focal region of a parabolic reflector.

Paradoxically this inherent property of strong shocks that leads to an unstable behavior of a cylindrical shock can and is used in the present study to form dynamically stable polygonal shock fronts. It has been shown theoretically, experimentally and numerically that a symmetric polygonal shock is dynamically stable, see e.g. Schwendeman & Whitham (1987), Apazidis & Lesser (1996), Apazidis et al. (2002), Apazidis (2003), Eliasson et al. (2007a), Eliasson et al. (2007b). The shock front will undergo a periodic transformation between n and 2n sided polygonal form retaining the symmetry of the shock structure which is vital for the high energy concentration at the focal point. As shown by Eliasson et al. (2007b) these polygonal shock waves create light emissions that are more repeatable in strength compared to circular shock waves. Since reproducibility between each shock tube run is very important for the presented measurements, polygonal shock waves are preferred.

The form of the imploding shock may be controlled by various methods, e.g. by a specific form of the reflector boundary or by small objects placed in the chamber such as small cylinders, see Eliasson  $et\ al.\ (2007a)$ , Eliasson  $et\ al.\ (2007b)$ . The present study makes use of biconvex wing profiles to shape the shock waves.

Having the shock wave converge in monatomic argon instead of in air has been shown to produce significantly higher luminosity (Perry & Kantrowitz (1951)). The spectrometric measurements presented here are performed using argon as test gas and helium as driver gas.

By this method of shaping the shock front and using the combination of helium and argon as driver and test gases, we have been able to produce gas conditions in the focal region resulting in a formation of hot luminescent gas core at the center of the chamber. The radiation from the light flash, distinctly visible to a naked eye in daylight, has been recorded and investigated. The intensity of the radiation has been monitored by a photomultiplier and the spectrum of the light flash recorded by a spectrometer and analyzed. The duration of the flash obtained from the photomultiplier is about  $8-10~\mu s$ . The intensity increases abruptly at the beginning of the time interval and falls off gradually with time.

A quantitative estimate of the temperature variations during the flash is performed by dividing the flash into a number of spectra with short exposure times of 60 ns. The temperature has its highest value at the time of shock focus, whereafter it continuously decreases. Apparent blackbody temperatures of the gas are deduced from fits of the measured spectra, revealing the temperature variation over the flash duration with a peak of  $\sim 6000~\rm K.$ 

## 2. Experimental setup

The present work utilizes the same shock tube as that used in previous experiments by the group, but with modifications on the shock shaping geometry in the test section. The tube is specifically designed to create a converging cylindrical shock structure. The light created by shock implosion in the gas

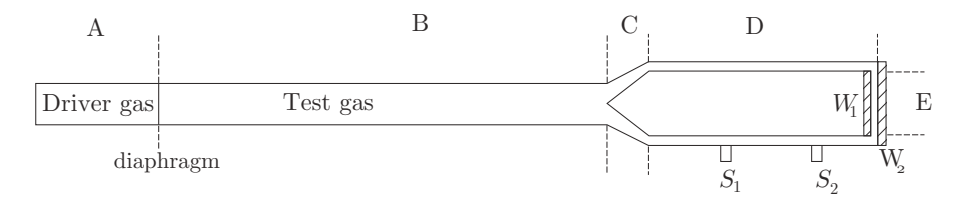


Figure 2: Schematic drawing of the shock tube: A, driver section; B, inlet pipe; C, transformation section; D, annular tube; E, test section.  $S_1$  and  $S_2$ , shock sensors;  $W_1$  and  $W_2$ , glass windows framing the test section.

is measured both with an echelle type spectrometer and a photomultiplier, recording the spectrum in the wavelength interval 300-880 nm and the total intensity variation over time, respectively. Flow visualization is provided with a schlieren optics system. The shock propagation in air and argon is compared with the numerical results.

#### 2.1. Shock tube

The basic shock tube configuration has been described in detail in previous work (Eliasson et al. (2006), Eliasson et al. (2007a), Eliasson et al. (2007b)) therefore only a brief outline of the apparatus is presented here. Only the modifications or changes of the original setup are described in detail. A schematic of the apparatus is given in Fig. 2. The shock tube is made up of a short cylindrical driver section (A) and a driven section, separated by a rupturable membrane. The latter section consists of four parts: a long inlet pipe with circular cross section (B), a channel transformation part (C) changing the cross section from circular to annular, an intermediate section (D) where a plane annular shock is established and where the shock speed is measured and a cylindrical test chamber (E) where the shock moves radially towards the center. The central part of the test section is framed by 15 mm thick glass windows (Schott Borofloat 33) giving optical access to the shock focusing region.

Either air or helium are used as driver gases. Test gases are either air or argon of commercial grade (ARCAL TIG-MIG, purity rate 99.99%, Air Liquide). An aluminum diaphragm (thickness 0.5 mm) separates the two sections. Increasing the pressure difference forces the diaphragm towards a knife-edged cross located in the inlet of the driven section and causes the diaphragm to rupture. Good quality aluminum membrane and a sharp edged cross ensure small variation in the bursting pressure,  $\pm 25$  kPa at a nominal pressure difference of 1.7 MPa. The pressures in driver and driven sections are monitored with electronic pressure transducers ( Druck DPI 150). For an initial low pressure  $p_1=10$  kPa in the driven section, different gas combinations give shock Mach

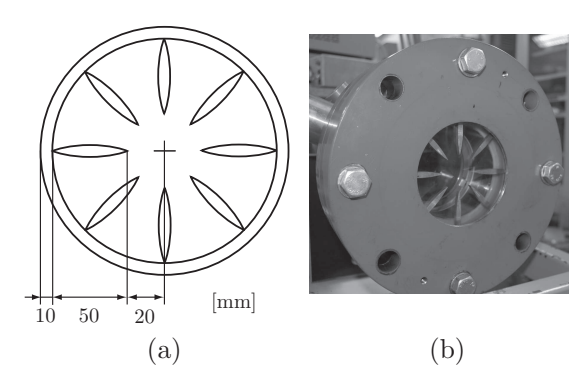


Figure 3: Test section: (a) drawing of the wing profiles, where the outer ring represents the annular channel; (b) photograph of the test section with the profiles installed in the chamber.

numbers between  $M_s$ =2.3 and  $M_s$ =3.8 in the annulartube before entering the test chamber.

### 2.2. Test section and shock wave shaping

The test section is divided into radial channels by flow dividers. These are 50 mm long biconvex wing profiles with the chord along the radius of the chamber. The leading edges are mounted flush with the inner surface of the annular channel and the trailing edges of the profiles are positioned 20 mm from the channel center. Fig. 3 shows the biconvex wings mounted in the test section. The form of the circular cylindrical shock wave entering the channels is changed due to the new flow conditions with shocks normal to the profiles. Complex interaction between the flow along the walls and in the center changes the shape of the shocks propagating from inlet to outlet. If arranged properly, the shock wave attains polygonal structure with almost plane sides when leaving the channels.

Previous work (Eliasson et al. (2006), Eliasson et al. (2007a), Eliasson et al. (2007b)) in the same shock tube used circular objects or polygonal reflectors in the test section. The purpose of the wings is to improve the shock shape and allow the same blockage ratio regardless of the number of wings - and consequently the number of sides of the polygonal shock wave - by altering the thickness of the wings from case to case. The present study has a configuration with eight wings, creating an octagonal shock wave. The number eight is a compromise between demands on repeatability and ability to concentrate energy. The completely circular shock wave is optimal for concentration but suffers from low repeatability. A polygonal shock with eight sides is stable and

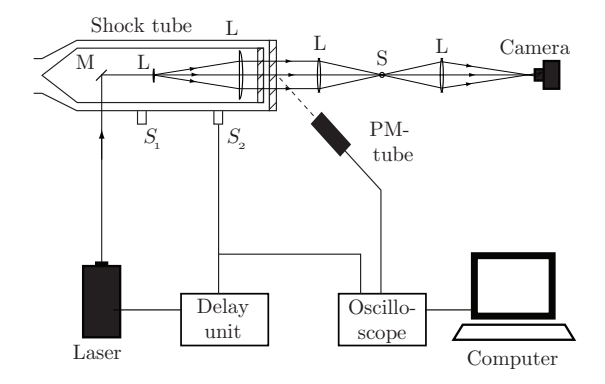


Figure 4: Arrangement of the schlieren optics. L, lens, M, mirror and S, the schlieren stop.  $S_1$  and  $S_2$  are the pressure sensors used for triggering and measuring the shock speed in the annular tube.

at the same time close to an optimal but unstable circular form. It has also been observed Takayama et al. (1987) that the supporting struts of the inner body introduce disturbances in the flow that eventually destabilize the circular shape. In the shock tube at KTH, two sets of four struts are used, one set rotated 45°. The influence of the struts is diminished if eight wings are placed corresponding to the strut positions.

# 2.3. Flow visualization

A schlieren system, schematically drawn in Fig. 4 is used to visualize the flow in the test section. The light source is a laser whose beam is directed into the inner body of the annular section through one of the support struts, and expanded to illuminate the test section through the glass window. On the receiving side the collimated light is focused on a schlieren stop. To be able to detect density gradients in all radial directions a metal microsphere is used as a stop. Photographs are taken with either a CCD camera (PCO SensiCam) electronically connected to the timing system or a digital still camera (Nikon D80) with an open shutter. The SensiCam can take either single or multiple exposures. In the single-exposure mode an Nd:YAG laser (New Wave Orion) is employed as light source, while a continous argon-ion laser (Spectro-Physics BeamLok 2060) is used in the other mode.

The optical setup is shielded from unwanted stray light. Using an open shutter causes the still camera to take double exposure of the test section, the first enlightened by the laser source the second by the light created during the implosion. The unwanted exposure due to the implosion light flash is damped by placing filters in front of the camera and compensating with increased laser

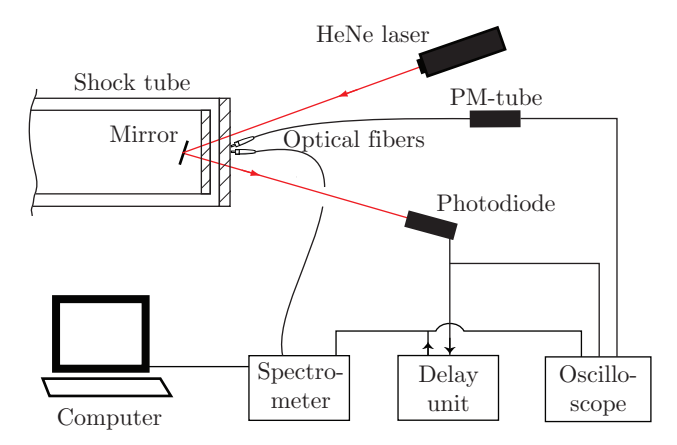


Figure 5: Spectrometric setup. The spectrometer is triggered by the shock wave passing and deflecting the HeNe laser beam, detected by a photodiode. The time between the signal and capture is determined with a delay unit.

power. The shock sensor  $S_2$  (see Fig. 4) is connected to a digital delay generator (Stanford Research Systems DG535), which in turn triggers the Nd:YAG laser. The laser pulse is about 5 ns long. Only one schlieren image is taken at each test run. The  $S_2$  sensor and the photomultiplier are connected to an oscilloscope. The latter is used to time-correlate the images with the time of the shock focusing; both the Nd:YAG laser pulse and the light emission flash are recorded by the oscilloscope.

### 2.4. Spectrometric arrangements

A schematic drawing of the setup is presented in Fig. 5. Light generated at the shock focus is collected by two optical fibers with their openings flush to the glass. One fiber feeds a photomultiplier while the other is connected to a spectrometer (Mechelle 7500, Multichannel Systems, Sweden) with an ICCD camera (Andor Istar). Light is collected from a conical volume with a mean radius of 7 mm around the center. The spectrometer is able to record spectra in the wavelength interval 180-880 nm. However, the test section glass window limits the light transmission to between 350 and 880 nm. The spectrometer makes use of an echelle grating, that divides the spectrum into several vertically separated diffraction orders. The complete spectrum is reconstructed by software. The separation causes the sensitivity to drop close to the edges of each order, as can be seen in Fig. 15. The spectrometer was wavelength calibrated during the experiments using a Hg lamp. Deviation from theoretical positions of twelve Hg lines are minimized by a least-square fit method.

The spectrometer unit is triggered by an optical method using a small HeNe laser. The laser beam is directed through the test section 25 mm from its center. It is then reflected back through the windows by a mirror inside the inner body and falls on a photodiode. When the beam is deflected by the passing shock wave the change of beam direction is detected as an intensity change by the photodiode. The signal is amplified and used as a trigger signal for the digital delay generator (DDG). A delay is set on the DDG and the output signal opens the ICCD camera shutter on the spectrometer. Simultaneously the light emission from the focused shock is registered with the photomultiplier. The signals from the photomultiplier, the photodiode amplifier and the ICCD camera trigger pulse are monitored and recorded with a digital oscilloscope. In order to synchronize the shutter opening times with the light flash as measured with the photomultiplier tube, the unknown time delay of the trigger system was measured with a pulse laser and determined with an accuracy of 10 ns.

### 3. Experimental Results and Discussion

Two sets of experiments were made. A first set using the schlieren setup to determine the shock propagation and degree of symmetry and repeatability that could be achieved with the shock shaping system. This was made for two combinations of gases: air as both test and driver gas, resulting in a shock strength of  $M_s = 2.3$  in the annular section, and argon as test gas and helium as driver gas ( $M_s = 3.8$ ). The second set of runs was with the spectrometric setup, measuring the light pulse from a shock converging in argon. The initial low pressure for all cases was 10.0 kPa.

### 3.1. Shock wave propagation

Schlieren images were taken for one set using air as both driver and test gas, and one using argon as test gas and helium as driver gas. The propagation time of the shock wave from sensor  $S_1$  to the center of the test section was  $542\pm2~\mu s$  using air as test gas and  $363\pm5~\mu s$  using argon, corresponding to initial Mach numbers of 2.3 and 3.8 in the annular channel. Fig. 6 shows the propagation of the converging shock wave through the test section in air. The six images are obtained from different shock tube runs. The  $\Delta t$  given in the captions is the time of the image capture relative to the focusing instant as measured by the photomultiplier.

Image 6(a) shows the shock wave entering the central, open part of the test section after passing through the channels, having attained a roughly plane shape, thereby forming an eight-sided polygon. As the separate fronts exit the channels each plane shock reflects from those emerging from the adjacent channels. When the incoming waves reflect, Mach stems appear at the intersection. As the incident shocks and Mach stems are almost plane, they propagate at almost constant velocities. Initially short, the stems have higher speeds than the adjacent waves 6(b and c). Eventually the Mach stems form a new octagon,

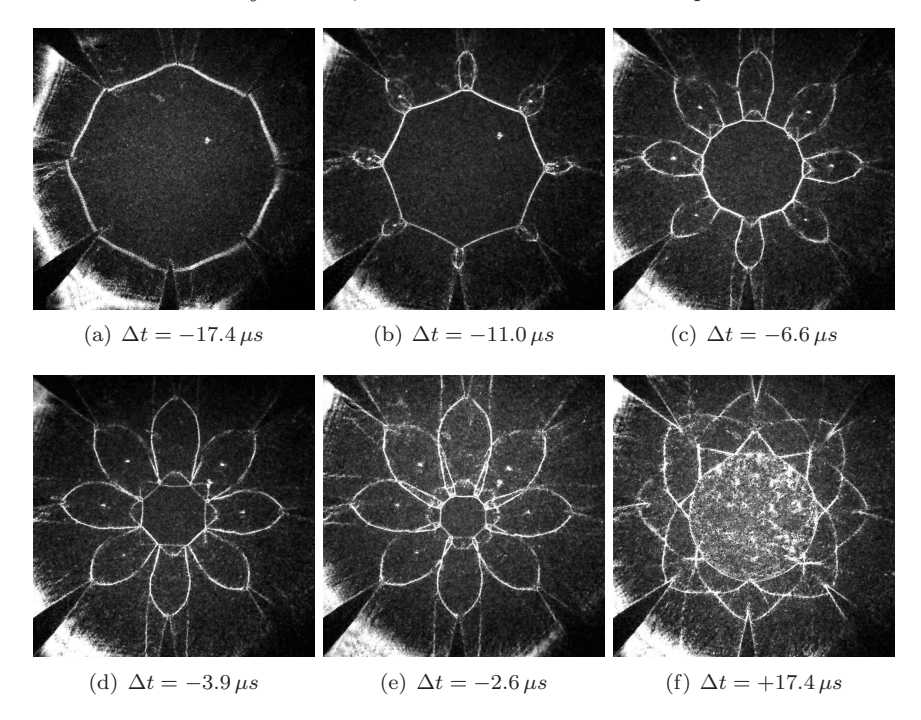


Figure 6: Schlieren images of converging cylindrical shock waves in air at 13.3 kPa. The Mach number of the initial annular shock was  $M_s = 2.3$ . The time between image capture and focusing instant is displayed under each image. Images (a)-(e) show the converging shocks before focusing, while (f) shows the reflected diverging shock. The distance between opposite wing tips is 40 mm.

rotated by 22.5°, which is accomplished in Fig. 6(d). Thereafter the process repeats itself. Much of the acceleration of the polygonal shock wave is therefore due to the Mach reflections. Fig. 6(f) shows the outgoing, reflected shock which is stable, in contrast with the converging shock. The outgoing shock tends to obtain a circular form but is influenced by the flow ahead, created by the initial converging shock.

An idealized drawing of the reflections is showed in Fig. 7, corresponding to Fig. 6 (a) and (b) or (c). The system exhibits both stationary and moving shocks. At the trailing edge, stationary oblique shocks appear due to the supersonic flow induced by the preceding shock wave, traveling from left to right in the picture. Vortices are created at the trailing edge due to the not completely simultaneous arrivals of the shock fronts on each side of the wing. These follow the flow downstream and may be seen in the middle of the "flower leaves" in Figs. 6 (b)-(e). It should be stressed that Fig. 7 is an idealized

picture which does not contain all the unsteady interactions resulting from the not completely symmetric reflection.

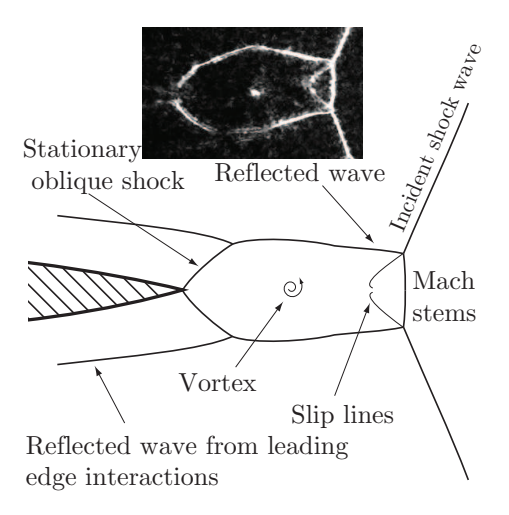


Figure 7: Idealized diagram over the shock interactions responsible of forming the polygonal shape. Detail from Fig. 6(c) inserted.

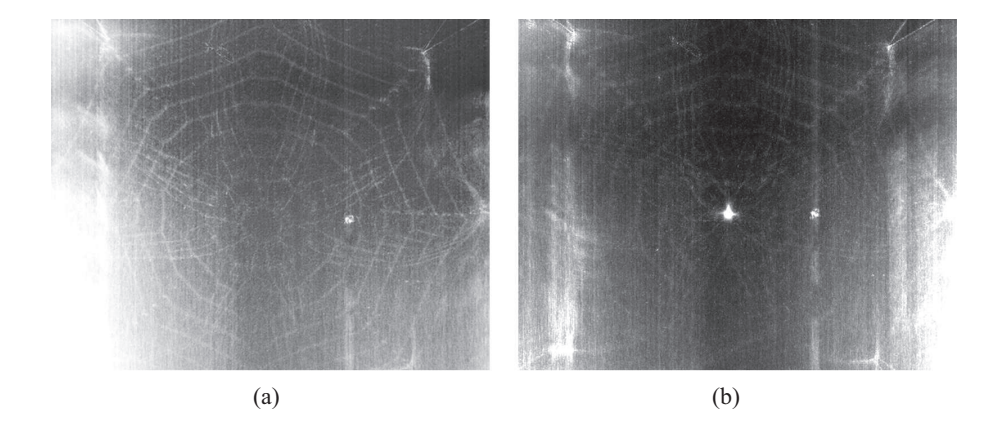


Figure 8: Two examples of the multiply exposed schlieren photographs used for determining shock position and velocity; (a) in air and (b) in argon. The light spot seen in the middle of (b) is the luminescent gas core.

The radius of the shock wave is measured as the average of the radial distance to the midpoint of the eight main principal shocks that make up the polygon. This has the effect that initially the radius is measured to the midpoint of each original side of the polygon. When the Mach stems overtake the original shocks, the radius is taken as the distance from the center to the stems. If perfect symmetry would apply, this is equivalent to the radius of the largest circle that can be inscribed inside the shock wave. The experimental data points are collected from several multiple-exposure schlieren images, of which two examples are presented in Fig. 8. The central bright spot in (b) is the light flash from the implosion. Figs. 9 and 11 present time-diagrams of the measured positions.

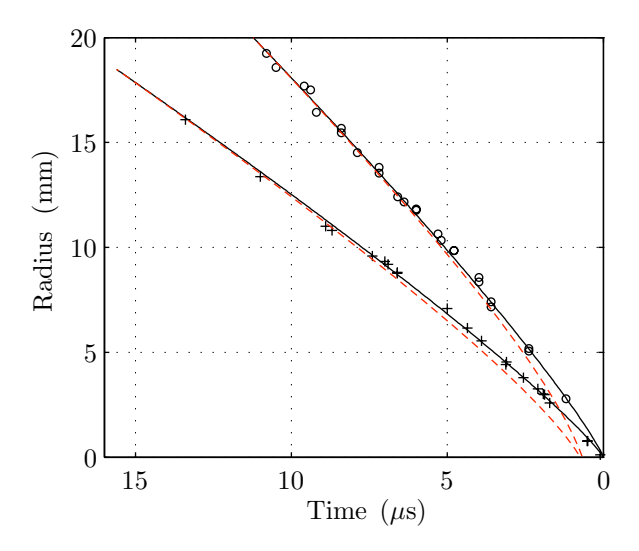


Figure 9: Propagation of polygonal shock wave in air (+) and argon (o) compared with circular Guderley solutions (dashed lines). Power law fits (full lines) to the experimental data are added for comparison.

The polygonal shock wave converges slower than a circular with the same initial Mach number and radius. This can be demonstrated using the power-law solution for circular and spherical shock waves by Guderley,

$$\frac{r}{R_0} = \left(1 - \frac{t}{t_C}\right)^a \tag{1}$$

where  $R_0$  is the initial radius and  $t_C$  the time needed for the shock front to reach the center. For a circular cylindrical shock wave converging in air,  $a \approx 0.834$ (Guderley (1942)), which has been confirmed experimentally (Takayama *et al.* 

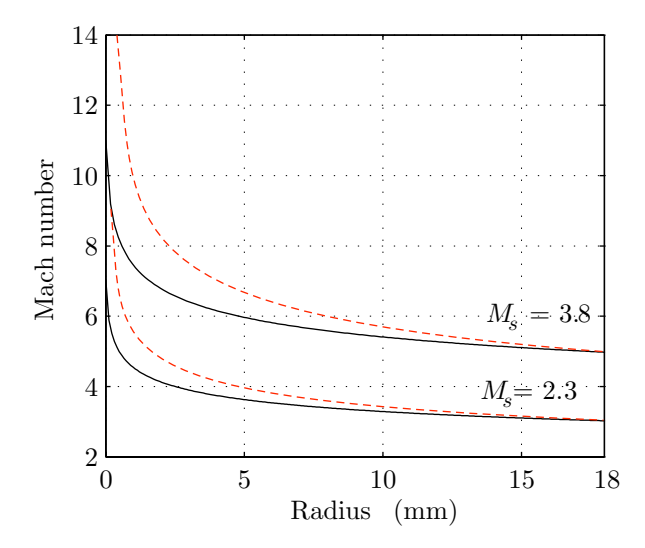


Figure 10: Mach number from fits to experimental data (full lines) and circular cylindrical Guderley solution (dashed lines). The upper curves represent the shock in argon with initial  $M_s = 3.8$  and the lower in air, with initial  $M_s = 2.3$ . The experimental fit represents averaged Mach number of the polygonal wave.

(1987)). To compare with the circular case, a fit of Eq. 1 was made to the experimental data. The propagation of the polygonal shock wave approximately follows Eq. 1, and the exponent acquired from the fit was  $a\approx 0.875\pm0.010$ . The circular Guderley solution has smaller exponent and approaches the focus faster. The same was found for the shock wave in argon, where the experimental data gave  $a\approx 0.862\pm0.015$ , to be compared with the circular  $a\approx 0.816$  (Lazarus & Richtmyer (1977)). Figure 9 shows the measured effective radii of converging polygonal shocks compared to the circular Guderley solution. The corresponding experimental Mach numbers obtained from the power law fits are compared to the Guderley solutions in Fig. 10. The circular solution was given the same starting position and velocity as the experimental fit at  $R_0=18.5$  mm. As apparent from the figures, the circular shock accelerates and converges faster.

The converging process of polygonal shock waves was described by Schwendeman & Whitham (1987) using geometrical shock dynamics. Their treatment predicted the Mach number ratio of the shock fronts making up any two successive octagons as  $M_1/M_0 = 1.201$  for air ( $\gamma = 1.4$ ). Designating the Mach number of the incident shocks  $M_1$ , of the Mach stems from the initial reflection

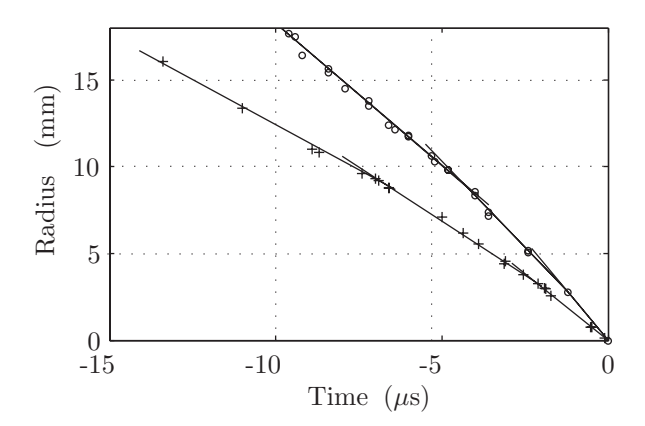


Figure 11: Linear fits to the shock front position to determine Mach numbers of incident shock and Mach stems for shock wave in air (+) and in argon (o).

 $M_2$  and of the Mach stems appearing at the second reflection  $M_3$ , corresponding ratios may be estimated from the experimental data. Linear fits for air resulted in  $M_2/M_1 \approx 1.20 \pm 0.02$  and  $M_3/M_2 \approx 1.19 \pm 0.03$ . For the shock wave in argon,  $M_1/M_0 = 1.22 \pm 0.03$ .

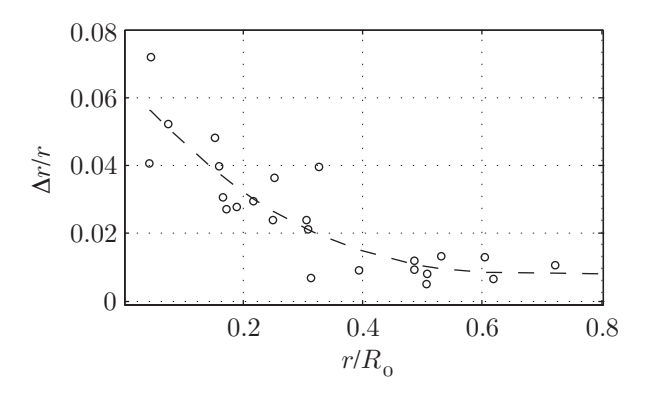


Figure 12: Deviation of the shock wave shape versus radius.

As the amount of the energy concentration is coupled to the ability to focus the polygonal shock an interesting parameter is the asymmetry appearing in the focusing process. Fig. 12 shows the deviation  $\Delta r$  from the mean radius of the converging shock wave, normalized by the mean radius r.  $R_0$  is the radius of the central, open section, 18.5 mm. There is an asymmetry in the polygonal

shape, originating from when the shock enters the open section: as seen in Fig. 6(a), the fronts arrive at marginally different times. This makes the shape slightly elongated. The radius and deviation presented in Fig. 12 have been calculated as the mean values of the distances from the center point to the mid point of each of the eight main shock fronts. The value is an indication of the ability to keep the symmetric polygonal shape.

3.1a. Photomultiplier records. The light flash has a total duration of roughly 10  $\mu$ s. Photographs of the emitting gas core at the instant of shock implosion are shown in Fig. 13. The images are taken from an oblique angle to show the extent of the core. The shutter was left open and the only light source was the luminescent gas itself. The emitting volume at the focus is seen to have the form of a thin cylinder, stretching the full 5 mm span between the framing windows of the test section. This result indicates that the polygonal shock convergence in the test chamber preserves the two-dimensional structure of the shock to the end of the focusing process.

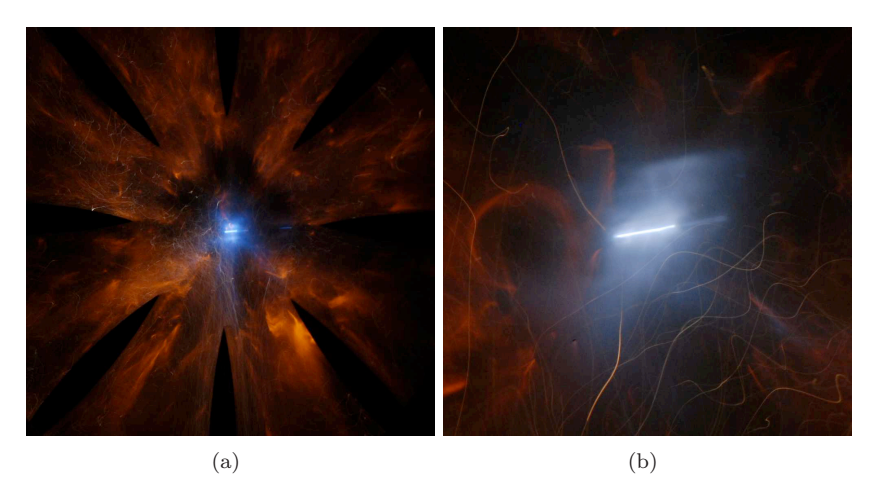


Figure 13: Photographs of the light emitting gas core: (a) photo showing the full view of the test section; (b) a photo taken from a closer distance.

Photomultiplier records from more than a hundred runs using various combinations of gases show a fairly reproducible strength of light intensity for each set of gas combinations. The set presented in Fig. 14 shows the signals from twenty runs using helium and argon as driver and test gas, respectively. The negative peak signal strength varies little, with a mean value of -0.49 V and standard deviation 0.02 V. The spread increases after the collapse. The actual fall time is short, about 12 ns, but is preceded by a small decrease in output

voltage prior to the peak. This indicates that the gas behind the shock starts to emit light at least 100 ns before the actual focusing instant.

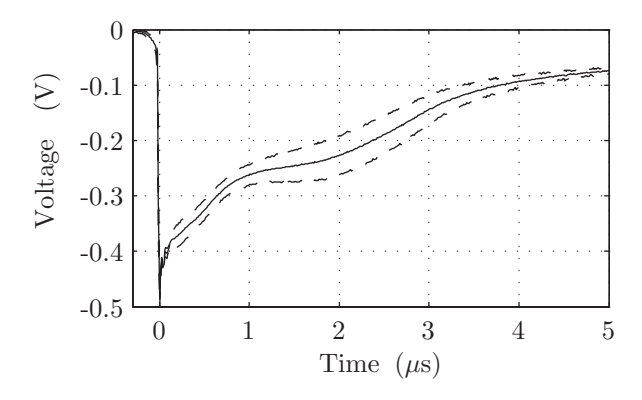


Figure 14: Photomultiplier records of light emissions from converging polygonal shock waves in argon with helium as driver: mean value and standard deviation (dashed lines) from twenty runs.

Summarizing, although the flow divider matrix produces a slightly asymmetric converging shock wave, it manages to create the desired shock wave shape and behavior. Photomultiplier records show a good reproducibility in light emission intensity, whereas the circular shock produces highly fluctuating results (Eliasson  $et\ al.\ (2007b)$ ).

# 3.2. Spectrometric results

A series of spectrometric measurements of the light emission during the focusing in argon have been made. The initial pressure in the test section was  $10.0\pm0.05$  kPa and the high pressure  $1.67\pm0.03$  MPa. Helium was used as the driver gas, resulting in a shock Mach number  $M_s=3.8$  in the annular section. The variation of the Mach number between different runs was less than one percent. The photomultiplier records shown in Fig. 14 were acquired during these runs.

The emission has both been measured in its entirety and divided into a sequence of 60 ns long exposures. Fig. 15 shows a time-integrated spectrum, taken with the shutter open during the whole emission interval. The data shows continuum radiation, on which a series of emission lines is superimposed. The emission lines originate from electron transitions between excited states in neutral argon atoms. The effects of the echelle prism in the spectrometer can be seen in the bumpy appearance of the continuum. Each parabola corresponds to one order and shows the sensitivity drops at the edges of each order. These

drops are due to the equipment construction, and are not related to the light emission.

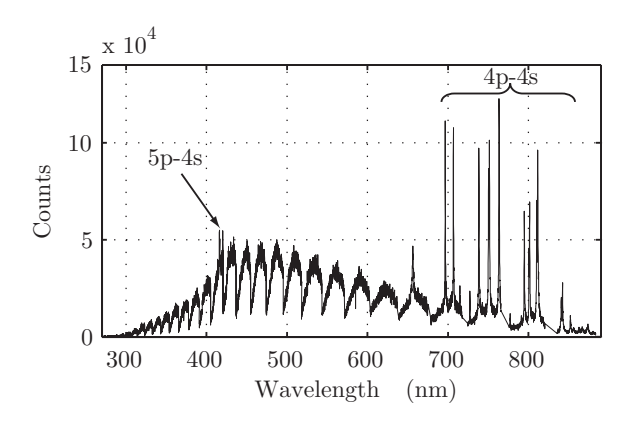


Figure 15: Raw time-integrated emission spectrum of the entire light flash. A continuum and two groups of lines from electron transitions in neutral argon atoms were especially notable.

Time-resolved spectra with 60 ns exposure times have also been made. The measured spectra have a lower signal-to-noise ratio due to the very short exposure time. An overview of filtered spectra is presented in Fig. 16. The displayed time is the time difference between the sharp peak of the photomultiplier signal, signifying the implosion of the shock wave, and the opening of the shutter.

In the beginning of the light flash, a continuum is detected. After about 1  $\mu$ s the single emission lines that also can be seen in the time-integrated spectrum start to appear. As the gas is cooling, the continuum starts to fade away leaving only the neutral argon lines to be measured. After about 7  $\mu$ s no emission could be sensed with the spectrometer with the current exposure time.

A number of emission lines originating from electron transitions in neutral argon were detected. The identified transitions start from either the  $3p^54p$  or  $3p^55p$  manifolds, and terminate in the first level of excited states in argon,  $3p^54s$ . Transitions from the  $3p^55p$  level were only observed in the time-integrated spectrum; the significantly lower intensities drowned in the noise in the 60 ns window spectra. Possible transitions from these states to the ground state have wavelengths below the detection range.

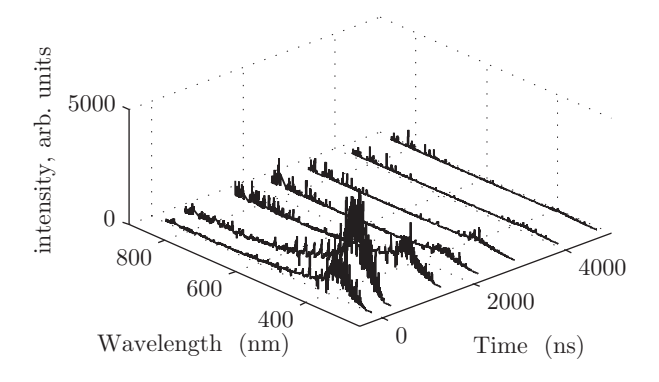


Figure 16: Time-resolved spectra of the light flash. The spectra, taken with exposure times of 60 ns, show the evolution of the continuum and the appearance of the argon emission lines. The spectra have been corrected for CCD sensitivity. Each spectrum is taken at a separate run.

3.2a. Comparison with blackbody radiation. The continuum spectra were compared with the blackbody function,

$$I(\lambda, T) = \frac{2hc^2}{\lambda^5} \frac{1}{\exp(hc/\lambda kT) - 1}$$
 (2)

where h is Planck's constant and c the speed of light. A least squares method was employed and corrections made for the quantum efficiency of the camera and the transmission losses in the glass window. Since the spectra suffer from noise, they were first treated with a digital moving-average filter. The filtered spectra agree reasonably well with the blackbody spectra over the whole spectral range. The highest apparent blackbody temperature,  $5,800\pm200~\rm K$ , was found for an exposure starting about 100 ns into the flash. As the measured continuum spectra get weaker the signal-to-noise ratio decreases. The last spectrum to be compared with a blackbody curve was recorded at  $\Delta t = 2100~\rm ns$ , indicating a temperature of  $4,600\pm200~\rm K$ . Later spectra do show a small rise above the base level, but are excluded due to imprecision in temperature estimation. Fig. 18 shows two typical filtered spectra with blackbody fits. The blackbody curves have been corrected for the overall wavelength sensitivity curve of the CCD but not for the order sensitivity.

#### 4. Numerical calculations

The present experimental investigation of the flow field in the test chamber has been complemented by a numerical study. The numerical solution is obtained by the artificially upstream vector splitting scheme (AUFS), for solving the

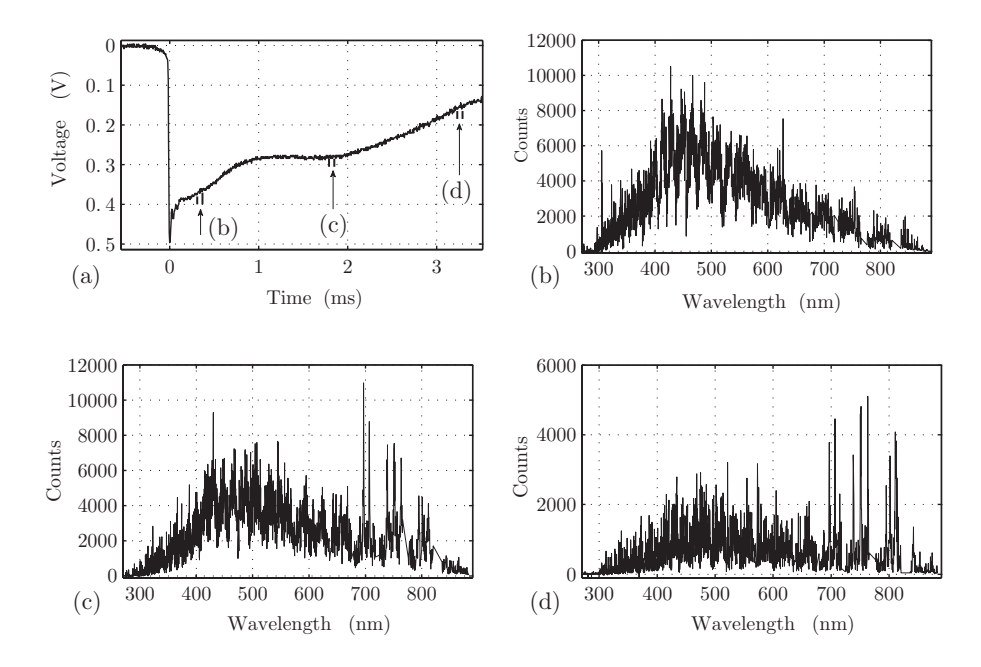


Figure 17: Spectra taken during 60 ns at three different times after the implosion instant: (a) photomultiplier signal with marks indicating the time of each spectrum; (b)  $\Delta t = 310$  ns; (c)  $\Delta t = 1790$  ns; (d)  $\Delta t = 3230$  ns. The intensity scales differ between the graphs.

2D Euler equations, introduced by Sun & Takayama (2003). The complex geometry of the test chamber with the wing-shaped objects placed radially in the chamber requires a robust and stable flow solver with sufficient flow resolution which is able to model the demanding boundary conditions.

## 4.1. Meshing of the computational domain

The AUFS scheme is implemented on an unstructured triangular mesh with automatic mesh refinement applied along boundaries, sharp edges and downstream of the wing profiles closer to the center of the test section to provide for a high flow resolution in these regions. A mesh with approximately  $3.5 \times 10^5$  nodes and enhanced resolution in the critical areas was able to resolve the minute flow details observed in the experiments.

The size of the mesh cells in the vicinity of the wing tip is shown in Fig. 20. The region around the tiny circle at the right tip of the left horizontal wing in Fig. 20(a) is magnified in (b) showing the triangular mesh in the vicinity

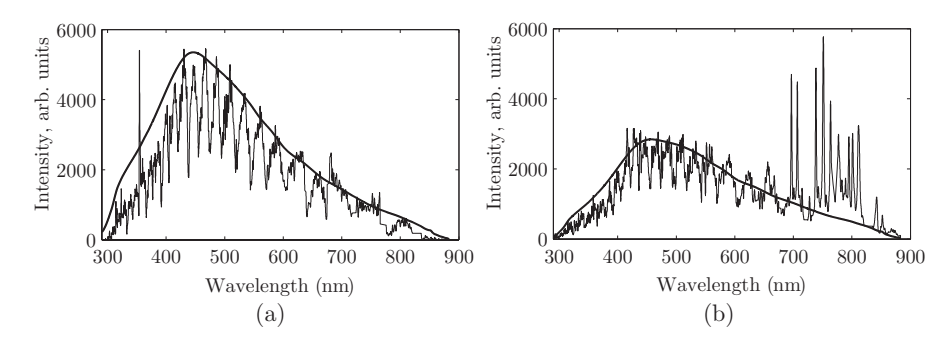


Figure 18: Filtered spectra with blackbody curve fits. The blackbody curves are corrected for the quantum efficiency of the camera and the glass window transmission losses. The time at start of exposure and blackbody temperature are: (a)  $\Delta t = 310$  ns, T=5400 K; (b)  $\Delta t = 3230$  ns, T=4650 K.

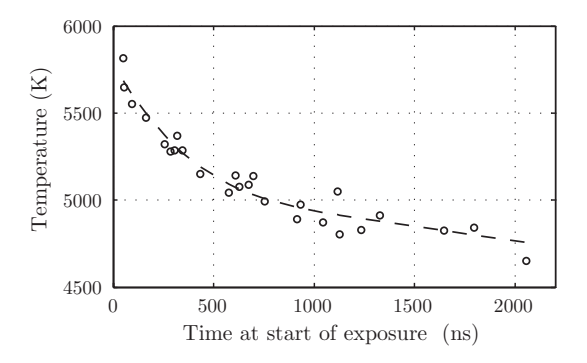


Figure 19: Temperatures acquired from blackbody fits of time-resolved spectra with 60 ns exposure time. Each data point represents measurements made on separate runs. The temporal errors are  $\pm$  20 ns.

of the tip. This mesh size can be readily compared with the size of the shock structure shown in Fig. 6.

### 4.2. Problem formulation

In our calculations we have used the ideal gas model as well as the gas model accounting for the ionization effects. The influence of the ionization in argon showed to be negligible for the present case with maximum temperatures below 7,000 K. For temperatures and pressure levels under the present flow conditions the ionization degree  $\alpha$  in argon, obtained from the Saha equation does not

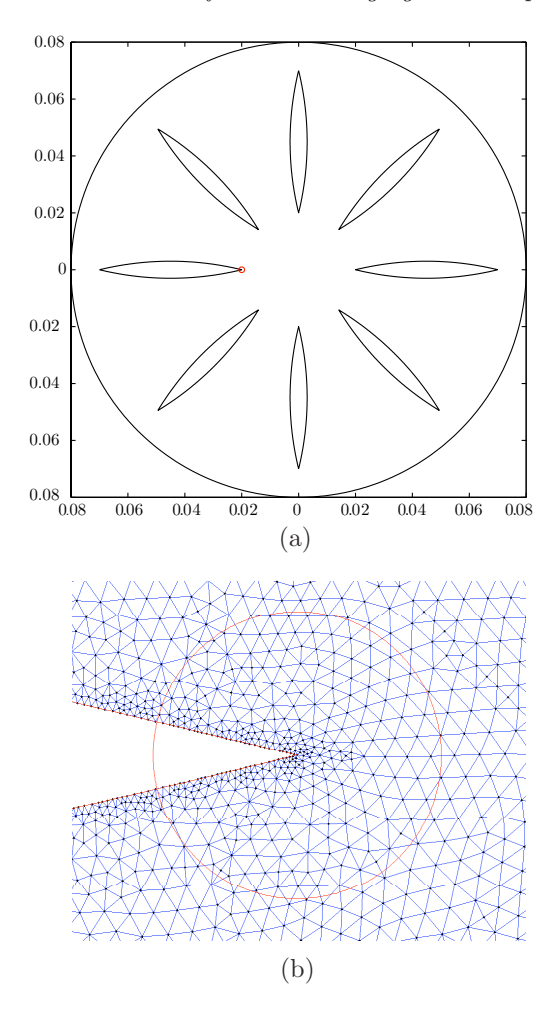


Figure 20: The computational domain (a) and a magnification small a circular region around the right tip of the left horizontal wing (b).

exceed  $\alpha=10^{-5}$ . For such conditions the ideal gas model and the model accounting for ionization produce the same flow field in the chamber. The ideal gas model is however not valid for the extreme conditions at the very center and the influence of various levels of ionization on shock dynamics of strong converging cylindrical and spherical shocks in argon is investigated in detail theoretically and numerically in a separate study by the present authors.



Figure 21: Comparison of a detail of a schlieren photograph Fig. 6(d), computational mesh and numerical schlieren image computed at the same instant  $\Delta t = -3.9 \ \mu s$  prior to implosion.

#### 4.3. Numerical results

Calculations for air and argon were performed with initial (at the chamber boundary) Mach numbers 2.7 and 4.1 respectively. These initial Mach numbers at the chamber boundary result in shock propagation in the central part that is well correlated with the experimental measurements. Experimental and numerical Mach number values as the shock approached the center of convergence are found to be around M=10 for argon. Meshes with the order of  $3.5\times10^5$  nodes are able to successfully produce the complex flow details visible in the experimental images. Fig 22 illustrates the converging shock fronts in air with initial Mach number M=2.7 at various times from the implosion instant at t=0. The time difference between each of the subfigures in Fig. 22 showing the global shock system in the chamber is  $\Delta t=13~\mu s$ . Shock structure in the central part of the chamber is shown in Fig. 23.

The numerical schlieren images are calculated for the time instants corresponding to the experimental images displayed in Fig. 6.

As we see the numerical scheme is able to capture and reproduce the flow details visible in the experimental images for converging as well as in the expanding shock.

Fig. 21 shows a comparison of experimental (white on black) and numerical (black on white) schlieren images. A blow up of a detail in Fig. 23(d) is compared to corresponding calculated shock structure at the same time instant  $\Delta t = -3.9~\mu s$  before implosion. The computational sell size is given

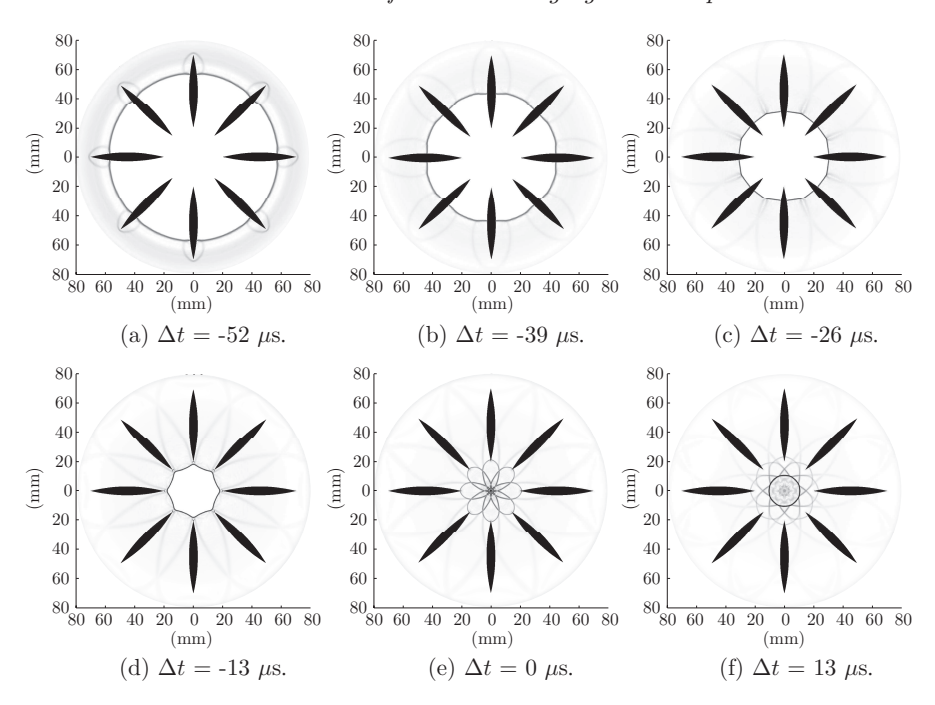


Figure 22: Numerical schlieren images of the global shock system in the air-filled chamber at equidistant times. Initial Mach number M=2.7.

for reference. As seen experimental and calculated shock structures are well correlated.

Fig. 24 shows the effective radius of the converging shock front as function of time. The radius is chosen as the radius of the largest circle enclosed by the polygonal shock. The numerical result agrees well with the experimentally deduced radius, which is reproduced from the experimental results presented earlier.

## 5. Conclusions

The specially designed shock tube has been modified to create polygonal shock waves in order to improve the stability and reproducibility of the experiment. A matrix with eight concave flow dividers reshaped the shock waves into a octagonal form, which proved to be stable and repeatable in terms of focusing time and intensity of the light signal. The polygonal shocks were also found to retain their 2D structure to the end of the focusing process, as evident from photographs of the light-emitting core, see Fig. 13.

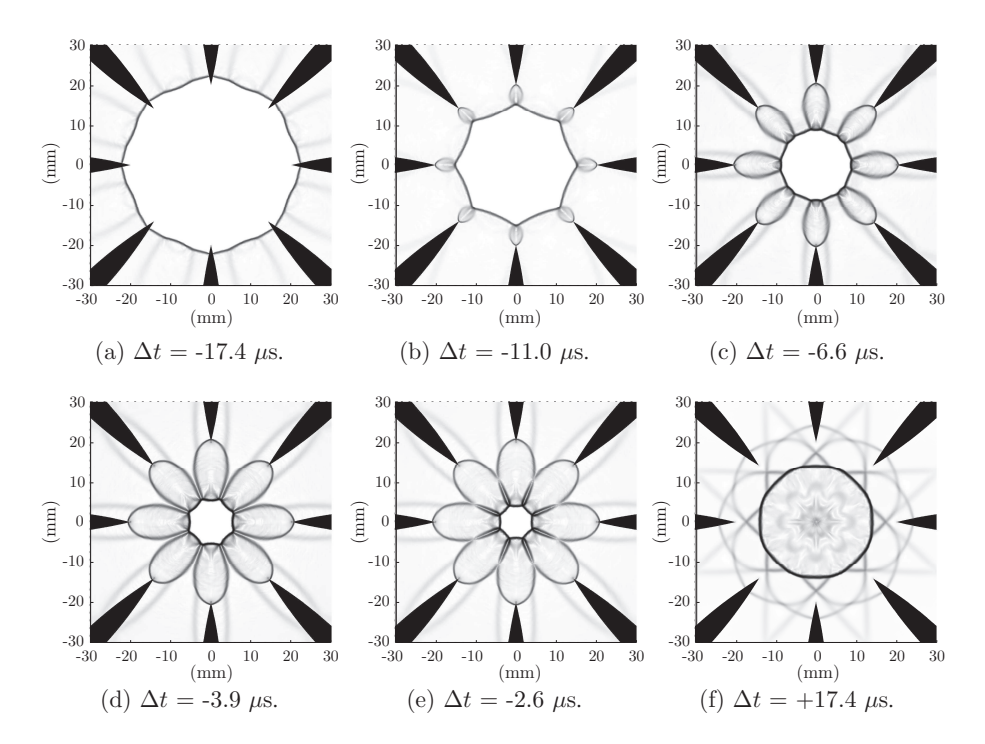


Figure 23: Numerical schlieren images of the central part of the air-filled chamber showing the converging shock fronts at the time instants corresponding to the experimental schlieren photographs shown in Fig. 6. Initial Mach number M=2.7.

The structure of converging polygonal shocks was recorded by experimental schlieren images of the flow and the corresponding effective radii and Mach numbers were obtained through multiple-exposure images. The numerical scheme implemented on an unstructured triangular mesh with automatic mesh refinement was able to capture the flow details and agreed well with the experimental schlieren images as well as values of the effective convergence radius as seen in Fig. 24. The speed of shock convergence was compared to the circular cylindrical Guderley solution as well as to the predictions based on Whitham's theory applied to polygonal converging shocks. It was found that the octagonal shock in the present case was somewhat slower than the circular shock, see Fig. 9. We also shown that Whitham's approximate theory correctly predicts the Mach number increase of a converging octogonal shock in air.

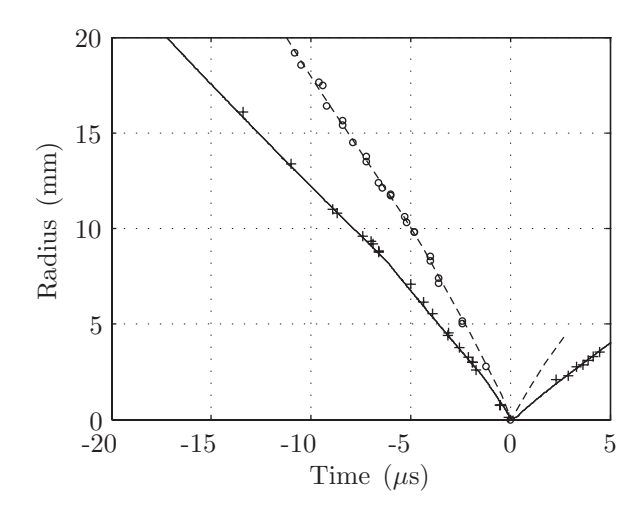


Figure 24: Effective radius of converging and diverging polygonal shock fronts. Experimental and numerical data for the shock in air with air as driver gas (+, full line) and argon with helium as driver gas (o, dashed line).

The main goal of the present study was to investigate the nature of light emission in the final stages of focusing procedure. Both photometric and spectrographic measurements of the light emission during the implosion of the converging polygonal shock wave have been made. The duration and the form of the light flash was recorded by a photomultiplier. The light intensity increased abruptly to the maximum value and vanished gradually within 10  $\mu$ s, see Fig. 14. The emission was measured spectrometrically and was both timeintegrated over the whole flash and broken down in discrete 60 ns windows. The whole wavelength-resolved spectrum from 300 to 900 nm was measured. The spectrum of the flash was found to consist of a quickly appearing continuum which, after 1  $\mu$ s into the pulse, is accompanied by strong single lines from electron transitions in neutral argon. The continuum appeared to agree well with the blackbody function and corresponding blackbody temperatures were obtained through fits of individual spectra from each of the 60 ns windows, giving the temperature variation over the pulse, see Fig. 19. The exact source of the continuum is currently not known. The light emitted during the flash may originate from the surface of an opaque, partly ionized gas. Non-uniformity of the temperature distribution also affects the validity of the measurements: the area of the radiating part of the gas is changing in an unknown manner, while light is collected from the whole radiating volume. Estimates of absolute values of intensity are therefore difficult to achieve. It should also be noted, that the highest measured temperature was acquired some time after the actual implosion, when the total light strength has dropped significantly from its peak. The final Mach number calculated from experiments indicates temperatures of above 9,000 K before the actual implosion. As the light is collected from a larger volume it is expected that lower temperatures are detected. Future measurements should be spatially resolved to find the radial distribution of light and temperature.

Flannigan & Suslick (2005) measured the time-integrated sonoluminescence spectra from an argon bubble in liquid. One of the current hypotheses explains the the light production in the cavitating bubble by shock waves causing the extreme conditions in the final stages of the bubble collapse. The spectrum measured by Flannigan and Suslick is very similar to the spectrum measured here, with a continuum superimposed with line emission from the  $3p^54p \rightarrow 3p^54s$  transitions also found in the present study. This is a concrete example that converging shock waves are at least able to create gas conditions that generate similar radiation to that of sonoluminescence.

Several authors have made measurements on the light from imploding shocks, concluding that the gas at the focus behaves as a blackbody radiator (Roberts & Glass (1971), Roig & Glass (1977), Saito & Glass (1982), Matsuo et al. (1985)), based on measurements at discrete wavelengths. The present study confirms the blackbody form of the radiation, but it is difficult to make quantitative comparisons due to different initial pressures and shock wave strengths. Compared to the cited authors, we have used initial pressures lower by several orders of magnitude.

Although no quantitative results could be found from the line emissions, they do give valuable information. The upper states from where the transitions originate, are energy levels ranging from 13.1 eV to 14.7 eV. In comparison, the ionization level of argon is 15.8 eV. The transitions from excited states appear after roughly 1  $\mu$ s and are still detectable after the continuum radiation disappears.

# Acknowledgements

We would like to acknowledge the collaboration with Professor Lars-Erik Berg and Docent Olli Launila at the Physics Department, KTH, and express our thanks to them for the loan of the spectrometer and valuable discussions and suggestions on spectroscopic results. Essential parts of the experimental equipment were obtained on the means from The Göran Gustafsson Foundation, which is gratefully acknowledged. The present work was partially supported by a grant from the Swedish Research Council (VR).

# References

- Apazidis, N. 2003 Focusing of strong shocks in an elliptic cavity. Shock waves 13,
- Apazidis, N. & Lesser, M. B. 1996 On generation and convergence of polygonal-shaped shock waves. *J. Fluid Mech.* **309**, 301–319.
- Apazidis, N., Lesser, M. B, Tillmark, N. & Johansson, B. 2002 An experimental and theoretical study of converging polygonal shock waves. *Shock waves* 12, 39–58.
- ELIASSON, V., APAZIDIS, N. & TILLMARK, N. 2007a Controlling the form of strong converging shocks by means of disturbances. Shock Waves 17, 29–42.
- ELIASSON, V., APAZIDIS, N., TILLMARK, N. & LESSER, M. B. 2006 Focusing of strong shocks in an annular shock tube. *Shock Waves* **15**, 205–217.
- ELIASSON, V., TILLMARK, N., SZERI, A. & APAZIDIS, N. 2007b Light emission during shock wave focusing in air and argon. *Phys. Fluids* **19**, 106106.
- Flannigan, D. J & Suslick, S. 2005 Plasma formation and temperature measurement during single-bubble cavitation. Nature  ${\bf 434}$ , 52–55.
- Guderley, G. 1942 Starke kugelige und zylindrische Verdichtungsstöße in der Nähe des Kugelmittelpunktes bzw. der Zylinderachse. Luftfahrtforschung 19, 302–313.
- KNYSTAUTAS, R., LEE, B. H. K. & LEE, J. H. S. 1969 Diagnostic Experiments on Converging Detonations. *Phys. Fluids Suppl. I* pp. 165–168.
- LAZARUS, R. B. & RICHTMYER, R. 1977 Similarity Solutions for Converging Shocks.

  Los Alamos Scientific Laboratory of the University of California, Los Alamos, NM.
- Matsuo, H., Ebihara, K., Ohya, Y. & Sanematsu, H. 1985 Spectroscopic study of cylindrically converging shock waves. *J. Appl. Phys.* **58**, 2487–2491.
- Perry, R. W. & Kantrowitz, A. 1951 The production and stability of converging shock waves. J. Appl. Phys 22, 878–886.
- ROBERTS, D. E & GLASS, I. I. 1971 Spectroscopic investigation of combustion-driven spherical implosion waves. *Phys. Fluids* **14**, 1662–1670.
- Roig, R. & Glass, I. I. 1977 Spectroscopic study of combustion-driven implosions.  $Phys.\ Fluids\ {f 20},\ 1651-1656.$
- Saito, T. & Glass, I. I. 1982 Temperature Measurements at an Implosion Focus. *Proc. R. Soc. Lon. A* **384**, 217–231.

- SCHWENDEMAN, D. W. & WHITHAM, G. B. 1987 On Converging Shock Waves. Proc. R. Soc. Lon. A 413, 297–311.
- STURTEVANT, B. & KULKARNY, V. A. 1976 The focusing of weak shock waves. J. Fluid Mech. 73, 651–671.
- Sun, M. & Takayama, K. 2003 An artificially upstream flux vector splitting scheme for the Euler equations. *J. Comput. Phys.* **189**, 305–329.
- Takayama, K., Kleine, H. & Grönig, H. 1987 An experimental investigation of the stability of converging cylindrical shock waves in air. *Exps. Fluids* 5, 315–322.
- WATANABE, M. & TAKAYAMA, K. 1991 Stability of converging cylindrical shock waves. Shock Waves 1, 149–160.
- Wu, J. H. T., Elabdin, M. N., Neemeh, R. A. & Ostrowski, P. P. 1977 Production of converging cylindrical shock waves by finite element conical contractions. In Shock tube and shock wave research: Proc. Eleventh Intern. Symp. on Shock Tubes and Waves, pp. 107–114. Seattle, Wash., USA: University of Washington Press.

# Paper 2

# Shock dynamics of strong imploding cylindrical and spherical shock waves with real gas effects

# By Malte Kjellander, Nils Tillmark and Nicholas Apazidis

Department of Mechanics, Royal Institute of Technology, SE-100 44 Stockholm, Sweden

Published in Physics of Fluids 22, 116102 (2010)

Strong cylindrical and spherical shock implosion in a monatomic gas is considered. A simple solution is obtained by Whitham's geometrical shock dynamics approach modified to account for the real gas effects. The real gas effects are introduced by jump relations over the shock and include several levels of ionization, Coulomb interaction as well as internal energy of the excited electrons. It is shown that ionization has a major effect on temperature and density behind the converging shock as well as on the shock acceleration. The temperature and acceleration being substantially reduced and density substantially increased as compared to the ideal non-ionizing case. The ionization effect on the pressure behind the converging shock is less pronounced. It is also shown that for the considered test case of initial Mach number  $M_0 = 8$  the gas becomes completely ionized behind the spherical shock at approximately 1% of the initial radius from the focal point and its speed being decreased by a factor of 1.8 as compared to the ideal case.

#### 1. Introduction

Despite decades of extensive research shock focusing remains an exciting phenomenon still able to provide surprising results. One of the main reasons for continuing interest in shock focusing is its ability to create extremely high temperatures and pressures at the implosion focus. The main goal of the present study is to investigate the influence of the real gas effects such as ionization on the flow parameters behind the converging shock. The solution is based on the geometrical shock dynamics approach following Whitham as well as on jump relations including real gas effects.

An analytical solution to cylindrically and spherically converging shocks was obtained by Guderley Guderley (1942), whose self-similar solution was based upon the assumption of an already strong initial shock. He found that the radius of a converging shock wave approaching the center from a large distance, was related to the time to the implosion instant raised to a small

power. The strength of the shock wave therefore approaches infinity as it converges. Guderley's solution was extended to initially infinitesimally weak shock waves by Ponchaut et al. Ponchaut et al. (2006). Another solution to the problem was found independently by Chester Chester (1954), Chisnell Chisnell (1955) and Whitham Whitham (1973), using the approximate theory of shock dynamics which agrees well with the Guderley solution. The different approaches, as well as a numerical Euler solution, were recently compared by Hornung et al. Hornung et al. (2008) and all found to agree well. Good agreement was also found experimentally by Takayama, Kleine and Grönig Takayama et al. (1987).

The shock propagation has been well predicted by the power-law solution and Whitham's approach. However as the converging shock strength increases the real gas effects become significant. These effects need to be accounted for in order to correctly describe the post shock conditions and acquire information on the attainable pressures and temperatures by shock focusing.

Both previous solutions use the non-reactive Rankine-Hugoniot equations, which will overestimate the attainable temperature as the shock strength increases. In a real monatomic gas, energy is transferred into internal energy, electronic excitation, ionization and, for higher temperatures, radiation.

The aim of the present study is to investigate the real gas effects as the shock wave implodes on the focus. The present study is initiated following recent experimental work on converging cylindrical imploding shocks in argon at our shock tube facility at KTH, Kjellander et al. (2010). Whitham's approach of shock dynamics will be adopted, modifying the jump equations accordingly, to account for ionizational and excitational equilibrium behind the shock. For the present conditions, radiation is deemed to play a minor part and is neglected.

As the strength of the converging shock increases the non-reactive Rankine-Hugoniot shock relations will result in non-equilibrium gas conditions in the so-called frozen zone immediately behind the converging shock front. Relaxation to equilibrium conditions will then take place in a relaxation zone behind the shock. The structure of this zone as well as the balance equations governing the relaxation process in monatomic gases have been investigated in detail by a large number of researchers during the past decades, for example Petschek & Byron (1957), Gross (1965), Wong & Bershader (1966), Biberman et al. (1971), Kaniel et al. (1986).

The goal of the present work is not to investigate the details of the relaxation process but to obtain the flow variables behind this zone where the gas is brought to local thermodynamical equilibrium (LTE). Within the relaxation zone the electron gas and the gas consisting of heavy particles have different temperatures, but as equilibrium is reached they attain a single temperature. The approximation of LTE is used for the cases when the thickness of the relaxation zone is small compared to the radius of the converging shock. The thickness of the relaxation zone, as well as the relaxation time, depend on the shock strength and initial conditions. Approximate relaxation times and zone thickness in pure argon may be found in Zel'dovich & Raizer (2002). For example for M=10 and initial pressure of  $p_1=10$  mm Hg the thickness of the relaxation zone is about 6 cm, whereas it decreases with stronger shocks and higher initial pressures. For M=13 and initial pressure of  $p_1=10$  mm Hg the zone thickness is reduced to 0.2 cm. The present study was initiated in connection with our experimental work on cylindrical shock focusing in argon, Kjellander et al. (2010). In the experimental case the initial pressure was  $p_1 = 75$  mm Hg, that is approximately 7 times higher than the initial pressure in Zel'dovich & Raizer (2002). The thickness of the relaxation zone is inversely proportional to the gas density that is the zone thickness cited above is reduced by a factor of 7 in our experimental case giving a thickness of approximately 1 cm at M=10. In our experiments with the initial values of  $r_0=7$  cm and  $M_0 = 3.7$  the Mach number of 10 was obtained in the last stages of the focusing process when the radius of the converging cylindrical shock was about 0.5 cm. The relaxation zone can thus not be considered as thin with respect to the shock curvature in our experiments and a full analysis of the zone structure would be required. The present theory is therefore applied to initially stronger shocks with larger initial radii. With the increasing shock strength the thickness of the relaxation zone is decreased exponentially and for M=30 its extension is comparable with the shock thickness, see Biberman et al. (1971). The values of the initial Mach number, pressure and convergence radius that are appropriate for the present thin relaxation zone approximation are discussed in section II in connection with the computed example.

The paper is organized as follows. General assumptions and notations as well as shock dynamics and the set of jump equations, which together are used to calculate the shock propagation and temperature evolution are formulated in section II and III. A short summary is in section IV. The resulting calculations are presented in section V, with details on which effects were accounted for and which were not. Two cases are considered - cylindrical and spherical converging shocks to highlight the differences between the 2D and 3D convergence. The influence of the real gas effects on temperature, density and pressure are discussed by comparison to the ideal non-reacting case.

#### 2. Shock dynamics

A cylindrical or spherical shock wave of an initial Mach number  $M_0$  and radius  $r_0$  propagates towards the center of the circle or sphere in a monatomic gas. The shock position has a radius r with an area A(r). The Mach number M and the thermodynamic equilibrium conditions behind the shock are to be determined for all shock positions.

The problem is treated with the geometric shock dynamics as presented by Whitham, taking in consideration changes introduced by a variable area, but neglects nonlinear interactions with the flow behind the shock. The method uses the simplification that the shock wave propagates along rays being  $C_+$  characteristics. This approximation has been shown to provide accurate results Whitham (1973), Apazidis et al. (2002), Hornung et al. (2008) especially for continuously accelerating shocks. Consider a shock propagating down a tube with a cross section A(r). The problem formulation can be approximated as quasi one-dimensional if the area change is not too rapid. The characteristic equation along the  $C_+$  characteristic states that (Whitham 1973)

$$\frac{dp}{dr} + \rho a \frac{du}{dr} + \frac{\rho a^2 u}{u + a} \frac{1}{A} \frac{dA}{dr} = 0 \tag{1}$$

where p is the pressure, u the velocity and a the speed of sound. With cylindrical and spherical geometries,  $A(r) \propto r^{\nu-1}$ , where  $\nu=2$  or  $\nu=3$  for the respective case. Using the Rankine-Hugoniot relations for a gas with constant composition this can be reformulated into an area-Mach-number relation:

$$\frac{M\lambda(M)}{M^2 - 1}\frac{dM}{dr} = -\frac{1}{A}\frac{dA}{dr} = -\frac{\nu - 1}{r} \tag{2}$$

where  $\lambda$  and  $\mu$  are defined as:

$$\lambda(M) = \left(1 + \frac{2}{\gamma + 1} \frac{1 - \mu^2}{\mu}\right) \left(1 + 2\mu + \frac{1}{M^2}\right) \tag{3}$$

$$\mu^2 = \frac{(\gamma - 1)M^2 + 2}{2\gamma M^2 - (\gamma - 1)} \tag{4}$$

This approach has shown good agreement with experimental shock front propagation data and the exact solution provided by Guderley's approach. However, as the shock approaches the center, the perfect gas assumption predicts the temperature and pressure to increase exponentially towards infinity and the shock relations leading to the simplifications in Eqs. (2) - (4) are no longer valid. In order to allow for real gas effects a solution is instead sought by integrating Eq. (1) directly. The gas conditions p,  $\rho$ , u and a are still found from the shock relations, but with allowance for said effects they need to be calculated using an iterative method described below. Differentiating and inserting the expression for the surface area  $A(r) = 2\pi(\nu - 1)r^{\nu-1}$  yields:

$$dp + \rho a du = -\frac{\rho a^2 u}{u+a} \frac{(\nu-1)}{r} dr \tag{5}$$

Integrating between states 1 and 2, corresponding to two Mach numbers  $M_1$  and  $M_2$  we get

$$\int_{1}^{2} \frac{u+a}{\rho a^{2}u} dp + \int_{1}^{2} \frac{u+a}{au} du = -(\nu-1) \ln \frac{r_{2}}{r_{1}}$$
 (6)

Using equivalent notation to Hornung et al. (2008), we note that the radius of the shock wave at two consecutive time instants can be expressed as

$$r_2 = f_{1-2}r_1 \tag{7}$$

$$f_{1-2} = \exp\left(-\frac{1}{(\nu - 1)} \left[ \int_{1}^{2} \frac{u + a}{\rho a^{2} u} dp + \int_{1}^{2} \frac{u + a}{a u} du \right] \right)$$
(8)

Starting from an initial Mach number  $M_1$  and radius  $r_1$ , the shock front propagation can now be calculated. The change in radius as the shock wave accelerates to a new Mach number  $M_2 = M_1 + dM$  is acquired by calculating the post-shock conditions for  $M_1$  and  $M_2$ , inserting into Eq. (7) and evaluating the integral numerically.

The front of the shock is a region with a thickness of a few mean free paths in which a frozen condition is reached, where the energy is transferred to translational temperature of the neutral gas and no atoms have been ionized. Behind this region is a relaxation zone in which the gas is ionized and reaches thermodynamical equilibrium. We can motivate the use of the equilibrium conditions in the calculation of the shock propagation above if the extent of this zone is small compared to the curvature of the shock. The calculation of the equilibrium values is presented in the next section.

# 3. Shock jump relations

Shock jump relations accounting for various combinations of dissociation, radiation or ionization have been studied extensively, see for example Resler et al. (1952), Kozlov & Stupitskii (1968), Michaut et al. (2004) or Nieuwenhuijzen et al. (1992). We limit the present study to a monatomic gas model taking in consideration ionization, electronic excitation and departures from a perfect gas due to Coulomb interactions. The gas is assumed to be in local thermodynamic equilibrium (LTE). Radiative contributions to the energy and pressure are presumed negligible. Ionization of the species A is considered up to  $\ell$ :th level. The upper bound for  $\ell$  is the atomic number of the species. The volumetric particle density of ions in stage i is denoted  $n_i$  and the total particle density of heavy particles is denoted  $n_H$ . The fraction of heavy particles in ionization stage i (with i=0 referring to the neutral state) is denoted  $\alpha_i = n_i/n_H$ . Hence

$$\sum_{i=0}^{\ell} n_i = n_H \qquad or \qquad \sum_{i=0}^{\ell} \alpha_i = 1 \tag{9}$$

Due to charge conservation, the electron number density  $n_e$  and mean level of ionization  $\alpha_e$ , or equivalently, the average number of free electrons per heavy particle, can be expressed as

$$\alpha_e = \sum_{i=1}^{\ell} i\alpha_i \tag{10}$$

$$n_e = \sum_{i=1}^{\ell} i n_i = n_H \sum_{i=1}^{\ell} i \alpha_i = n_H \alpha_e$$
(11)

Writing the common equations describing a one-dimensional normal shock in a frame of reference following the shock front, the conservation of mass, momentum and energy are

$$\rho_1 u_1 = \rho_2 u_2 \tag{12}$$

$$\rho_1 u_1^2 + p_1 = \rho_2 u_2^2 + p_2 \tag{13}$$

$$\rho_1 u_1^2 + p_1 = \rho_2 u_2^2 + p_2$$

$$h_1 + \frac{u_1^2}{2} = h_2 + \frac{u_2^2}{2}$$
(13)

where  $\rho$  denotes the volumetric mass density, u the velocity relative to the shock front and p the total pressure. With the ionic contribution the enthalpy per mass h can be written Zel'dovich & Raizer (2002)

$$h = \frac{5}{2}(1 + \alpha_e)RT + R\sum_{i=1}^{\ell} \alpha_i \sum_{j=1}^{i} \frac{I_j}{k}$$
$$+ RT^2 \sum_{i=0}^{\ell} \alpha_i \frac{\partial \ln Q_i^{el}}{\partial T} + \delta h_C$$
(15)

where R is the specific gas constant and k is the Boltzmann constant. Since LTE is assumed, all species have the same temperature: T is the absolute temperature of electrons and heavy particles alike. The second term is the potential energy of ions, where  $I_j$  is the j:th ionization potential. For argon,  $I_1 \approx 15.8 \text{ eV}, I_2 \approx 27.6 \text{ eV}, \text{ and so on NIST (2008)}.$  The sum indicates that to ionize an atom to the i:th level, the energy  $I_1 + I_2 + ... + I_i$  is required to remove each successive electron. The third term in Eq. (15) accounts for energy of electronically excited states, including in neutral atoms, and is determined by statistical methods from the electronic partition functions  $Q^{el}$ . The last term,  $\delta h_C$ , is due to contributions from the Coulomb interactions.

The equation of state with the Coulomb forces making a contribution  $\delta p_C$ takes the form

$$p = \rho(1 + \alpha_e)RT + \delta p_C \tag{16}$$

The LTE distribution of species is found from the law of mass action, here rewritten in a more convenient form as a set of Saha equations using the particle fractions,

$$\frac{\alpha_{i+1}}{\alpha_i} = \frac{1 + \alpha_e}{\alpha_e} \left(\frac{2\pi m_e}{h^2}\right)^{3/2} \frac{(kT)^{5/2}}{p - \delta p_C} \frac{2Q_{i+1}^{el}}{Q_i^{el}} \times \exp\left(-\frac{I_{i+1} - \delta I_{i+1}}{kT}\right)$$
(17)

where  $m_e$  is the mass of an electron, h is Planck's constant and  $Q_i^{el}$  is the electronic partition function of species in ionization stage i.

The derivation of the Saha equations can be found in e.g. Zel'dovich & Raizer (2002) or Cambel & Jennings (1967). We solve them for  $\alpha_e$  with known T and p using the iterative method presented by Trayner & Glowacki (1995). The values of each  $\alpha_i$  can then be found from the requirements on charge neutrality and nucleus conservation.

The Saha equation as well as the excitational energy term involve the electronic partition functions and they were computed in the following manner. The electronic partition function consists of a summation over all possible energy levels the electrons may populate:

$$Q_{elec} = \sum_{i=1}^{\infty} g_i e^{-e_i/kT} \tag{18}$$

This is an infinite sum over the energy levels  $e_i$  with corresponding degeneracies  $g_i$ : if a cutoff is not made, the sum diverges. Various methods of cut-off may be found in the literature, including summing over an arbitrary number of levels. We have employed one of the most common methods: cut-off at the reduced potential due to Coulombic screening according to the Debye-Hückel model. Coulomb interactions between the charged particles reduces the energy required to remove an electron from its orbit around a nucleus see Zel'dovich & Raizer (2002), Gündel et al. (1991), Griem (1963). This gives a natural cut-off point at this effective potential, as electrons cannot occupy bound states above this limit.

When this model is used, consistency requires that the Coulomb forces are considered in the same manner when evaluating the thermodynamic variables see Mihalas & Mihalas (1999), Zaghloul (2003). The Debye screening radius expressed in the variables used in section II:

$$r_D = \left[\epsilon_0 kT / (e^2 n_H (\alpha_e + \sum_{i=1}^{\ell} i^2 \alpha_i))\right]^{1/2}$$
 (19)

where  $\epsilon_0$  is the vacuum permittivity, e the electron charge and T the temperature in Kelvin. The reduction in ionization potential and the enthalpy and pressure contributions Griem (1962) then become:

$$\delta I_{i+1} = \frac{(i+1)e^2}{4\pi\epsilon_0 r_D} \tag{20}$$

$$\delta h_C = -\frac{kT}{\rho 6\pi r_D^3} \tag{21}$$

$$\delta p_C = -\frac{kT}{24\pi r_D^3} \tag{22}$$

The summation of Eq. (18) is taken for all states lying below the reduced potential, that is, for which  $e_i < I_i - \delta I_i$ . Practically this means an extra step in the calculation of the equilibrium distribution: the number of levels to include in calculation of each ionic partition function is guessed, and Eq. (17) is solved as before. The resulting distribution is used to calculate the potential reduction according to Eqs. (19) and (20). From this the number of levels to include can be determined as described earlier in this paragraph. If this differs from the guessed values, the new ones are used for another iteration. For comparison calculations have also been made disregarding Coulomb forces, in which case the summation of the partition function is made over all known states. Data for the electronic levels have been taken from Bond (1954) and NIST (2008).

The shock relations can be calculated by solving Eqs. (12) - (17). The system is closed with respect to the unknowns, but an iterative method is necessary. The pre-shock conditions,  $\rho_1, p_1, u_1, h_1$  are known. A shock adiabatic is presented in Fig. 1(a) for the initial conditions  $p_1 = 0.1$  atm and  $T_1 = 300$  K. The adiabatic starts deviating from the non-reacting asymptote  $\rho/\rho_1 = 4$  around M = 10. The local maximum occurs slightly before the maximum of the first ionization stage, which occurs at M35 as seen in Fig. 1(b).

#### 4. Summary of the solution procedure

The shock propagation and post-shock conditions of the converging shock waves are calculated in the following manner: an initial Mach number and radius are predetermined. Then, for small increments in Mach number  $M_{i+1} = M_i + dM$ , corresponding new radii are acquired from Eq. (7) by finding the post-shock conditions behind a wave of strength  $M_{i+1}$  as described in section III. The integration continues until either a final Mach number or radius of choice is reached. Calculations were performed with successively smaller dM until no noticeable change was seen.

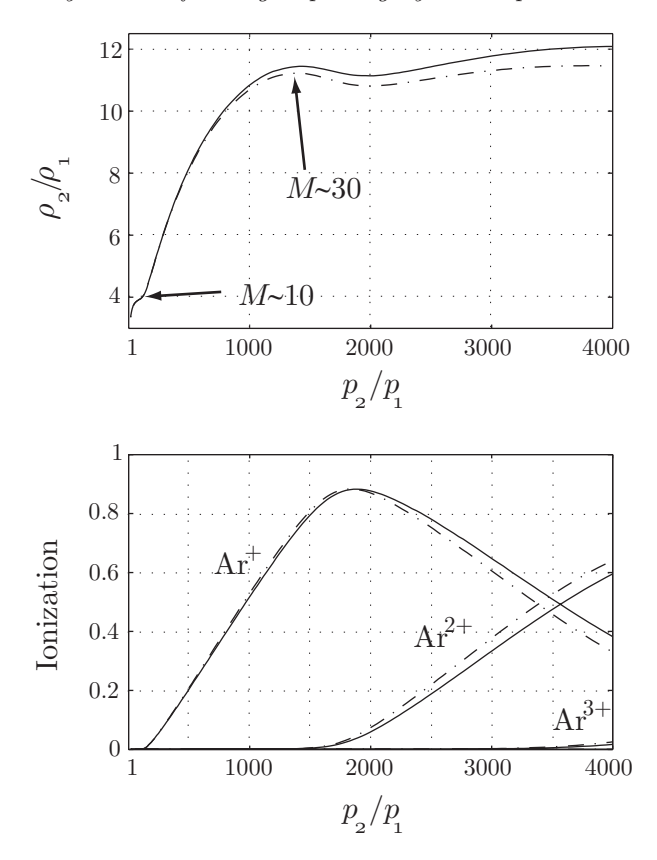


Figure 1: Shock adiabatic (a) and post-shock equilibrium ionization (b) for a shock passing through argon at  $p_1 = 0.1$  atm and  $T_1 = 300$  K, allowing for ionization and excitation. Dashed-dotted lines show the same excluding excitation. Four stages of ionization were accounted for.

The equilibrium speed of sound, necessary for the integration of Eq. (7), may be expressed as in Eq. (23) below, whose derivatives are evaluated numerically.

$$a_e^2 = \left(\frac{\partial p}{\partial \rho}\right)_s = \gamma \left(\frac{\partial p}{\partial \rho}\right)_T = \frac{c_p}{c_v} \left(\frac{\partial p}{\partial \rho}\right)_T,$$

$$c_p = \left(\frac{\partial h}{\partial T}\right)_p, \quad c_v = \left(\frac{\partial e}{\partial T}\right)_v$$
(23)

#### 5. Results

This study was initiated following the experimental work by the present authors on cylindrical shock convergence, Kjellander et al. (2010). Although the solutions of the specified problem for different initial radii only concerns a scaling of the presented solution, the validity of the method does depend on the radius. Behind a strong shock there is a non-equilibrium zone where the ionization occurs. This zone must be small in comparison to the change of curvature dr in the integration of Eq. (7) for the method to be motivated. Although the current work started in connection with the experiments at our shock tube facility the present theory cannot be applied to this case. In the experimental case with  $M_0 = 3.7$  and  $r_0 = 70$  mm the relaxation time is substantially longer than the time dt the shock needs to propagate a distance dr. The flow is essentially frozen and ionization equilibrium is not reached until after the shock has focused, reflected and diverged. It is obvious that the present approach is not useful for this case, however as the Mach number increases the relaxation zone gets considerably smaller. At  $M \approx 30$ , see Biberman et al. (1971), its width is comparable to the shock thickness and the present approximation of immediate equilibrium may be applied. Even at lower Mach numbers when the thickness of the relaxation zone is of order of few millimeters the present approximation may be justified for shocks with sufficiently large, compared to the zone thickness, radius.

As an example we have considered the convergence processes of a cylindrical and a spherical shock with specific initial conditions. Initial gas and shock conditions were the same in both cases: the gas was argon with initial temperature  $T_1 = 300$  K and pressure  $p_1 = 75$  mm Hg or  $p_1 = 0.1$  atm. The initial Mach number was chosen to  $M_0 = 8$ . The initial shock conditions were thus chosen to fulfill the thin relaxation zone approximation, that is the radius of the converging shock was assumed to be large compared to the thickness of the relaxation zone. The values of the initial radius for the present conditions are discussed in greater detail below. The calculations were performed including and excluding excitation. Ions up to and including the fourth stage were considered, as it became evident that higher stages were essentially unpopulated for the considered Mach numbers and initial conditions.

The shock relations for the stated initial conditions are shown in Figs. 2 - 3 while the Mach number and temperature evolution for the cylindrical and spherical converging shocks are presented in Fig. 4.

Figures 2 and 3 show the equilibrium conditions behind a normal shock wave in argon with initial temperature  $T_1$ =300 K and pressure  $p_1$ =0.1 atm. The dashed lines are the Rankine-Hugoniot relations for perfect gas without ionization, depending only on the Mach number. The full lines show relations including ionization and excitation while the dashed-dotted lines omit excitation. As seen, the ionization has a strongly limiting effect on the temperature as

energy is transferred from translational to potential energy. Whereas the compression approaches an asymptotic value  $(\rho_2/\rho_1 = 4 \text{ for } \gamma = 5/3)$  for constant composition gas this is not the case for the ionizing shock. The compression is dependent on how large the potential ionization and excitation energies are relative to the translational energy. The creation of a local maximum corresponds to the increasing number of particles as the first ionization stage approaches its maximum. The free electrons lead to an increased translational energy relative to the potential energy, resulting in a local decrease in compression Zel'dovich & Raizer (2002) (cited earlier). The compression resumes to increase as the second stage ionization ramps up.. As seen from Fig. 3(a) the ionization does not have the same striking effect on pressure as it has on the temperature behind the shock as compared to perfect gas conditions without ionization. We can also see that the inclusion of the excitational term in the energy equation has a minor effect on the flow parameters. It has most influence on the compression ratio, which is increased due to the additional energy transferred to internal modes. Fig. 3(b) shows the first ionization degrees for the the considered case as well as the remaining degree of neutral atoms. The first ionized stage has its maximum at  $M \approx 35$ , while most neutral atoms have been ionized at around  $M \approx 50$ .

Propagation of the converging ideal and ionizing cylindrical and spherical shocks is compared in Figs. 4(a) and 4(b). Since the solution of Eq. (7) boils down to coupling Mach number to a radius, the cylindrical and spherical solutions are basically identical and only a coordinate transformation differs the two cases. However when the Mach number and temperature behind the shock are shown as functions of the convergence radius the difference between the cylindrical and spherical convergence is fully illuminated with the latter case producing substantially higher Mach number values and temperatures for the same value of the convergence radius. The shock fronts in gas including ionization and excitation are seen to accelerate substantially slower as compared to the ideal solution. Fig. 4(a) shows that the Mach number is reduced by a factor of 1.3 for the cylindrical shock and by a factor of 1.8 for the spherical shock at  $r/r_0 = 0.01$  or 1% of the initial radius from the focal point as compared to the ideal case in the present example. The slowdown of the shock due to ionization is then further increased as the shock converges on the focus. As it is also seen from Fig. 4(b) the decrease in temperature behind both cylindrical and spherical shocks as compared to the ideal case is even more drastic. Fig. 2(b) together with Fig. 3(b) shows that the deviation from the ideal case starts long before the gas is completely ionized. According to Fig. 3(b) a shock with a 10 % ionization fraction,  $\alpha_1 = 0.1$  has a Mach number,  $M \approx 18$  at the initial conditions considered here. At this value of the Mach number the temperature behind the shock is reduced by a factor of 2 as compared to the ideal case, according to Fig. 2(b). For stronger shocks the temperature reduction becomes significantly larger.

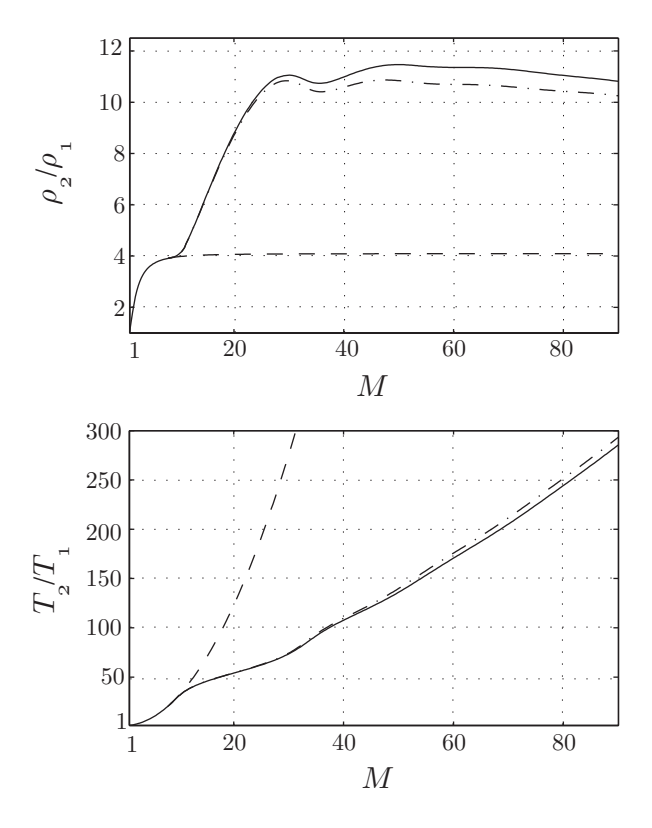


Figure 2: Jump relations for a shock propagating through argon at  $T_1$ =300 K and  $p_1$ =0.1 atm; (a) compression and (b) temperature jump. Full lines show relations including ionization and excitation while the dash-dotted omit excitation. The dashed lines show the ideal relations for comparison.

We now address the question of the proper initial radius for the thin relaxation zone approximation to be valid. As seen from Fig. 4(b) the Mach number behind the cylindrical shock is  $M\approx 12$  whereas it is  $M\approx 15$  behind the spherical shock at  $r/r_0=0.1$ . For  $M\approx 13$  and initial pressure of  $p_1=0.013$  atm the relaxation zone thickness in argon is estimated to approximately 0.2 cm, see Zel'dovich & Raizer (2002). In our case the initial pressure is  $p_1=0.1$  atm or approximately 7 times higher which reduces the zone thickness to 0.03 cm. Suppose that the shock radius at this position is 100 times greater than the zone thickness, that is r=3 cm giving an initial shock radius of approximately  $r_0=30$  cm for the present example with the initial Mach number  $r_0=8$ .

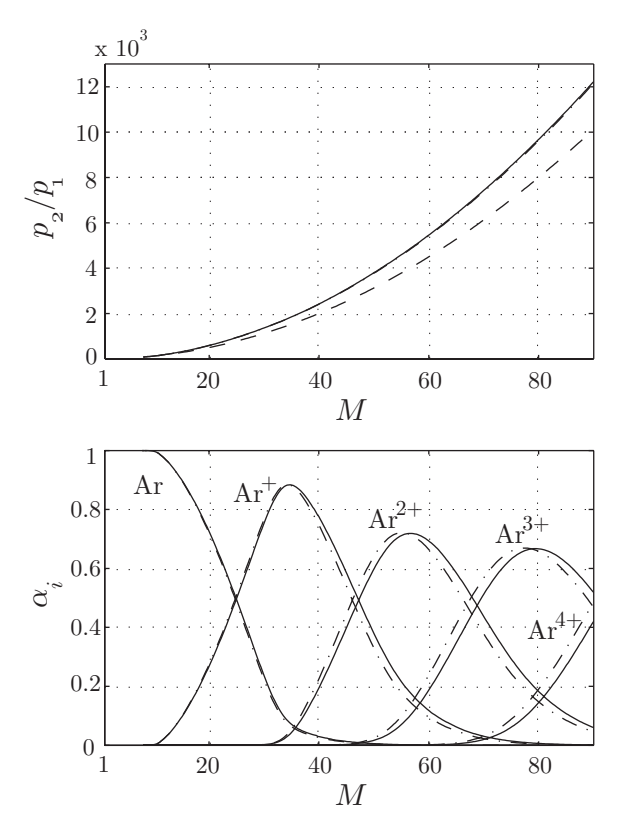


Figure 3: Jump relations for a shock propagating through argon at  $T_1$ =300 K and  $p_1$ =0.1 atm; (a) pressure jump and (b) ionization fractions  $\alpha_i$  for the neutral and four first ionized stages. Full lines show relations including ionization and excitation while the dash-dotted omit excitation. In (a) the dashed line shows the ideal relation for comparison.

Finally, Fig. 5 shows the equilibrium gas composition behind the converging spherical shock as function of the convergence radius.

### 6. Conclusions

The implosion of spherical and cylindrical shock waves were studied theoretically using shock dynamics with allowance for real gas effects. This specific investigation was limited to monatomic gases, but Eq.(8) is general and effects such as dissociation can be included by modifying the jump relations accordingly. Here, ionization, excitation and Coulomb interactions in the resulting electron-ion gas were considered. The major effect on resulting temperature,

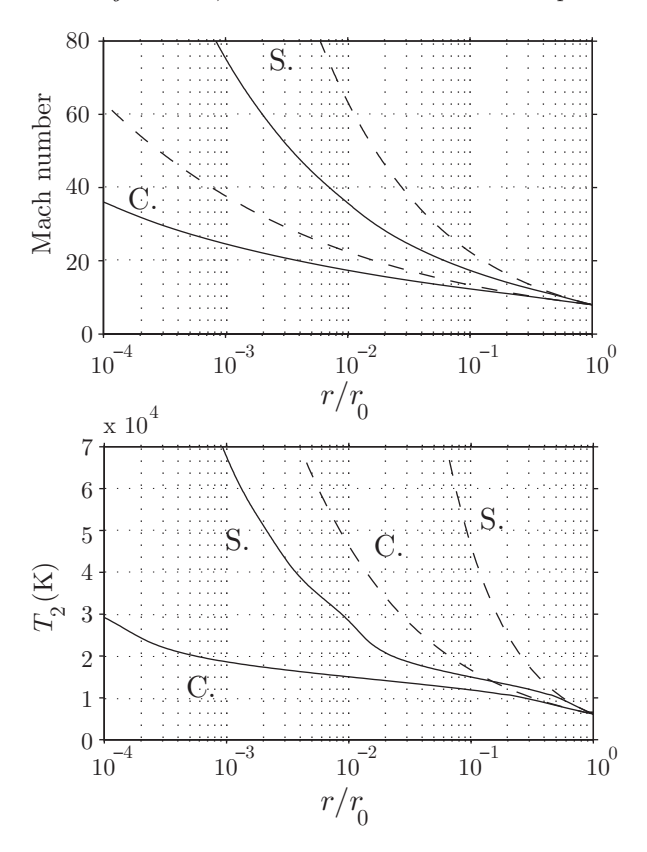


Figure 4: Mach number (a) and post-shock equilibrium temperatures (b) for cylindrical (C) and spherical (S) shocks with initial Mach number  $M_0 = 8$ . Full lines show relations including ionization and excitation while the dashed lines show the ideal non-ionizing case.

Mach number and compression during shock focusing due to ionization was shown and calculated for the specific case of initial  $M_0=8$  and  $p_1=0.1$  bar. The inclusion of ionization has a strongly limiting effect on the temperature, as kinetic energy is transferred to other energy modes. Acceleration of the converging shock front is also significantly decreased as compared to the ideal non-ionizing case. Ionization has also a major effect on the compression ratio which is substantially increased as compared to the non-reacting case. The ionization does not have the same striking effect on the pressure. Fig. 3(b) shows that for the considered test case, the first ionization stage reaches its maximum  $M \approx 35$ . From Fig. 4(a), this corresponds to 0.001% of the initial radius for the cylindrical case and 1% for the spherical case. As mentioned previously the

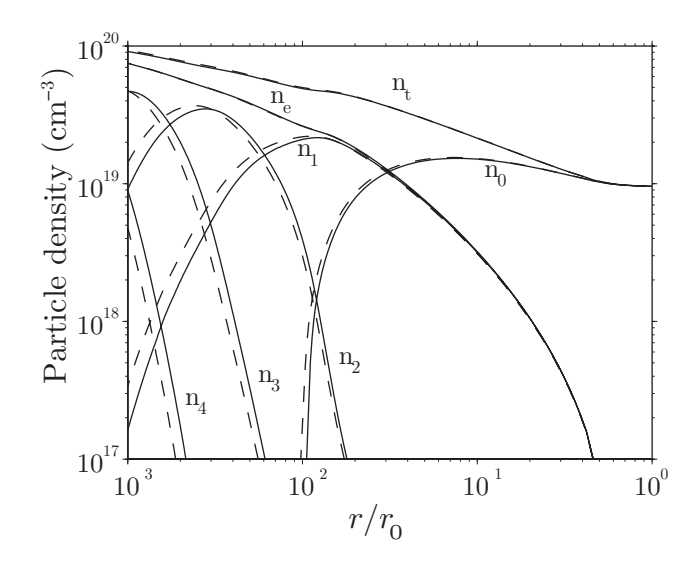


Figure 5: Equilibrium gas composition behind the spherical shock wave for different shock front positions:  $n_t$ : total particle density,  $n_e$ : electron density,  $n_0$  to  $n_4$ : density of the different ion species. The full lines show calculations including both ionization and excitation while dashed lines are without excitation.

present study investigates the overall effect of ionization behind the converging cylindrical and spherical shocks and does not consider the detailed structure of the relaxation zone which is assumed to be thin as compared to the shock radius.

# Acknowledgements

The authors would like to gratefully acknowledge the financial support received from the Swedish Research Council (VR).

# References

- APAZIDIS, N., LESSER, M. B., TILLMARK, N. & JOHANSSON, B. 2002 An experimental and theoretical study of converging polygonal shock waves. *Shock waves* 12, 39–58.
- BIBERMAN, L. M., MNATSAKANYAN, A. KH. & YAKUBOV, I. T. 1971 Ionization relaxation behind strong shock waves in gases. Sov. Phys. Usp. 13, 728–744.
- BOND, J. 1954 The structure of a shock front in argon. Los Alamos Sci. Lab Rept. LA-1693 .
- Cambel, A. B. & Jennings, B. H. 1967 Gas Dynamics. Burgess Hill, New York.
- CHESTER, W. 1954 The quasi-cylindrical shock tube. Phil. Mag. 45, 1293–1301.
- Chisnell, R. F 1955 The normal motion of a shock wave through a nonuniform one-dimensional medium. *Proc. R. Soc. London* 232, 350–370.
- GRIEM, H. R. 1962 High density corrections in plasma spectroscopy. *Phys. Rev.* 128, 997–1003.
- GRIEM, H. R. 1963 Validity of local thermal equilibrium in plasma spectroscopy. *Phys. Rev.* **131**, 1170–1176.
- GROSS, R. 1965 Strong ionizing shock waves. Rev. Mod. Phys. 37, 724–743.
- GUDERLEY, G. 1942 Starke kugelige und zylindrische Verdichtungsstöße in der Nähe des Kugelmittelpunktes bzw. der Zylinderachse. Luftfahrtforschung 19, 302–313.
- GÜNDEL, H., HANTSCHE, E. & HESS, H. 1991 Low temperature plasmas. Eur. J. Phys.  ${\bf 12},$  39–46.
- HORNUNG, H. G., PULLIN, D. I. & PONCHAUT, N. 2008 On the question of universality of imploding shock waves. *Acta Mech.* **201**, 31–35.
- Kaniel, A., Igra, O., Ben-Dor, G. & Mond, M. 1986 Ionization behind strong normal shock waves in argon. *Phys. Fluids* **29**, 3618–3625.
- KJELLANDER, M., TILLMARK, N. & APAZIDIS, N. 2010 Thermal radiation from a converging shock implosion. *Phys. Fluids* **22**, 046102.
- KOZLOV, G. I. & STUPITSKII, E. L. 1968 State of argon behind a shock wave at Mach numbers from 20 to 50, with allowance for excitation, multiple ionization, and Coulomb interactions. *Zh. Prikl. Mekh. Tekh. Fiz.* **9**, 94–97.
- MICHAUT, C., STEHLÉ, C., LEYGNAC, S., LANZ, T. & BOIREAU, L. 2004 Jump conditions in hypersonic shocks. *Eur. Phys. J. D* 28, 381–392.

- Mihalas, D. & Mihalas, B. 1999 Foundations of Radiation Hydrodynamics. Dover Publications, Mineola.
- NIEUWENHUIJZEN, H., DE JAGER, C., CUNTZ, M., LOBEL, A. & ACHMAD, L. 1992 A generalized version of the rankine-hugoniot relations including ionization, dissociation, radiation and related phenomena. *Astron. Astrophys*, **28**, 195–200.
- NIST 2008 Atomic spectra database, version 3.0.
- Petschek, H. & Byron, S. 1957 Approach to equilibrium ionization behind strong shock waves in argon. *Ann. Phys.* 1, 270–315.
- PONCHAUT, N., HORNUNG, H. G. & MOUTON, D. I. 2006 On imploding cylindrical and spherical shock waves in a perfect gas. *J. Fluid. Mech.* **560**, 103–122.
- RESLER, E. L., LIN, S. C. & KANTROWITZ, A. 1952 The production of high temperatures in shock tubes. *J. App. Phys.* 23, 1390–1399.
- TAKAYAMA, K., KLEINE, H. & GRÖNIG, H. 1987 An experimental investigation of the stability of converging cylindrical shock waves in air. Exps. Fluids 5, 315–322.
- TRAYNER, C. & GLOWACKI, M. H. 1995 A new technique for the solution of the saha equation. J. Sci. Comput. 10, 139–149.
- WHITHAM, G. B. 1973 Linear and nonlinear waves. John Wiley and Sons, New York.WONG, H. & BERSHADER, D. 1966 Thermal equilibrium behind an ionizing shock.J. Fluid Mech. 26, 459–479.
- ZAGHLOUL, M. R. 2003 A consistant model for the equilibrium thermodynamic functions of partially ionized flibe plasma with coulomb effects. *Physics of Plasmas* 10, 527–538.
- ZEL'DOVICH, YA. B. & RAIZER, YU. P. 2002 Physics of Shock Waves and High-Temperature Hydrodynamic Phenoma. Dover Publications, Mineola, New York.

# Paper 3

# Regular versus Mach reflection for converging polygonal shocks

By V. Eliasson, M. Kjellander & N. Apazidis

Department of Mechanics, Royal Institute of Technology, SE-100 44 Stockholm, Sweden

Published in Shock Waves 17, pp. 43-50 (2007)

The onset of Mach reflection or regular reflection at the vertices of a converging polygonal shock wave is investigated experimentally in a horizontal annular shock tube. The converging shock waves are visualized by schlieren optics. Two different types of polygonal shock convergence patterns are observed. We compare the behavior during the focusing process for triangular and square-shaped shocks. It is shown that once a triangular shaped shock is formed, the corners in the converging shock will undergo regular reflection and consequently the shape will remain unaltered during the focusing process. A square shaped shock suffers Mach reflections at the corners and hence a reconfiguring process takes place; the converging shock wave alternates between a square and an octagon formation during the focusing process.

#### 1. Introduction

Shock wave focusing has been studied in several research communities since the beginning of the 1940's when a similarity solution was presented for a converging cylindrical shock wave in Guderley (1942). Analytical, numerical and experimental investigations have been performed since then, for example see Schwendeman & Whitham (1987) and Takayama et al. (1984). It is well known that a converging cylindrical shock wave is unstable. It is unstable in the sense that it looses its original shape if it is perturbed by disturbances in the flow. The disturbed shape tends to produce a polygonal structure with plane sides and sharp corners. The polygonal shape will lack symmetry if the perturbations in the flow are not symmetric or strong enough. It is, however, possible to generate converging shocks with polygonal symmetric shapes that are stable, i.e. shapes that evolve during the focusing process in a predictable way. Such stable shapes were generated analytically and numerically in Schwendeman & Whitham (1987), numerically in Apazidis & Lesser (1996), experimentally and numerically in Apazidis et al. (2002), Eliasson et al. (2006) and Eliasson et al. (2007). Depending on the type of reflection that occurs at the vertices of the polygonal shapes, some of these shapes will transform continuously during the focusing process, changing from a n-corner shape into a 2n-corner shape and then back again. The new plane segments emerging from corners as a result of Mach reflection have higher Mach number than the adjacent sides. They travel faster and absorb the adjacent sides. When such two segments finally meet, they build a new corner. The new polygon has the same number of sides at the end of each cycle but is rotated with respect to the old polygon so that the corners are opposite to the midpoints of the old sides. This reorientation process is due to the nonlinear interaction between the local velocity and the shape of the shock front. For example, a square shaped shock wave will transform into an octagon and then back to a square again, with the second square oriented opposite to the first square. The above reconfiguration process which stems from the Mach reflection at the corners constitutes, in fact, the basis for the Mach number increase on the shock front; each time the reconfiguration cycle is completed the Mach number over the shock front is increased stepwise, see Schwendeman & Whitham (1987) and Apazidis & Lesser (1996). Some elements of this 2D process, that is the tendency to form planar pieces, is also visible for converging spherical shocks, see Schwendeman (2002).

There exists however another mechanism of symmetric polygonal shock focusing in which the Mach number remains bounded. A self similar solution for the focusing process of 2D equilateral triangular shock waves was investigated in Betelu & Aronson (2001). This solution shows that the corners of the triangular shock wave undergo regular reflections and preserve the triangular shape during the whole focusing process for certain values of Mach numbers and initial conditions. The energy density is bounded for this solution which means that the Mach number will approach a constant value at the focus. Triangular shocks are thus undergoing regular reflection at the vertices. This is in contrast to symmetric polygonal shocks with number of sides greater than three, that suffer Mach reflection at the vertices, where the Mach number increases as the shock approaches the focus. If the stability criteria for the triangular shock wave are violated, then a reconfiguring process takes place in which the corners develop into plane sides and the plane sides into corners as mentioned earlier.

There are several criteria for transition from a regular reflection (RR) to a Mach reflection (MR). Three of these were proposed in von Neumann (1943) and since then many more have been suggested, see e.g. Ben-Dor (1992, 2006). The length scale concept was introduced in Hornung et al. (1979) and is the criterion that agrees best with pseudo steady flow in experimental shock tube facilities. The ongoing research on transition conditions for RR←MR is motivated by difficulties in matching theoretical results with experimental. One problem is the persistence of regular reflections well past the theoretical maximum limit and many publications address this problem, see e.g. Barbosa & Skews (2002).

Following the ideas in Betelu & Aronson (2001), we investigate two different types of reflection, RR or MR, that can occur at the vertices of a converging polygonal shock wave. The polygonal shock waves are generated in the same shock tube and with the same method as in Eliasson  $et\ al.$  (2007). In the present study we generate triangular and square shaped shocks. Their focusing behavior is compared and it is found that while the triangular shock preserves its form and orientation the square shock transforms to an octagon and then back to a square shape which is rotated 45° with respect to the initial configuration. According to the previous numerical work, see e.g. Schwendeman & Whitham (1987) and Apazidis & Lesser (1996), this reconfiguration process continues until the shock wave reaches the focusing center.

We start by describing the experimental setup and the method used to create the polygonal shock waves, followed by the experimental results. Finally we conclude and summarize the results.

#### 2. Experimental setup

The experimental setup consists of a 2.4 m long horizontal annular shock tube where the shock wave is generated and focused. A laser (an air-cooled Nd:Yag, NewWave Orion) is used as a light source for the visualization equipment that consists of a schlieren system with a CCD camera, (PCO SensiCam, 12 bits,  $1280 \times 1024$  pixels, pixel size:  $6.7 \times 6.7 \mu m$ ). See Fig. 1 for a schematic overview of the experimental setup. The shock tube consists of two main parts, a high pressure chamber and a low pressure channel. The two parts are separated by a 0.5 mm thick aluminum membrane. As the high pressure chamber fills up with gas, the membrane will break at a given pressure difference. After the membrane breaks, a plane shock wave is formed and starts to travel downstream in the shock tube through the low pressure channel. The low pressure channel is divided into three sections; an inlet section where the plane shock wave is formed, a transformation section where the plane shock wave becomes annular and the test section which is located at the rear end of the shock tube where the shock wave is focused and reflected. The annular part of the shock tube is composed of an inner body mounted coaxially inside the wider diameter outer tube. The inner body is represented by the dotted line at the low pressure channel shown in Fig. 1. The inner body consists of a cone followed by a cylindrical tube and is suspended by two sets of four supports. The two sets are placed 30.75 cm apart and the supports are shaped as wing profiles to minimize the disturbances on the flow. The second set of supports is rotated 45° relative to the first set. The cross-section area of the shock tube is held constant through the inlet section and into the transformation section and is then reduced by 50% in the test section.

The shock wave enters the test section radially through a sharp 90° bend and then the focusing and reflection process takes place. The test section has glass windows to enable visualization of the focusing and reflection process.

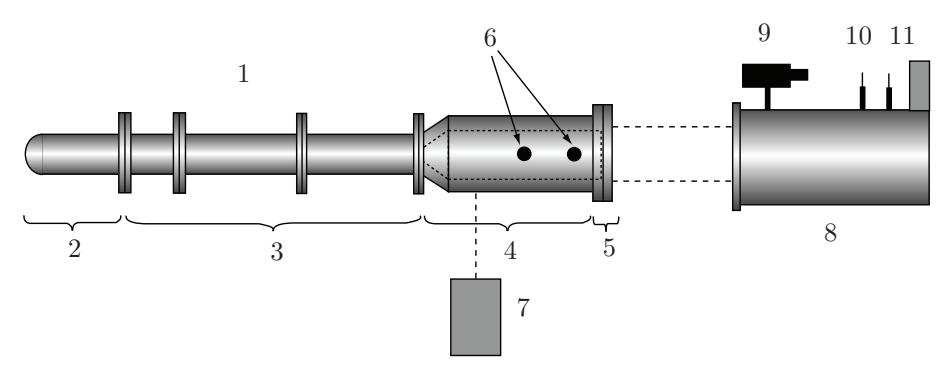


Figure 1: Schematic overview of the experimental setup: 1. shock tube, 2. high pressure chamber, 3. low pressure channel: inlet section, 4. low pressure channel: transformation section, 5. low pressure channel: test section, 6. shock speed sensors, 7. laser, 8. schlieren system, 9. CCD camera, 10. lens, 11. schlieren edge.

The outer boundary of the test section is circular with a radius of 80 mm. The width of the air gap in the test section, between the two facing glass windows, is 5 mm.

The present experimental study uses air as gas in both the high and low pressure part of the tube. The pressure in the low pressure channel is 13.3 kPa and in the high pressure chamber about 1500 kPa. This pressure difference produces strong shocks at Mach number  $M_s=2.3$ , measured in the annular part of the shock tube before the shock wave enters the test section. Further details of the experimental setup can be found in Eliasson *et al.* (2006).

### 2.1. Method to create polygonally shaped converging shock waves

A polygonally shaped converging shock wave is created by disturbing the shape of the initially cylindrical converging shock wave. The disturbances are produced by small metal cylinders placed inside the test section. Depending on the size and the positions of the cylindrical obstacles it is possible to tailor the shape of the cylindrical converging shock wave into a desirable polygonal shape, as shown in Eliasson  $et\ al.\ (2007)$ . Two different diameters of cylinders are used in this experiment, 10 mm and 15 mm, see Fig. 2 (a). They are placed at two radial positions,  $r_1=46.5$  mm and  $r_2=61.5$  mm. Two different geometrical setups are used, an equilateral triangular and a square pattern, see Figures 2 (b) and (c).

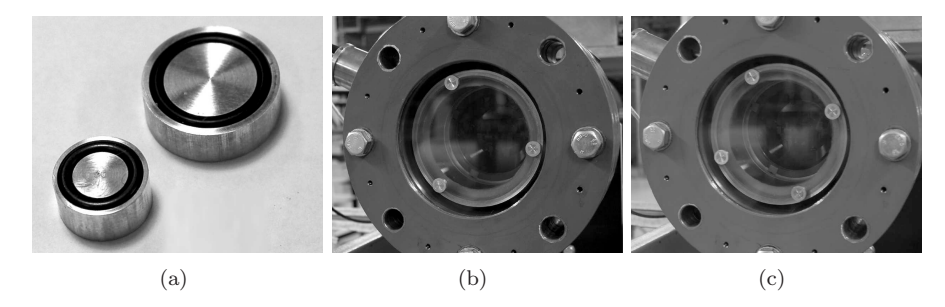


Figure 2: (a) Two sizes of cylinders were used, 10 and 15 mm in diameter. (b) The equilateral triangular pattern and in (c) the square pattern of cylindrical obstacles.

### 3. Experimental results

Two different geometrical shapes of shock waves are generated; triangular and square shaped shocks. To visualize the focusing process, the schlieren system together with the CCD camera is used to take single exposures at various time delays for each run in the shock tube. The reason for taking only one exposure during each run in the shock tube is due to limitations in the light source equipment and the CCD camera. The time delay unit, a Stanford Research System DG535, enables schlieren exposures of the converging and reflecting shock at different time instants inside the test section. The size of the visualized area is 75 mm in diameter. The repeatability is good and the error in the shock speed,  $U_s$ , between consequent runs in the shock tube is about 0.5%. The results from the various setups are presented and discussed in the following two sections.

#### 3.1. Diffraction of a cylindrical shock wave from three cylinders

Three cylinders with diameters of 15 mm are placed inside the test section in an equilateral triangular pattern, see Fig. 2 (b), at a radial position of  $r_1=46.5$  mm. Schlieren photographs showing the convergence process of the diffracted shock wave are shown in Fig. 3. Each photograph is from an individual run in the shock tube and  $M_s$  is 2.3. In the beginning, the shock wave has a hexagonal shape, see Figs. 3 (a) – (c), consisting of the disturbed plane parts and undisturbed convex parts. The plane parts are Mach shocks, formed after the shock is diffracted over the cylindrical obstacle. The undisturbed parts will decrease and finally disappear as the focusing process continues; hence the shape of the shock wave becomes triangular, see Fig. 3 (d). In this frame the sides of the triangle are not planar but slightly curved.

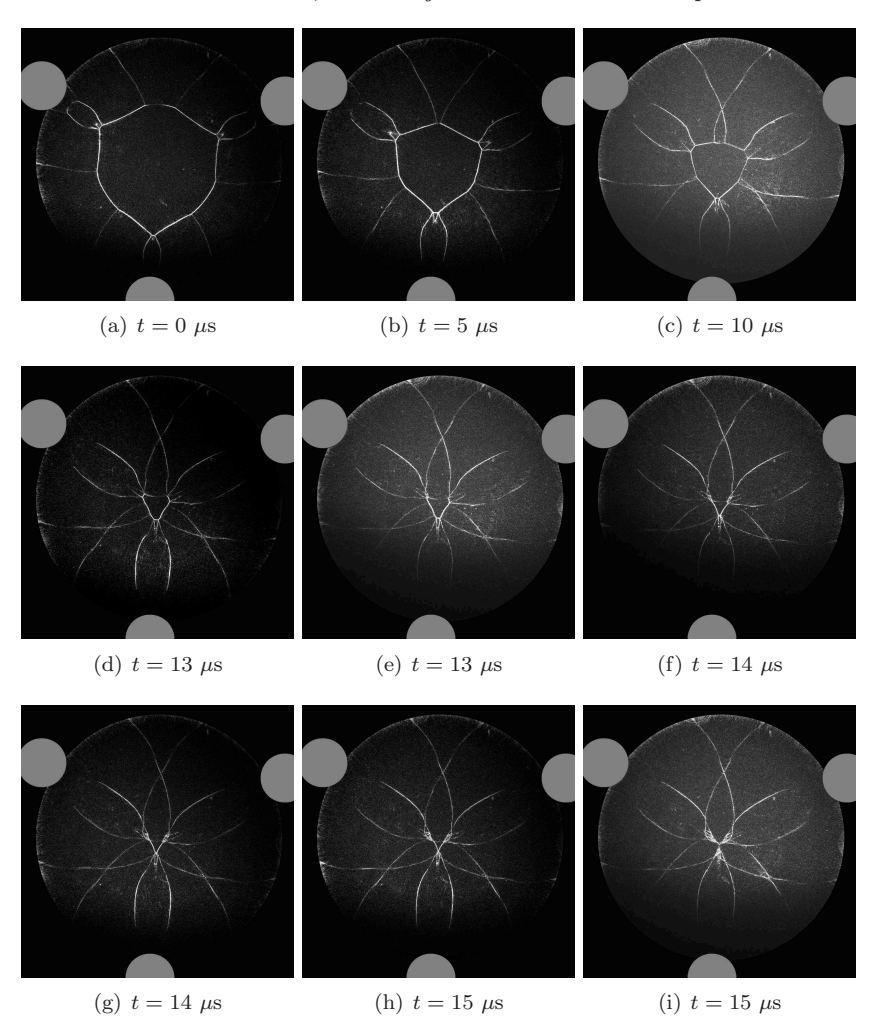


Figure 3: Schlieren photographs at different time instants. Each photograph is from an individual run in the shock tube. The cylindrical shock wave is diffracted over three cylinders with diameters of 15 mm placed at r=46.5 mm from the convergence center. The grey circles represent the cylinders.

As the shock wave approaches the center of convergence, the sides eventually become planar, see Figs. (d) – (f). Due to the angle between the reflected sides, the incident angle, and the shock Mach number, a regular reflection occurs at the corners of the triangle and the triangular shape remains unaltered until it has focused completely, see Figs. 3 (g) – (i). There are three pairs

of photographs, (d) and (e), (f) and (g) and (h) and (i), that are taken at the same time instant but are slightly different in position. This is due to the fact that each shock is from an individual run in the shock tube and that will produce small variations in the conditions, thus showing the same time instants but slightly different positions. This is more pronounced closer to the center of focusing since the shock waves move faster there.

In the next experimental setup, the three cylinders are moved to the second radial position,  $r_2 = 61.5$  mm, outside the frame of the visualized area, and then the above described experiment is repeated. Schlieren images are shown in Fig. 4. The converging shock wave behavior is similar to the previous case. In addition, two photographs of the reflected shock wave are shown in Figs. 4 (h) and (i). In (h), the outgoing shock wave has a somewhat disturbed triangular shape. Later, the reflected shock wave becomes influenced by the still incoming flow, and the shape changes into a shape that resembles the shape of the ingoing shock wave in an early stage, as the one shown in (a). The shock shape in (i) is less hexagonal and more cylindrical than the shock wave in (a). In Eliasson et al. (2006), the reflected shock wave first had a cylindrical shape that later became influenced by the incoming flow and changed into a shape that was similar to the shape of the converging shock wave in an early stage.

In the third experiment, the 15-mm diameter cylinders in the previously mentioned setup are replaced by 10-mm diameter cylinders. Schlieren photographs can be seen in Fig. 5. Compared to the previous case, it is seen that the Mach stem is more pronounced in an earlier stage for this setup. The overall shape of the shock wave is less disturbed than in the previous case, it is more cylindrical than hexagonal. Still, as the shock wave converges it attains a triangular shape and when that shape is reached it does not change, rather it decreases until it has reached the center of focus.

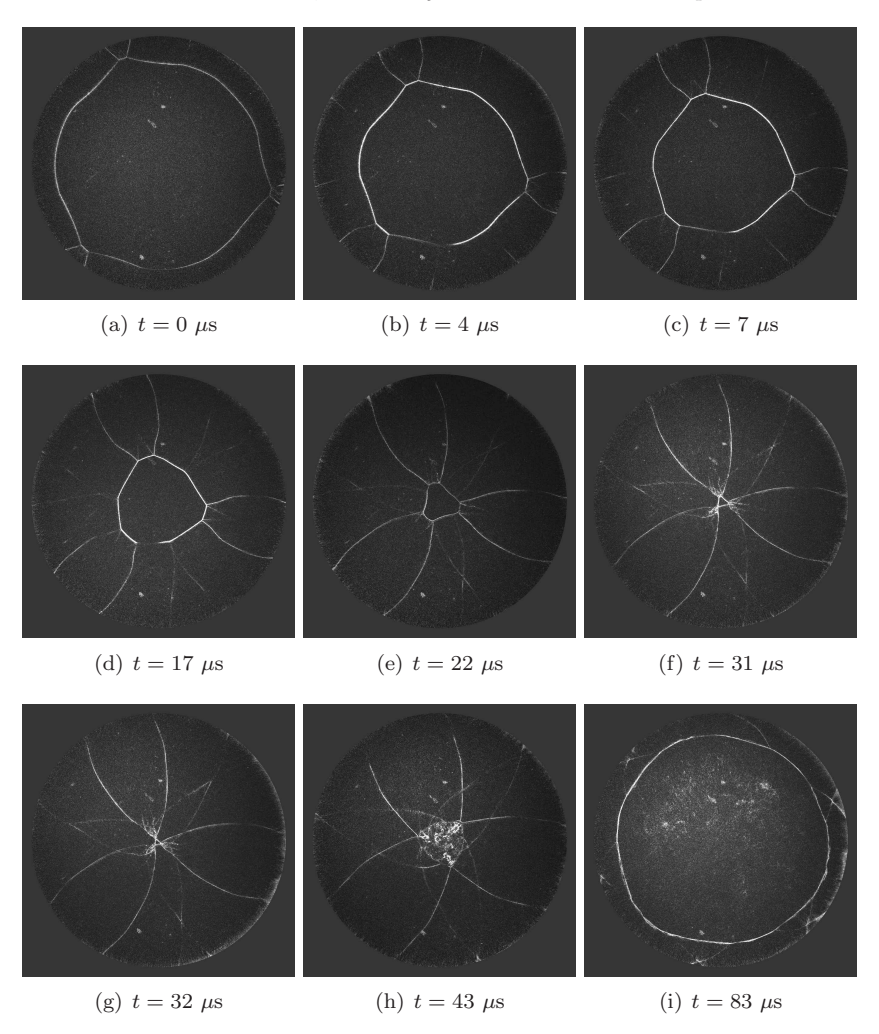


Figure 4: Schlieren photographs at different time instants. Each photograph is from an individual run in the shock tube. The cylindrical shock wave is diffracted over three cylinders with diameters of 15 mm placed at r=61.5 mm from the convergence center.

# 3.2. Diffraction of a cylindrical shock wave from four cylinders

For a square shaped shock in air, the angle of incidence is  $\pi/4$  and according to the detachment criterion, see Betelu & Aronson (2001), a regular reflection will be possible only for  $M_s \leq 1.24$ . An increase in Mach number will always

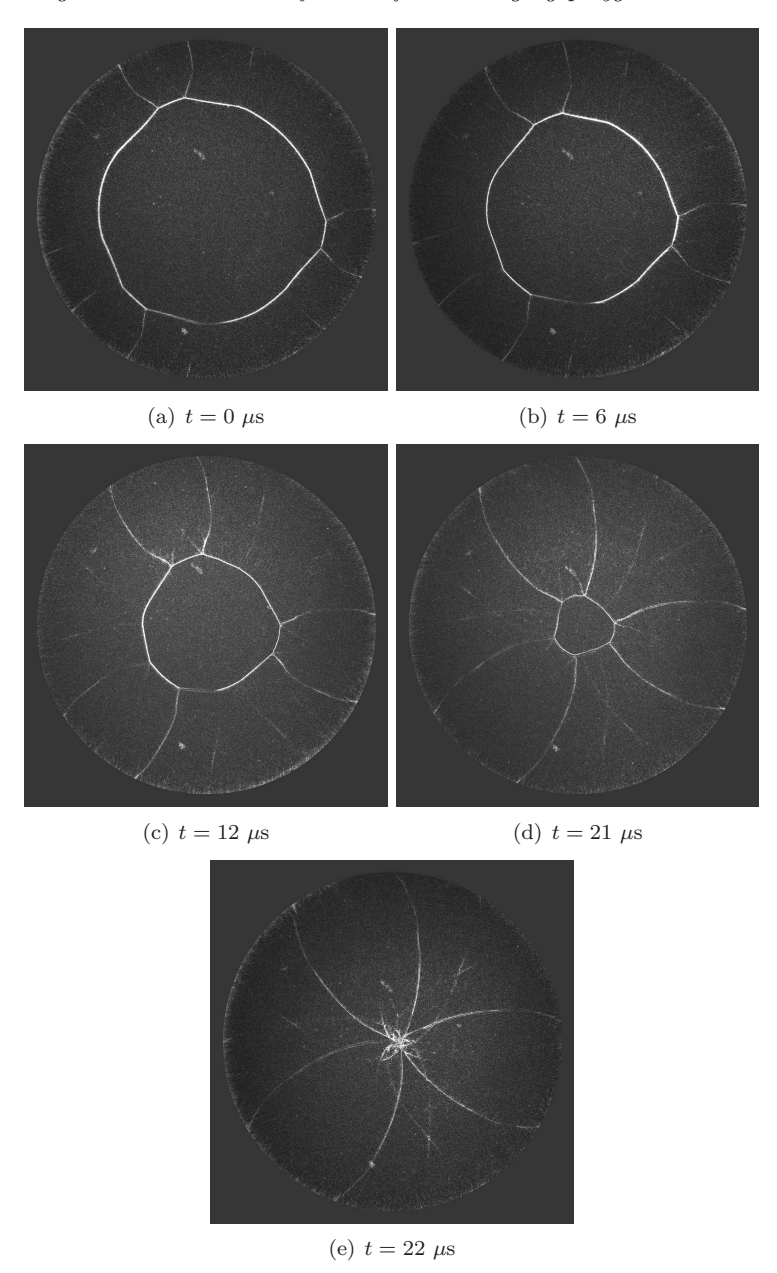


Figure 5: Schlieren photographs at different time instants. Each photograph is from an individual run in the shock tube. The cylindrical shock wave is diffracted over three cylinders with diameters of 10 mm placed at r=61.5 mm from the convergence center.

end with Mach reflection at the corners of the polygonal shock wave and hence the previously mentioned reconfiguring process will take place.

Four cylinders are positioned as the corners in a square, at a radial position of  $r_2 = 61.5$  mm, and then the above mentioned experiments are repeated. The Mach number used in the present study,  $M_s = 2.3$ , is higher than the limiting value for a regular reflection, resulting in a Mach reflection at the corners of the square shaped shock wave during the focusing process. Earlier results (Eliasson et al. (2007)), also using Mach numbers higher than the limiting value for a regular reflection, show that when a converging shock wave obtains a square-like shape it will reconfigure between a square and an octagon during the focusing process. In Fig. 6, schlieren photographs are shown for the setup with 15 mm diameter cylinders. In Fig. 6 (a), the shock wave has just reached the visualization area and the undisturbed parts still remain cylindrical. Thereafter the shock wave approaches a square-like shape, shown in Figs. 6 (b) – (c). The sides of the square are divided into several shorter pieces, that together produce an almost planar side, see (c). The individual pieces constructing one side originate from the undisturbed part of the shock wave in between two Mach stems emanating from the diffraction over the cylindrical obstacle. As the convergence process continues, the sides of the square blend into one slightly curved smooth part. Later, the slightly curved sides become planar and Mach stems are formed at the corners. At this time the reconfiguring process starts. The Mach stems at the corners can be seen in Fig. 6 (g) and an octagonal shape is seen in (h). The first cycle of the reconfiguration process is ended when a square shaped shock wave with an orientation opposite to (d) - (g) is formed as shown in (i).

In Fig. 7 three images from the case with 10 mm diameter cylinders are shown. The behavior is similar to the previous case meaning the shock wave will first develop planar sides and then start to reconfigure and change orientation. The last image, (c), shows the first reoriented shock wave. Whether the last visible shock wave originates from the disturbance caused by the four cylinders or by the four supports located at the rear part of the annular part in the shock tube has been investigated. The square formation of cylinders is rotated angularly compared to the four supports to make sure that it is possible to tell which one is acting as disturbance generator. The orientation of the square shaped shock wave, visible in the last stage of the focusing process, tells us that it is the disturbance from the four cylinders that is responsible for the shape of the shock wave. It has been shown earlier that the supports for the annular parts of horizontal shock tubes cause disturbances that are visible when the shock wave is close to the center of convergence, see Takayama et al. (1984, 1987); Watanabe & Takayama (1991).

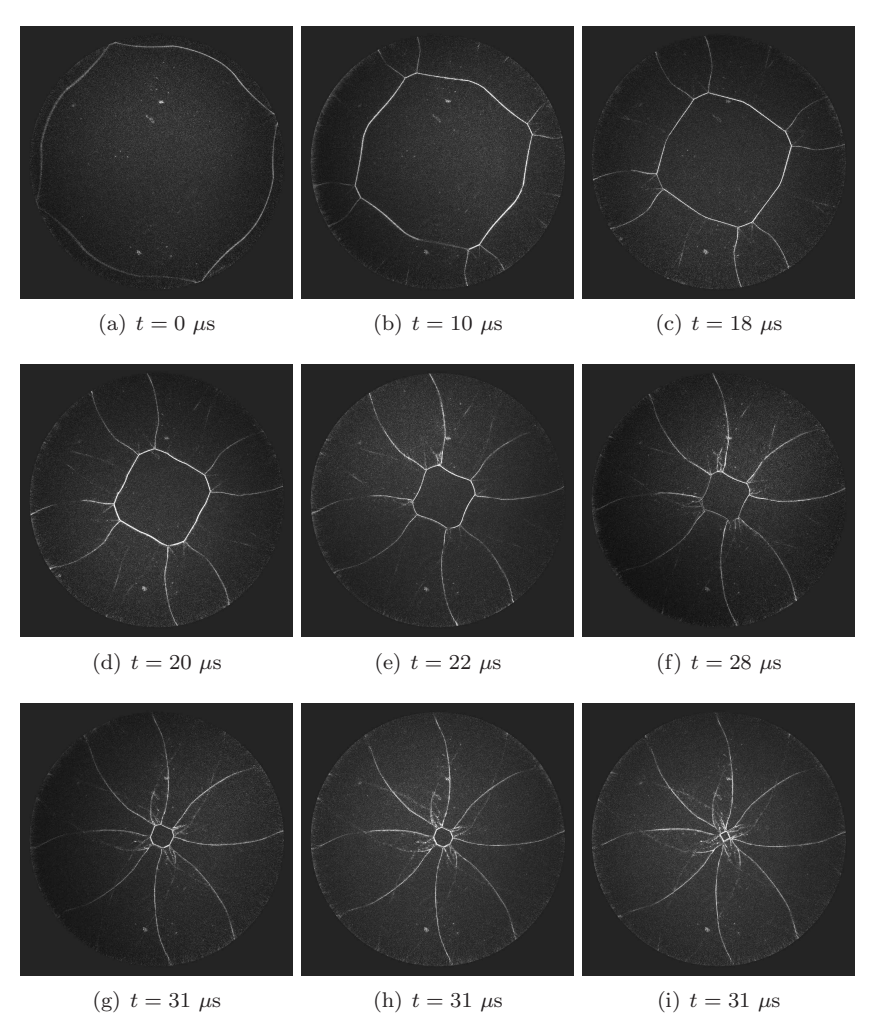


Figure 6: Schlieren photographs at different time instants. Each photograph is from an individual run in the shock tube. The cylindrical shock wave is diffracted over four cylinders with diameters of 15 mm placed at r=61.5 mm from the convergence center.

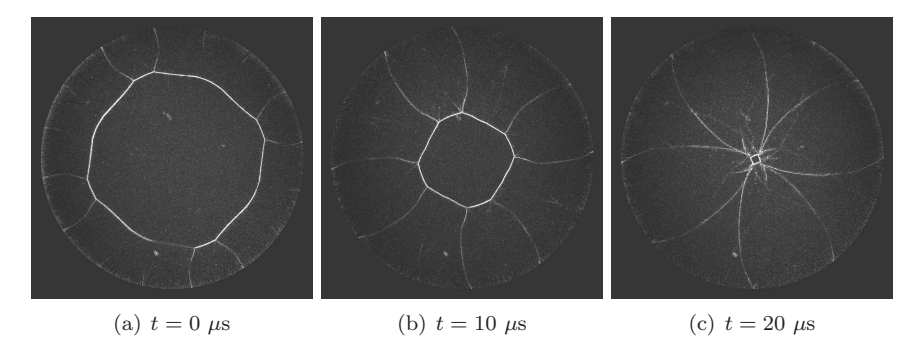


Figure 7: Schlieren photographs at different time instants. Each photograph is from an individual run in the shock tube. The cylindrical shock wave is diffracted over four cylinders with diameters of 10 mm placed at r=61.5 mm from the convergence center.

#### 4. Conclusions

An experimental investigation of converging triangular and square shaped shock waves was performed in an annular horizontal shock tube. A schlieren system combined with a CCD camera was used to visualize the focusing process. The system took snapshots of the converging shock wave at different time instants. An initially cylindrical converging shock wave was perturbed by cylindrical obstacles inside the test section. The obstacles were configured in an equilateral triangular or a square formation. As a result two different types of shock convergence behavior were observed. In a triangular case, a triangle-shaped shock was formed and converged with unaltered form and orientation during the rest of the focusing process, indicating that the vertices of the triangle undergo regular reflection. A square formation produced a square-like shock. The corners of the shock suffered Mach reflection and a reconfiguring process took place. After one cycle a new square, oriented opposite to the old one was formed. The present experimental results complement previous results, both analytical and numerical, see Betelu & Aronson (2001), Schwendeman & Whitham (1987) and Apazidis & Lesser (1996).

is not resolved in the present experimental setup. This would require a resolution of a wide range of length scales, which was not possible at the moment of this experiment.

#### Acknowledgements

We would like to thank Prof. P. H. Alfredsson for financial support during this work. The authors would also like to thank Mr Ulf Landén at KTH Mechanics for careful construction of the cylindrical obstacles. Our sincere thanks to

Dr. Nils Tillmark for help and advice during the setup of the experiment. The funding from the Göran Gustafsson Foundation provided means for the construction of the shock tube and for acquisition of the experimental equipment which is gratefully acknowledged.

# References

- APAZIDIS, N. & LESSER, M. B. 1996 On generation and convergence of polygonal-shaped shock waves. J. Fluid Mech. 309, 301–319.
- APAZIDIS, N., LESSER, M. B., TILLMARK, N. & JOHANSSON, B. 2002 An experimental and theoretical study of converging polygonal shock waves. Shock waves 12, 39–58.
- BARBOSA, F. J. & SKEWS, B. W. 2002 Experimental confirmation of the von neumann theory of shock wave reflection transition. *J. Fluid Mech.* 472, 263–282.
- BEN-DOR, G. 1992 Shock wave reflection phenomena. Springer-Verlag New York Inc.
- Ben-Dor, G. 2006 A state-of-the-knowledge review on pseudo-steady shock-wave reflections and their transition criteria. *Shock Waves* 15, 277–294.
- Betelu, S. I. & Aronson, D. G. 2001 Focusing of noncircular self-similar shock waves. *Phys. Rev. Letters* 87, 3058–3068.
- ELIASSON, V., APAZIDIS, N. & TILLMARK, N. 2007 Controlling the form of strong converging shocks by means of disturbances. *Shock Waves* 17, 29–42.
- ELIASSON, V., APAZIDIS, N., TILLMARK, N. & LESSER, M. B. 2006 Focusing of strong shocks in an annular shock tube. *Shock Waves* **15**, 205–217.
- GUDERLEY, G. 1942 Starke kugelige und zylindrische Verdichtungsstöße in der Nähe des Kugelmittelpunktes bzw. der Zylinderachse. Luftfahrtforschung 19, 302–313.
- HORNUNG, H. G., OERTAL, H. J. & SANDEMAN, R. J. 1979 Transitions to mach reflection of shock waves in steady and pseudo steady flow with and without relaxation. *J. Fluid Mech.* **90**, 541–560.
- VON NEUMANN, J. 1943  $Collected\ Works\ VI.$  Pergamon, New York.
- Schwendeman, D. W. 2002 On converging shock waves of spherical and polyhedral form. J. Fluid Mech. 454, 365–386.
- SCHWENDEMAN, D. W. & WHITHAM, G. B. 1987 On Converging Shock Waves. *Proc. R. Soc. Lon. A* 413, 297–311.
- TAKAYAMA, K., KLEINE, H. & GRÖNIG, H. 1987 An experimental investigation of the stability of converging cylindrical shock waves in air. Exps. Fluids 5, 315–322.
- TAKAYAMA, K., ONODERA, O. & HOSHIZAWA, Y. 1984 Experiments on the stability of converging cylindrical shock waves. *Theor. Appl. Mech.* **32**, 305–329.
- WATANABE, M. & TAKAYAMA, K. 1991 Stability of converging cylindrical shock waves. Shock Waves 1, 149–160.

4

# Polygonal shock waves: comparison between experiments and geometrical shock dynamics

# By Malte Kjellander, Nils Tillmark and Nicholas Apazidis

Department of Mechanics, Royal Institute of Technology, SE-100 44 Stockholm, Sweden

In proceedings 28th International Symposium on Shock Waves, 2011, University of Manchester, Manchester, United Kingdom

The propagation of converging polygonal shock waves are documented using schlieren photography in order to compare with geometrical shock dynamics. Shock waves shaped as symmetric polygons of 6, 8 and 12 sides are created in a shock tube. The results are compared with the theoretical predictions and show good agreement.

## 1. Introduction

The propagation of converging polygonal shocks was studied theoretically and numerically by Schwendeman & Whitham (1987). Using the approximate theory of geometrical shock dynamics (GSD), they found solutions of the behaviour of cylindrical polygonal shock waves. They showed that an initial polygonal shape repeats at different intervals during the converging process. We have conducted experiments creating similarly shaped shock waves and compared with their work.

Polygonal shocks have been studied previously at the department of Mechanics, (Apazidis & Lesser 1996; Apazidis  $et\ al.\ 2002$ ; Eliasson  $et\ al.\ 2007a,b$ ) using different measured to control the shape of the shock. The method to shape the shocks in the present work was used in spectrometric investigations (Kjellander  $et\ al.\ 2010$ ). The measurements required good repeatability and the polygonal shocks proved to be more stable from run to run. However, we found the peculiar behaviour of the re-orienting polygons interesting enough in itself to warrant some additional study. The purpose with this paper is to present results on the dynamics of the shocks and how they stand a comparison with GSD.

### 2. Theory

This section is a short summary of the paper by Schwendeman & Whitham (1987), which is recommended for further reading. In the strong shock approximation, the area-Mach number relation becomes

$$A = f(M) \propto M^{-n},\tag{1}$$

where n = 5.074 for  $\gamma = 1.4$ . The predicted behaviour of a converging shock wave is displayed in Fig. 1(a). The initial shock wave consists of a number of plane fronts of strength  $M_0$  making up a polygon, here a hexagon. At each corner the plane sides reflect against each other, with Mach stems appearing at the intersections. These will move with a stronger Mach number  $M_1$  and eventually form a new polygon rotated with the angle  $\angle$ BON whereupon the process starts over. The converging process is equivalent for other polygons where Mach reflections occur in the corners. A triangular shock experiences regular reflection; this has been subjected to studies by Betelu & Aronson (2001), Eliasson et al. (2007b). Reflected shocks also appear, but for the sake of brevity they will be ignored for the length of this work.

The increase in Mach number at each repeated interval P was shown to be, with P = 0 being the initial polygon:

$$\frac{r_P}{r_0} = \left(\frac{M_0}{M_P}\right)^n \tag{2}$$

The radii  $r_P$  are measured from the centre to the side mid-points, and not to the vertices. Further, the Mach number ratios can be expressed as:

$$\frac{M_P}{M_0} = \mu^P,\tag{3}$$

where the constant  $\mu$  is dependent on the number of sides in the polygon. Values for  $\mu$  obtained by Schwendeman & Whitham are tabulated in Table 1 at the end of the paper.

#### 3. Experiment

The experiments were performed in the same shock tube facility as the previously conducted studies at KTH Mechanics cited above. The experimental setup is illustrated in Fig. 2. The tube is a plane-annular-cylindrical construction akin to that of Takayama et al. (1987), designed to create cylindrically converging shocks. A co-axially aligned inner body transforms the incoming plane shock wave into an annular shape. The annular channel ends into a chamber with a sharp  $90^{\circ}$  bend. The test section consists of the central part of the chamber which is framed on both sides by glass windows.

A conventional parallel-light schlieren system was used for visualisation. Light is provided with either an Nd:YAG pulse laser or a continuous HeNe

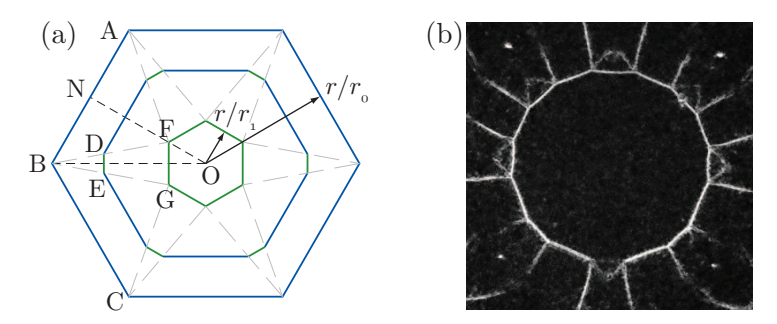


Figure 1: (a) Converging process of hexagonal shock wave, after Schwendeman & Whitham (1987). The plane shocks AB and BC of Mach number  $M_0$  reflect against one another, forming the Mach stem DE. DE propagates at a higher Mach number  $M_1$ , overtaking the adjoining shocks and eventually forming the side FG in a new hexagon, P=1. Image (b) Shows a schlieren image of the middle step illustrated in (a), of an octagonal shock (detail from Kjellander et al. 2010).

laser. A metal sphere with a diameter of 0.67 mm is used as a schlieren stop and photographs taken with a SensiCam PCO CCD camera or a Nikon D80 system camera. The SensiCam allows images to be taken with several individual exposures. The continuous HeNe laser is comparatively weak, resulting in relatively long individual exposures, around 0.2  $\mu$ s. The shock Mach number was measured in the annular channel by two platinum film temperature sensors. These are inserted flush with the outer wall of the channel, separated by 25 cm.

To form the shock wave into the desired polygonal forms, the test section has been divided into separate radial channels. Shaped as circular segments, 50 mm long, flow dividers were inserted with their centre lines aligned radially. The outer edges are touching the annular channel entering the test section, and the inner edges ends 20 mm from the centre. Through reflections and change of curvature due to the wing-shaped dividers, the initially curved shock is divided into straight segments at the exit of the radial channels. This method was used in Kjellander et al. (2010), where more details may be found. A drawing of the layout of the test section with an octagonal configuration of flow dividers is provided in Fig. 2(b).

#### 4. Results and Discussion

Symmetric polygonal shock waves with six, eight and twelve sides were generated. Test gas was air and the initial low pressure was  $p_1$ =13.3 kPa. Shock strength was M=2.4 in the annular channel. As the shocks waves reached the

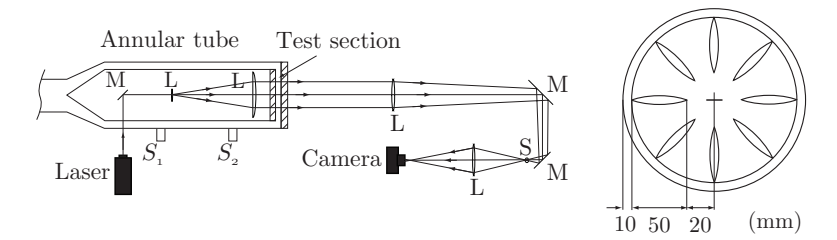


Figure 2: Experimental setup: (a) sketch of the end of the shock tube and the schlieren setup. L, lens, M, mirror and S, the schlieren stop.  $S_1$  and  $S_2$  are the shock sensors. Image (b) shows a sketch of the test section from the front with an octagonal channel configuration.

trailing edges of the flow dividers in the test section, they had accelerated to  $M{=}3.0$ . A series of stronger shocks were made with the twelve-sided configuration, with  $M{=}3.0$  in the annular section and  $M{=}4.9$  at the trailing edges. The Mach number at the edges becomes the initial Mach number of the sides making up the first, starter polygon. Single and multiple exposure schlieren photographs were taken to study the dynamics.

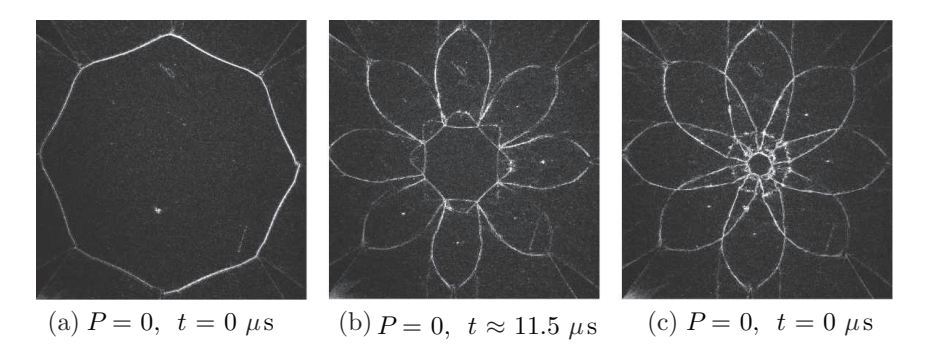


Figure 3: Schlieren photographs of octagonal shocks.

Figure 3 shows three polygonal shock waves at different times with a configuration of eight wings. In image (a) the shock wave has just passed the trailing edges and each side started reflecting against the adjoining sides. This corresponds roughly to the first iteration of the octagon, P=0. The Mach number of the incident shock is  $M_0=3$ . In the second image the appearing Mach stems have overtaken the incident shocks and the front retaken an octagonal shape, rotated by  $22.5^{\circ}$ . New small Mach stems have already appeared. The process

is repeated and a third octagon, interval P=2, appears, now reoriented with the vertices in the same positions as the original. The shape of the shock is not entirely symmetric, which is most visible in the perturbed front in (b). The photograph in Fig. 1(b) is an intermediate step between Fig. 3(a) and (b).

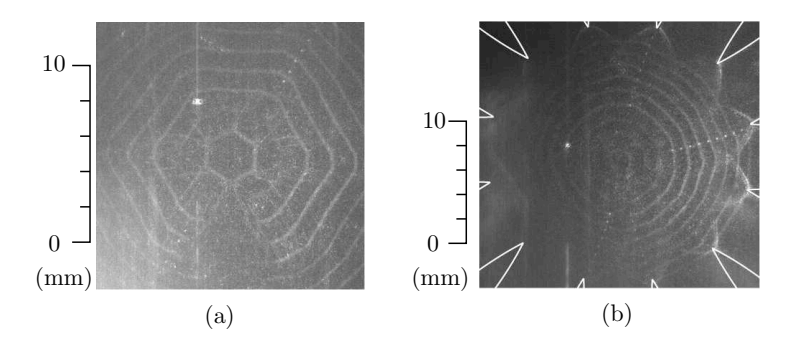


Figure 4: Multiply exposed schlieren images of hexagonal (a) and dodecagonal (b) shock waves. The wings have been outlines in (b), while they are off the picture in (a). For the two cases, the time between each exposure was 1.8  $\mu$ s and 1.4  $\mu$ s, respectively, while each exposure was 0.3  $\mu$ s, in both cases.

Figure 4 shows multiple-exposure photos of initially six- (a) and twelve-sided (b) shocks. The radius and Mach-number variation with radius were deduced from photographs exposed at ten different intervals  $0.8\text{-}1.8~\mu\mathrm{s}$  apart, with each exposure being  $0.1\text{-}0.3~\mu\mathrm{s}$  long. Figure 5(a) shows the radius of two dodecagonal shock waves of different initial Mach numbers. The radii were measured along two diagonals, one between the focal point and an initial vertex and another between the centre and an initial side midpoint (corresponding to lines ON and OB in Fig. 1), thereby showing the propagation of the initial and new sides corresponding to AB and DE. Different symbols have been used in the figure to clarify when reflections occur: each symbol is used for one side from its creation until it is completely overtaken by the adjoining shocks. The fronts had almost constant velocity until reflection. For example, the circles represent the position of original incoming shock front AB propagating from N to F, again referring to Fig. 1.

As the individual parts of the shock were not accelerating, the acceleration of the overall shock took part through reflections where faster shocks appeared. This is a slight simplification, as the supposedly straight shocks always have a small curvature and not entirely constant velocity. As this effect was visibly small, linear fits were made to determine  $M_0, M_1, M_2$  and  $M_3$ , the Mach numbers of each successive iteration. The twelve-sided shape experienced more recognisable iterations than the other configurations. In the octagonal case,

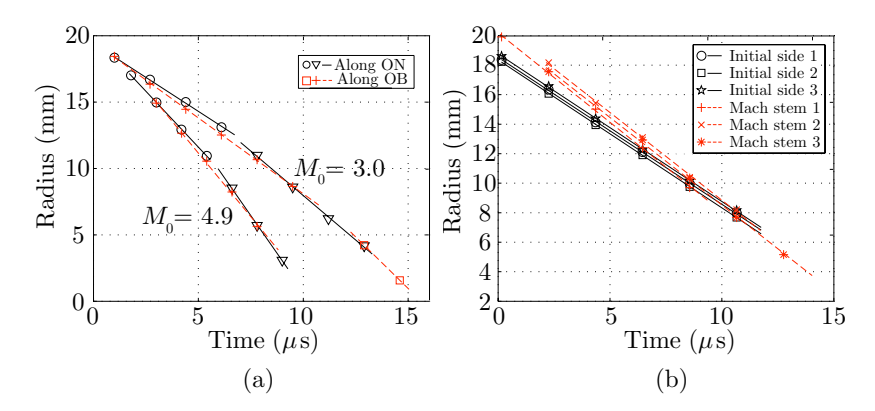


Figure 5: (a) Position of converging dodecagonal shock waves of two different initial Mach numbers,  $M_0=3.0$  and  $M_0=4.9$ . The radial position along two diagonals, ON and OB, are plotted, see Fig. 1. (b) Radius of different segments of the same octagonal shock wave. Full lines: initial sides, dashed lines: new sides appearing through the Mach reflections. The lines are best fits to the different segments.

N	$\mathrm{GSD}^1$	This paper		
6	1.289	<del>-</del>		
8	1.201	$1.21 \pm 0.03  M_0 = 3.0$		
12	1.126	1.14 $\pm$ 0.04 $M_0 = 3.0$ 1.15 $\pm$ 0.04 $M_0 = 4.9$		

Table 1: Table over values of  $\mu = M_{P+1}/M_P$  for polygons with number of sides N. No meaningful experimental value for N=6 could be obtained.

Mach numbers up to  $M_2$  could be measured. Table 1 shows the obtained values compared to the theoretical. The experimental values are averaged over all available ratios  $M_{p+1}/M_p$ , several runs and along three sides for each run. Figure 5(b) demonstrates the variation in one single run. The hexagonal case was problematic: the shock fronts were far from straight when arriving in the test section. The flow dividers were too short for straight shocks to form. This means that a quantitative comparison with the idealised case is not reasonable and no computation of the ratios were performed.

The degree symmetry of the shock waves was highly sensitive to the inner body alignment. This initial asymmetry may be seen in Figs. 3(a) and 4(b),

<sup>&</sup>lt;sup>1</sup>Schwendeman & Whitham (1987)

where vortices created during the shear at the trailing edge are seen. Care was taken to align the body to produce as symmetric shock shapes as possible. During the presented experiments, the initial relative deviation from the radius, measured as  $(r_{i,max} - r_{i,min})/\overline{r_i}$ , where  $r_i$  is the radius of the sides i making up the polygon, was about 3%. We believe it is possible to gain better symmetry, but this was deemed adequate for our purposes. It is also possible to use the flow dividers as a test of symmetry, also when circular shock waves are to be studied. In any case, to avoid effect of asymmetry, the quantitative results of the radius and Mach number ratios were only taken from sections where adjacent shocks arrived in the open section at virtually the same instant.

#### 5. Conclusions

Converging polygonal shock waves were studied using schlieren optics. The octagonal and dodecagonal shapes showed the predicted alternating pattern, but the hexagonal shape was not achieved due to how the flow dividers were constructed. The dynamic process of the alternating polygons were observed and the Mach number increase measured and compared with geometrical shock dynamics, showing reasonable agreement. Slightly higher values for  $\mu$  was found experimentally than theoretically, but the error of margin is too large to draw any conclusions. Increasing the Mach number showed no significant change.

# References

- APAZIDIS, N. & LESSER, M. B. 1996 On generation and convergence of polygonal-shaped shock waves. *J. Fluid Mech.* **309**, 301–319.
- Apazidis, N., Lesser, M. B., Tillmark, N. & Johansson, B. 2002 An experimental and theoretical study of converging polygonal shock waves. *Shock waves* 12, 39–58.
- Betelu, S. I. & Aronson, D. G. 2001 Focusing of noncircular self-similar shock waves. *Phys. Rev. Letters* 87, 3058–3068.
- ELIASSON, V., APAZIDIS, N. & TILLMARK, N. 2007a Controlling the form of strong converging shocks by means of disturbances. Shock Waves 17, 29–42.
- ELIASSON, V., KJELLANDER, M. & APAZIDIS, N. 2007b Regular versus mach reflection for converging polygonal shocks. Shock Waves 17, 43-50.
- KJELLANDER, M., TILLMARK, N. & APAZIDIS, N. 2010 Thermal radiation from a converging shock implosion. *Phys. Fluids* **22**, 046102.
- SCHWENDEMAN, D. W. & WHITHAM, G. B. 1987 On Converging Shock Waves. Proc. R. Soc. Lon. A 413, 297–311.
- TAKAYAMA, K., KLEINE, H. & GRÖNIG, H. 1987 An experimental investigation of the stability of converging cylindrical shock waves in air. Exps. Fluids 5, 315–322.

5

# Experimental determination of self-similarity constant for converging cylindrical shocks

# By Malte Kjellander, Nils Tillmark and Nicholas Apazidis

Department of Mechanics, Royal Institute of Technology, SE-100 44 Stockholm, Sweden

Published in Physics of Fluids 23, 116103 (2011)

Guderley's self-similarity solution  $r = r_0(1 - t/t_0)^{\alpha}$  for strong converging cylindrical shocks is investigated experimentally for three different gases with adiabatic exponents  $\gamma = 1.13; 1.40; 1.66$  and various values of the initial Mach number. Corresponding values of the similarity exponent  $\alpha$  which determines the strength of shock convergence are obtained for each gas thus giving the variation of  $\alpha$  with  $\gamma$ . Schlieren imaging with multiple exposure technique is used to track the propagation of a single shock front during convergence. The present experimental results are compared with previous experimental, numerical and theoretical investigations.

#### 1. Introduction

The first study on converging shock waves was performed by Guderley (1942), who presented his well-known self-similarity solution of strong converging cylindrical and spherical shock waves close to focus. The solution for the shock radius r at a certain time t may be written in the self-similar form: r = $r_0(1-t/t_0)^{\alpha}$ , where  $r_0=r(t=0)$  and  $t_0=t(r=0)$  are the initial radius and time of implosion, respectively. The similarity constant  $\alpha$  determines the strength of convergence, or equivalently the curvature of the r-t trajectory. The constant  $\alpha$ , which depends on the adiabatic exponent  $\gamma$  is in general a rational number which Guderley determined to be  $\alpha \approx 0.835$  for cylindrical and  $\alpha \approx 0.717$  for spherical shock waves in air. A great number of analytical and numerical studies have since followed, expanding the solution and refining the calculated convergence exponent with an increasing number of digits (Butler 1954; Stanyukovich 1960; Fujimoto & Mishkin 1978; Nakamura 1983; Hafner 1988; Van Dyke & Guttman 1982; Ponchaut et al. 2006). Lazarus & Richtmyer (1977) provided solutions to a wide range of adiabatic exponents, which was even further expanded by Lazarus (1981).

Approximate geometrical methods neglecting the influence of the flow behind the shock wave were developed independently by Chester (1954), Chisnell

(1957) and Whitham (1957). The approach, often referred to as the CCW method, agrees well with Guderley's solution and provides an explicit expression for  $\alpha = f(\gamma)$ . Finally, a comparison of the solutions of self-similar theory, geometric shock dynamics as well that of a numerical Euler solver was presented by Hornung *et al.* (2008), showing good agreement.

Experimental investigations to confirm the similarity constant have been fewer. The first cylindrically converging shocks were produced by Perry & Kantrowitz (1951) in a shock tube and many later works - including the present - made use of similar methods. Matsuo and collaborators (Matsuo & Nakamura 1980, 1981) examined the converging shocks in air created by exploding shells in a cylindrical frame. Using ionization probing systems they compared the shock trajectories with Guderley's self-similar solution and found them to practically collapse but did not present a determination of the parameter from their data.

Baronets (1984) studied the formation and propagation of cylindrical shocks in argon and xenon ( $\gamma=1.66$ ) created by pulsed induction discharges in a cylindrical chamber. Using visual methods to acquire the trajectories of the shocks waves, he found that the self-similar parameter varied with shock velocity. Accordingly, wave speeds less than 2 km/s resulted in a linear propagation ( $\alpha=1$ ), whereas for higher velocities - about 6 km/s, the exponent approached the analytical 0.816. He also measured a self-similar exponent for diverging shocks created by a spark discharge, and found  $\alpha=0.84\pm0.02$  (Baronets 1994).

Takayama et al. (1987) conducted several experiments where cylindrical shock waves in two different shock tubes working on similar principle as that of Perry & Kantrowitz. They measured  $\alpha$  by doing least square fits to streak camera recordings of a shock waves in air ( $\gamma=1.4$ ) with initial Mach numbers in the range 1.1-2.1. They presented obtained values of 0.832+0.028/-0.043 for the tube in Aachen and  $0.831\pm0.002$  for the other tube, in Sendai.

Although the present paper is concerned with cylindrical shocks, it might be worth mentioning that Hosseini and Takayama found the exponent  $\alpha$ =0.738 for converging spherical shock waves in air. Shocks created at the center of a chamber diverged and reflected on the chamber wall and then converged. The discrepancy from the theoretical 0.717 was due to that the shocks converged through a flow field induced by the preceding diverging blast wave.

To the best of the authors' knowledge, no experiments have been published that have measured the self-similarity constant for different adiabatic exponents and Mach numbers in the same device. Guderley's solution is so frequently employed that this provided the motivation for the the present experiments, which aim to: i) capture the variation of  $\alpha$  with the adiabatic exponent  $\gamma$  and ii) to determine if  $\alpha$  depends on the shock Mach number. All experiments were performed in the same shock tube and three different gases were used: argon, nitrogen and propane. Schlieren photography was used to track the shock fronts and least square fits were made to the self-similar solution to

determine the similarity constant  $\alpha$  from the experimental data. To measure the instant of focusing the light emission of the shocked gas at the center of convergence was registered by a photomultiplier tube. As discovered by Perry & Kantrowitz, the converging shocks create high enough temperatures to make the gas emit light. Later studies, e.g. by Roberts & Glass (1971); Saito & Glass (1982); Matsuo et al. (1985); Eliasson et al. (2007); Kjellander et al. (2010), have shown that the light intensity displays a sharp peak at collapse, which in the present paper was used to set the focusing instant. The light emission is intriguing on its own merits, and the interested reader is referred to the cited papers.

## 2. Experiment

#### 2.1. Shock tube

A schematic drawing of the shock tube is shown in Fig. 1. The shock tube is made of steel and consists of a 0.35 m long driver section A and a 2 m long driven section, separated by a rupturable membrane. The driven section consists of several parts: an inlet pipe B (1.3 m long) with a 80 mm diameter circular cross section followed by a transformation section C (0.17 m), where the channel cross section changes from circular to annular, expanding the outer channel radius to 160 mm and a co-axial annular section, D (0.53 m) with a constant 10 mm clearance between the facing walls. The channel cross section area is constant throughout all sections. A cylindrical test chamber, E, where the shock moves radially towards the center is connected to the end of section D. The test section is 5 mm wide and framed by glass windows (Schott Borofloat 33) to give optical access to the shock focusing region. The central body of the annular section is held in place by 8 wing shaped support struts crossing the annular space. The struts are located in two flow axial-normal planes containing 4 struts each. The struts are separated 90° in the plane and the strut pattern is displaced 45° between the planes to minimize strut interference with the flow. The annular section also contains platinum film stripe sensors to measure the shock velocity.

#### 2.2. Flow visualization

A schlieren system, schematically drawn in Fig. 2 visualizes the flow in the test section. The light source in the experiments is a continuous He-Ne laser. The beam is led into the inner body of the annular section through one of the hollow support struts and expanded to a collimated beam passing through the test section and the glass window. On the receiving side the light is focused on a schlieren stop. To detect density gradients in the flow in all radial directions a metal micro sphere is used as a stop. Photographs are taken with a CCD camera (PCO SensiCam) electronically connected to the timing system. The

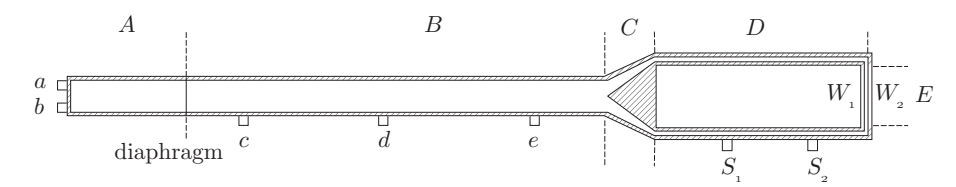


Figure 1: Schematic drawing of the shock tube. A: driver section, B: inlet pipe, C: transformation section, D: annular channel, E: test section, a: high pressure transducer port, b: driver gas inlet port, c: low pressure transducer port, d: test gas inlet port, e: vacuum pump port.  $S_1$  and  $S_2$ : shock sensors,  $W_1$  and  $W_2$ : glass windows framing the test section.

camera takes ten exposure in a single image, enabling tracking the single shock front.

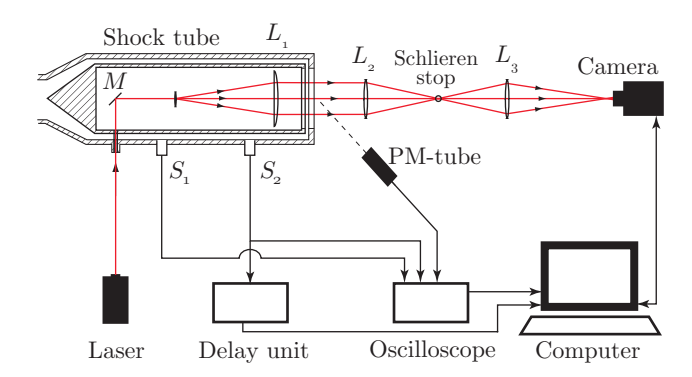


Figure 2: Arrangement of the schlieren optics. M: mirror,  $L_1$ : collimating lens,  $L_2$ : focusing lens f=1350 mm,  $L_3$ : imaging lens f=180 mm.  $S_1$  and  $S_2$  are the pressure sensors used for triggering and measuring the shock speed in the annular channel.

The shock sensor  $S_2$  (see Fig. 2) is connected to a digital delay generator (Stanford Research Systems DG535). The camera software handling the exposures receives a trigger signal from the delay unit. A digital oscilloscope records the signals from the sensors  $S_1$  and  $S_2$  to determine the shock speed. To measure the time of focusing a photomultiplier tube mounted close to the test chamber registers the light emitted by the imploding shock. When the shocks collapse the emitted light starts with a sharp peak indicating the focusing moment.

#### 3. Numerical calculations

Axisymmetric numerical calculations were performed to investigate the shock structure in the test section. Calculations were performed on two meshes: one representing the whole shock tube and a second finer mesh covering the end of the annular channel and the test section. Specifically we were interested in the influence of the transformation section from plane to annular and the 90° bend into the test section. The aim was to certify that a shock wave with constant strength is formed in the annular section and to asses the three-dimensional effects introduced by the bend into the test section.

The axisymmetric Euler equations were solved using the in-house numerical code. The code is based on the upstream flux vector splitting (AUFS) scheme introduced by Sun & Takayama (2003) for solving the Euler equations. The numerical scheme is implemented on an unstructured triangular mesh and enhanced by automatic mesh refinement and is able to cope even with most demanding boundary geometries including sharp corners and edges. The perfect gas law was used.

3.0a. Simulation 1: Full tube. These simulations were made for two reasons: (i) to provide initial conditions for the second simulation case and (ii) to verify that the experimental test cases created a stable shock wave with a constant velocity in the annular section, such that no expansion wave caught up with the front before entering the test section. The computational domain is sketched in Fig. 3. The number of grid cells were increased until solution convergence was reached. The computation was run until the shock reached the 90° bend and the test section was therefore not resolved. Final number of grid cells was about  $10^5$ . Initial conditions were set corresponding to experimental case \$1\$ through \$8\$, see Table 1.

The results showed that the shocks have the same strength in the annular section as in the circular section for all test cases. The Mach numbers from the simulations agree within 4% with those measured in the experiments and the strength of the shock waves were not changed significantly in the channel, indicating that the transformation section works as designed.



Figure 3: Bounded region for the axisymmetric simulation of the flow through the entire tube. The axis of symmetry is the dash-dotted line.

3.0b. Simulation 2: Test section. The domain of simulation is sketched in Fig. 4. The grid consists of about  $7 \times 10^5$  cells. This case is a continuation of the full tube simulation but with finer mesh - the initial conditions were taken from the full tube simulation for test case  $\sharp 4$ : when the shock wave was at the position corresponding to x=50 mm in Fig. 4, the results were interpolated to new domain. At x=0 supersonic inflow boundary conditions corresponding to the post-shock state were applied while the remaining boundaries were treated as solid walls. Figure 5 shows a series of numerical schlieren images at different time instants for a shock wave in nitrogen with incoming shock strength  $M_s=2.4$  in the annular channel. When the incoming shock front arrives at the bend, the inner (lower) part diffracts into the test section, while the outer (upper) part continues until it reflects against the rear wall, see Fig. 5 (i)-(ii). A high pressure zone is created behind the reflected shock.

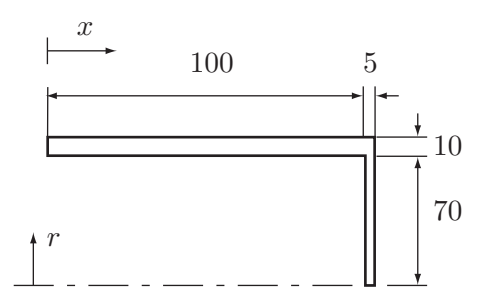


Figure 4: Bounded region for the axisymmetric calculation of shock focusing in the test section. The axis of symmetry is the dash-dotted line.

The reflected shock propagates at a higher velocity and overtakes and merges with the initial diffracted shock: this process is seen in Fig. 5 (iii) where the reflected and diffracted shocks are connected with triple point. When the reflected shock has completely merged with the diffracted shock - which is the same as saying that the triple point has reached the wall - Mach reflection occurs, see Fig. 5 (iii). The shock front is thus made up of two shocks with the triple moving back and forth between the walls transversally: the triple point is moving towards the right in (iv), towards the left in (v) and (vii) and is reflecting from the left wall in (vi).

As the front converges, the curvature decreases and the reflected waves behind it become weaker. In order to quantify the strength of the triple point and the reflected cross-directional wave, the difference between the pressures behind the two parts of the shock front - called  $p_A$  and  $p_B$  - was calculated in relation to the maximum pressure jump over the shock  $(p_i - p_1)$ . Figure 6 shows the results together with an idealized sketch explaining the designations. The sketch is a simplification of the physical situation: in fact there is not

only one but several crosswise waves behind the shock front - however, as one is much stronger than the others the weaker are therefore ignored. Initially, (at  $r\approx 65$  mm) the ratio is as large as 70% since  $p_A$  and  $p_B$  are taken as the pressures behind the diffracted and reflected shock, respectively. The value then decreases to an asymptotic value of 15%. The corresponding asymptotic ratio in Mach numbers of the two parts making up the shock front - called  $M_A$  and  $M_{B^-}$  is less than 10%.

Turning focus to the flow behind the shock wave: the induced flow into the test section is complex and driven by the large pressure increase caused by the reflected annular shock. Before the shock front reaches  $r\approx 40$  mm the flow in the whole section is changing rapidly, but once the shock has reached this

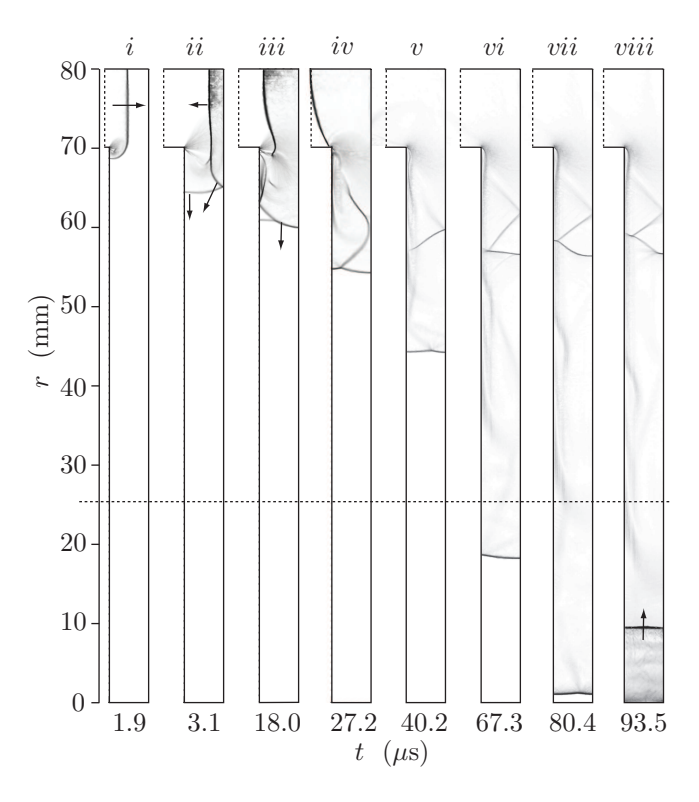


Figure 5: Numerical schlieren images of the converging shock pattern in the axisymmetric test section. Time in microseconds from entrance of shock into test chamber. The dashed line crossing the image shows where the start of the measurement section is in the physical shock tube. Image (viii) shows the diverging shock wave after focus.

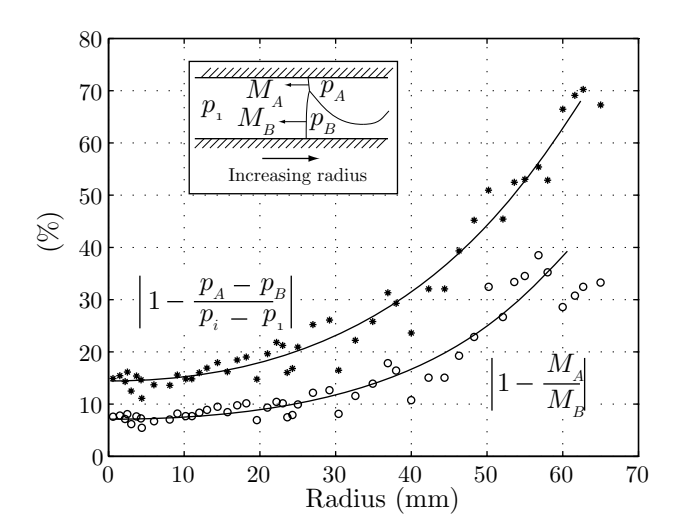


Figure 6: Three-dimensionality of the converging shock wave due to cross-wise waves. Relative variation of the two parts making up the shock front. The inlaid image shows a simplified sketch of the situation. The pressure  $p_i$  is the largest of  $p_A$  and  $p_B$  at corresponding shock radius.

point the flow stabilizes to a state which appears almost steady, driven by the high pressure in the bend section. After the expansion at the 90° corner, the flow is straightened through a series of semi-stationary oblique shocks localized around r=60 mm, see Fig. 5 (vi)-(viii), experiencing first regular and then Mach reflection. Once past this section the flow direction deviates with less than 10% from the radial direction. Figures 7 (a) and (b) show velocity and pressure as functions of radius along the vertical mid line (at x=102.5 mm) of the test-section. The pressure, velocity and density variations in the x-direction were found to be less than 10% at any point r<40 mm.

To compare with the Guderley solution, the propagation of the shock front in the mid cross-section of the test section is shown in Fig. 8 (circles). The discontinuity of the trajectory around r=60 mm corresponds to the first diffracted wave being overtaken and merged with the stronger shock reflected at the back wall. Two self-similar plots ( $\alpha=0.835$ ) are added for comparison. They have the same collapse time as the Euler solution, but different initial radii. One has initial radius r=70 mm and the other initial radius r=40. The solution starting at r=40 mm shows that the Euler solution behaves like the self-similar solution in the central part of the test section.

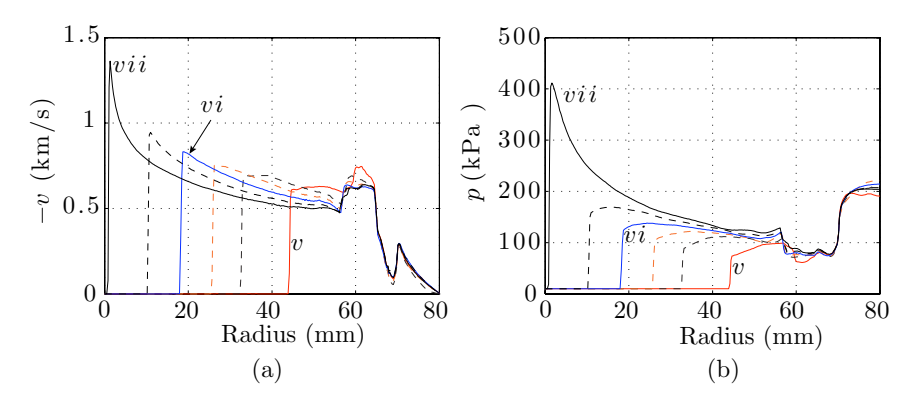


Figure 7: Vertical velocity v (a) and pressure (b) along the vertical centerline of the test section at five different times. Those plotted with full lines correspond to images (v), (vi) and (vii) in Fig. 5, while the dashed lines show the flow at intermediate times. The negative sign in front of v is to clarify that the flow is going down toward the centerline, while the positive direction is defined outwards.

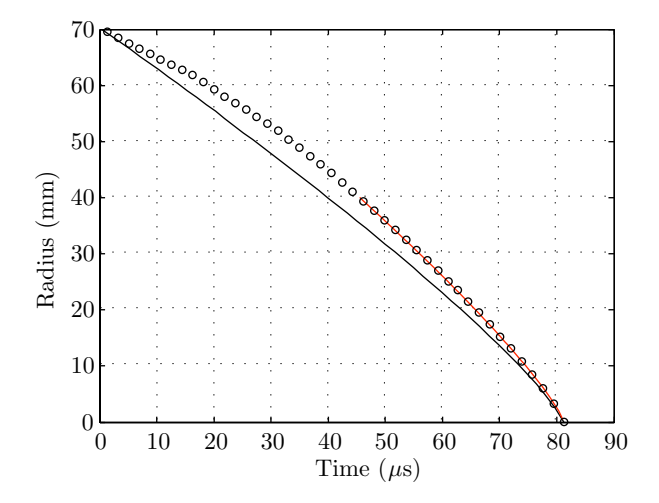


Figure 8: Propagation of the front of the shock: radius from calculations (circles) compared with two theoretical self-similar trajectories (full lines,  $\alpha$ =0.835), one trajectory with starting point at radius r=70 mm and another with starting point at r=40 mm, both with the same final focus instant  $t_0 \approx 81$   $\mu$ s as the Euler solution.

#	$\gamma$	Test gas	Driver	$M_s$	$p_1$	$p_4$
					(kPa)	(kPa)
1	1.13	$C_3H_8$	$N_2$	1.9	50.0	900
2	1.13	$C_3H_8$	$N_2$	2.1	25.0	900
3	1.40	$N_2$	air	1.9	30.0	850
4	1.40	$N_2$	air	2.4	13.3	1800
5	1.40	$N_2$	He $(5\% \text{ air})$	2.8	35.0	1900
6	1.66	$\operatorname{Ar}$	air	1.9	37.0	850
7	1.66	Ar	air	2.4	20.0	1800
8	1.66	$\operatorname{Ar}$	He $(5\% \text{ air})$	2.8	48.0	1900

Table 1: List of performed test cases.

#### 4. Results

In the experiments three gases with different heat capacities ratios were used: argon (Ar,  $\gamma = 1.66$ ), nitrogen (N<sub>2</sub>,  $\gamma = 1.40$ ) and propane (C<sub>3</sub>H<sub>8</sub>,  $\gamma = 1.13$ ). Several initial Mach number  $M_s$ , as measured by the shock sensors in the annular channel, was tested for all gases. The Mach number variation, including measurement errors, within each test case was  $\pm 0.05$ . The performed test cases are listed in Table 1.

The test gases were of industrial grade and the purity was 99.9% for argon, 99.99% for nitrogen and 98.5% for propane. To avoid the risk of igniting the  $C_3H_8$  the high pressure section was evacuated from air and then filled with  $N_2$  as driver gas. With the present leak rate the oxygen in the low pressure section amounted to less than 0.1%.

Figure 9 shows two schlieren image sequences of the converging shock propagation in argon each with different initial Mach number. In the center of Fig. 9(b) the light created at the shock focusing instant is clearly seen. Shocks in propane however did not produce any light that could be detected with the photomultiplier tube.

#### 4.1. Chemical stability of propane

The chemical stability of propane under the present conditions was examined. With the given initial Mach number range as presented in Table 1 the normal shock relations give a gas temperature below 1000 K, a temperature under which the gas is stable. However, the complex diffraction and reflection pattern could result in areas with locally extreme conditions. Using inputs from the numerical calculations, the most extreme conditions during the shock focusing down to r=2 mm were chosen to calculate possible decomposition. Lifshitz & Frenklach (1974) applied a reduced reaction scheme for calculations in the

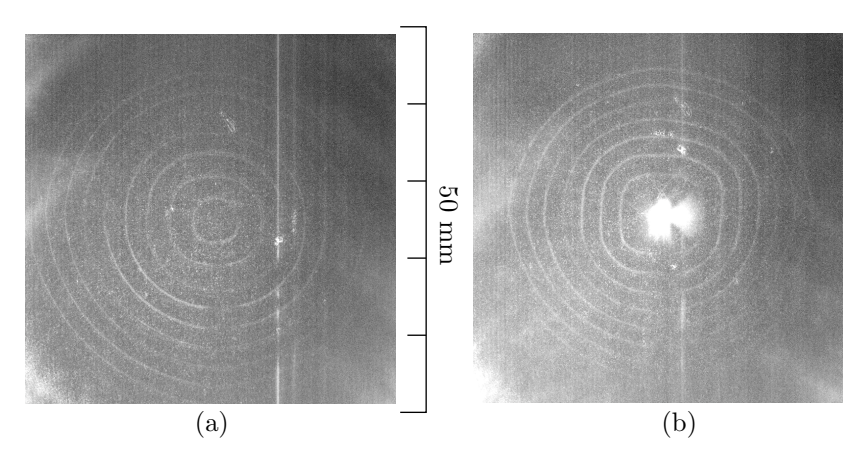


Figure 9: Multiple exposure images of the converging shock for two different initial Mach numbers: (a),  $M_s = 1.9 \pm 0.01$  and (b)  $M_s = 2.4 \pm 0.01$  where also the light emitted by shock focusing is seen in the center.

temperature range T=1100-1700 K; we adopted the same model, which consists of 10 species and 11 reactions. The reaction rate constants used in their work were adopted in the present study. It was found that no decomposition occurred for any of the test cases for the convergence range used in the evaluation of  $\alpha$ .

### 4.2. Evaluation procedure

Quantitative data for the shock deviation and propagation were acquired from the schlieren images. Each shock front was manually located by fitting curved sector segments to the fronts in a graphical application. After this procedure the radius and the deviation from circular symmetry of each shock front could be found by image processing in Matlab. In this way the position of the separate fronts could be extracted with good precision. Figure 10 illustrates the technique applied. Figures 11, 12 and 13 show the relative error of the obtained shock radius.

## 4.3. Shock instability

The cylindrical shock in an annular shock tube with supports for the central body is well known to be unstable due to the perturbations introduced when the shock passes the supporting struts (Takayama et al. 1987; Eliasson et al. 2006). It is necessary to know the deviation from the circular shape as it strongly affects the convergence. The breakdown of the shock shape causes a deviation from the self-similarity. The deviation of the shock radius for the

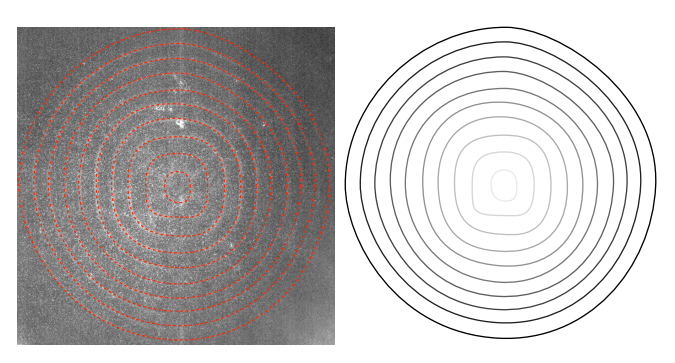


Figure 10: Extraction of shock front position from schlieren images.

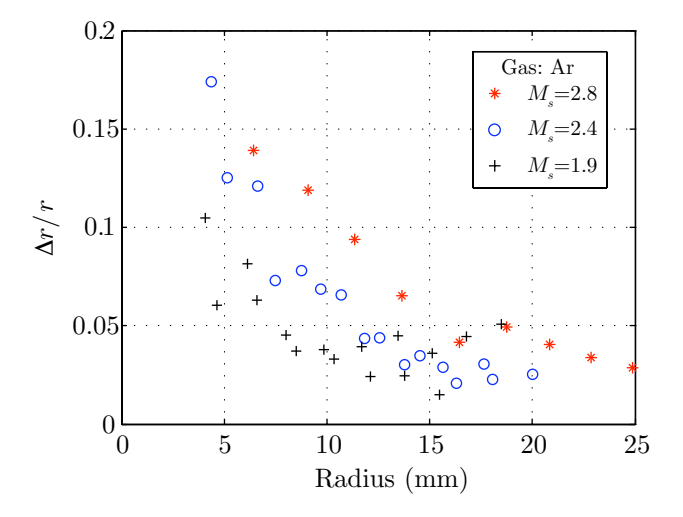


Figure 11: The shock front relative deviation from a cylindrical form as function of the shock radius in argon.  $+:M_s=1.9,\bigcirc$  (blue online):  $M_s=2.4,*$  (red online):  $M_s=2.8.$ 

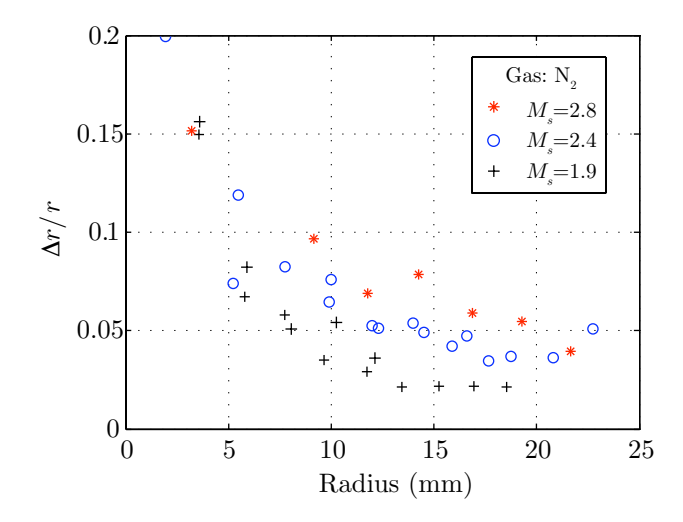


Figure 12: The shock front relative deviation from a cylindrical form as function of the shock radius in nitrogen.  $+: M_s = 1.9$ , (blue online):  $M_s = 2.4$ , \* (red online):  $M_s = 2.8$ .

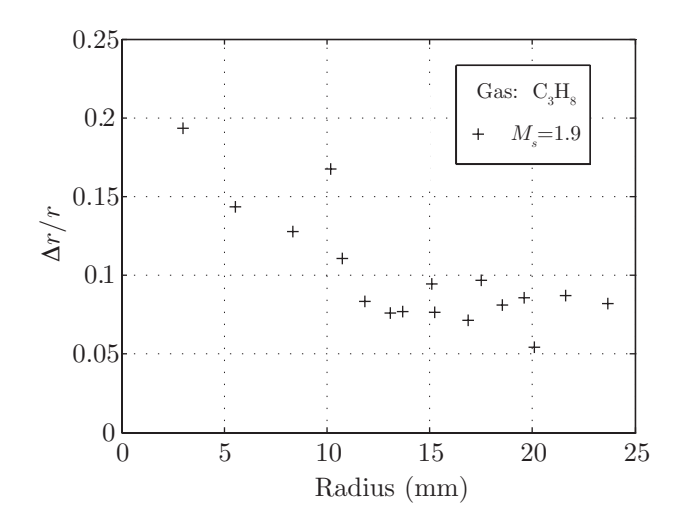


Figure 13: The shock front relative deviation from a cylindrical form as function of the shock radius in propane.  $M_s = 1.8 - 1.9$ .

various cases is presented in Figs. 11-13. It was noticed that the shock waves in propane developed shock-shocks earlier than those in argon and in nitrogen.

### 4.4. Comparison with theory

Data acquired from the schlieren photographs were used to determine  $\alpha$  from the self-similar solution:

$$\frac{r}{r_0} = \left(1 - \frac{t}{t_0}\right)^{\alpha} \tag{1}$$

The initial radius  $r_0 = r(t = 0)$  was taken as the radius of the outmost shock front in a given data set. The radius was measured from the point of focus, which was not necessarily exactly in the geometric center of the test section. The change of position of the focal point from run to run was in the order of a millimeter. As mentioned in the previous paragraph, the breakdown of circular symmetry causes the acceleration to decrease as the shock front becomes more square like, resulting in an increased  $\alpha$ .

To acquire the proper values of  $\alpha$  and  $t_0$  for completely circular shock waves, fits were made for data points where the deviation from the circular shape was less than 5 – 10%. This means that  $t_0$  is calculated from such data points instead of the actual time of collapse  $t_{\ell}$ .

The values of  $t_0$  and  $\alpha$  are calculated from the experimental data points using the least-square procedure by minimizing the deviation from the self-similar solution. The results for argon, nitrogen and propane are shown in Figs. 14-16, both in linear and logarithmic scale. In case of the self-similar solution the dependence of  $ln(r/r_0)$  vs  $\alpha ln(1-t/t_0)$  should be linear. As we can see from Figs. 14(b)-16(b) this is the case for the acquired values of  $t_0$  and  $\alpha$ 

Figure 14 displays radius vs time diagrams for shocks in argon for three different initial Mach numbers. Figure 15 shows shocks in nitrogen, also for three different initial Mach numbers, while Fig. 16 shows the results for propane at  $M_s \approx 1.9$ . In Figs. 14(a)-16(a) fits to the self-similar solution for each individual shock are shown as dashed lines. In the logarithmic plots self-similar solutions using mean values of  $\alpha$  from the least-square fits to all runs in each gas are plotted as full lines. Dashed lines show 5% larger and smaller  $\alpha$ -values.

To estimate the error caused by the evaluation explained above, the procedure was repeated from start for a single case. The result for a randomly selected run - in argon - was  $\alpha_1 = 0.813 \pm 0.004$  and  $\alpha_2 = 0.811 \pm 0.003$ . This emphasizes the necessity to average over many runs.

The shock Mach number as function of the radial distance is presented in Figs. 18-19 for several values of the initial Mach number. The Mach number according to the self-similar solution is plotted along with the experimental data, using as starting Mach number the Mach number at r=50 mm obtained

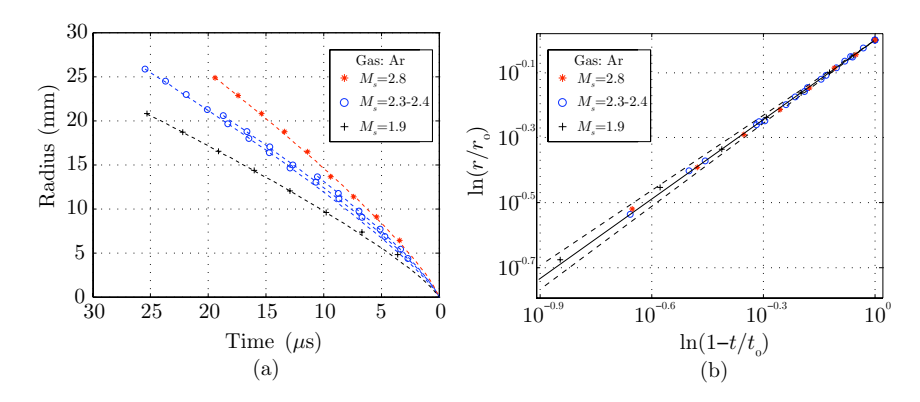


Figure 14: Shock position as function of time for different initial Mach numbers in argon.  $+: M_s = 1.9$ ,  $\bigcirc$  (clue online):  $M_s = 2.3 - 2.4$  and \* (red online):  $M_s = 2.8$ . Linear (a) plot with fitted self-similar paths (dashed lines) and logarithmic (b) where the full line has slope  $\alpha = 0.813$  and the dashed lines show the variation of  $\alpha$  with  $\pm 5\%$ .

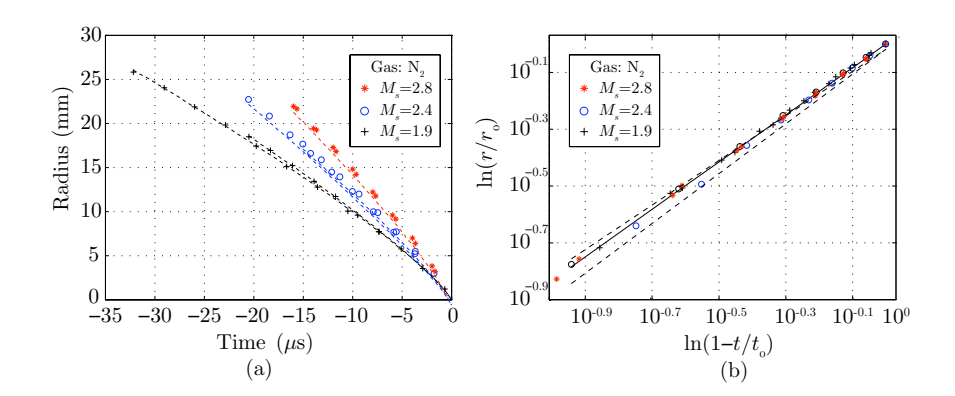


Figure 15: Shock position as function of time for different initial Mach numbers in nitrogen.  $+: M_s = 1.9$ ,  $\bigcirc$  (blue online):  $M_s = 2.4$  and \* (red online):  $M_s = 2.8$ . Linear (a) plot with fitted self-similar paths (dashed lines) and logarithmic (b) where the full line has slope  $\alpha = 0.836$  and the dashed lines show the variation of  $\alpha$  with  $\pm 5\%$ .

in the numerical calculations. The point where the experimental data starts to deviate from the theoretical curves corresponds reasonably with breakdown of circular symmetry of the shock front.

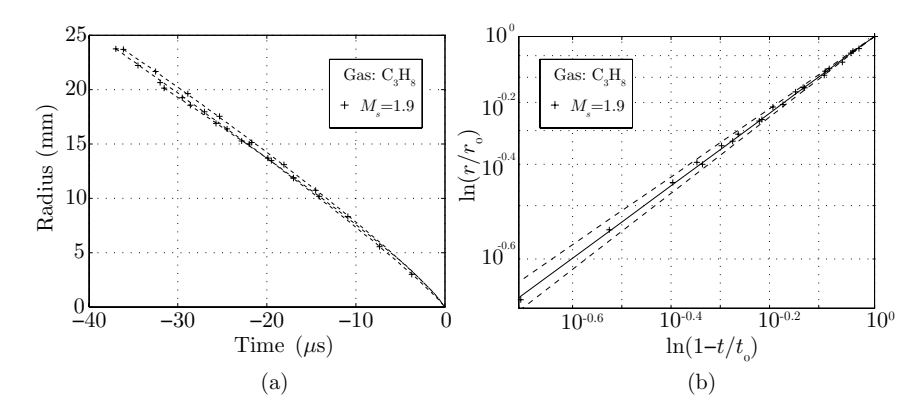


Figure 16: Shock position as function of time for different initial Mach numbers in propane.  $+: M_s = 1.8 - 1.9$ . Linear (a) plot with fitted self-similar paths (dashed lines) and logarithmic (b) where the full line has slope  $\alpha = 0.88$  and the dashed lines show the variation of  $\alpha$  with  $\pm 5\%$ .

In Table 2 the results for  $\alpha$ , averaged over five or more runs, are tabulated and compared with previous analytical and experimental values. The present values agree well with the analytical and experimental results, although we do not see the velocity-dependence reported by Baronets (1984) for shocks in argon. The acquired values (circles) are plotted in Fig. 20 together with analytical data (Lazarus 1981, Table 6.4, p. 331). The error bars represent the standard deviation of the acquired values for the individual runs. The expression in Eq. 2, derived by Chisnell (1957) and Chisnell (1998) is plotted as a dashed line for comparison:

$$\frac{\alpha}{1-\alpha} = 1 + \frac{2}{\gamma} \left(\frac{2\gamma}{\gamma - 1}\right)^{\frac{1}{2}} \tag{2}$$

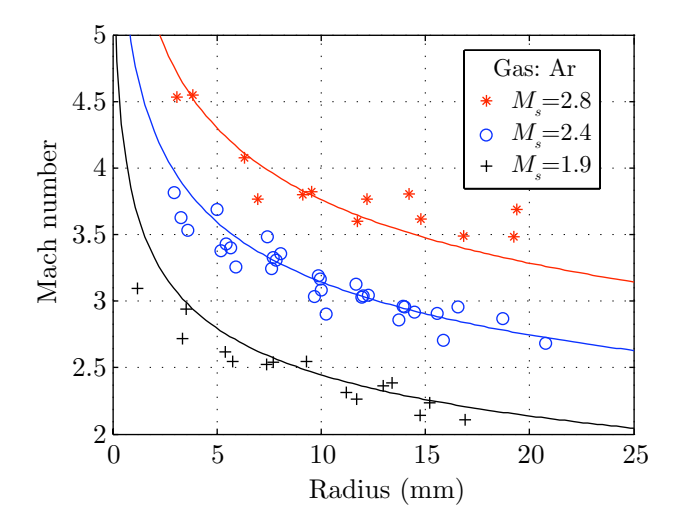


Figure 17: The shock Mach number as function of the distance to the focus in Ar for three initial Mach numbers.  $+: M_s = 1.9$ ,  $\bigcirc$  (blue online):  $M_s = 2.4$ , \* (red online):  $M_s = 2.8$ . Lines represent the theoretical self-similar profiles with  $\alpha = 0.816$ .

$\gamma$	$\alpha$ , Analytical Other authors	$\alpha$ , Experimental Other authors	$\alpha$ , This paper
1.13	$0.8778^{12}$		$0.88 \pm 0.02$
1.40	$0.8353^{1}$	$0.831 \pm 0.002^3$	$0.84 \pm 0.01$
1.66	$0.8156^{1}$	$0.820 \text{ to } 1.0^4$	$0.81 \pm 0.01$

Table 2: Values of the self-similar exponent  $\alpha$  acquired from the present study: comparison with analytical works and previous experiments.

### 4.5. Influence of three-dimensional flow

The Guderley problem is one-dimensional, while the experiments have three-dimensional qualities. The variations in the transverse angle and eventual instability of the circular shape are caused by perturbations mainly introduced by the supporting struts. This distortion of the circular shape is manifested close to the center and we avoided this problem by limiting the determination

<sup>&</sup>lt;sup>1</sup>Lazarus (1981)

<sup>&</sup>lt;sup>2</sup>Interpolated by the authors.

<sup>&</sup>lt;sup>3</sup>Takayama et al. (1987)

 $<sup>^4</sup>$ Baronets (1984), the large range depended on shock velocity, see text.

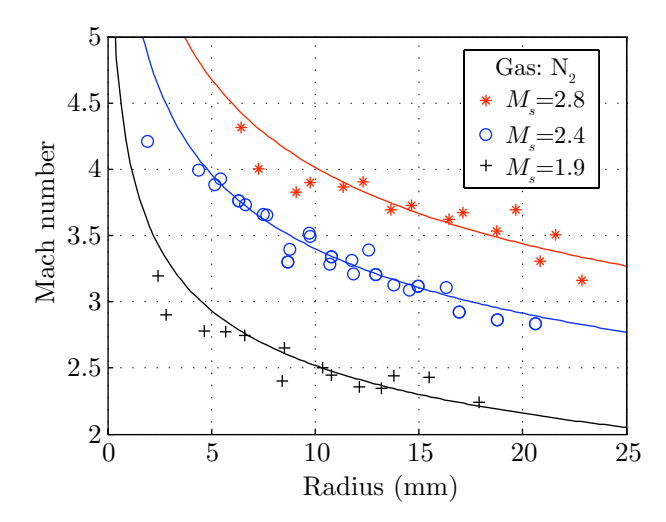


Figure 18: The shock Mach number as function of the distance to the focus in N<sub>2</sub> for initial Mach numbers:  $+: M_s = 1.9$ ; (blue online):  $M_s = 2.4$ ; \* (red online):  $M_s = 2.8$ . Lines represent the theoretical self-similar profiles with  $\alpha = 0.835$ .

of the curvature of the r-t trajectory to the region where the shock waves were circular. With a vertical shock shock tube configuration, as used by Hosseini et al. (2000), this region would presumably be expanded toward the focus as compared to in a strut-supported horizontal tube.

Depth-variations - variations in the x-direction - are primarily caused by the sharp bend configuration as shown by the numerical calculations. The variations were quantified by the numerical tests and were deemed sufficiently small and hence were neglected.

The final structure of the hot radiating gas core at the center of the convergence has been previously investigated by Kjellander et al. (2010). The photographs show the luminescent gas core as a straight thin (diameter 0.2 mm) cylinder stretching over the entire 5 mm width between the facing windows of the test chamber. This indicates the 2D nature of the converging shock in the immediate vicinity of the focus.

Another option to improve the stability and avoid two- or three-dimensional effects could be a gas lens, which has been studied theoretically by Dimotakis & Samtaney (2006). They suggested a two-dimensional gas-lens configuration was able to produce circular shocks (recently Vandenboomgaerde & Aymard. (2011) applied the same theory for a three-dimensional lens).

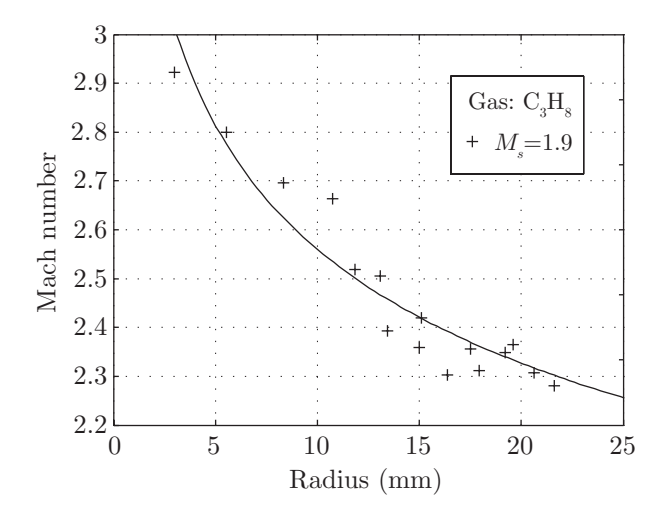


Figure 19: The shock Mach number as function of the distance to the focus in propane, initial  $M_s \approx 1.9$ . The line is Guderley's solution with  $\alpha = 0.878$  for comparison.

### 5. Conclusions

The propagation of cylindrical shock waves was studied to experimentally determine the exponent  $\alpha$  in equation (1) for different adiabatic constants  $\gamma$ . The experiments were made in a shock tube with a cylindrical chamber with radius 70 mm. Numerical simulations were performed to investigate how well this shock tube configuration could create two-dimensional cylindrical converging shock waves. The results showed that, although the initial shape was profoundly three-dimensional, about halfway to the center the differences had evened out and the shock approached a plane two-dimensional shape converging in a self-similar manner.

Test gases were argon, nitrogen and propane. The runs were performed at different initial Mach numbers in the range  $M_s=1.9-2.8$  for argon and nitrogen. The initial Mach number for propane was  $M_s\approx 1.9$ . Schlieren photography was used to trace the shock propagation and fits were made to the self-similar function. The propagation of the shocks followed the Guderley solution well down to a radius of 3-6 mm (depending on gas and Mach number) from the focus, where perturbations broke down the circular shape. Fits to determine  $\alpha$  were made to the part of the shock which was still circular in order to compare with the theory (for shock positions  $r\approx 30$  to  $r\approx 5$  mm). The variation with  $\gamma$ , presented in Fig. 20, was captured and the values agreed reasonably well with analytical solution. No dependence on Mach number was seen.

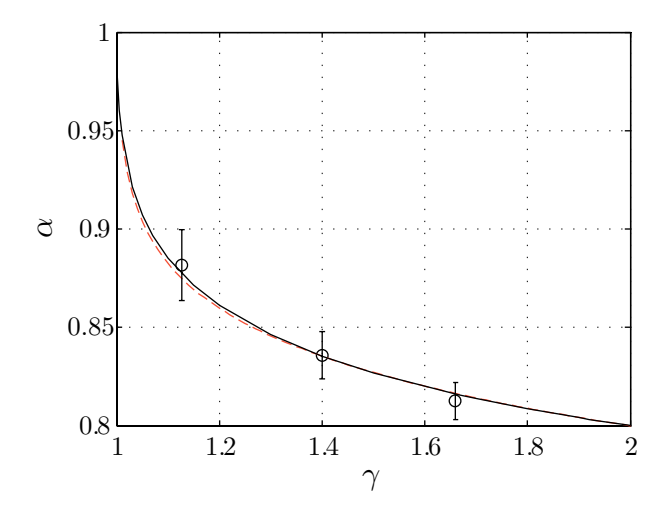


Figure 20: Acquired experimental values and standard deviation of  $\alpha$  compared to the analytical solution (full line; values from Ref. Lazarus (1981)) and geometrical shock dynamics (dashed line, Eq. 2, taken from Chisnell (1957, 1998)).

# Acknowledgements

We gratefully acknowledge the financial support by the Swedish Research Council (VR) and, for experimental equipment, the Göran Gustafsson Foundation.

# References

- BARONETS, P. N. 1984 Imploding shock waves in a pulsed induction discharge. *Fluid Dynamics* **19**, 503–508.
- BARONETS, P. N. 1994 Cylindrical shock waves generated by a spark discharge and their interaction with the shock waves from a pulsed induction discharge. *Fluid Dynamics* **29**, 129–132.
- Butler, D. S. 1954 Converging spherical and cylindrical shocks, Report No. 54/54. Burgess Hill, New York.
- Chester, W. 1954 The quasi-cylindrical shock tube. Phil. Mag. 45, 1293–1301.
- Chisnell, R. F. 1957 The motion of a shock wave in a channel, with applications to cylindrical and spherical shocks. *J. Fluid Mech.* 2, 286–298.
- CHISNELL, R. F. 1998 An analytic description of converging shock waves. J. Fluid Mech. 354, 357–375.
- DIMOTAKIS, P. E. & SAMTANEY, R. 2006 Planar shock cylindrical focusing by a perfect-gas lens. *Phys. Fluids* **18**, 031705.
- ELIASSON, V., APAZIDIS, N., TILLMARK, N. & LESSER, M. B. 2006 Focusing of strong shocks in an annular shock tube. *Shock Waves* 15, 205–217.
- ELIASSON, V., TILLMARK, N., SZERI, A. & APAZIDIS, N. 2007 Light emission during shock wave focusing in air and argon. *Phys. Fluids* **19**, 106106.
- Fujimoto, Y. & Mishkin, E. 1978 Analysis of spherically imploding shocks. *Phys. Fluids* **21**, 1933–1938.
- Guderley, G. 1942 Starke kugelige und zylindrische Verdichtungsstöße in der Nähe des Kugelmittelpunktes bzw. der Zylinderachse. Luftfahrtforschung 19, 302–313.
- HAFNER, P. 1988 Strong convergent shock waves near the center of convergence: A power series solution. J. Appl. Math.. 48, 1244–1261.
- HORNUNG, H. G., PULLIN, D. I. & PONCHAUT, N. 2008 On the question of universality of imploding shock waves. *Acta Mech.* **201**, 31–35.
- HOSSEINI, S. H. R., ONODERA, O. & TAKAYAMA, K. 2000 Characteristics of an annular vertical diaphragmless shock tube. *Shock Waves* **10**, 151–158.
- KJELLANDER, M., TILLMARK, N. & APAZIDIS, N. 2010 Thermal radiation from a converging shock implosion. *Phys. Fluids* **22**, 046102.
- LAZARUS, R. B. 1981 Self-similar solutions for converging shocks and collapsing cavities. SIAM J. Numer. Anal. 18, 316–371.

- LAZARUS, R. B. & RICHTMYER, R. D. 1977 Similarity Solutions for Converging Shocks. Los Alamos Scientific Laboratory of the University of California, Los Alamos, NM.
- LIFSHITZ, A. & FRENKLACH, M. 1974 Mechanism of the high temperature decomposition of propane. *J. Phys. Chem.* **79**, 686–692.
- Matsuo, H., Ebihara, K., Ohya, Y. & Sanematsu, H. 1985 Spectroscopic study of cylindrically converging shock waves. *J. Appl. Phys.* 58, 2487–2491.
- Matsuo, H. & Nakamura, Y. 1980 Experiments on cylindrically converging blast waves in atmospheric air. J. Appl. Phys. 51, 3126–3129.
- Matsuo, H. & Nakamura, Y. 1981 Cylindrically converging blast waves in air. J. Appl. Phys.  ${\bf 52},\,4503-4507.$
- NAKAMURA, Y. 1983 Analysis of self-similar problems of imploding shock waves by the method of characteristics. *Phys. Fluids* **26**, 1234–1239.
- Perry, R. W. & Kantrowitz, A. 1951 The production and stability of converging shock waves. J. Appl. Phys 22, 878–886.
- PONCHAUT, N., HORNUNG, H. G. & MOUTON, D. I. 2006 On imploding cylindrical and spherical shock waves in a perfect gas. *J. Fluid. Mech.* **560**, 103–122.
- ROBERTS, D. E. & GLASS, I. I. 1971 Spectroscopic investigation of combustion-driven spherical implosion waves. *Phys. Fluids* **14**, 1662–1670.
- Saito, T. & Glass, I. I. 1982 Temperature Measurements at an Implosion Focus. *Proc. R. Soc. Lon. A* **384**, 217–231.
- Stanyukovich, K. P. 1960 Unsteady motion of continous media. Pergamon, Oxford.
- Sun, M. & Takayama, K. 2003 An artificially upstream flux vector splitting scheme for the Euler equations. *J. Comput. Phys.* **189**, 305–329.
- TAKAYAMA, K., KLEINE, H. & GRÖNIG, H. 1987 An experimental investigation of the stability of converging cylindrical shock waves in air. *Exps. Fluids* 5, 315–322.
- Van Dyke, M. & Guttman, A. 1982 The converging shock wave from a spherical or cylindrical piston. *J. Fluid Mech.* **120**, 451–462.
- Vandenboomgaerde, M. & Aymard., C. 2011 Analytical theory for planar shock focusing through perfect gas lens and shock tube experiment designs. *Phys. Fluids* 23, 016101.
- Whitham, G. B. 1957 A new apporach to problems of shock dynamics. part 1. two-dimensional problems. *J. Fluid Mech.* 2, 145–171.

Paper 6

R

# Numerical assessment of shock tube with inner body designed to create cylindrical shock waves

# By Malte Kjellander and Nicholas Apazidis

Department of Mechanics, Royal Institute of Technology, SE-100 44 Stockholm, Sweden

Technical report.

#### 1. Introduction

This report contains a description of the numerical methods and a case study on the shock tube at *KTH Mechanics* designed to create cylindrical converging shocks. Inviscid, compressible and non-reactive Euler equations for multiple species have been discretized and solved with an upwinding explicit algorithm. The method is cheap but resolves shocks with good accuracy and is able to solve contact surfaces. As the purpose is primarily related to the front shock propagation the neglect of viscosity, which has large effects in the flow behind the front shock, is therefore deemed justified. To further enhance the shock resolution a simple mesh adaption algorithm has also been included.

The first experimentally created cylindrical shock waves were produced by Perry & Kantrowitz (1951) using a body shaped as a tear-drop in the end of a shock tube. Similar designs have been used by Wu et al. (1977), Kleine (1985) and Takayama et al. (1987). The basic design of the devices is the same: they differ in the details. Specifically, the differences between the three-dimensional bends from an annular to a cylindrical shape have large influences on the efficiency of strengthening the converging shocks.

The tear drop inner body of device of Perry & Kantrowitz was supported by struts which give rise to disturbances as the shock wave passes them. The tube in Sendai (Takayama et al. 1987) is an improvement of the design. Instead of a tube with a constant outer diameter, the cross-section is transformed to an annular channel with a long passage way where the disturbances from the struts have time to be attenuated before a relatively sudden bend forces the shock to assume a cylindrical shape in a compartment which will be called "convergence chamber" here. The tube at KTH, shown in Fig. 1, was constructed resembling the tube in Sendai, with a few significant differences: the transformation between the plane and annular section is made in such a way that the total

cross section area is constant, with the idea that the shock wave then retains its original strength instead of being attenuated. The bend design is the most significant difference. Instead of a smooth transformation with constant gap, a sharp bend is inserted and the width of the convergence chamber is half that of the annular channel height (5 mm compared to 10 mm).

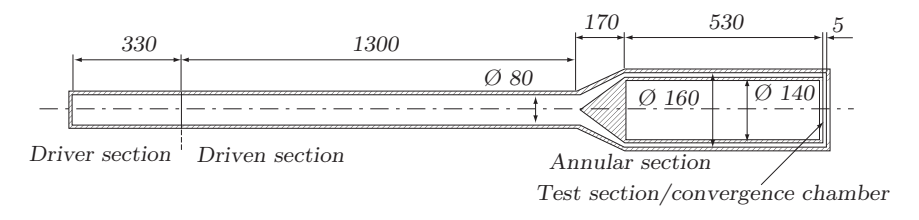


Figure 1: The dimensions of the shock tube. Measures in mm.

Questions have been raised on the usefulness of similar bend designs as they invariably introduce three-dimensional qualities in the form of reflected waves travelling between the walls of the test section (Takayama 1977; Watanabe & Takayama 1991). If these lateral waves are too strong, it will greatly diminish the usefulness of the design. As it was reported that smooth bends were preferable it is of interest to examine how well the sharp bend works. The aim of the present study is primarily to numerically study the performance of the contracting bend of the shock tube at KTH Mechanics but also the flow through the whole tube.

Chapter 1 contains a description of the numerical code used for the calculations, including tests of code performance. Chapter 2 contains the study on the shock tube as a whole and the test section in particular. A parametric study varying the test gas and initial shock Mach number was performed and evaluated. The flow in the bend is discussed and the effect of three-dimensional influences are studied. The acceleration of the shocks are compared with the self-similar solution of Guderley (1942).

#### CHAPTER 1

# Numerical modelling

The flow in the shock tube is simulated using the compressible and inviscid Euler equations. The fluid is treated as a non-reactive mixture of a number of ideal gases. At the centre of the test section, where the shock wave is converged and reflected back into the shocked flow, non-equilibrium and real gas effects are expected for cases with higher initial shock velocities and the present models are not able to fully predict the conditions at the centre after the implosions. As the purpose is to investigate the ability of the tube configuration to create intensified shock waves, the actual conditions after focus are not considered and real gas effects are neglected.

#### 1. Gas model

A system consisting of N species is considered. Each species is considered as a thermally perfect gas,

$$p_s = \rho_s R_s T \tag{1}$$

$$e_s = \rho_s c_{v,s} T \tag{2}$$

where  $p_s$  is the partial pressure,  $R_s$  the specific gas constant,  $e_s$  the internal energy per unit mass and  $c_{v,s}$  the specific heat capacity at constant volume of species s. The specific gas constants are found from the universal gas constant  $\mathcal{R}$  through the species molar mass  $\mathcal{M}_s$  as  $R_s = \mathcal{R}/\mathcal{M}_s$ . The heat capacity is considered constant for the purposes of this study. As per the assumptions, all species are in thermodynamical equilibrium with a common translational temperature T. The gas mixture conditions are calculated from the individual species in the usual manner: the global density  $\rho$  is the sum of the separate densities, the pressure p is the sum of the partial pressures according to Dalton's law and the internal energy per unit mass of the whole mixture e is the sum of the internal energy of each species:

$$\rho = \sum_{i=1}^{N} \rho_s \tag{3}$$

$$p = \sum_{i=1}^{N} p_s = \sum_{i=1}^{N} \rho_s R_s T \tag{4}$$

$$e = \sum_{i=1}^{N} \frac{e_s}{\rho} = \sum_{i=1}^{N} \frac{\rho_s}{\rho} c_{v,s} T$$
 (5)

The specific gas constant R and heat capacity ratio  $\gamma$  of the gas mixture are calculated from the reduced specific heats,

$$c_p = \sum_{i=1}^{N} \frac{\rho_s}{\rho} c_{p,s} \tag{6}$$

$$c_v = \sum_{i=1}^{N} \frac{\rho_s}{\rho} c_{v,s} \tag{7}$$

$$R = \sum_{i=1}^{N} \frac{\rho_s}{\rho} R_s = c_p - c_v \tag{8}$$

$$\gamma = \frac{c_p}{c_n} \tag{9}$$

The speed of sound of the mixture is then calculated from  $c^2 = \gamma RT$ .

# 2. Governing equations

The Euler equations for inviscid compressible 2D/axisymmetric flow written in conservative form:

$$\frac{\partial \eta \mathbf{U}}{\partial t} + \frac{\partial \eta \mathbf{F}}{\partial x} + \frac{\partial \eta \mathbf{G}}{\partial y} = \mathbf{W}$$
 (10)

where the vector **U** contains the conserved variables while **F** and **G** are the fluxes in x- and y-directions. The terms for axisymmetric swirl-free flow are the right hand source term  $\mathbf{W} = [0, ..., 0, p, 0]^T$  and  $\eta = y$  (for a purely two-dimensional flow,  $\mathbf{W} = 0$ ,  $\eta = 1$ ). The conserved variables and fluxes:

$$\mathbf{U} = \begin{pmatrix} \rho_{1} \\ \vdots \\ \rho_{N} \\ \rho u \\ \rho v \\ \rho E \end{pmatrix}, \quad \mathbf{F}(\mathbf{U}) = \begin{pmatrix} \rho_{1} u \\ \vdots \\ \rho_{N} u \\ \rho u^{2} + p \\ \rho v u \\ \rho E u + p u \end{pmatrix}, \quad \mathbf{G}(\mathbf{U}) = \begin{pmatrix} \rho_{1} v \\ \vdots \\ \rho_{N} v \\ \rho u v \\ \rho v^{2} + p \\ \rho E v + p v \end{pmatrix}$$

$$(11)$$

where  $\rho_s = \rho_1, ..., \rho_N$  is the mass density of each species s = 1, 2, ..., N,  $\rho u$  and  $\rho v$  are the x- and y-momentum and  $\rho E$  is the energy per unit volume. It is assumed that each species follow the same bulk flow  $\mathbf{u} = (u, v)$ . To solve the system of equations it is necessary to express the pressure of the gas mixture p and the temperature T as functions of the conserved variables  $\mathbf{U}$ . The energy of the gas mixture per unit mass is the sum of the specific internal energy and the kinetic energy:  $E = e + |\mathbf{u}|^2/2$ , and

$$\rho E = \sum_{i=1}^{N} \rho_s c_{v,s} T + \rho \frac{|\mathbf{u}|^2}{2}$$
 (12)

from where the temperature can be extracted. Once T is known, the partial pressures are found from the ideal gas law (Eq. 1) and the global pressure from Dalton's law (Eq. 4).

## 3. Finite volume discretisation

The partial differential equation Eq. 10 is discretised on an unstructured triangular mesh and solved using an upwinding explicit scheme. Figure 2 shows a sketch of a grid cell i and explanation of the stored variables. For the purpose of interpolation the flow variables are set at the cell centers  $(x, y)_i$ . Designating the domain of the triangle i as  $\mathcal{A}$  and its boundary as  $\ell$ , the triangular cell i is treated as a control volume in which Eq. 10 is integrated. Applying Green's formula gives:

$$\int_{\mathcal{A}} \frac{\partial \eta \mathbf{U}}{\partial t} d\mathcal{A} = -\int_{\mathcal{A}} \nabla \cdot (\mathbf{F}, \mathbf{G}) \eta d\mathcal{A} + \int_{\mathcal{A}} \mathbf{W} d\mathcal{A}$$

$$= -\int_{\ell} (\mathbf{F}, \mathbf{G}) \cdot \mathbf{n} \eta d\ell + \int_{\mathcal{A}} \mathbf{W} d\mathcal{A} \tag{13}$$

where **n** is the normal vector of the boundary. Approximating the variables in the whole cell with the cell center values,  $\mathbf{U}=\mathbf{U}_i$  and  $\mathbf{W}=\mathbf{W}_i$ , the left hand side and the source term are easily integrated. Let  $\hat{\mathbf{F}}_k = \hat{\mathbf{F}}(\mathbf{U}_i, \mathbf{U}_k)$  be the normal flux at the edge k and let  $A_i^y$  and  $L_k^u$  be defined as

Variable	Description $(k, j = 1, 2, 3)$
$(x,y)_i$	Cell center coordinates
$A_i$	Area of cell $i$
$(x_v, y_v)_j$	Vertice coordinates
$[n_x, n_y]_k$	Normal vector of edge $k$
$h_k$	Cell height from edge $k$
$L_k$	Length of edge $k$
$\mathbf{U}_i$	Conserved variables in cell $i$
$\mathbf{U}_k$	Conserved variables in cell $k$
$\hat{\mathbf{F}}_k$	Numerical flux at edge $k$

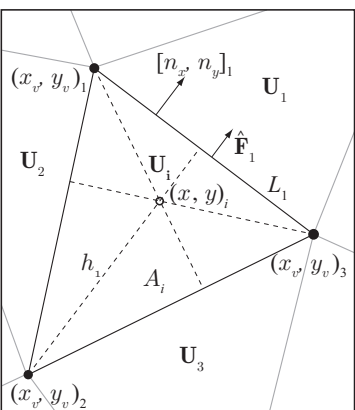


Figure 2: A grid cell i with neighbour cells k = 1, 2, 3. Explanations of the variables in the table.

$$A_i^{\eta} = \int_{\mathcal{A}} \eta d\mathcal{A} \quad \text{and} \tag{14}$$

$$L_k^{\eta} = \int_{\ell} \eta d\ell. \tag{15}$$

which in the pure two-dimensional case equal the cell area and side length:  $A_i^{\eta} = A_i$  and  $L_k^{\eta} = L_k$  for  $\eta = 1$ . Using the notation in Fig. 2 for coordinates of the cell vertices,  $(x_{v,1}, y_{v,1})$ ,  $(x_{v,2}, y_{v,2})$  and  $(x_{v,2}, y_{v,2})$  and a corresponding notation for the edge vertices of edge k,  $(x_{v,k,1}, y_{v,k,1})$  and  $(x_{v,k,2}, y_{v,k,2})$ , the axisymmetric values  $A_i^{\eta} = A_i^y$  and  $L_k^{\eta} = L_k^y$  can be evaluated as

$$A_i^y = A_i \frac{y_{v,1} + y_{v,2} + y_{v,3}}{3} = A_i y_i \text{ and}$$
 (16)

$$A_i^y = A_i \frac{y_{v,1} + y_{v,2} + y_{v,3}}{3} = A_i y_i \text{ and}$$

$$L_k^y = L_k \frac{y_{v,k,1} + y_{v,k,2}}{2}.$$
(16)

Assuming the flux to be constant along the edges, the flux integral turns into a sum over all sides and with the above assumptions the Eq 13 turns into:

$$A_i^{\eta} \frac{\partial \mathbf{U}_i}{\partial t} = -\sum_{k=1}^{3} \hat{\mathbf{F}}_k L_k^{\eta} + A_i \mathbf{W}_i$$
 (18)

which yields, after first-order time discretisation:

$$\mathbf{U}_{i}^{t+\Delta t} = \mathbf{U}_{i}^{t} - \Delta t \sum_{k=1}^{3} \frac{L_{k}^{\eta}}{A_{i}^{\eta}} \hat{\mathbf{F}}(\mathbf{U}_{i}^{t}, \mathbf{U}_{k}^{t}) + \Delta t \frac{A_{i}}{A_{i}^{\eta}} \mathbf{W}_{i}$$
(19)

Explicitly written out for the two-dimensional and axisymmetric cases, respectively, the schemes to solve Eq. 19 become

$$\mathbf{U}_{i}^{t+\Delta t} = \mathbf{U}_{i}^{t} - \Delta t \sum_{k=1}^{3} \frac{2\hat{\mathbf{F}}(\mathbf{U}_{i}^{t}, \mathbf{U}_{k}^{t})}{h_{k}} \quad \text{and}$$
 (20)

$$\mathbf{U}_{i}^{t+\Delta t} = \mathbf{U}_{i}^{t} - \Delta t \sum_{k=1}^{3} \frac{(y_{v,k,1} + y_{v,k,2})\hat{\mathbf{F}}(\mathbf{U}_{i}^{t}, \mathbf{U}_{k}^{t})}{h_{k}y_{i}} + \Delta t \frac{\mathbf{W}_{i}}{y_{i}}$$
(21)

where it has been used that  $2A_i = L_k h_k$ . It should be noticed that  $y_i \neq 0$  for a cell with finite size.

The numerical fluxes are calculated by interpolating (first- or second-order) the flux functions in the neighbour cells on the edges and using the artificial upstream flux-splitting method (AUFS) introduced by Sun & Takayama Sun & Takayama (2003). The one-dimensional form of Eq. 10 is  $(U)_t + (F)_n = 0$  and the N+3 eigenvalues of the Jacobian matrix  $\mathbf{A} = \partial \mathbf{F}/\partial \mathbf{U}$  are  $\lambda_1 = u_n - c$ ,  $\lambda_2, ..., \lambda_{N+2} = u_n$  and  $\lambda_{N+3} = u_n + c$ , with  $u_n = u n_x + v n_y$  being the normal velocity. Provided that  $u_n < c$  somewhere, the system therefore contains waves going both upstream and downstream which makes up-winding difficult. The AUFS splitting method is based on introducing artificial wave-speeds  $s_1$  and  $s_2$  such that the flux at the edges can be split in one vector containing only nonnegative or non-positive wave speeds and another containing only stationary waves and waves moving at the speed of sound, one in each direction. For details of the derivation and merits of the splitting method we refer to the cited reference.

Referring again to Fig. 2, consider the numerical flux at the edge between a cell i and its neighbouring cell k. The numerical flux is split as follows, using the normal velocity  $u_n = un_x + vn_y$  and tangential velocity  $v_n = -un_y + vn_x$ :

$$\hat{\mathbf{F}}(\mathbf{U}^i, \mathbf{U}^k) = (1 - S)\hat{\mathbf{F}}_1 + S\hat{\mathbf{F}}_2 = (1 - S)\left[\frac{1}{2}(\mathbf{P}^i + \mathbf{P}^k) + \delta\mathbf{U}\right] + S\left[\mathbf{U}^d(u_n^d - s_2) + \mathbf{P}^d\right]$$
(22)

where  $S=s_1/(s_1-s_2)$ ,  $s_1$  and  $s_2$  being the artificially introduced wave-speeds. The system also introduces an isentrope artificial viscosity  $\delta \mathbf{U}$  which is defined below. The pressure term is  $\mathbf{P}=(0,...,0,pn_x,pn_y,pu_n)$ . The second vector  $\hat{\mathbf{F}}_2$  only contains waves going in a single direction and d is either i (if  $s_1>0$ ) or k (if  $s_1\leq 0$ ), i.e. the values of the flux depends only on the conserved values in the cell from which the waves are going. With the artificially added wave speeds the eigenvalues of the new system  $\partial \mathbf{F}_{1,2}/\partial \mathbf{U}$  become  $\lambda_1=u_n-c-s_{1,2}$ ,  $\lambda_2,...,\lambda_{N+2}=u_n-s_{1,2}$  and  $\lambda_{N+3}=u_n+c-s_{1,2}$ , where  $s_{1,2}$  are chosen so that the eigenvalues are strictly non-positive or non-negative. The choice used here:

$$s_1 = \frac{u_n^i + u_n^k}{2} \tag{23}$$

$$s_2 = \begin{cases} min(0, u_n^i - c^i, u_n^* - c^*) & \text{if } s_1 > 0, \\ max(0, u_n^* + c^*, u^k + v^k) & \text{if } s_1 \le 0. \end{cases}$$
 (24)

where

$$u^* = \frac{1}{2}(u_n^i + u_n^k) + \frac{c^i - c^k}{\gamma - 1}$$
 (25)

$$c^* = \frac{1}{2}(c^i + c^k) + \frac{1}{4}(\gamma - 1)(u_n^i - u_n^k)$$
(26)

Finally, the artificial viscosity term is:

$$\delta \mathbf{U} = \frac{1}{2\bar{a}} \begin{pmatrix} p_1^i - p_1^k \\ \vdots \\ p_N^i - p_N^k \\ (pu)^i - (pu)^k \\ (pv)^i - (pv)^k \\ \frac{\bar{a}^2}{\bar{\gamma} - 1} (p^i - p^k) + \frac{1}{2} ((pU^2)^i - (pU^2)^k) \end{pmatrix}$$
(27)

where  $U^2=u^2+v^2$  and  $\bar{a}=(a^i+a^k)/2$  and  $\bar{\gamma}=(\gamma^i+\gamma^k)/2$ .

### 3.1. Boundary conditions

The types of boundaries used here are solid wall, axis of symmetry and in- or outflow boundaries. At the wall slip conditions are enforced using ghost cells in the standard manner. The flow variables  $\rho$ ,  $\rho e$  and the tangential velocity are given symmetric values in the ghost cells, while the normal velocity is set antisymmetric. In- and outflows are treated as determined by the waves passing the boundaries in the standard manner: at supersonic inflows all conserved variables are pre-set as all waves are entering the domain from the outside. At supersonic outflows all waves are exiting and the flow variables at the boundary are extrapolated from the interior. At subsonic inflows the flow directions and total temperature and pressure are preset. The speed of sound at the boundary is calculated from the outgoing Riemann invariant acquired from the interior cells, which allows the conserved variables to be extracted from the set total conditions. Finally, at subsonic outflows the pressure is specified, and the densities and momentum are extrapolated from the interior. All terms in the energy are then known. Symmetric boundary conditions are fulfilled by employing reflected ghost cells in the same manner as the solid walls.

### 3.2. Mesh refinement

The Euler solver was coded in Matlab and run on a single CPU: the calculations are very cheap but quite limited regarding grid size. This is in most cases not a problem as the intended use of the code covers simple geometries, but to better resolve the front shocks an adaptive mesh refinement was also implemented. The initial meshes are prepared using *DistMesh*, a delauney triangulation code for MATLAB developed by Persson & Strang (2004).

The general purpose of the refinement is to increase the number of cells around discontinuities, especially shock waves. The following basic algorithm was implemented, and is a simplified method based on Berger & Oliger (1984):

- 1. Select the target level of refinement according to some selection criteria
- 2. Divide all selected cells
- 3. Repeat 1-2 until the target level of refinement is reached
- 4. Select the cells to be de-refined by means of a sensor function and some selection criteria
- 5. Divide all selected cells
- 6. Repeat 4–5 until the target level of refinement is reached

The whole process is then repeated at every  $n_{step}$  time-step.

3.2a. Cell division. Triangles marked for selection (see below) are divided by adding three new vertices at the mid point of each edge. The triangle is subsequently divided into four equilateral triangles by connecting the new vertices with edges. To conform with the matrix-based flux calculations which are dependent on a set number of edges per triangles, the neighbouring cells which are not set for refinement are split in half to connect the courser and finer regions. Figure 3 illustrates the process. The method was chosen over other strategies as the four-way splitting keeps the aspect ratio of the triangles and although the connecting half-splitting worsen it, the initial meshes have well-behaved aspect ratios and skew triangles have not been found to cause trouble.

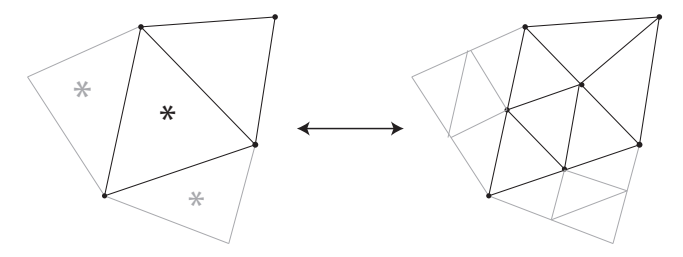


Figure 3: Division strategy: stars show cells marked for refinement. As the top right cell is not marked for refinement, it is split in half as one cell may only have three nodes. Some cells are gray for illustrational purposes.

3.2b. Cell selection. A simple sensor function  $C_i$  was used to determine which cells are to be refined, indirectly based on density gradients in order to resolve discontinuities. For each cell:

$$C_{i} = \frac{\sum_{k=1}^{3} (\rho_{i} - \rho_{k})}{\sum_{k=1}^{3} (\rho_{i} + \rho_{k})}$$
(28)

The sensor is then compared to preset values in order to determine what target level of refinement for each cell. The criteria for de-refinement use the same function but the values are set lower to avoid cells flipping back and forth between being refined and de-refined when the sensor is close to the limits. Eq. 28 was chosen as it is fast to compute and showed to work fine. To prevent resolved discontinuities to propagate into less refined regions, a buffer zone of refined cells needs to be created around each discontinuity. This was arranged by simply smearing the sensor function in space before cell selection. Except the sensor function, a number of selection criteria were implemented to create a smooth refinement:

- No more then one level of refinement may differ between two neighbouring cells.
- If a cell has two or three neighbouring cells set for refinement, that cell too will be refined.
- If half-split cell (i.e. a triangle divided in two) is set for refinement, it will first be joined with its split partner and the united cell will be divided in four.

3.2c. De-refinment. When the mesh is de-refined, the original configuration is saved such that cells set for de-refinement are only united with triangles that also belonged to the same original triangle. A separate matrix stores the indices of each cell and which cells have been split from it so the process can be run backwards. The determination of cells to be reunited is made with the same sensor function as for refinement, but the selection criteria is more demanding than for splitting:

- To unite a split cell, all four split cells must be selected by the sensor function
- At least two of the neighbour of the compund cell must either also be set for de-refinement or be a half-split cell.

#### 4. Test of numerical scheme

A number of tests were run to assess how well the code can predict different flow cases relevant for the purpose of the study. Standard shock tube problems were run with different gas and pressure combinations based on previous experiments. Benchmark tests with a plane shock interacting with wedges of different inclinations were also performed.

#### 4.1. Shock tube tests

Shock tube calculations were performed to try the stability and accuracy of the code when multiple species were used. The computational domain was a two-dimensional 1 m tube with height 5 cm. The membrane was positioned at the tube mid point and the states in the high and low pressure sections are designated state 4 and 1 respectively. The tests are tabulated in Table 1, where the Mach number of the front shock is compared with its theoretical value. The initial temperature was for all cases  $T_1 = T_4 = 293$  K.

#	Driver	Test gas	$p_4$ (kPa)	$p_1$ (kPa)	$p_4/p_1$	$M_S$	$T_2$ (K)	$p_2$ (kPa)	$M_S$ (1D)
1	air	air	10	1	10	1.61	408	2.85	1.61
2	air	air	1500	15	100	2.37	591	96.2	2.37
3	air	air	1500	1.5	1000	3.2	860	17.7	3.15
4	air	air	1500	0.15	10000	4.1	1230	19.5	3.85
5	Air mix	Air mix	10	1	10	1.61	409	2.85	1.61
6	Air mix	Air mix	1500	15	100	2.38	593	96.2	2.37
7	Air mix	Air mix	1500	1.5	1000	3.2	860	17.7	3.15
8	Air mix	Air mix	1500	0.15	10000	4.1	1220	19.5	3.85
9	$_{ m He}$	Ar	850	25	34	3.0	1050	267	2.96
10	Не	Ar	1700	10	170	4.4	1988	236	4.37
*11	Не	Ar	1700	0.13	13077	8.35	6640	11.3	8.20
12	He+6% air	Ar	1700	13	131	3.83	1595	236	3.87
13	He+6% air	Ar	1700	1.3	1308	5.7	3177	53	5.77
*14	He+6% air	Ar	1700	13	131	3.86	1578	236	3.87
*15	He+6% air	Ar	1700	1.3	1308	5.74	3225	52.5	5.77
*16	He+6% air	Ar	1700	0.13	13077	7.5	5400	9.1	7.48
17	$N_2$	$C_3H_8$	900	50	18	1.96	359	201	1.95
*18	$ m N_2^2$	$C_3H_8$	1700	5	340	3.27	490	55.9	3.20

Table 1: Shock tube problem calculated using the Euler-solver. The gas "Air mix" is a mixture consisting of 78.03% N<sub>2</sub>, 20.95% O<sub>2</sub>, 0.90% Ar and 0.03% CO<sub>2</sub>. The star in front of a number signifies that mesh refinement was used.

Tests 5-8 were performed with an air mixture and compared with runs 1-4 where air as a single species was used The mixture composition was 78.03% N<sub>2</sub>, 20.95% O<sub>2</sub>, 0.90% Ar and 0.03% CO<sub>2</sub>. The composition was altered to yield mixture values of  $\gamma$  and R equal to those set for the single-species air. These tests were made to check the performance of the multi-species composition compared to the single-gas composition and to see whether or not greatly varying partial pressures introduce errors. Cases 5-8 were carefully compared with the cases 1-4 with one-species air and the results for virtually identical.

The final state of test 12 at t=0.25 ms is shown in Fig. 4. The test was run on mesh of around 150 cells in the length-wise direction. As for all cases 9–18 the low and high pressure sections are filled with different species. The front shock is resolved sharply and the expansion agree well with theory, but the contact surface is smeared, which is partly due to courser mesh refinement and partly numerical smearing.

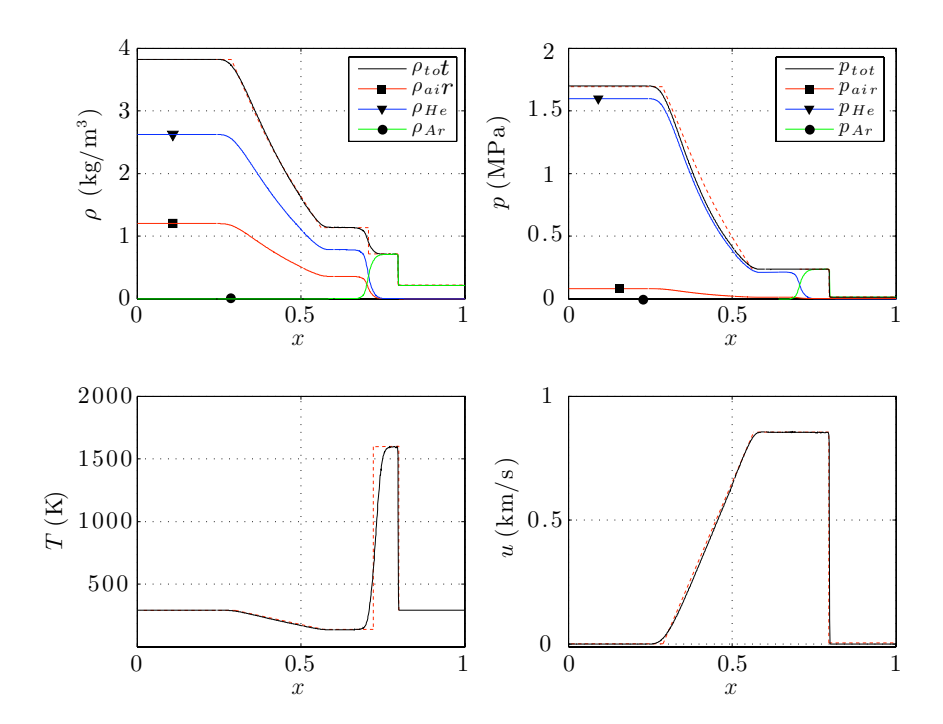


Figure 4: Final state for test 12 at t=0.25 ms. The high pressure section is filled with a mixture of air and helium at 1700 kPa and the low pressure section with argon at 13 kPa. Comparison with the ideal 1D-solution (dashed red).

The values used for  $\gamma$  and R for the different species are tabulated in Tab. 2. These values were used throughout this report.

Gas	$\gamma$	R (J/kgK)
$N_2$	1.40	297
$O_2$	1.40	260
$\operatorname{Ar}$	1.66	208
$_{\mathrm{He}}$	1.66	2080
air	1.40	287
$C_3H_8$	1.13	189
$CO_2$	1.13	189

Table 2: Specific heat ratios and specific gas constants used for the calculations.

### 4.2. Shock reflection

The benchmark test proposed in *Shock Waves* Vol. 2 No. 4 and reported by Takayama & Jiang (1997) was performed. The computational domain is 1x1 m, with an inserted inclination which starts at x=0.25 m. A from the left incoming shock wave with Mach number 2.0 reflects upon the wedge and the simulation is run until the shock is at x=0.9. Two test cases are performed: one with an angle  $46^{\circ}$  and another with  $49^{\circ}$ , chosen purposefully around the transition between Mach and regular reflection. Initial values are  $p_1=30$  kPa,  $T_1=300$  K with a shock wave at x=0.1. The conditions behind are determined by the normal shock relations. A supersonic inlet boundary condition is at x=0, while the remaining boundary is treated as slip wall (there is no need for an outflow boundary as the simulation is stopped prior to the shock reaching the wall).

The test was run on an unstructured grid of  $65\times10^3$  cells without mesh adaption. Isopycnics for the two cases are presented in Fig. 5. The shock passing over the  $49^\circ$  wedge reflects regularly, while the emergence of a Mach stem is seen in the  $46^\circ$ -case. This agrees well with experiments and theory. Glaz *et al.* (1985)

Additional tests were made with the same configuration, but with with 2nd-order interpolation of the fluxes and mesh adaption on a courser base mesh of  $<10\times10^3$  cells. The results are plotted in Figs. 6. The calculation time is faster, but the results sharper to those of the finer static mesh. A small Mach stem can be discerned in in the 49° case, which was missing in the test without mesh refinement. Comparing with the reported interferograms in the previously cited paper (Takayama & Jiang 1997), good agreement were seen and the results deemed satisfactory.

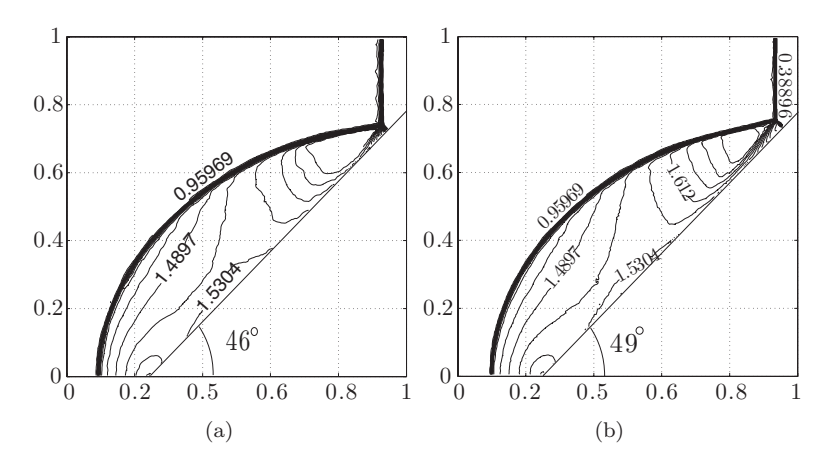


Figure 5: Isopycnics of shock reflection on a wedge with angle  $46^\circ$  (a) and  $49^\circ$  (b). Values in kg/m³.

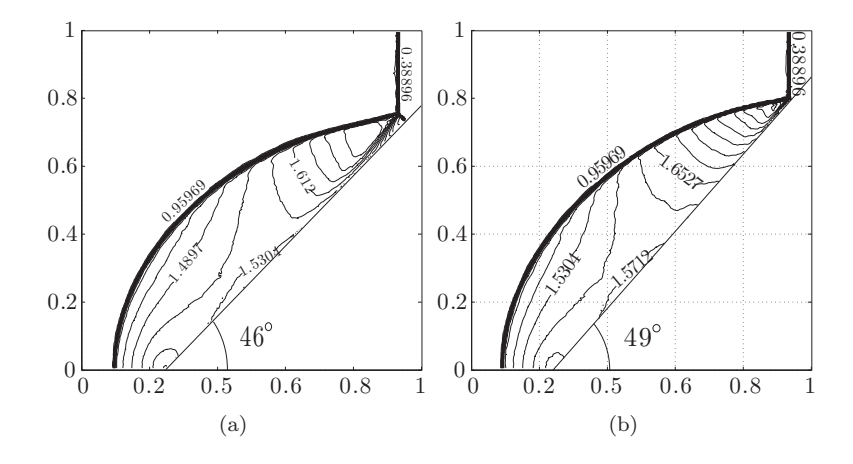


Figure 6: Isopycnics of shock reflection on a wedge with angle  $46^\circ$  (a) and  $49^\circ$  (b). 2nd order in space, automatic mesh refinement. Values in kg/m³.

#### CHAPTER 2

# Calculations: cylindrical shock tube at KTH

Two sets of numerical studies were performed: 1)the whole tube flow was solved for a number of cases and, more importantly, 2) more refined tests were performed on the sharp bend and the convergence chamber. All runs were performed using the axisymmetric Euler solver presented above (the radial coordinate y will be referred to as r in this part) with adaptive mesh refinement. The maximum level of refinement was set to two (i.e. up to 16 times higher cell density) and the refining was performed each fifth time-step.

The two main purposes of the whole tube study was to provide initial conditions for finer tests on the 90° bend and convergence chamber and to answer the following questions: 1) whether the shock waves kept their strength through the transition section or not; and 2) if the shock when passing through the annular section achieved a plane form and had constant velocity.

The study on the bend and test section aimed to answer the questions raised about the ability of the design to create strong converging shocks at all and how dominant the three-dimensional effects are.

### 1. Shock tube

A number of test cases were run on the domain sketched in Fig. 7, with different initial conditions corresponding to previous and planned experiments. The numerical domain is the upper half (r>=0) of the shock tube. All non-symmetric boundaries are treated as slip walls and the initial conditions are determined by the states 1 and 4.

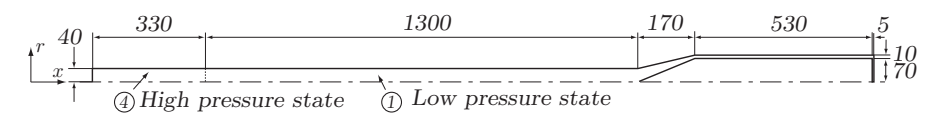


Figure 7: Computational domain for the whole shock tube.

The numerical test showed that, for all cases, the shock wave retained its strength through the transformation section and moved at a constant velocity. The reflected expansion did not catch up with the shock and the shock wave

#	Driver	Test gas	$p_4$ (kPa)	$p_1$ (kPa)	$M_S$	$M_S$ (from experiments)
1	He+6% air	Ar	1550	10	3.9	3.9
2	$N_2$	$C_3H_8$	900	50	2	1.9
3	$N_2$	$C_3H_8$	900	25	2.2	2.1
4	air	$N_2$	850	30	1.9	1.9
5	air	$N_2$	1800	13.3	2.4	2.4
6	He+6% air	$N_2$	1900	35	2.8	2.8
7	air	Ar	850	37	1.95	1.9
8	air	Ar	1800	20	2.5	2.4
9	$\mathrm{He}{+6\%}$ air	Ar	1550	10	3.9	3.9
10	He	$\operatorname{Ar}$	1550	0.88	6.2	6.1

Table 3: Tests with the shock tube configuration.  $T_1$ = $T_4$ =293 K. Air was treated as a single species. Numerical and experimental  $M_S$  is measured in the annular section. Errors on measured Mach number are about 2% for experimental data.

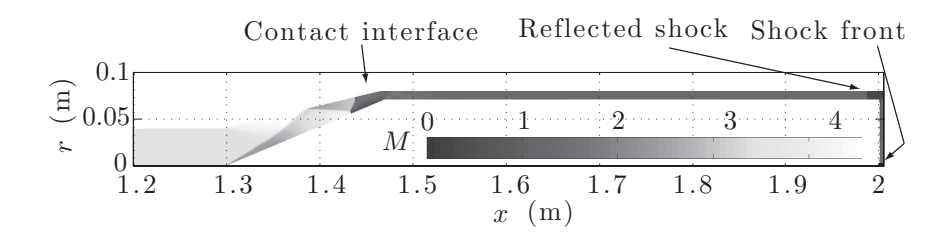


Figure 8: Mach number distribution in the tube for a run in air, initial  $M_S$ =2.4, at the moment just before shock focusing. The Mach number in the transformation section is high since the contact surface has just passed it and it is filled with cold expanded gas at a high velocity.

focused and reflected in the convergence chamber long before upstream disturbances reached the end section. As the flow in the annular section was uniform for all cases, simple initial and boundary conditions could be applied for the finer test section runs.

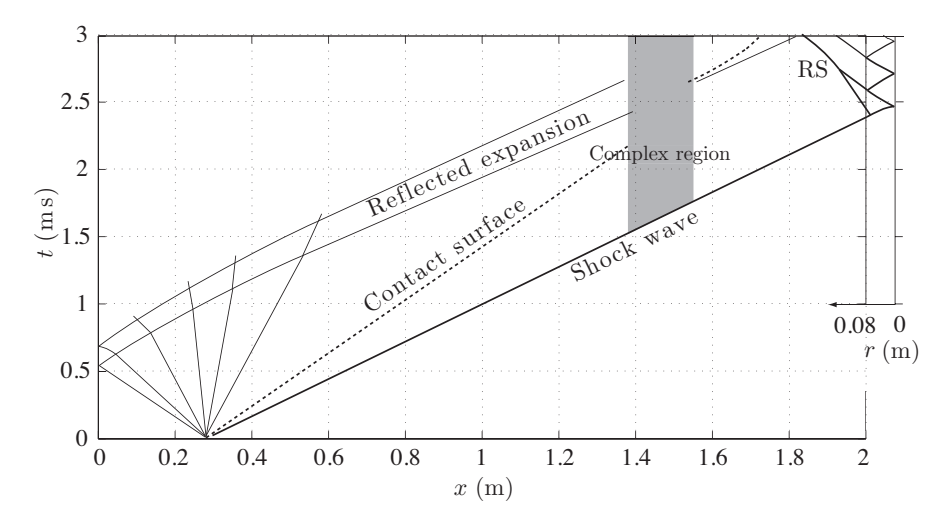


Figure 9: Wave diagram of run 9, He/air-Ar run,  $M_S$ =3.8. To the right of the horizontal x-scale the radial position in the test section has been added: focus is at r=0. The intersection between the x and r-scales represents the 90° bend. The "complex region" is the transformation section; neither the standing waves or the unsteady waves passing it can be well represented one-dimensionally.

### 2. Test section

The numerical domain is shown in Fig. 10. For later references, the origin is placed in the inner corner at the centreline of the convergence chamber, marked with an O in the figure. The number of initial grid points was around  $7 \times 10^4$ . The calculations were started with a standing shock wave of strength  $M_S$  at x=-15 mm with the post-shock conditions determined from the normal shock relations. The flow velocity behind the shock was super-sonic in the laboratory frame in all cases but one. The shock was given a relatively long passage before the bend to numerically stabilize the shock before entering the bend (in hindsight it proved to be un-necessarily long). Before the simulation was started the mesh was refined to prevent initial smearing of the shock front. The simulation was run until the shock reached the axis of symmetry.

Table 4 provides a list of the performed test cases. The Mach number was varied from a weak shock of  $M_S=1.2$  to a highest value  $M_S=5$  for air and  $M_S=7$  for argon. The higher Mach numbers approached the limit where the perfect gas law is still applicable. As the shock accelerates in the convergence section the validity of the gas law had to be checked afterwards as the maximum shock velocity was not known exactly beforehand. Also, the perfect gas law is reasonably valid for higher Mach numbers in argon than in

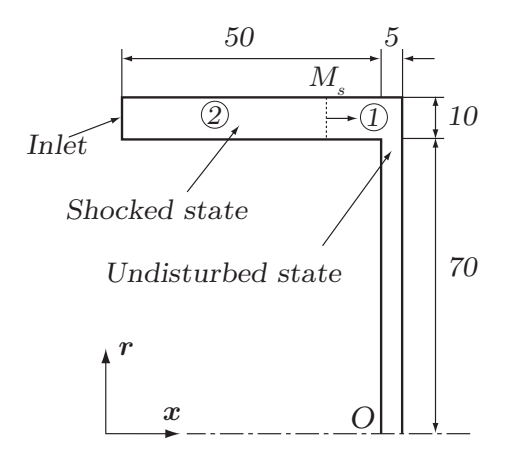


Figure 10: Computational domain and initial conditions. The inlet is treated as a supersonic inflow for all cases, except for case 1, where it is subsonic. The other walls are treated as slip walls. The conditions in state 2 are determined from the normal shock relations for a shock of strength  $M_S$  propagating into a gas in state 1.

air. In air vibrational and rotational excitation as well as dissociation become significant at comparably low temperatures.

#	Test gas	$p_1 \text{ (kPa)}$	$M_S$
1	air	10	1.2
2	air	10	1.9
3	air	10	2.8
4	air	10	3.8
5	air	10	5.0
6	Ar	10	1.9
7	Ar	10	2.8
8	Ar	10	3.8
9	Ar	10	5.0
10	$C_3H_8$	10	1.9

Table 4: Sharp bend and convergence tests.  $T_1 = 293$  K for all cases. Air was treated as a single species.

2.0a. Shock propagation and mechanisms in the bend. The propagation of the shock through the test section is illustrated by the numerical schlieren (shade of gray depending on  $|\nabla \rho|$ ) images presented for a case in argon with  $M_S$ =2.8 (Figs. 11) and air,  $M_S$ =5.0 (Fig. 12). The presented cases are representative for all cases as the basic flow is similar. When the shock front enters the bend, the lower part of the shock is diffracted around the corner while the upper part continues and reflects off the end wall. The reflected shock propagates back into the annular channel and down into the test section where it overtakes the diffracted shock. The merged shocks converges towards the centre. As a result of the reflections, a triple point on the shock front is moving back and forth between the walls. Due to these three-dimensional shock interactions the shock front is not completely straight.

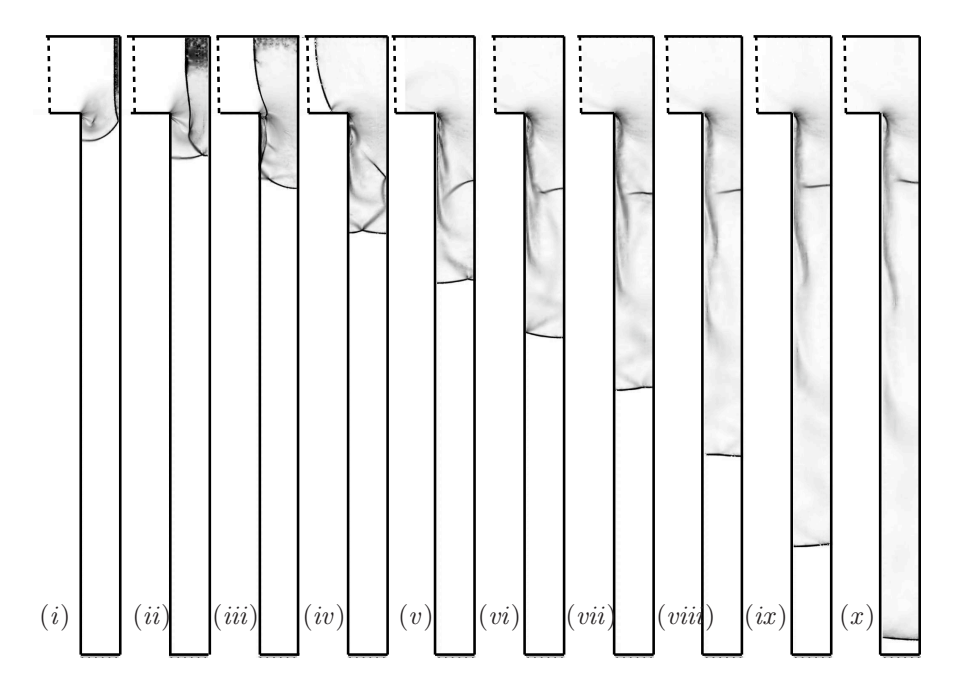


Figure 11: Numerical schlieren of flow in the convergence chamber, shock in argon,  $M_S=2.8$ .

Here follows an elaborated description of the argon case. In image (i), the lower part of the shock has diffracted around the corner while the upper part which has not been reached by the signals generated at the corner<sup>1</sup> propagates uninterrupted until is reflects on the end wall, which has just happened in the image (i). The snapshots in Fig. 11 (ii) and (iii) are also shown in Fig. 13

in the form of isobars and flow direction. In Fig. 11(ii) resp. Fig. 13(b) the reflected shock is seen propagating through the expansion generated at the corner, curving downwards in the process. The high pressure generated by the reflection of the incoming shock, about 200 kPa, to be compared with 48 kPa behind the incoming shock, is gradually weakened through the expansion. When the reflected, curved shock eventually overtakes the diffracted shock, it is weaker than the incoming shock in the annular section - the pressure behind it is roughy 28 kPa. The immidiate loss at the bend can be evaluated by this attenuation.

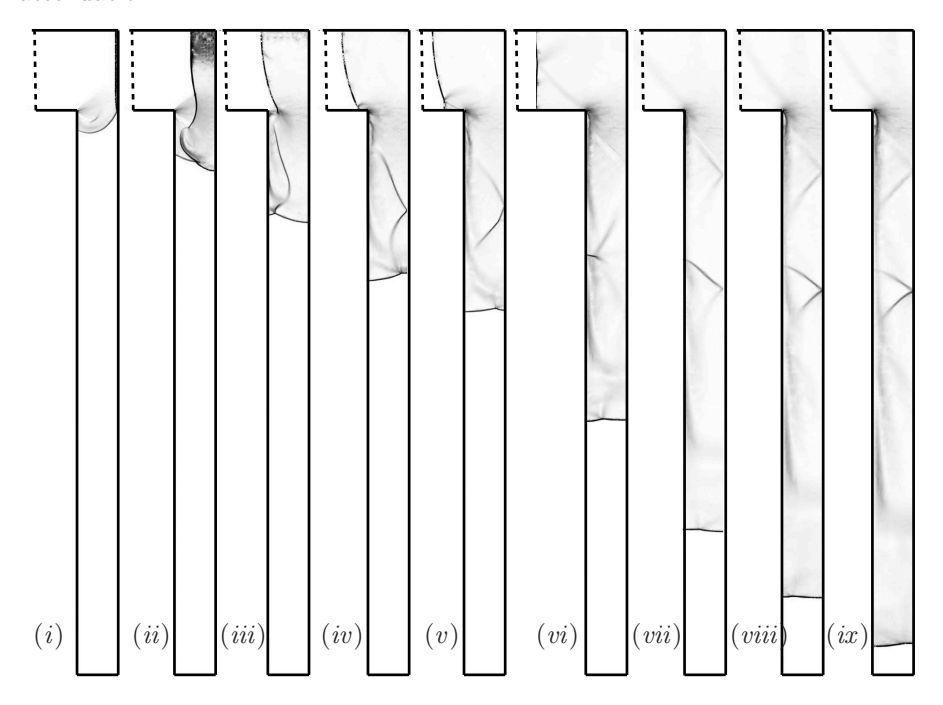


Figure 12: Numerical schlieren of flow in the convergence chamber, shock in air,  $M_S = 5$ .

The high pressure zone works to drive the front shock and the flow behind it. Whereas the shock returning through the annular section (top, images Fig. 11(iii) and (iv)) completely halts the flow in the upper section, the higher pressure in the corner area drives a flow into the convergence chamber and provides energy for the converging shock. The flow is not uniform, as evident

<sup>&</sup>lt;sup>1</sup>The propagation path of this information, corresponding to the characteristic coming from the bend, can be discerned as the density gradients in Fig. 11(i) and (ii).

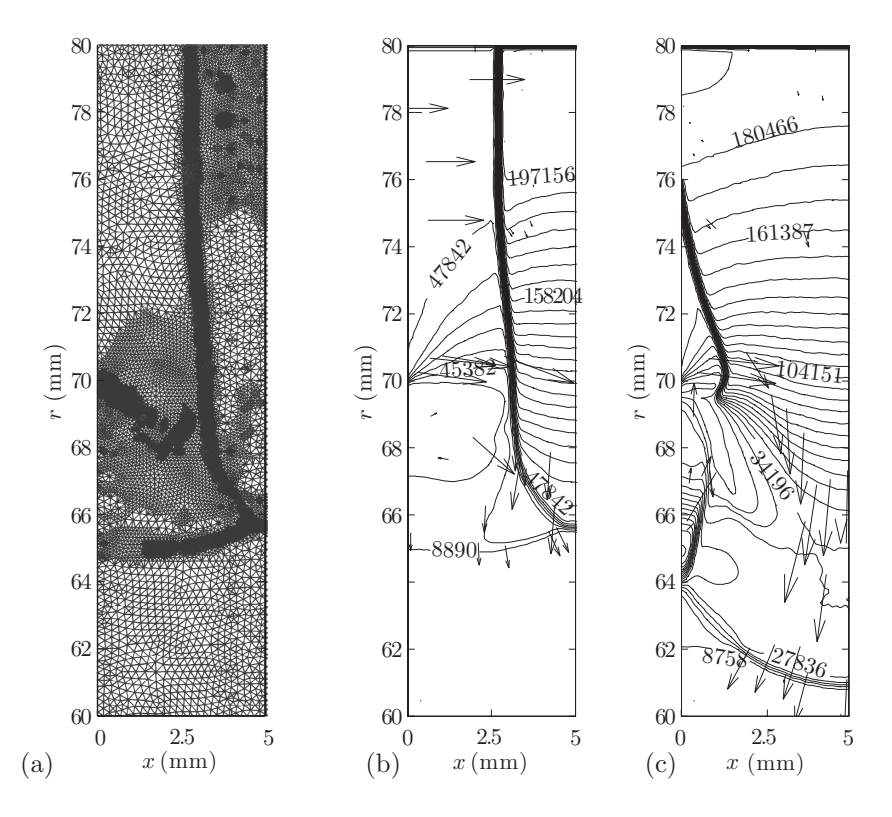


Figure 13: Isobars and flow direction (b) and (c) at time instants corresponding to Fig. 11 (i) and (i) respectively. Shock in argon,  $M_S = 2.8$ . The arrow indicate direction and magnitude of the flow velocity. In (a) is a snapshot of the adaptive mesh at the time of (b).

by the standing shocks around  $r \approx 50-60$  mm which eventually reach a steady state, Fig. 11(vi) through (x). In argon the standing shock is normal to the wall, while in the cases in air several oblique shocks are instead present, which can be seen in Fig. 12. Figs. 14, 15, 16 and 17 show the centre-line flow (along x=2.5 mm) for the different cases at different time instants.

For  $M_S$ =1.2 case in air Fig. 14 shows how the initial diffraction around the corner results in a subsonic pressure wave. It appears like it coalescs into a shock; this is however not the case. The diffracted wave is overtaken by the reflected shock around r=40 mm before it has time to break into a shock. As the flow behind is entirely subsonic no expansions or shocks are to be found. In all other cases the flow is supersonic and standing shocks appear

in the outer region where gas enters the convergence chamber. In all cases, the flow approaches a pseudo-steady state (which can also be seen in the schlieren images in Fig. 11). The flow in argon had a tendency to stabilize at earlier times. In argon the standing shock tended to be normal to the wall, while several oblique shocks appear in air runs.

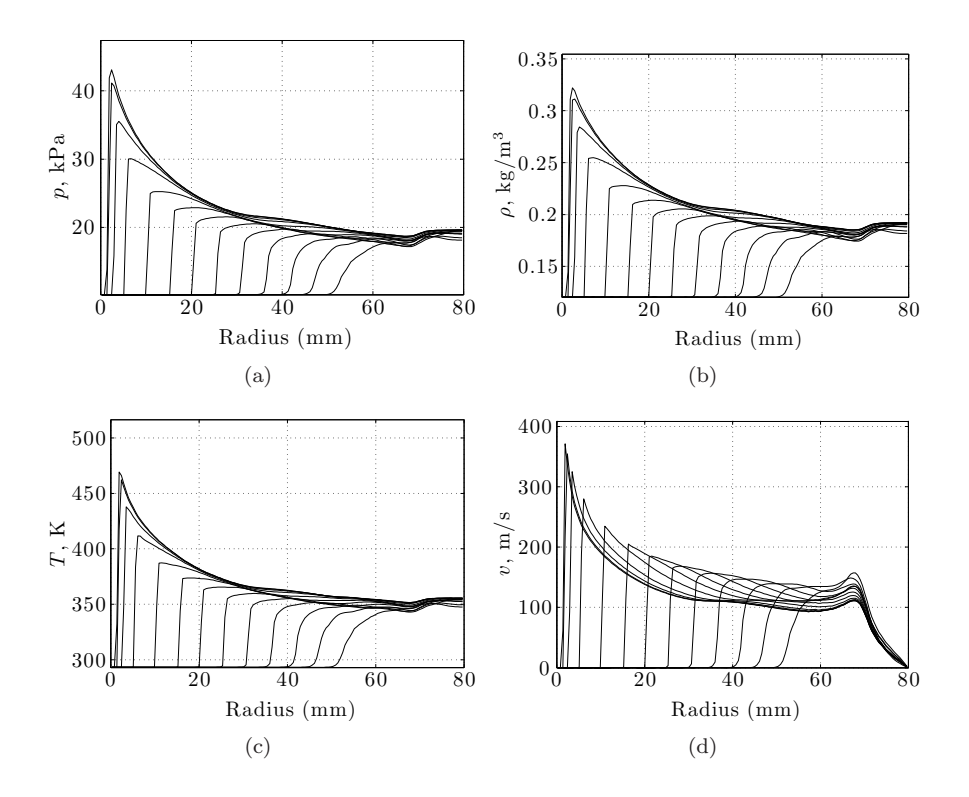


Figure 14: Flow condition behind shock front at different times: (a) pressure, (b) density, (c) temperature and (d) radial velocity. Air,  $M_S$ =1.2.

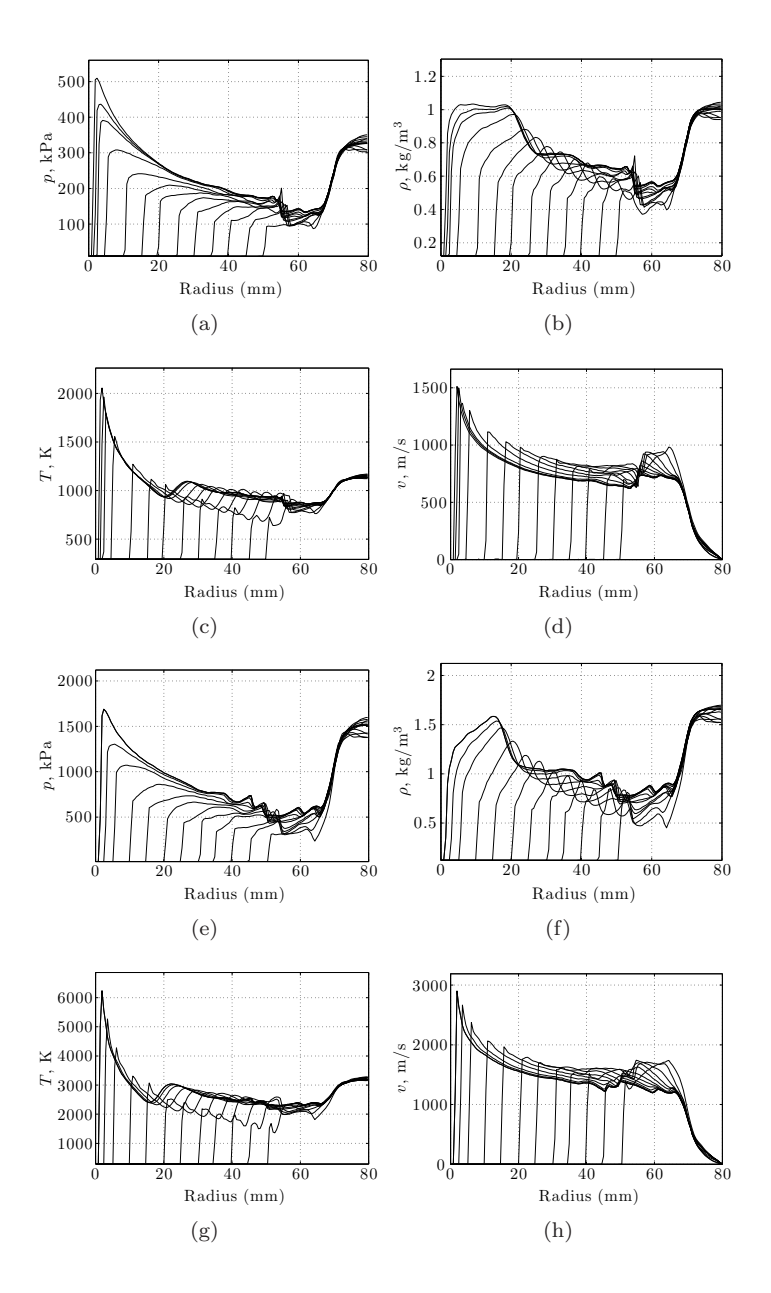


Figure 15: Flow condition behind shocks waves in air at different times:  $M_S=2.8$ : (a) pressure, (b) density, (c) temperature and (d) radial velocity.  $M_S=5.0$ : (e) pressure, (f) density, (g) temperature and (h) radial velocity.

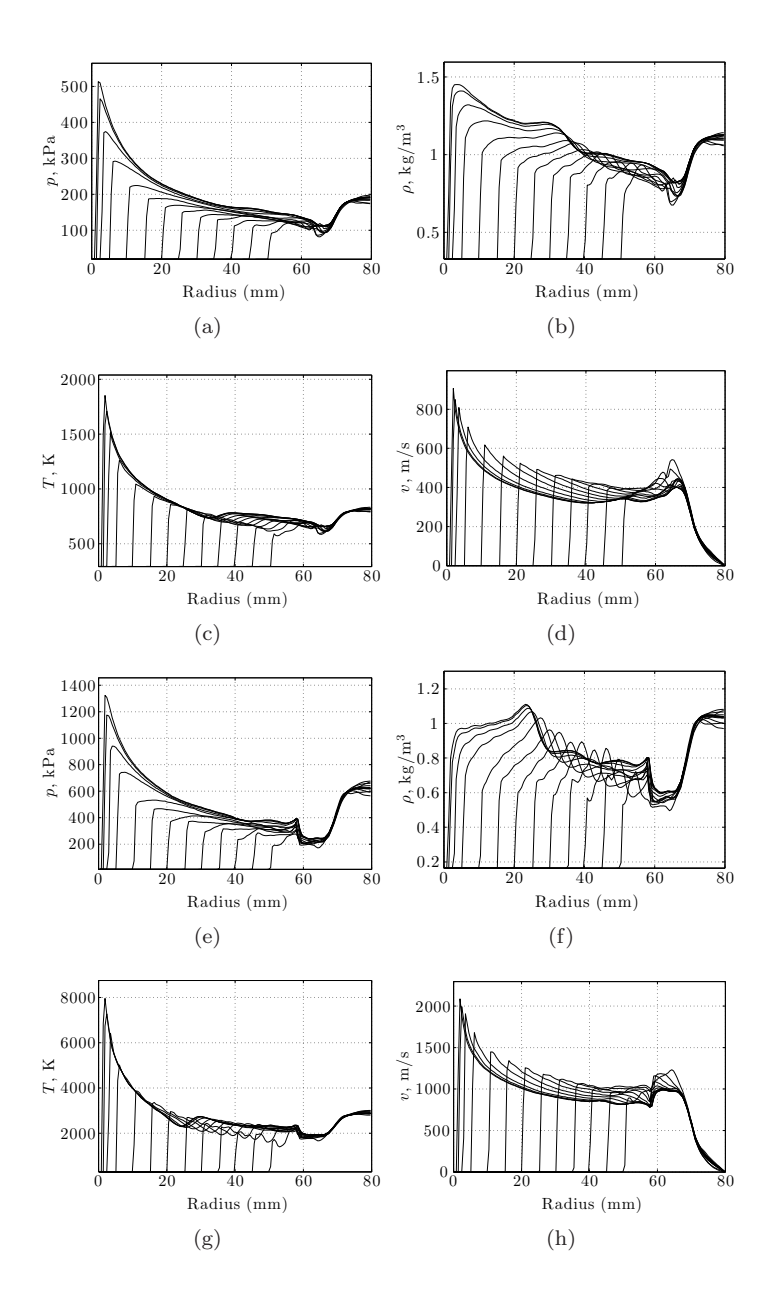


Figure 16: Flow condition behind shocks waves in argon at different times:  $M_S=1.9$ : (a) pressure, (b) density, (c) temperature and (d) radial velocity.  $M_S=3.8$ : (e) pressure, (f) density, (g) temperature and (h) radial velocity.

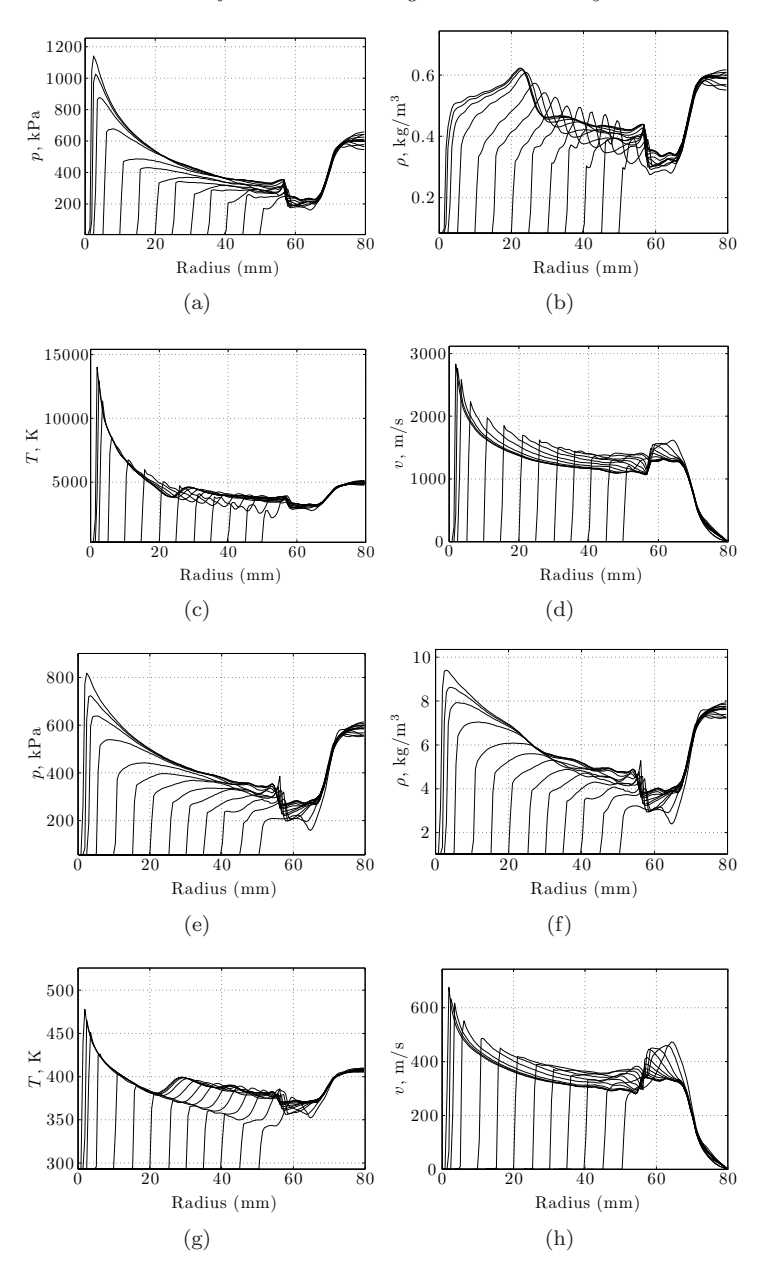


Figure 17: Flow condition behind shocks waves in at different times: In argon,  $M_S = 5.0$ : (a) pressure, (b) density, (c) temperature and (d) radial velocity. In propane,  $M_S = 1.9$ : (e) pressure, (f) density, (g) temperature and (h) radial velocity.

2.0b. Three-dimensionality. Due to the reflections, several waves are propagating behind the front in the lateral direction and triple points move laterally along the shock front. One triple point is dominant over the others and divide the shock front in two all the way to focus. It is most easily visible in (iii) through (vi). As the front shock accelerates and the cross-wise waves become smeared out through reflections and the strong 3-d effects are diminishing with radius. To assess the influence of the predominant triple point, the Mach number of the two parts of the front on either side of the it is plotted in Fig. 18 for two cases in argon,  $M_S = 1.9$  and 5. The Mach number along the inner (left) and outer wall, designated A and B, is plotted together with the centre-line Mach number.

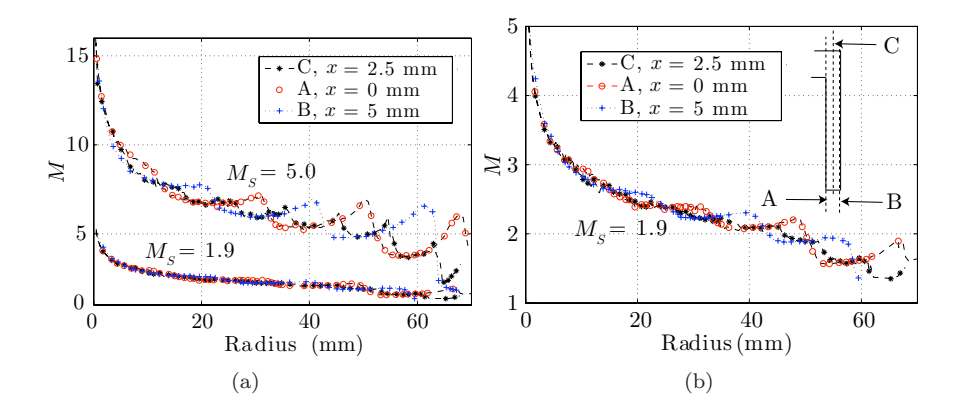


Figure 18: Oscillation of shock front Mach number along three different cross-sections of the test domain: inner wall, outer wall and middle - the cross-sections are sketched in (b). Two shocks in argon (a):  $M_S = 5.0$  and  $M_S = 1.9$ . Figure (b) shows the weaker shock from (a) in a different scale.

Figure 19 shows the variation of pressure behind the shock front and Mach number of the front for different initial Mach numbers along the inner and outer walls (A and B as sketched in Fig 18(b)). The peculiar periodical behaviour is a result of the cross-wise waves: the reflection of the main triple point is manifested by the differences going to zero.

2.0c. Shock strength intensification. The acceleration of the shock waves is plotted in Fig. 20 which shows the shock front Mach number in the middle of the test section (cross-section C, see above). In the outer part of the region the Mach number changes violently around r=65-70 mm but soon starts oscillating around the analytical solution to the ideal problem. The Mach number still wobbles due to the cross-wise waves, but the plotted comparison

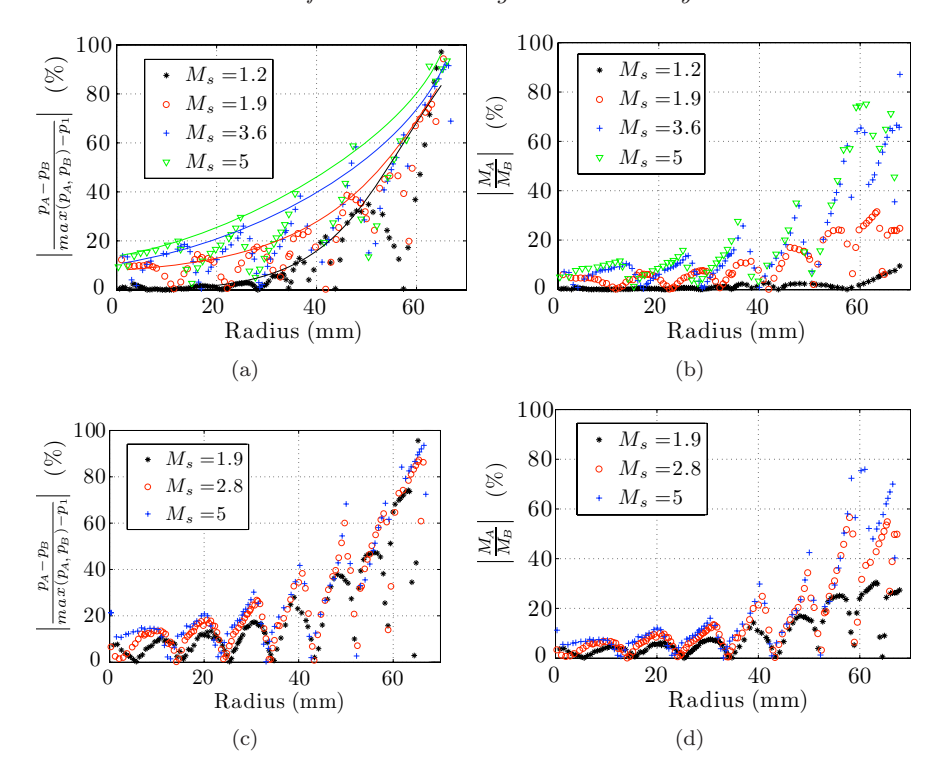


Figure 19: Shock waves in air (a, b) and argon (c, d): pressure (a, c) and Mach number variation (b, d) over the shock front in the x-direction (depth). The jumps show where the major triple point reflects at the inner and outer walls.

(dashed lines) with the self-similar solution starting at r=50 mm shows that the agreement with the self-similar solution is very good except for the weakest shock in air,  $M_S=1.2$ , which is showed specifically in the inlaid figure in Fig. 20.

Figure 21 show the Mach number of the accelerated shock front at a radius of 1 mm. As expected from the self-similar exponent, the shocks in gases with higher heat capacity ratios are intensified more. Although the amplification seems linear, Fig. 21(b) shows that this is indeed not the case; the ratio  $M(r=1\text{mm})/M_S$  has a maximum which for argon is between  $M_S=4$  and 5. The increasing influence of 3D effects for higher Mach numbers has a deteriorating effect on the shock intensification. The low amplification of the  $M_S=1.2$  shock is due to that a shock front in the convergence chamber is not formed until later than in the other cases, as explained in section 2.0a.

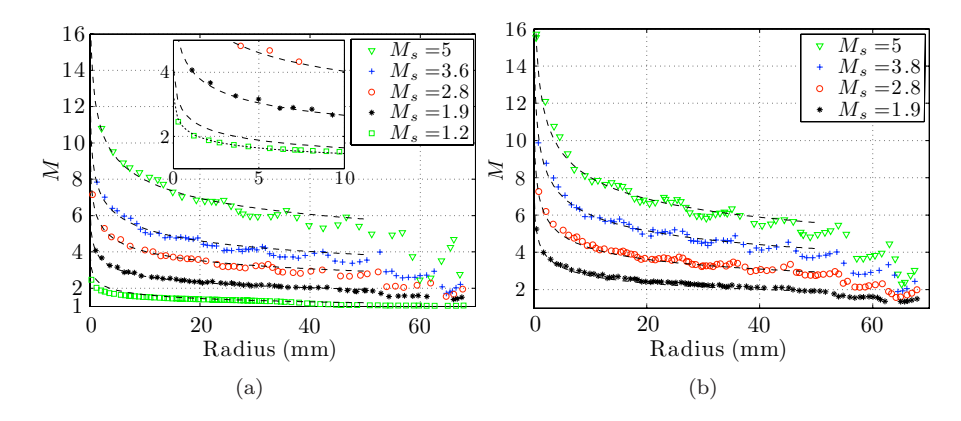


Figure 20: Strength of shock as it converges: shocks in air (a) and argon (b). Dashed lines: comparison with Guderley's solution (dashed), starting at r=50 mm. The inlaid image in (a) shows two self-similar paths for  $M_S=1.2$ ; one starting at r=50 mm and a second (finer dashes) starting at r=40 mm, showing how the weak shock does not converge according to the self-similar solution until later than the other cases.

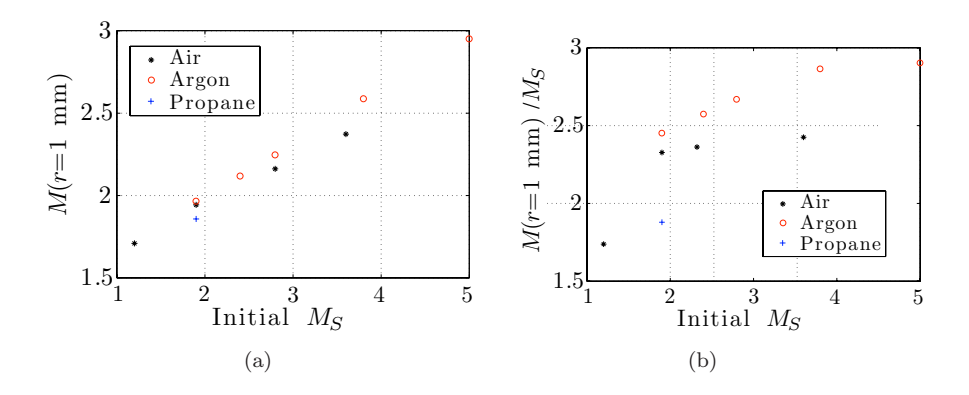


Figure 21: Resulting shock Mach number at radius r=1 mm for various initial Mach numbers  $M_S$ ; (a) shows the actual shock Mach number while (b) displays the amplification.

#### 3. Conclusions

Calculations were performed to assess the performance of the circular shock tube at KTH designed to produce strong converging cylindrical shock waves. The flow in the entire tube was calculated long beyond the time of focus in the convergence chamber to get an overview of the full problem. The main questions were whether the shock and flow in the annular section are constant and uniform and if the reflected expansion has time to catch up and interfere with the shock before the convergence. On both questions the answers were favourable: the shock front, after passing through the transformation section through a series of reflections, retained a uniform annular-plane shape and proceeded with its original velocity. The reflected expansion wave did not, for any case, reach the front shock before focus.

The 90° bend design is able to produce strong convergent cylindrical shocks which are greatly intensified. The incoming shock wave reflects off the back wall, and into the test section. When hitting the wall the shock a high pressure zone is created in the corner which acts as a reservoir driving the flow into the test section. A downside is the non-planarity of the resulting converging shock. Cross-wise waves are propagating between the walls in the test-section, attached to the front at a triple point, which moves along a zig-zag line towards the centre. The strength of these cross-wise waves was quantified by considering the local Mach number and pressures on each side of the triple point. It was found that the effects became relatively weaker as the shock converged. The influence of these cross-wise waves were also larger for larger initial Mach numbers, although close to focus the relative strength of these waves was of the same order for all initial Mach numbers - an exception was the case for  $M_S=1.2$  in air, where the cross-waves were attenuated. For the worst cases, at r = 10 mm, the Mach number variation over the shock front was less then 10%.

The acceleration of the shock in the test section was compared with the similarity solution of Guderley for the ideal 1D case. Despite losses due to lateral flow, the acceleration showed a surprisingly good agreement with the theory, and we conclude that the sharp bend with a contraction is efficient at producing strong converging shocks.

# References

- Berger, M. J. & Oliger, J. 1984 Adaptive mesh refinement for hyperbolic partial differential equations. J. Comput. Phys. 53, 484–512.
- GLAZ, H., COLELLA, P., GLASS, I. I. & DESCHAMBAULT, R. 1985 A numerical study of oblique shock-wave reflections with experimental comparisons. *Proc. R. Soc. London, Ser. A* 398, 117–140.
- GUDERLEY, G. 1942 Starke kugelige und zylindrische Verdichtungsstöße in der Nähe des Kugelmittelpunktes bzw. der Zylinderachse. Luftfahrtforschung 19, 302–313.
- KLEINE, H. 1985 Time resolved shadow graphs of focusing cylindrical shock waves. *Tech. Rep.*. RWTH, Aachen, Germany.
- Perry, R. W. & Kantrowitz, A. 1951 The production and stability of converging shock waves. *J. Appl. Phys* **22**, 878–886.
- Persson, P. -O. & Strang, G. 2004 A simple mesh generator in matlab. SIAM Rev. 46, 329–345.
- Sun, M. & Takayama, K. 2003 An artificially upstream flux vector splitting scheme for the Euler equations. *J. Comput. Phys.* **189**, 305–329.
- TAKAYAMA, K. 1977 Shock propagation along 90 degree bends. In *Proc. 11th Intern. Symp. on Shock Waves*, pp. 74–81. University of Washington Press, Seattle.
- Takayama, K. & Jiang, Z. 1997 Shock wave reflection over wedges: a benchmark test for CFD and experiments. Shock Waves 7, 191–203.
- TAKAYAMA, K., KLEINE, H. & GRÖNIG, H. 1987 An experimental investigation of the stability of converging cylindrical shock waves in air. *Exps. Fluids* 5, 315–322.
- WATANABE, M. & TAKAYAMA, K. 1991 Stability of converging cylindrical shock waves. Shock Waves 1, 149–160.
- Wu, J. H. T., Elabdin, M. N., Neemeh, R. A. & Ostrowski, P. P. 1977 Production of converging cylindrical shock waves by finite element conical contractions. In Shock tube and shock wave research: Proc. Eleventh Intern. Symp. on Shock Tubes and Waves, pp. 107–114. Seattle, Wash., USA: University of Washington Press.

Paper 7

7

# Generation of spherical converging shocks in a shock tube by wall shaping

By Malte Kjellander, Nils Tillmark and Nicholas Apazidis

Department of Mechanics, Royal Institute of Technology, SE-100 44 Stockholm, Sweden

Manuscript.

#### 1. Introduction

Converging shock waves have have been studied during the past seventy years, the research driven by the ability to focus the energy of the shock wave to the convergence focus where extremely high pressures and temperatures can be achieved. The research was initiated in 1942 by Guderley who published a self-similar solution of the amplification of strong converging spherical and cylindrical shock waves close to the center of convergence. Another solution to the problem was presented by Stanyukovich (1960), and since then a large number of analytical and numerical studies have been conducted, e.g. Butler (1954). Lazarus & Richtmyer (1977), Wang (1982). When the shock waves converge they accelerate as they approach the focal point, where extreme condition are created as the shock front converge and reflects, passing through the already heated gas once more. Ideally the acceleration is infinite but when real length scales are introduced the theory naturally breaks down when the size becomes too small: in practice however, the acceleration and achievable energy concentrations seem to be mainly limited by the symmetry and stability of the shock wave.

Perry & Kantrowitz (1951) made the first experiments with converging shocks. Using a shock tube with a tear-drop inner body plane shock waves were shaped into a cylindrical form. They found that the shock strength was amplified to such a degree that the gas emitted a sharp light flash at shock implosion. Further experiments in tubes following the basic principles of their design have been made by Wu et al. (1977), Takayama et al. (1987), Watanabe & Takayama (1991), Eliasson et al. (2006) among others.

The pressure and temperature concentrations are not only interesting from an academic point of view and studies on practical applications have been made, e.g. diamond synthesis (Glass & Sharma 1976) ,attempts to initiate fusion reactions (Glass & Sagie 1982; Terao *et al.* 1995). Currently converging

shocks are used to shatter kidney stones in vitro, although the potential future applications in medical, material science and other fields warrant more studies in the field.

All else equal, spherical shock waves focus the energy more efficiently than cylindrical shock waves. Previous studies at the Department of Mechanics at KTH involved creation of cylindrical shocks in a shock tube with a shockshaping end section similar to those of Kleine and Takayama. The aim of the present study is to create a spherical convergence process by forming the plane shocks into a spherical segment and compare the results with the cylindrical studies. Setchell et al. (1972) used a setup with a shock tube ending with a uniform cone. Although the strength of the shock increased, it was done by successive Mach reflections at the wall and axis. The diffraction cycle continued through the whole length of the cone. The diffraction process in the twodimensional equivalent, a wedge, was recently thoroughly studied by Bond et al. (2009). To overcome such diffraction losses Dumitrescu (1983) and Saillard et al. (1985) theorized about a continuously changing wall to smoothly curve the shock front before entering a conical end section. Dumitrescu (1992) provided a proof of the existence of such a shape, its form determined with Whitham's ray-tube theory (1959). Recently Zhai et al. (2010) applied the same method to create cylindrical shock waves.

In this study, we present a three-dimensional device such as envisioned by Dumitrescu. However, as he pointed out, viscous boundary layer effects are expected to be so influential in the narrow channel that a rigorous calculation of an ideal shape is a superfluous task. We instead opted to use a simple smooth curve which was first tested numerically and tweaked until it produced nearly spherical shocks. Such a transformation section was manufactured and attached to a circular shock tube with a cross-sectional diameter of 80 mm. The transformation ends into a 21 mm long cone with 21° angle. The tip of the ending cone is cut and a quartz window allows optical measurements. In this first prototype no intruding sensors have been placed inside the convergence section to avoid introducing disturbances which might break up the highly sensitive symmetry. When the shock wave converges to the end point of the contraction a bright light pulse is emitted as the gas is heated to high temperatures. Non-intrusive spectrometric and photometric measurements of these light pulses were made for a range of different initial pressures and Mach numbers. Runs have been made in argon with initial shock Mach numbers ranging from  $M_S \approx 1.5$  to  $M_S \approx 6$ . We present some preliminary results showing spectra from the light emission indicating blackbody temperatures of up to  $\sim$ 27,000 K created by the implosion of a shock with initial Mach number 3.9.

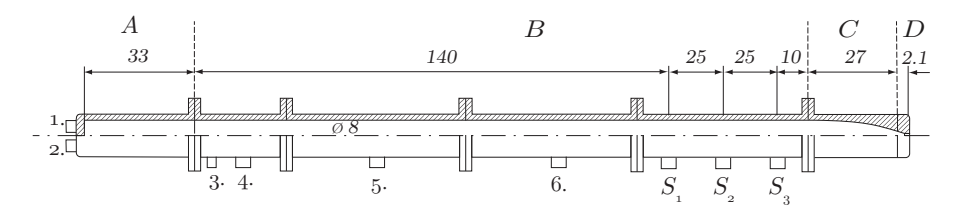


Figure 1: Circular shock tube used in the experiments. Legend, tube parts: (A) high pressure section; (B) inlet tube; (C) transformation section; (D) end cone. Connections: (1) driver gas inlet and pump; (2) pressure transducer; (3) membrane rupture indicator; (4) pressure transducer; (5) test gas valve; (6) vacuum pump.  $(S_1) - (S_3)$ : shock sensors. Measures in centimeters.

# 2. Experimental setup

#### 2.1. Shock tube

The experiments were conducted in the shock tube illustrated in Fig. 1. The tube has a circular cross section with diameter 80 mm and consists of a 0.33 m long high pressure section, 2 m long inlet tube, a transformation section 270 mm long ending into a 21 mm cone with  $21^{\circ}$  angle. The shape of the transformation is parameterized as

$$\begin{cases} x = Asin\theta \\ y = B - R(1 - cos\theta) \end{cases}$$
 (1)

where  $0 \le \theta \le 0.35\pi$ , A = 300.7 mm, B = 40.0 mm and R = 57.3 mm. It is made of a plastic cast held in place by a steel housing. The end cone is manufactured in steel with the tip cut 0.4 mm from its apex leaving a circular opening with radius 0.3 mm. The opening is sealed with 1.5 mm thick quartz window mounted in a frame of the steel tube and secured by brass sleeves. Argon of 99.99% purity was used as the main test gas and a few runs were made with nitrogen. The air is repeatedly evacuated and the tube filled with test gas. The membrane is opened mechanically: the high pressure section is filled with the driver gas through the inlet at (1) until the membrane bursts. The pressure pushes the membrane against a cross-knife which creates an even opening at a pressure-difference determined by membrane strength. The membranes used in the experiments were made from aluminum or mylar plastic film. The filling with driver gas - either helium or air - is made slowly to create uniform conditions in the high pressure section and avoid heating the driver. A second pump is connected to the high pressure section to evacuate the air in case pure helium is used as driver. A pressure transducer (Druck DPI 150)

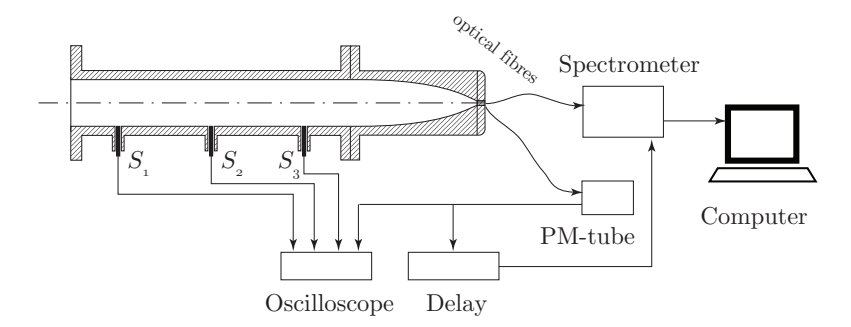


Figure 2: Schematic diagram of the spectrometric setup. The photomultiplier (PM) tube detects the first light from the shock wave, triggers a delay unit which in turn triggers the spectrometer. An oscilloscope stores the signals from the PM-tube and the shock sensors  $S_1 - S_3$ .

connected at (2) measured the breaking pressure, which varied with maximum 5% for any given membrane type.

#### 2.2. Diagnostics

A conductor with an insulating core is inserted through the tube wall in the low pressure section immediately behind the diaphragm, Fig. 1, connection (3). When the diaphragm is ruptured it is split in four leaf-shaped parts which hit the tube inner wall: the conductor is placed so that one leaf impacts on its tip creating a short-circuit to the tube which gives an indication of the start of the run.

The shock Mach number in the plane section is measured by shock sensors placed at three locations, x = 1.60, 1.85 and 2.10 m from the membrane  $(S_1, S_2, S_3)$ . The sensors are made of temperature-sensitive platinum film connected to high-pass amplifiers registering the sharp temperature gradients caused by passing shock waves.

Two optical fibers are mounted observing the opening through the window: one is placed along the axis of the tube directly against the window and a second at an angle, also directly against the glass. The fibers are used to collect light to photomultiplier tubes and/or a spectrometer. The spectrometer is an echelle type spectrometer, Aryelle 200 (Lasertechnik Berlin) with an ICCD camera (Andor Istar DH734 F.18). A solarization resistant fiber is used to enable UV recordings: as one unit the spectrometric setup can measure the light of wavelengths between 250 and 850 nm.

Figure 2 shows a diagram of the spectrometric arrangement. The spectrometer was triggered with an external trigger using a pulse generator (Stanford Systems DGP). Two ways to trigger the DGP were used: either the signal from

the photomultiplier tube when it detected the first light or with one of shock sensors. Neither way is optimal: using the photomultiplier a total delay of 200 ns occurs between the beginning of the implosion light pulse and the beginning of the spectrometer exposure such that the very beginning of the light pulse can not be measured. Using the signal from the shock sensor makes it difficult to time precisely, as the time between the shock passing the sensor and reaching the end point varies with  $\sim 2~\mu s$ .

The signals from the shock sensors and photo-multipliers were recorded on digital oscilloscopes (Tektronix TDS 2014).

2.2a. Spectrometer calibration. Wavelength calibration was made with a mercury lamp with the aid of the supplied software. The spectrometer has an echelle grating which splits the spectrum into an array of roughly a hundred different orders on the CCD. Within each of these orders the intensity varies towards the edges. To properly reconstruct the spectrum a radiometric calibration against a known source is necessary. A relative calibration was made with a calibrated deuterium lamp (Avantes D-Cal) and a wolfram lamp with known filament temperature (3000  $\pm$  50 K). The temperature of the wolfram filament was measured using two pyrometers and calculated by measuring the resistance  $R_{ref}$  at room temperature of the lamp and using tabulated values of  $R/R_{ref}$  vs T. The value of T is very sensitive to  $R_{ref}$ , and care was taken to measure it. The tension of the lamp was measured as close to the filament as possible, and the zero resistance was determined by extrapolation of R = U/I to U = 0. The resulting sensitivity curve for the spectrometer is shown in Fig. 3.

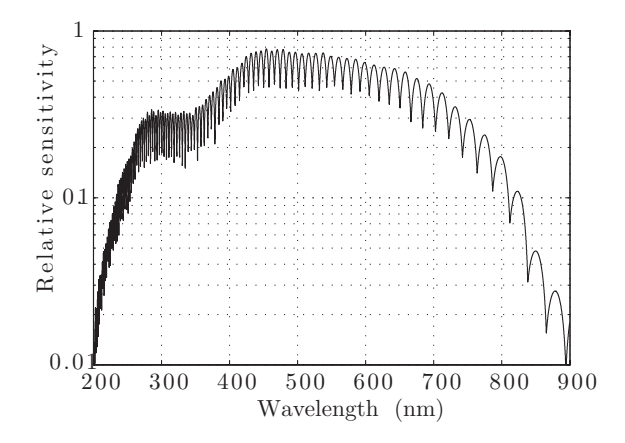


Figure 3: Relative sensitivity for the Aryelle system, including optical fiber.

#### 3. Calculations

The problem is simulated using the compressible and inviscid Euler equations. The fluid is treated as a non-reactive mixture of a number of ideal gases. The aim with the calculations is to predict the performance of the contraction, the symmetry of the shock waves and the shock acceleration. Ideal calculations can not predict the extreme conditions at focus after the shock has reflected at the end, and only the dynamics of the converging shock have been studied. Written in conservative form, the axisymmetric Euler equations are

$$\frac{\partial y\mathbf{U}}{\partial t} + \frac{\partial y\mathbf{F}}{\partial x} + \frac{\partial y\mathbf{G}}{\partial y} = \mathbf{W}$$
 (2)

where the vector **U** contains the conserved variables while **F** and **G** are the fluxes in x- and y-directions. The right hand side contains the axi-symmetric source term  $\mathbf{W} = [0, ..., 0, p, 0]^T$ . The conserved variables and fluxes are written as follows:

$$\mathbf{U} = \begin{pmatrix} \rho_{1} \\ \vdots \\ \rho_{N} \\ \rho u \\ \rho v \\ \rho E \end{pmatrix}, \quad \mathbf{F}(\mathbf{U}) = \begin{pmatrix} \rho_{1} u \\ \vdots \\ \rho_{N} u \\ \rho u^{2} + p \\ \rho v u \\ \rho E u + p u \end{pmatrix}, \quad \mathbf{G}(\mathbf{U}) = \begin{pmatrix} \rho_{1} v \\ \vdots \\ \rho_{N} v \\ \rho u v \\ \rho v^{2} + p \\ \rho E v + p v \end{pmatrix}$$
(3)

where  $\rho_1, ...., \rho_N$  are the mass densities of each species,  $\rho u$  and  $\rho v$  are the x- and y-momentum and  $\rho E$  the energy density. It is assumed each species follow the same bulk flow  $\mathbf{u} = (u, v)$  and diffusion is neglected. The energy of the gas mixture per unit mass is the sum of the specific internal energy and the kinetic energy:  $E = e_1 + ... + e_N + |\mathbf{u}|^2/2$ , where the internal energy of each species  $e_i = c_{p,i}T$ . Each species are assumed to individually fulfill the ideal gas law and the pressure is acquired from Dalton's law. The equations are discretized on an unstructured triangular mesh and solved with the flux-splitting AUFS schemed devised by Sun & Takayama (2003).

#### 3.1. Boundary conditions

At the wall slip conditions are enforced using ghost cells. The flow variables  $\rho$ ,  $\rho e$  and the tangential velocity are given symmetric values in the ghost cells, while the normal velocity is set anti-symmetric. In- and outflows are treated as determined by the waves passing the boundaries in a standard manner. At supersonic inflows all conserved variables are pre-set. At subsonic inflows the flow directions and total temperature and pressure are preset. The speed of sound at the boundary is calculated from the outgoing Riemann invariant acquired from the interior cells, which allows the conserved variables to be extracted

from the pre-determined total conditions. Symmetric boundary conditions are fulfilled by employing reflected ghost cells in the same manner as the solid walls.

#### 3.2. Test section

Several simulations were performed to tweak the shape of the transformation section prior to constructing it. The shape given in Eq. 1 was settled for and a parametric study was made to estimate its performance. The computational domain is sketched in Fig. 4. The origin is set to the end point on the x-axis, which is the axis of symmetry. The section x > -21 mm is the straight end cone and the end diameter at x = 0 is 0.6 mm. An initial shock wave of strength  $M_S$  is placed at x = -300 mm; the gas state on the shocked side determined from the Rankine-Hugoniot jump equations. For all cases,  $T_1 = 293$  K, corresponding to the ambient laboratory temperature. Symmetry and wall boundary conditions apply on all sides except the inlet, which is either sub- or supersonic depending on  $M_S$ .

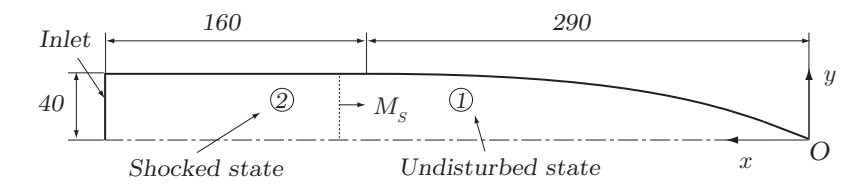


Figure 4: Computational domain.

The main goal of these simulations is twofold: to determine for different initial Mach numbers, (1) how circular and symmetric the shock waves are when exiting the transformation section and entering the end cone and (2) what degree of shock strengthening can be achieved?

Figure 5 shows numerical schlieren images at different time instants for a run with  $M_S=3.9,\ p_1=10$  kPa. The curving of the shock front begins at the foot and transplants towards the axis. As it propagates into the end cone it appears entirely circular by visual inspection. The deviation from a completely circular shape as a function of average radius inside the end cone is plotted in Fig. 6 for several initial Mach numbers. The geometry used for the calculation is shown in an inset image. The radius is measured from the virtual apex, situated 0.8 mm from the end wall and averaged for all angles  $0 < \theta < 21^\circ$ , whereas the radial deviation  $\Delta r$  is the maximum deviation from said average. The deviation oscillates around 4% for the whole Mach number range, although the fluctuations grow as the shock approaches to the end wall. It appears that the transformation section shapes the shock into

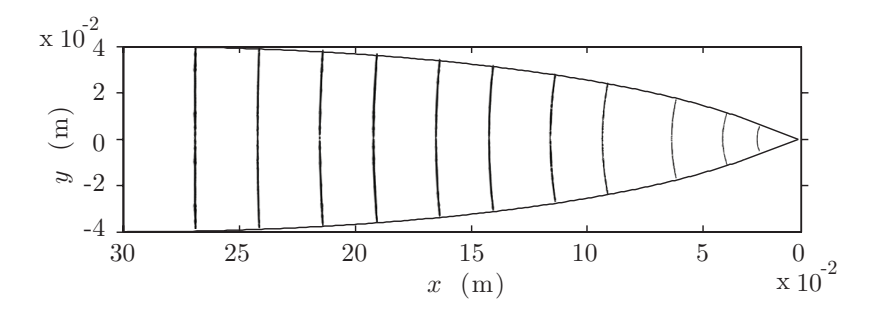


Figure 5: Numerical schlieren of the shock at different times. Calculations were made in the half-plane but the image is mirrored for clearer view.

an almost circular shape as it enters the cone, with little variation in Mach number. However, perturbations behind the shock wave eventually break down the symmetry just before collapse.

The acceleration of the shock front is plotted in Fig. 7. Self-similar curves are added for comparison according to Guderley's solution  $r = r_0(1 - t/t_0)^{\alpha}$ , where r is the radius and t the time,  $r_0$  and  $t_0 = t(r = r_0)$  the initial radius and time of focusing. The self-similarity constant for spherical shocks in argon  $(\gamma = 1.66)$  is  $\alpha = 0.688$ . The numerical solution agrees well with the self-similar path. For all Mach numbers the calculations show that the shape fulfills the design criteria well: an almost spherical shock wave propagating according to the self-similar convergent solution is formed. The shape is not flawless: unstable oscillations in the shock shape appear during the last millimeters. However, since in reality viscous effects will affect the flow the inviscid equations are not expected to yield more accurate predictions anyway, further tweaking to the shape was deemed gratuitous. Density contours behind the shock wave reveal the degree of asymmetry: Fig. 8 displays a few snapshots for a run with  $M_S$ =3.9,  $p_1$  = 10 kPa. Initially the density contours are close to circular, but as the shock wave progresses they become increasingly uneven. The origin of the dynamic instability shown in Fig. 6 can be seen. The deviation  $\Delta r/r \approx 0.075$ corresponds to that of a 18-sided polygon: at  $r \approx 0.5$  mm the shock front consists of two straight shocks normal to the wall meeting each other on the axis, corresponding to a cone-shaped shock in three dimensions. At this point the shock has accelerated to  $M \approx 25$ , a total amplification of  $\approx 6$ .

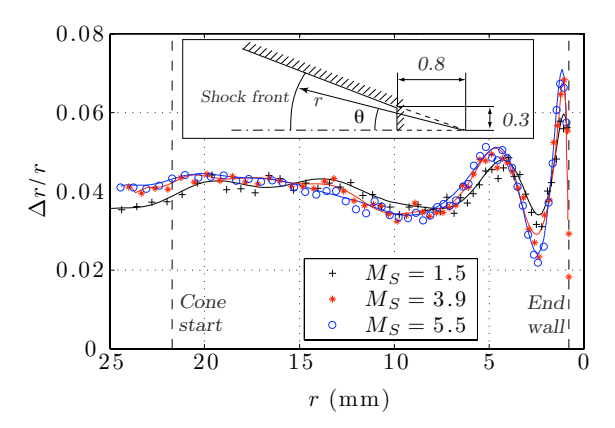


Figure 6: Deviation from spherical shock shape in the end cone for three initial Mach numbers,  $M_S = 1.5, 3$ . and 5.5. The deviation  $\Delta r$  in (a) is the maximum deviation from the average. Dashed vertical lines mark the positions of the cone base and the end wall, measured along the axis.

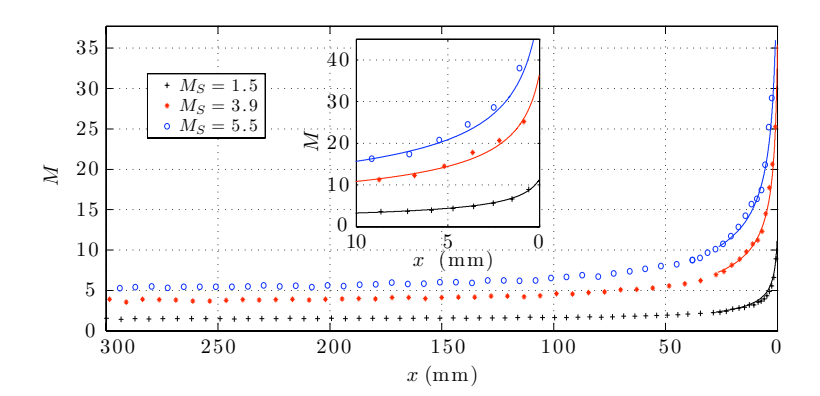


Figure 7: Shock front acceleration in the convergent section for three initial Mach numbers,  $M_S = 1.5, 3.9$  and 5.5. The Mach number along central axis is plotted; the major part of the shock strengthening takes place in the end cone, where the shock shape is nearly circular. Comparison with the spherical self-similar solution (full lines).

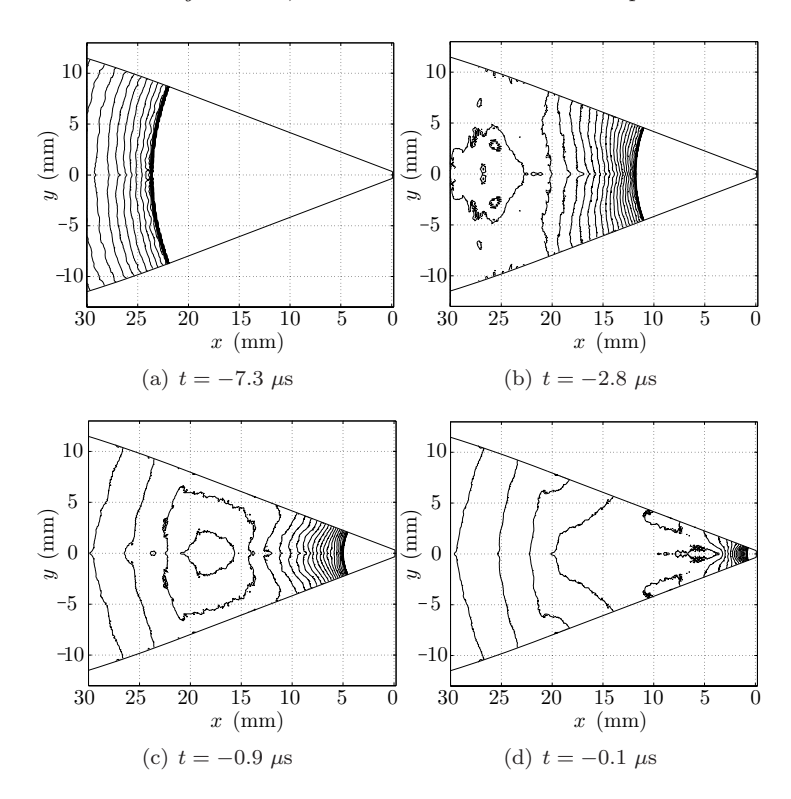


Figure 8: Isopycnics for shock wave with initial  $M_S = 3.9$  as it converges. The plots have been mirrored over the x-axis.

## 3.3. Whole tube

Simulations were made on the whole shock tube, with the computational domain as the shock tube with dimensions shown in Fig. 1. The origin is placed on the central axis at the membrane. All boundaries except the symmetric boundary were treated as slip walls. The purpose is to get a general feel of the shock tube flow. The initial conditions were determined from experiments, with a high and low pressure section of different gases and pressures, shown in Tab. 1. Results of the simulations are shown in the section Experiments - shock propagation.

# 4. Experiments

Several series of experiments were performed with argon as test gas. The propagation of the shock wave was measured for Mach numbers ranging from 1.8 to 6.0 and compared with calculations to confirm whether uniform flow with a constant velocity shock wave is formed. When the shock focuses, a bright light pulse is created in the hot gas and photometric measurements using two photomultiplier tubes connected to both optical fibers were made. A series of spectrometric measurements were made for initial Mach number and pressure  $M_S=3.9,\,p_1=10$  kPa, where spectra were measured at different times during the whole light pulse. Several experiments with weaker and stronger shock waves, in the range  $M_S=1.5-2.4$  and  $M_S=5.9-8$  were also conducted, and a few spectra measured. A series of runs in nitrogen were also performed, where the light was investigated.

#### 4.1. Shock propagation

The driver section is quite short which makes it vital to check whether the reflected expansion wave overtakes the shock front before convergence. One-dimensional calculations were made for the test cases in a tube with the same length but without changing cross-section using the standard methods (Oertel 1966). In all cases the shock reached the end wall long before upstream disturbances could reach the shock front. Numerical Euler calculations were performed for the shock tube geometry to compare with experimental data. The initial values for the calculations and experiments are listed in Tab. 1.

#	Driver	Test gas	$p_4$ kPa	$p_1$ kPa	$M_S$
1 2 3	$\begin{array}{c} \text{air} \\ \text{He+6\%} \\ \text{He} \end{array}$	Ar Ar Ar		$10.00 \pm 0.01$ $10.00 \pm 0.01$ $0.88 \pm 0.01$	$1.8 \pm 0.05$ $3.9 \pm 0.05$ $6 \pm 0.1$

Table 1: Tests on shock propagation, for all cases  $T_1 = T_4 = 293$  K. Measured experimental data of high and low pressures  $p_4$  and  $p_1$  and Mach number  $M_S$  with maximal variation between runs.

Numerical wave diagrams determined from the Euler calculations are shown Fig. 9 and 10. The time instants when the shock sensors detected the shock waves are indicated with circles and the photomultiplier signals detecting shock focus by squares. The corresponding shock sensor and photomultiplier records are shown in Fig. 11. In the  $M_S=6$  case the reflected shock wave meets the contact surface before the reflected expansion. The shock breaks at the

interface, a transmitted shock passes through it and a reflected shock returns downstream and converges. This second convergence is registered experimentally, but the timing is wrong. Significant numerical smearing of the contact surface makes quantification of the flow after the converging difficult. The main result however, is that the front shock converges in all cases without disturbances catching up with it.

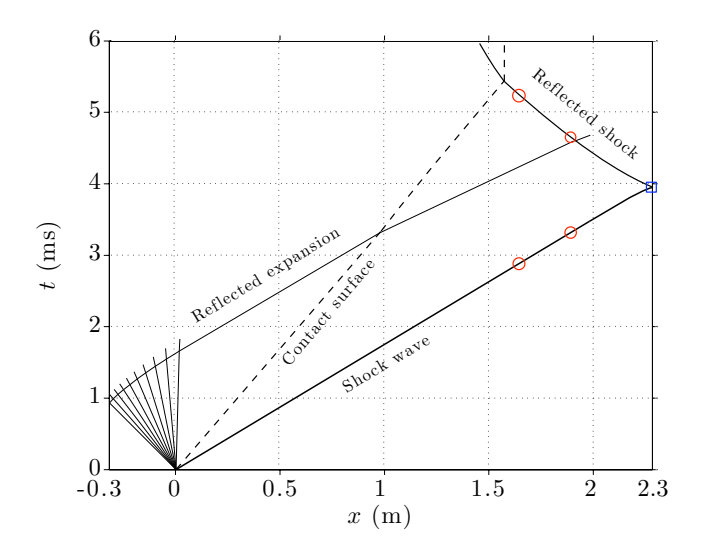
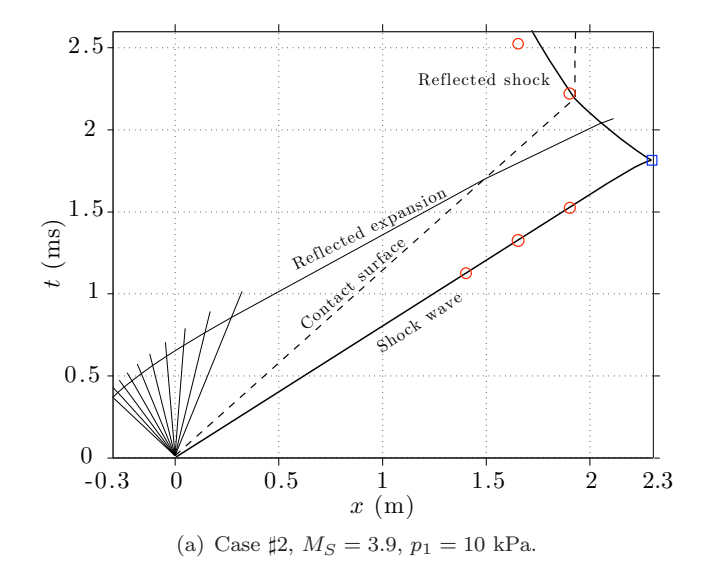


Figure 9: Numerical wave diagram of case  $\sharp 1$  in air-argon,  $M_S=1.8,\,p_1=23$  kPa, along the central axis of the tube. Circles indicate detection of shock waves passing the shock sensors and the square the instant of focusing as recorded by the photomultiplier tube. The diaphragm is positioned at x=0 and bursts at t=0.



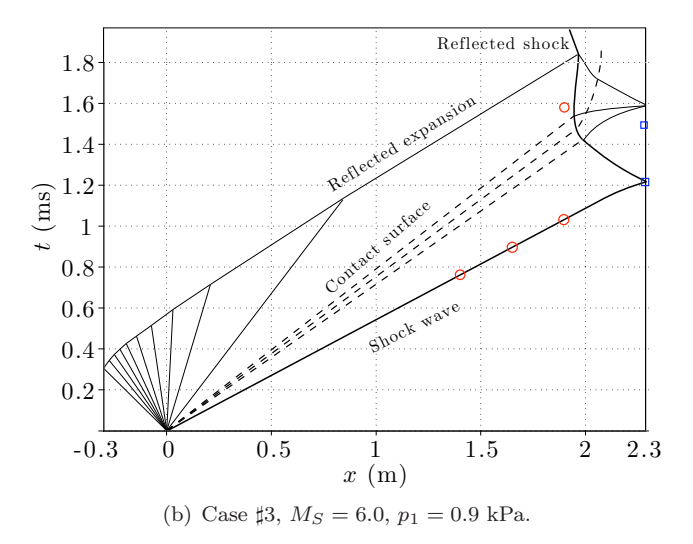


Figure 10: Numerical wave diagrams of shocks in argon, (a)  $M_S=3.9$  and (b)  $M_S=6$ , along the central axis of the tube. Circles indicate detection of shock waves passing the shock sensors and squares the instant of focusing as recorded by the photomultiplier tube. The diaphragm is positioned at x=0 and bursts at t=0.

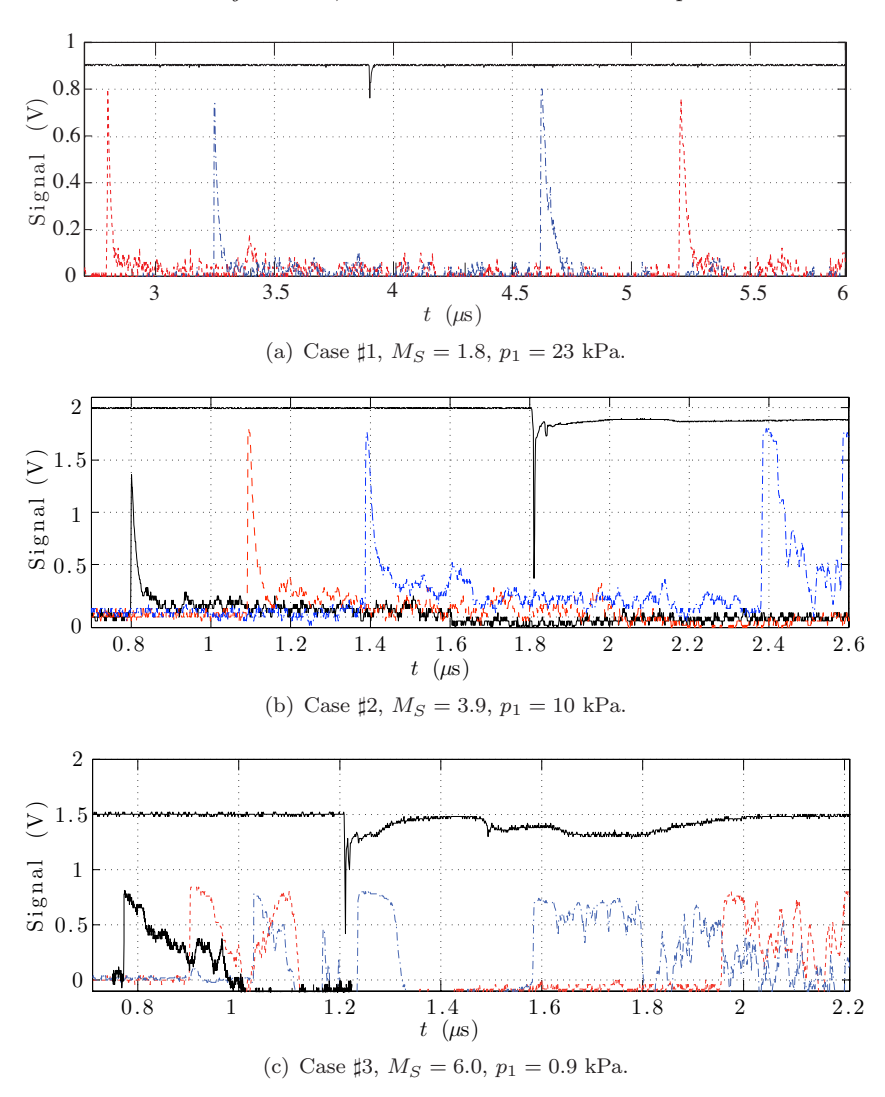


Figure 11: Shock sensor and photomultiplier signals from three experiments in argon, (a)  $M_S = 1.8$ ; (b)  $M_S = 3.9$ ; and (c)  $M_S = 6$ . The three shock sensors (black –, red – –, blue—) detect sharp temperature gradients whereas the photomultiplier (uppermost line) records the light emission at focus.

#### 4.2. Photomultiplier records

The light pulse at the implosion was measured with each fiber connected to a separate photomultiplier (PM) tube. In our setup the output PM signal drops as the light intensity increases. Fig. 12 shows the readouts from both fibers from the same run in argon,  $M_S$ =3.9 at  $p_1$  = 10.0 kPa. The red dashed line shows the signal from the axially mounted fiber while the full black line shows the signal from the oblique fiber. Both photomultipliers were supplied with the same bias voltage (-1000 V). Two distinguishing differences can be seen. The oblique fiber, viewing at most 0.5 mm into the chamber detects a sharp dip (corresponding to a peak in measured light) at shock implosion and a fading light for about 50  $\mu$ s. The axially mounted fiber detects a rise in light intensity before the implosion: the light emitted from behind the shock front is seen before the shock converges to the end. About 16  $\mu$ s after implosion a second peak in intensity occurs. The nature of the light in each peak will be further discussed below.

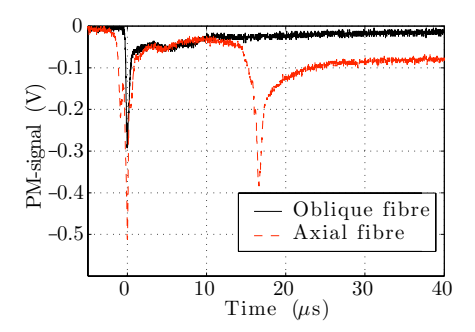


Figure 12: Photomultiplier records from shock in argon at  $M_S = 3.9$  at  $p_1 = 10.0$  kPa. Two photomultipliers were used, one was fed with light from fiber 1, viewing along the central axis of the tube, and the second from fiber 2, viewing only the 0.6 mm opening. The combined signals show that the shock becomes illuminating before hitting the glass, but the sharp first dip is created at the shock convergence The axially mounted fiber registers light emanating from further inside. Especially noticeable is the second large dip.

The light pulses show only minor variation between different runs for all tested Mach numbers and pressures. Figure 13 shows measured light pulses for different Mach numbers and pressures. For each case signals from several runs are plotted together to show run-to-run variations. It is apparent that the shock implosion is stable in the sense that very similar signals are generated; the first dip due to the immediate implosion shows the highest degree of repeatability.

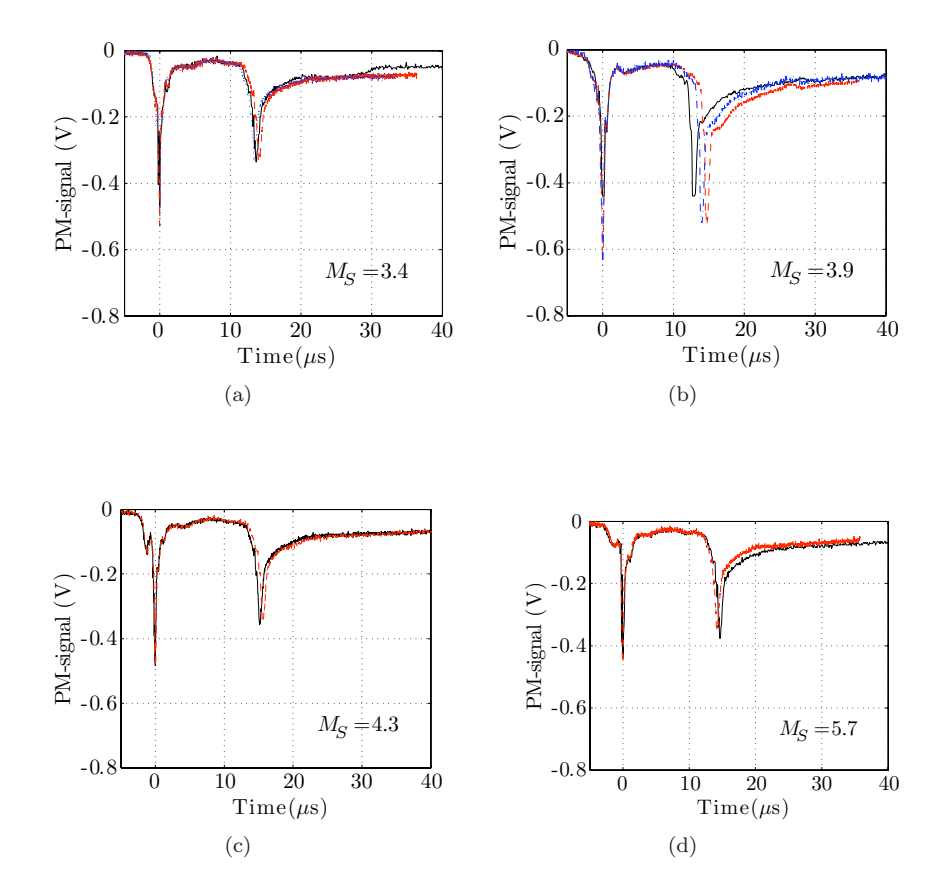


Figure 13: Photomultiplier records of runs in argon (axial fiber), (a)  $M_S = 3.4$  at initial pressure  $p_1 = 20.0$  kP; (b)  $M_S = 3.9$ ,  $p_1 = 10.0$ ; (c)  $M_S = 4.3$ ,  $p_1 = 5$  kPa.; and (d)  $M_S = 5.7$ ,  $p_1 = 1.00$ . The first dip corresponds to the convergence of the shock at the cone end.

The second peak is not visible with the fiber viewing the glass at an oblique angle; hence the emitting source is further inside the cone. A small variational study was performed to see the dependency on pressure and Mach number. Table 2 shows a number of runs comparing the delay between peaks and Fig. 14 shows the corresponding photomultiplier records. Increasing either the pressure or Mach number while keeping the other constant increases the time between the peaks. The weakest shock showed no second dip at all: it had either merged with the first or the conditions of its generation were not created.

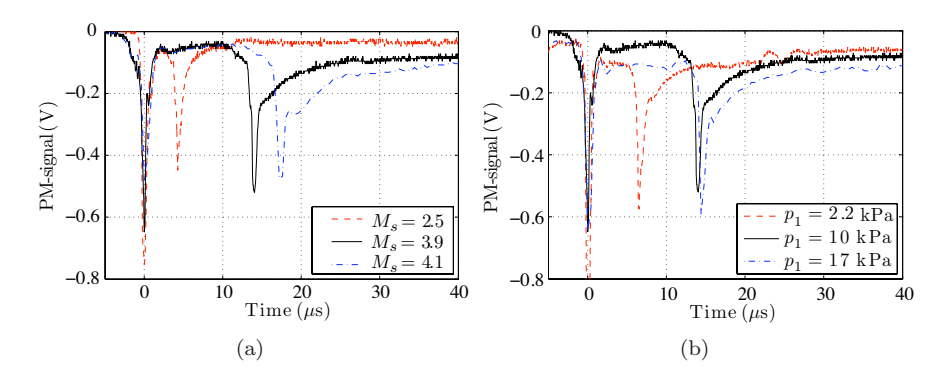


Figure 14: Photomultiplier records comparing the appearance of the second peak. Same initial pressures  $p_1 = 10$  kPa with varying Mach numbers (a) and same initial Mach numbers  $M_S = 3.9$  for different pressures (b).

$M_S$	$p_1$ (kPa)	Time between peaks ( $\mu$ s, $\pm 0.2$ )
2.1	10	one peak only
2.5	10.0	4.5
3.9	10.0	14
4.1	10.0	17
3.9	2.2	6.6
3.9	17	14.5

Table 2: Time between first and second peak in photomultiplier signals.

# 4.3. Spectrometric results

4.3a. Time-resolved,  $M_S=3.9$ ,  $p_1=10~kPa$ . Runs with  $p_1=10~kPa$  and  $M_S=3.9$  created emission of roughly 50  $\mu$ s duration. The spectra from the light pulses were measured at different time instants relative to the shock implosion (Fig. 15). The spectrometer only allows one exposure per run, but the high degree of repeatability as shown by the photomultiplier records allow this method to give a reasonable accurate overview of a single event. Fig. 15 shows calibrated spectra where each separate exposure lasts 100-3,000 ns. Each spectrum has been normalized by dividing the measured intensity with the exposure time. The spectrometer was triggered by the light collected in the obliquely mounted fiber connected to the photomultiplier tube. In Fig. 16(a) the average signal over ten runs is shown together with the standard deviation limits (dashed lines). In Fig. 16(b) the start of the exposure times for each spectrum in Fig. 15 is shown in a generic photomultiplier signal from the axially mounted fiber.

The spectra obtained in the beginning of the light pulse resemble blackbody radiation and fits were made to Planck's function:

$$I_{\lambda}(\lambda, T) = \frac{2hc^2}{\lambda^5} \frac{1}{\exp(hc/\lambda kT) - 1}$$
(4)

where  $I_{\lambda}$  is the intensity per unit wavelength  $\lambda$ , h is Planck's constant, c the speed of light and k Boltzmann's constant. Least square fits to the spectra obtained from 0.25 to 7  $\mu$ s after implosion show good agreement with the Planck curve. The fitted curves are plotted as dashed lines. The fits show apparent blackbody temperatures of maximum  $27,000 \pm 1,000$  K at approximately 250 ns after the maximum light intensity (see Fig. 16) and about 10,000 K as the time increased to 7  $\mu$ s. Due to trigging limitation the maximum intensity region has not yet been investigated spectrometrically. At about 11  $\mu s$  after the implosion, the continuum is replaced by two bands at 310-320 nm and 380-400 nm, which are believed to emanate from aluminum, see Fig. 15 (f). In order to capture the spectrum during the second light peak a longer delay time as well as a longer exposure time,  $t_{exp} = 3$  were chosen. The resulting spectrum shows a large number of lines at longer wavelengths originating from electronic excitations in neutral argon, see Fig. 15 (g). It should be noted that in this setup the photomultiplier collects light from the oblique fiber and it can thus not be verified that this spectrum was really taken during the second light peak, although the repeatability suggests it. At 20  $\mu$ s after the maximum light peak, the spectrum resembles the ones measured during the period of low intensity between the first and second light intensity peaks, see Fig. 15(f) and Fig. 16(b). Lines from neutral argon are still present.

4.3b. Nitrogen run. A few experiments using nitrogen as test gas were made. A photomultiplier record of a run with initial pressure and Mach number  $p_1=1.7$  kPa and  $M_S=5.3$  respectively is shown in the inset image in Fig. 17. The radiation intensity was measured with the axial fiber and a striking result is that the second light peak present in argon is entirely missing. The light spectrum was integrated over the whole light pulse and a typical result is presented in Fig. 17. No continuum radiation is present but a large number of bands and lines are seen. Two prominent bands of aluminum lines are found at 290–320 nm and 380–410 nm. Three successive bands of AlO emissions are seen in 450–540 nm. A persistent sodium line appeared at 583 nm, with two harmonics. In the infrared region several pairs of lines possibly originating in atomic iron are also present. No nitrogen lines are found, which may be explained by the fact that excited energy modes in nitrogen have far longer lifetimes than the time frames involved here.

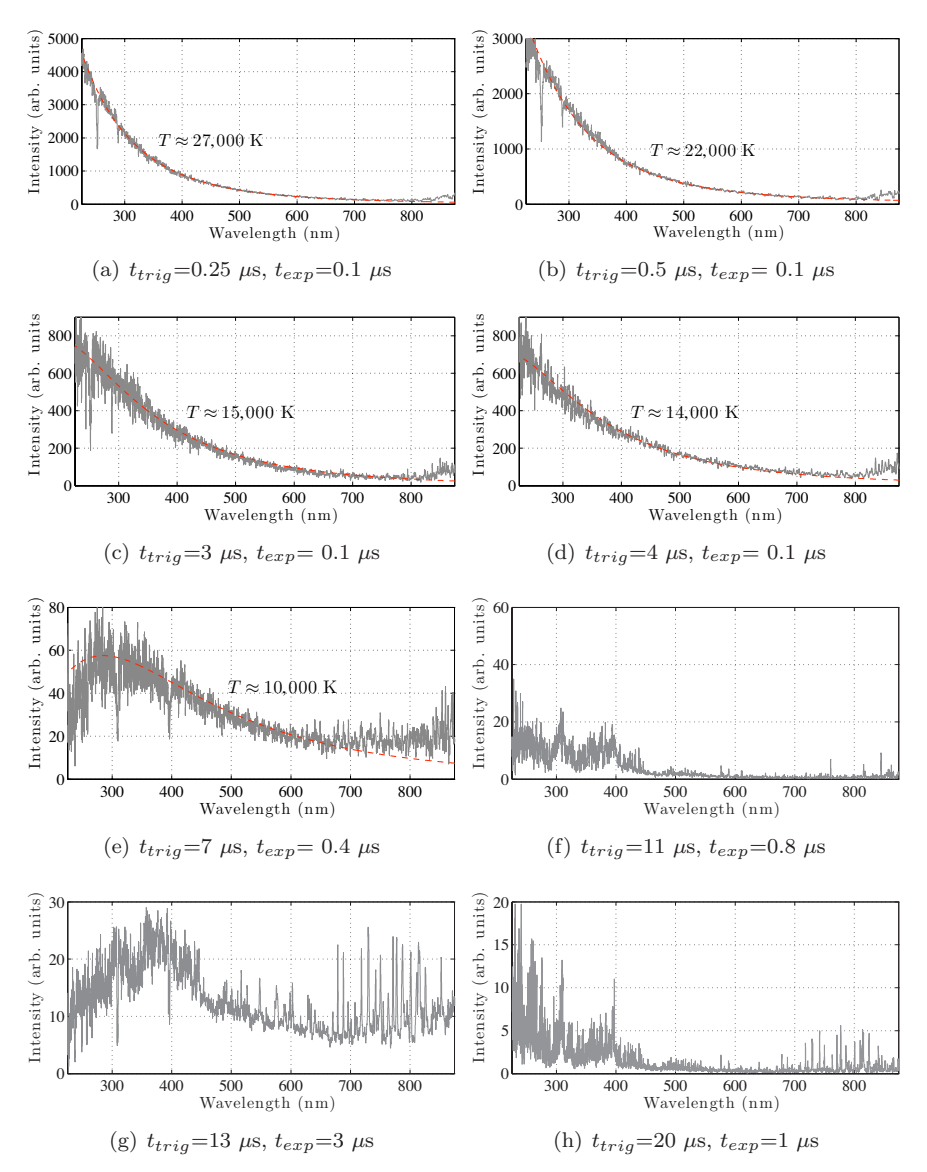


Figure 15: Spectra from converging shock in argon. Initial  $M_S$ =3.9,  $p_1$ =10 kPa. The spectra are taken during separate runs at different times relative to the shock implosion,  $t_{trig}$ , and with varying exposure times,  $t_{exp}$ . For (a)-(e), blackbody curve fits (dashed, red) are also plotted in the spectra. Note that (g) is taken during the second intensity peak.

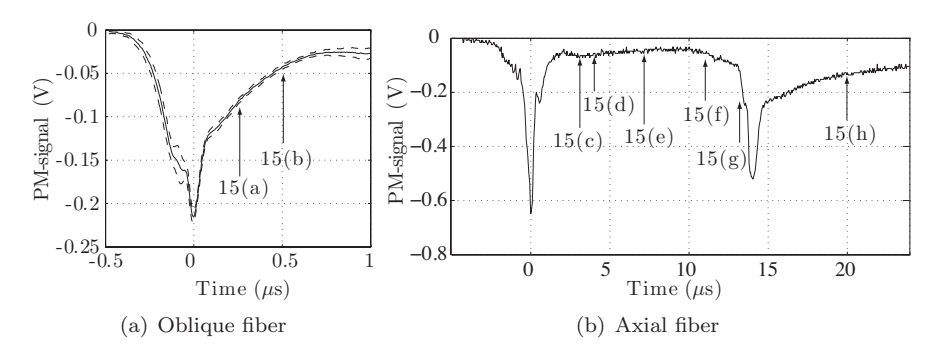


Figure 16: Photomultiplier signals of shock in argon at  $M_S = 3.9$ ; (a) signal from the oblique fiber, showing the averaged signal of ten runs, with standard deviation limits (dashed lines) and (b); signal from the axial fiber, a generic signal showing start time of spectrometer exposure (arrows) for the spectra in Fig. 15.

4.3c. Argon spectra for higher and lower initial Mach numbers. Referring to the wave diagram in Fig. 10(b): the original shock is after implosion reflected and propagates upstream the tube. It meets the contact surface and breaks, creating a transmitted and a reflected shock traveling downstream towards the convergence section. This creates a second converging shock which reaches the tip of the conical section around 300  $\mu$ s after the first shock implosion. The photomultiplier records this second convergence, as seen in Fig. 11(c). The light from this second implosion was measured with the spectrometer and the result is shown in Fig. 18. A continuum spectrum with apparent blackbody temperature of 7, 400±200 K is superimposed on lines from transitions between the 4s-4p shells in Ar. It is the same persistent lines seen in the spectrogram for the runs with  $M_S$ =3.9 as well as the previous cylindrical experiments (Kjellander et al. 2010), albeit many times stronger.

Runs with weaker shock waves were made using mylar film as diaphragms. With initial Mach numbers in the range between 1.5 and 2 significantly weaker light intensities are expected. From these runs, the strongest blackbody spectrum shows peak temperatures of  $10,000\pm1,500$  K. Below this temperature the blackbody spectrum is too weak in comparison with the strong "noise" spectrum which is most clearly visible in the nitrogen runs but is also present here.

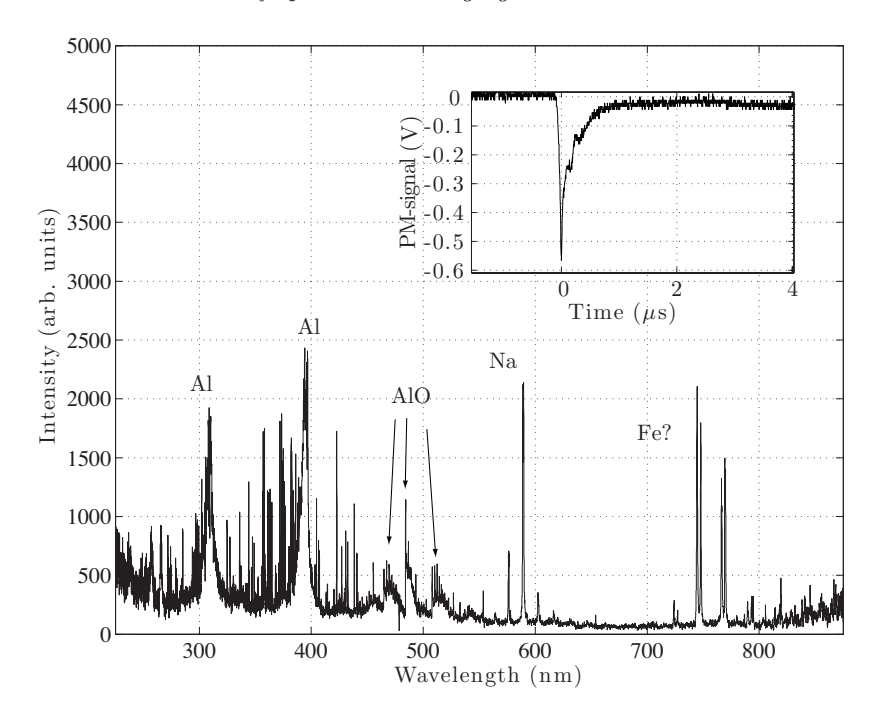


Figure 17: Spectrum of shock in nitrogen,  $M_S = 5.3$ ,  $p_1 = 1.7$  kPa. Inset image shows a typical photomultiplier signal (axial fiber) of the light pulse. The spectrometer exposure time was set to cover the whole pulse.

# 5. Discussion

The fiber collecting light for the spectrometer looks along the central axis of the tube. If the radiating gas is transparent, light is collected from an extended volume of gas with large gradients of temperature and pressure making quantitative analysis difficult. During the 4  $\mu$ s between the first four spectra in Fig. 15 the reflected shock wave has propagated approximately 1 cm back into the tube so the size of the hot region increased significantly. However, the measured intensity levels of the four spectra scale equally with the theoretical blackbody intensity, which indicates that the fiber only sees light from the surface of a dense gas appearing as a blackbody which screens the colder area further inside the tube. This lasts until about 5  $\mu$ s after shock collapse. At this time the spectrum (see Fig. 15e) has a higher intensity than would be expected from the intensities of the earlier spectra. This supports the idea that at later times the fiber sees a deeper volume emitting light.

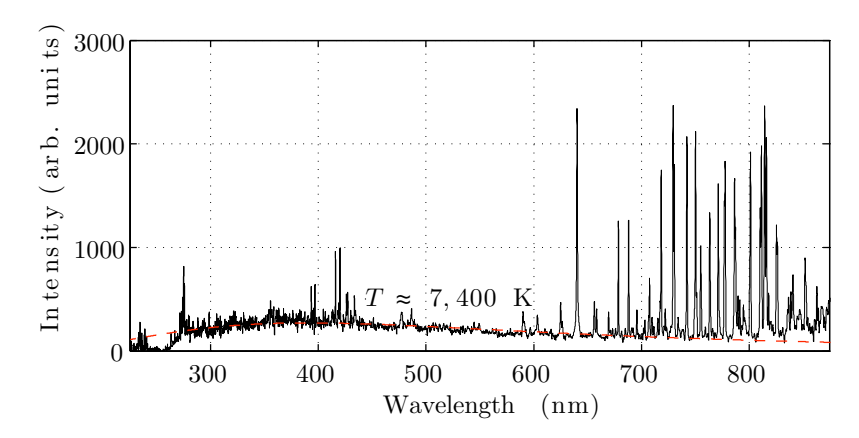


Figure 18: Spectrum taken from shot in argon during convergence of the reflection of the diverging shock, 300  $\mu$ s after initial focus of the primary shock wave. A continuum spectrum with apparent blackbody temperature of  $T=7,400\pm200$  K is superimposed on lines from transitions between the 4s-4p shells.

5.0d. Shock strength amplification. As the shock velocity was not measured in the end cone an estimate of the shock strengthening has to be made. For the  $M_S = 3.9$  case, the ideal calculations show a final Mach number of  $\sim 25$  when the front is less than 1 mm from the glass surface. The shape of the shock wave quickly brakes down during the last millimeter and does not further accelerate in the exponential manner of a spherical shock. In reality viscous and non-ideal effects are expected to negatively affect the symmetry and  $M \approx 25$  is therefore taken as an upper limit. After reflection at the end, the gas between the shock wave and the glass is excited to frozen conditions, determined by the Rankine-Hugoniot equations. Ionization proceeds, decreasing the temperature as electrons are separated from the atoms. The measured blackbody temperature of 27,000 K correspond to the frozen temperature behind a reflected shock of  $M \approx 11-12$ , which is taken as the lower limit. It should be noted that the measured temperature is not inconsistent with an upper limit of M=25. Although the frozen temperature behind a reflected shock of that strength is in excess of  $1 \times 10^5$  K, the equilibrium temperature after ionization is only around 33,000 K. Several theoretical studies (Bond 1954; Hoffert & Lien 1967; Biberman et al. 1971) and experimental studies (Petschek & Byron 1957; Brimelow & Glass 1974) on the shock structure in argon have been made, covering the relevant Mach ranges and a successful model of the processes has been created. Using the collision model of Hoffert & Lien the relaxation time to the ionization equilibrium behind a reflected shock with incident Mach number M=25 can be estimated to less than 10 ns. Further, the maximum measured temperature was acquired about 250 ns after the maximum peak in light intensity, where no spectroscopic measurements were made. A factor complicating the matter is that several different physical phenomena are involved in the plasma cooling process: ionization relaxation, expansion caused by the reflected shock wave and radiation. As the highest temperatures are concentrated to a very small space close to the window it is expected that radiative cooling rapidly lowers the temperature as most radiation can escape from the hot core. To answer the raised questions a collisional-radiative model accounting for ionization and radiation could be incorporated in the numerical calculations. In other words the maximum acceleration and temperature in the focusing shock is still an open question.

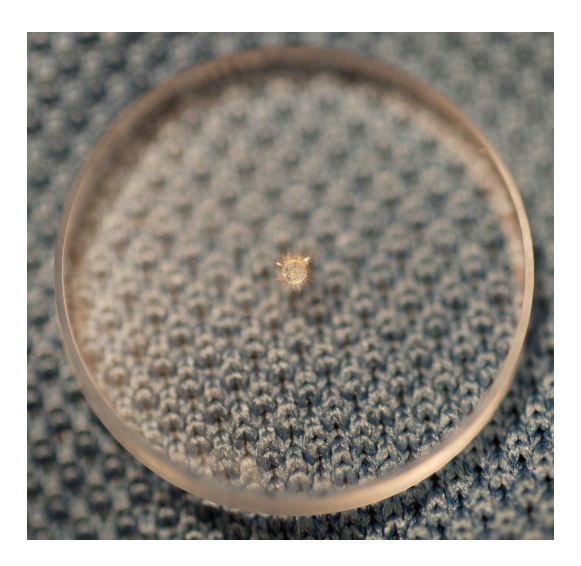


Figure 19: Viewing glass damage caused by the focused shock.

5.0e. Absorption and emission spectra. Absorption lines on a blackbody spectrum may signify a colder gas in front of the blackbody source. In the spectra taken close after the focusing instant, Fig. 15(a)-(c), there are abbsorption lines centered around 252 and 288 nm. These are presumably Si lines, indicating that part of the quartz surface has been vaporized. Later on, about 5–7  $\mu$ s after the peak, absorption lines around 310 and 390 nm appear, see Fig. 15(e). These lines seem to be directly related to the band emissions appearing around 10-11  $\mu$ s (f). The bands probably origin in aluminum indicating a possibility

that aluminum from broken membranes during previous runs have been transported to the cone<sup>1</sup>, where it is subsequently vaporized by the shock. The absorption and emission lines reappear in Fig. 15(g) and (h) respectively, during and after the second peak in light intensity. Fig. 19 shows the damage on the viewing glass. The viewing part of the glass was shifted after each run. With an undamaged surface facing the tube opening the aluminum can not have been deposited on the glass during previous runs. An explanation could be that there is a shock-evaporated Al-gas between the glass surface and the upstream moving shock. Initially the gas immediately behind the shock has a higher temperature relative the Al-gas and absorption lines appear as the strong blackbody radiation first passes through the aluminum. At later time the temperature relation is inversed, resulting in Al-emission lines.

5.0f. Second peak in intensity. It was first speculated that the second intensity peak is a result of reflections creating a high-temperature region, but test shots with nitrogen (see e.g. inset image in Fig. 17) did not produce a similar second peak and neither do calculations indicate any such occurrence. The spectrum taken during this time Fig. 15(g) shows increased emission-lines and continuum (not blackbody) from argon but it has not been further analyzed. The intensity seems too low compared to measured PM-signals which suggests that there is radiation outside the range of the spectrometer.

5.0g. Comparison with previous experiments. Roberts & Glass (1971) measured the light emission from explosive-driven shocks in a spherical chamber where the shock waves were initiated in the center by ignition of the combustible test gas and left to reflect on the periphery and converge back to the center. Saito & Glass (1982) continued the experiments and improved upon the measurements. Photographs of the 350-600 nm spectrum were made and they concluded that the plasma emitted as a blackbody. They also made time-resolved recordings of the emission at eight separate wavelengths and found a maximum temperature of 17,000 K. Although the observed area was almost identical in size as in the present experiments direct quantitative comparisons can not be made due to the difference in test gas and that, in their case, the shock wave converged in a gas already pre-heated by the combustion. In both experiments however, a clear blackbody spectrum was seen.

# 6. Conclusions

Spherical shock waves were created in a regular circular shock tube using a smooth converging transformation of the tube wall designed to shape the plane shock into the form of a spherical segment. Numerical calculations were made to find a shape of the transformation section that achieved that goal. Shock tube runs using argon and nitrogen as test gas were made. The light created at

 $<sup>^{1}</sup>$ Aluminum dust can be found on the wall inside the tube after many runs.

the implosion focus was measured with photomultipliers and spectrometer. For a series in argon at initial Mach number  $M_S=3.9$  strong blackbody spectra of apparent temperatures of up to 27,000 K were measured, indicating a minimum final shock Mach number of  $M\approx 12$ , but most probably the real value is much higher. The spectra were not measured during the time of most intense light, and the estimate of M=12 makes use of the frozen temperature. Ionization relaxation at the high pressures and temperatures involved is such a fast process that possibly only the temperature after equilibrium ionization was measured. A second peak in light intensity was detected, seemingly from an argon plasma continuum and emission-lines. The precise origin of the second peak is not known. It appeared in argon for  $M_S>2.1$ , but not at all in nitrogen.

## Acknowledgements

The authors gratefully acknowledge the loan of equipment from the KTH Applied Physics department and the communication with Olli Launila and Lars-Erik Berg, especially concerning interpretation of spectra. The project was funded by the Swedish Research Council (VR) and the Göran Gustafsson foundation.

# References

- BIBERMAN, L. M., MNATSAKANYAN, A. K. & YAKUBOV, I. T. 1971 Ionization relaxation behind strong shock waves in gases. Sov. Phys. Usp. 13, 728–744.
- BOND, C., HILL, D. J., MEIRON, D. I. & DIMOTAKIS, P. E. 2009 Shock focusing in a planar convergent geometry: experiment and simulation. *J. Fluid Mech.* **641**, 297–333.
- BOND, J. 1954 The structure of a shock front in argon. Los Alamos Sci. Lab Rept. LA-1693
- BRIMELOW, P. I. & GLASS, I. I. 1974 An interferometric investigation of shock structure and its induced shock-tube boundary layer in ionized argon. Institute for Aerospace Studies, University of Toronto.
- Butler, D. S. 1954 Converging spherical and cylindrical shocks, Report No. 54/54. Burgess Hill, New York.
- DUMITRESCU, L. Z. 1983 Studies on shock amplifications, focusing and stability. In *Shock waves and shock tubes; Proc. 14th Intern. Symp.* (ed. R. Archer & B. Milton). Sydney, Australia: Univ. of New South Wales Press.
- DUMITRESCU, L. Z. 1992 On efficient shock-focusing configurations. In 11th Australasian Fluid Mechanics Conference, pp. 723–725. Hobart, Tasmania: University of Tasmania.
- ELIASSON, V., APAZIDIS, N., TILLMARK, N. & LESSER, M. B. 2006 Focusing of strong shocks in an annular shock tube. *Shock Waves* **15**, 205–217.
- Glass, I. I. & Sagie, D. 1982 Application of explosive-driven implosions to fusion. *Phys. Fluids.* **25**, 269.
- GLASS, I. I. & SHARMA, S. P. 1976 Production of diamonds from graphite using explosive-driven implosions. AIAA J. 14, 402–404.
- GUDERLEY, G. 1942 Starke kugelige und zylindrische Verdichtungsstöße in der Nähe des Kugelmittelpunktes bzw. der Zylinderachse. Luftfahrtforschung 19, 302–313.
- HOFFERT, M. I. & LIEN, H. 1967 Quasi-one-dimensional, nonequilibrium gas dynamics of partially ionized two-temperature argon. *Phys. Fluids* **10**, 1769.
- KJELLANDER, M., TILLMARK, N. & APAZIDIS, N. 2010 Thermal radiation from a converging shock implosion. *Phys. Fluids* **22**, 046102.
- LAZARUS, R. B. & RICHTMYER, R. D. 1977 Similarity Solutions for Converging

- Shocks. Los Alamos Scientific Laboratory of the University of California, Los Alamos, NM.
- OERTEL, H. 1966 Stossrohre. Springer-Verlag, Wien.
- Perry, R. W. & Kantrowitz, A. 1951 The production and stability of converging shock waves. J. Appl. Phys 22, 878–886.
- Petschek, H. & Byron, S. 1957 Approach to equilibrium ionization behind strong shock waves in argon. Ann. Phys. 1, 270–315.
- ROBERTS, D. E. & GLASS, I. I. 1971 Spectroscopic investigation of combustion-driven spherical implosion waves. Phys. Fluids 14, 1662–1670.
- Saillard, Y., Barbry, H. & Mournier, C. 1985 Transformation of a plane uniform or spherical shock by wall shaping. In Shock waves and shock tubes; Proc. 15th Intern. Symp., pp. 147-154. Stanford, CA: Stanford University Press.
- Saito, T. & Glass, I. I. 1982 Temperature Measurements at an Implosion Focus. Proc. R. Soc. Lon. A 384, 217–231.
- SETCHELL, R. E., STORM, E. & STURTEVANT, B. 1972 An investigation of shock strengthening in a conical convergent channel. Phys. Fluids 56, 505-522.
- STANYUKOVICH, K. P. 1960 Unsteady motion of continous media. Pergamon, Oxford.
- Sun, M. & Takayama, K. 2003 An artificially upstream flux vector splitting scheme for the Euler equations. J. Comput. Phys. 189, 305–329.
- TAKAYAMA, K., KLEINE, H. & GRÖNIG, H. 1987 An experimental investigation of the stability of converging cylindrical shock waves in air. Exps. Fluids 5, 315–322.
- TERAO, K., AKABA, H. & SHIRAISHI, H. 1995 Temperatures in imploding detonation waves. Shock Waves 4, 187-193.
- WANG, J. C. T. 1982 On the theory of imploding shocks. J. Appl. Math. Phys. 33,
- Watanabe, M. & Takayama, K. 1991 Stability of converging cylindrical shock waves. Shock Waves 1, 149–160.
- WHITHAM, G. B. 1959 A new approach to problems of shock dynamics. part 2. three-dimensional problems. J. Fluid Mech. 5, 369–386.
- Wu, J. H. T., Elabdin, M. N., Neemeh, R. A. & Ostrowski, P. P. 1977 Production of converging cylindrical shock waves by finite element conical contractions. In Shock tube and shock wave research: Proc. Eleventh Intern. Symp. on Shock Tubes and Waves, pp. 107-114. Seattle, Wash., USA: University of Washington Press.
- ZHAI, Z., LIU, C., QIN, F., YANG, J. & LUO, X. 2010 Generation of cylindrical converging shock waves based on shock dynamics theory. Phys. Fluids 22, 041701.